UNIVERSITY OF SOUTHAMPTON

FACULTY OF ENGINEERING, SCIENCE AND MATHEMATICS

School of Chemistry

Extending *in situ* XAS of PEM Fuel Cells to more Realistic Conditions

by

Richard John Kenneth Wiltshire

Thesis for the degree of Doctor of Philosophy

April 2005

UNIVERSITY OF SOUTHAMPTON

ABSTRACT

FACULTY OF ENGINEERING, SCIENCE AND MATHEMATICS

School of Chemistry

Doctor of Philosophy

EXTENDING IN SITU XAS OF PEM FUEL CELLS TO MORE REALISTIC CONDITIONS

By Richard John Kenneth Wiltshire

One of the challenges facing the further development of fuel cells is an understanding of the catalyst structure and in turn, how this relates to performance. In an effort to advance research in this area, a miniature PEM fuel cell has been designed to enable *in situ* X-ray Absorption Spectroscopy (XAS) investigations of catalysts using fluorescence detection. The development of the cell is described, in particular the modifications required for elevated temperature operation and humidification of the feed gasses.

The electrocatalytic activity of a series of carbon supported PtRu anode catalysts towards the electro-oxidation of CO and oxidation of methanol were studied. It was found that in both cases, the PtRu 1:1 catalyst gave the highest performance. Particle segregation was observed in the platinum rich catalysts with a ruthenium rich core and a platinum rich surface relative to the bulk composition. Further XAS studies of the PtRu 1:1 catalyst were carried out in a PEM fuel cell. Operating conditions were found to have a significant impact on catalyst utilisation. The Pt component was readily reduced by hydrogen in the fuel, while the Ru component was only fully reduced under conditions of good gas flow and electrochemical contact. Upon introduction of reformate, no evidence of carbon neighbours were observed. This was interpreted in relation to the lack of surface sensitivity of the Extended X-ray Absorption Fine Structure (EXAFS) method.

The activity towards the oxygen reduction reaction was studied using carbon supported PtCr, PtCo and PtTi cathode catalysts. XAS studies revealed that the Pt-Pt distance, intrinsically linked to the Pt electronic properties, gave the best indication of oxygen reduction activity. No correlation was observed between the number of Pt-O coordination numbers and catalyst activity. This implies that under realistic fuel cell conditions, site blocking by oxide formation is not as significant as first thought.

TABLE OF CONTENTS

Chapter One: Introduction **1**

1 GENERAL INTRODUCTION **1**
1.1 History 1
1.2 Environmental Factors 2
1.3 Applications 3
2 FUEL CELL PRINCIPLES **4**
3 TYPES OF FUEL CELL **6**
3.1 AFC 6
3.2 PAFC 7
3.3 High Temperature FCs 7
3.4 PEMFC 8
3.4.1 Hydrogen 8
3.4.2 Reformate 9
3.4.3 Methanol 10
4 PEMFC STRUCTURE **12**
4.1 Membrane 12
4.2 Gas Diffusion Electrode 14
4.3 Anode Catalysts 14
4.4 Cathode Catalysts 15
5 PROJECT AIMS AND OBJECTIVES **16**
6 REFERENCES **17**

Chapter Two: Experimental Methods and Techniques **19**

1 ELECTRODE PREPARATION **19**
1.1 Reagents and Materials 19
1.1.1 Catalyst preparation 20
1.1.2 Nafion® 20
1.2 Pasted Electrodes 21
1.3 Painted Electrodes 22
1.4 Screen Printed Electrodes 23
1.5 MEA preparation 23
2 ELECTROCHEMICAL METHODS **24**
2.1 Linear Sweep and Cyclic Voltammetry 24
2.2 Apparatus and Experimental Procedure 26
2.2.1 Electrochemical cell 26
2.2.2 Practical procedure 28
2.2.3 CV of a platinum surface 28
2.2.4 CV of a CO poisoned platinum surface 30
2.3 Polarisation 31
2.3.1 Methanol oxidation 33
2.3.2 Oxygen reduction 34
3 X-RAY ABSORPTION SPECTROSCOPY **35**

3.1 Theoretical Aspects of XAS 36
3.1.1 General principles 36
3.1.2 The history of EXAFS 39
3.1.3 EXAFS equations 40
3.1.4 Data analysis 42
3.2 Experimental Aspects of XAS 45
3.2.1 X-ray source 45
3.2.2 Stations 7.1 and 16.5 47
3.2.3 Transmission mode 48
3.2.4 Fluorescence mode 50
3.2.5 Gas treatment cell 51
3.2.6 Electrochemical cell 52
4 X-RAY DIFFRACTION **54**
4.1 Theoretical Aspects of XRD 54
4.2 Experimental Aspects of XRD 56
5 REFERENCES **58**

Chapter Three: In-situ XAS Cell Design and Testing 60

1 INTRODUCTION **60**
2 ROOM TEMPERATURE PEMFC **63**
2.1 Cell Design 63
2.1.1 Graphite plates 64
2.1.2 Seals 68
2.1.3 Current collectors 69
2.1.4 End plates 69
2.2 Membrane Electrode Assemblies (MEA) 71
2.2.1 Components of the MEA 71
2.2.2 MEA preparation 73
2.3 Cell Operation 74
2.3.1 Cell setup 74
2.3.2 Experimental procedure 75
2.3.3 Cell performance (room temperature) 76
3 HUMIDIFIED PEMFC **81**
3.1 Methods of Humidification 81
3.1.1 External humidification 82
3.1.2 Internal humidification 83
3.2 Humidifier Design 84
3.3 Further Modifications 86
3.4 Cell Setup 87
3.5 Cell Performance (80 °C) 88
3.5.1 Cyclic voltammetry 88
3.5.2 Hydrogen polarisation 89
3.5.3 Oxygen polarisation 89
4 IN SITU OPERATION **90**
4.1 Experimental Setup 90
4.2 Operational Procedure 92
5 REFERENCES **93**

Chapter Four: Anode Catalyst - PtRu **95**

1 INTRODUCTION **95**
2 EXPERIMENTAL DETAIL **99**
2.1 Catalysts *99*
2.2 Electrode Preparation *99*
2.3 MEA Preparation *100*
2.4 Electrochemistry *100*
2.4.1 Cyclic voltammetry *100*
2.4.2 Methanol oxidation *100*
2.4.3 Mini-cell *101*
2.5 XAS *102*
2.5.1 Half-cell *102*
2.5.2 Mini-cell *102*
2.6 XRD *103*
3 RESULTS **104**
3.1 Electrochemistry – Half Cell *104*
3.1.1 Cyclic voltammetry *104*
3.1.2 Methanol oxidation *106*
3.2 Catalyst Characterisation *110*
3.2.1 Transmission Electron Microscopy – ex situ *110*
3.2.2 X-ray Diffraction *113*
3.2.3 XAS – Half Cell *116*
3.3 Electrochemistry – Mini-Cell *125*
3.3.1 Hydrogen polarisation *125*
3.4 XAS – Mini Cell *126*
3.4.1 XANES *126*
3.4.2 EXAFS *127*
4 DISCUSSION **135**
4.1 Particle Structure *135*
4.2 CO Oxidation on PtRu *137*
4.3 Methanol Oxidation on PtRu *139*
4.4 Comparison of Electrochemical and EXAFS Results *142*
4.5 Optimal Composition for Performance *144*
4.6 Mini Cell *146*
5 CONCLUSIONS **147**
6 REFERENCES **149**

Chapter Five: Cathode Catalysts – Pt:Cr, Co, Ti **153**

1 INTRODUCTION **153**
2 EXPERIMENTAL DETAIL **159**
2.1 Catalysts 159
2.2 Reference Compounds 159
2.3 Electrode Preparation 160
2.4 MEA Preparation 160
2.5 Electrochemistry 160
2.5.1 Cyclic voltammetry 160

2.5.2 Half-cell (ORR) 160
2.5.3 Mini-cell (ORR) 160
2.6 XAS 161
2.7 Reference Compounds 161
2.7.1 Half-cell 161
2.7.2 Mini-cell 161
3 RESULTS **162**
3.1 Cyclic Voltammetry – Half-cell 162
3.2 Dispersion 166
3.2.1 Experimental calculation 167
3.2.2 Theoretical calculation 167
3.2.3 Comparison of calculated values 168
3.3 Surface Composition 170
3.4 Catalyst Activity 172
3.4.1 Activity in liquid electrolyte 172
3.4.2 Activity in a PEMFC 174
3.4.3 Dilution effects 177
3.5 In situ XAS 178
3.5.1 XANES - Pt LIII edge 179
3.5.2 XANES – 2nd metal K edge 181
3.5.3 EXAFS 185
3.6 Ex situ XRD 210
4 DISCUSSION **213**
4.1 Electronic Properties 214
4.2 Surface Properties 215
4.3 Bulk Structural Properties 217
5 CONCLUSIONS **220**
6 REFERENCES **222**

Chapter Six: Conclusions and Further Work **225**

DECLARATION OF AUTHORSHIP

I, **Richard John Kenneth Wiltshire** declare that the thesis entitled:

Extending *in situ* XAS of PEM Fuel Cells to more Realistic Conditions

and the work presented in it are my own. I confirm that:

- This work was done wholly or mainly while in candidature for a research degree at this University;
- Where any part of this thesis has previously been submitted for a degree or any other qualification at this University or any other institution, this has been clearly stated;
- Where I have consulted the published work of others, this is always clearly attributed;
- Where I have quoted from the work of others, the source is always given. With the exception of such quotations, this thesis is entirely my own work;
- I have acknowledged all main sources of help;
- Where the thesis is based on work done by myself jointly with others, I have made clear exactly what was done by others and what I have contributed myself;

Signed: _____

Date: 17th June 2005

ACKNOWLEDGMENTS

Firstly, I would like to thank my supervisor, Dr. Andrea Russell for all her advice and enthusiasm during my PhD. I've learnt a huge amount from her and really appreciate her guidance and encouragement throughout my research. I would like to thank all those who have helped me at Johnson Matthey: Dave Thompsett, Sarah Ball, Brian Theobald and particularly Martin Hogarth who put in a great amount of time and effort building the mini-cell. For all their help at Daresbury, I would like to thank: Bob Bilsborrow, Fred Mosselmans, Lorrie Murphy and Chris Corrigan. Thanks to all the people in the technical workshop and glassblowers for their work making and fixing a number of cells I've used in my research.

There are a number of people I would like to thank from the group who have made my time in Southampton very enjoyable and have been good friends over the years. Firstly, all the EXAFS people who between them have helped me collect a huge proportion of the data in this thesis: Abbe for introducing me to the world of EXAFS, passing on all her knowledge and making the hours at Daresbury very entertaining, the members of the supposed 'Dream Team' consisting of Colin Compactor King and Peter Curry Wells. Conversations on quality time, bad singing and issues with red cars in (not so) dark places will always bring a smile to my face. Helen, Dave and Suzanne for making this a great group to work in and for putting up with really bad cakes (when I remembered). I must also thank those who have moved on for making it very easy to settle into the group: Chris, Fabrice and Sohrab. I'd also like to thank various members of the Hayden group and Jules for the many Friday evening staff club sessions.

I would like to thank my family all of whom have supported me in various ways throughout my PhD and hopefully for being polite enough to have a quick skim through this thesis before it becomes a doorstop.

Finally, I would like to thank Rachel who has managed to put up with the long hours, all the hikes/cycle rides (I know you only did it because you wanted to) and for standing by me all the way.

Chapter One: Introduction

1 GENERAL INTRODUCTION

1.1 History

The invention of fuel cells is based on the discovery in 1839 that water electrolysis could be reversed in order to generate electricity and is widely attributed to Sir William Grove [1]. Grove continued with his experiments and three years later demonstrated the first lab-scale fuel cell. Four glass cells filled with dilute sulphuric acid were coupled in series and thin platinum electrodes were used as electrodes.

The technology had no practical value until the 1930s when Francis Bacon began his groundbreaking research on alkaline fuel cells (AFCs). Bacon's first fuel cell used electrodes made from nickel gauze and were activated by alternatively oxidising and reducing in air and hydrogen, respectively. A tube of asbestos soaked with 27 % potassium hydroxide solution served as a separator [2]. However, it took Bacon years to overcome technical challenges such as corrosion and it was not until 1959 that he and his co-workers were able to demonstrate a practical fuel cell stack [3]. Bacon's research resulted in a large advance in fuel cell technology and lead the way to the first practical application of fuel cells. In the 1960s Pratt and Whitney adapted Bacon's AFC system for operation in space and supplied the fuel cell systems for the Apollo spacecraft. A device which produced electricity, heat and water proved to be a major advantage over other power sources such as batteries. Although niche markets such as space travel played an important role in the development of fuel cells, the cost factor of using catalysts with very high noble metal content limited its applications in other areas. In addition to cost, a disadvantage of the AFC is its sensitivity to carbon dioxide. The fuel cell and the oxidising agent usually contain carbon dioxide which reacts with the alkaline electrolyte, producing carbonates. The fuel must therefore be very pure hydrogen and the air supply containing the oxygen must be free from carbon dioxide [4].

To overcome the problems described previously, recent efforts have concentrated on understanding the basic electrochemical principles of fuel cell reactions with the aim of improving the component materials and reducing the noble metal content [5]. Recent advances have concentrated on proton exchange membrane fuel cells (PEMFCs) which offer the following advantages: reduced corrosion, simple fabrication, CO_2 tolerance, operability with hydrogen and reformed fuels, and possibilities for high power densities [4]. Despite the advantages, barriers still remain holding back the commercialisation of fuel cells. These include: use of platinum, carbon monoxide poisoning, water management and costs. However, encouraging results are being achieved to overcome the barriers. For example, since the 1980s there has been a significant lowering of the platinum loading of electrodes from about 4 to 10 mg cm^{-2} to about 0.4 mg cm^{-2} or less [6-8]. The problem of carbon monoxide poisoning has been addressed by selective catalytic oxidation [9], while cost reductions and increases in power density have been demonstrated [10]. As a result of these research efforts, PEMFC technology has been brought close to the commercial era.

1.2 Environmental Factors

Depleting stocks of natural resources as a result of widespread burning of fossil fuels has led a drive towards the development of fuel cells for both transport and stationary power sources. Diminishing resources are not the only concern as the damage to the environment becomes more apparent. Increased levels of atmospheric pollution and green house gases occur as NO_x, SO_x, CO_2 and particulate matter are released into the atmosphere [11].

California has the worst overall air pollution in the United States as a result of the automobile-dependent transport system, hot weather and mountainous topography. In an effort to combat these problems, legislation has been introduced to try and reduce the levels of pollution. Part of the legislation states that by 2010, 10 % of cars sold or leased in California must qualify as a zero or near zero emission vehicle [12]. Although the use of fuel cells is not specified in the legislation, they provide vehicle manufacturers with a very valuable option for complying with the requirements.

Many other government programs are being set up to provide support to manufactures to move away from dependence on fossil fuels [13].

The viability of fuel cells is strongly dependent on the source of hydrogen, which nearly all fuel cells consume. Hydrogen is mainly obtained via reforming energy carriers such as natural gas or methanol; both non-renewable sources. Potentially, hydrogen could be produced from electrolysis of water with no emission of pollutants. For this to be sustainable, the process must be based on renewable energy harvested as electricity using solar, wind, hydro or ocean power plants [14,15]. To utilise hydrogen as an effective energy carrier, it must be efficiently converted back to electricity. Fuel cells prove ideal as they allow direct conversion of chemical into electrical energy with high efficiency, producing water as the only product.

1.3 Applications

Fuelled by advances in fuel cell performance and continuing environmental concern, interest in all types of fuel cell systems for automotive, stationary and portable power applications is now very high.

Interest in the application of fuel cells as power sources for electric vehicles started in the 1970s. The introduction of the California environmental legislation (section 1.2) in the early 1990s furthered the advance. This was assisted by the Partnership for a New Generation of Vehicles (PNGV) program, initiated in the USA in 1993 to develop automobiles with three times the efficiency of conventional internal combustion engines [10]. PEMFCs prove to be the best choice of fuel cell for automobile applications. Some of the reasons include: the low operating temperatures enabling rapid startup times, the electrolyte is innocuous, and the fact that they exhibit the highest efficiencies and power densities. DaimlerChrysler and its affiliated companies demonstrated its first fuel cell concept car, NECAR (new electric cars), in 1994. Since then, 20 different vehicle prototypes have been developed and tested [16]. As part of the European Fuel Cell Bus Project, 30 Mercedes-Benz buses equipped with 205 kW Ballard® fuel cell engines are being driven on the roads of ten European cities. The gaseous hydrogen is compressed, stored in cylinders and is sufficient for a 400 km range [17,18].

High temperature fuel cells such as solid oxide fuel cells (SOFCs) have been the main consideration for stationary power applications. Operating at temperatures of 1000 °C means that natural gas can be easily converted into hydrogen so that reforming of the fuel gas is unnecessary and conversion can take place in the cell. However, advances in PEMFCs are making them an increasingly attractive option. Some companies and hospitals are choosing to install fuel cells where the benefit of extremely reliable, high quality power exceeds the cheaper cost of lower quality, grid-supplied power [10,13].

2 FUEL CELL PRINCIPLES

Fuel cells are electrochemical devices that convert the chemical energy of the reactions directly into electricity and heat, without combustion as an intermediate step. Unlike a battery, the fuel is not contained within the fuel cell compartment but is supplied continuously from an external source. The fuel which can be hydrogen or methanol is electrochemically oxidised using pure oxygen or air to give water. The overall redox reaction is subdivided into two half-cell reactions occurring at the two electrodes, the anode and the cathode. An ion-conducting electrolyte physically separates the two electrodes and also prevents electronic conduction (figure 1). When hydrogen is the fuel, the anode reaction is as follows:

$$H_2 \longrightarrow 2\,H^+ + 2\,e^- \qquad E^\circ = 0 \text{ V vs. RHE} \qquad \textbf{Eq. 1}$$

After the electrons pass through the external circuit, they arrive at the cathode where oxygen is reduced to give water.

$$O_2 + 4\,H^+ + 4\,e^- \longrightarrow 2\,H_2O \qquad E^\circ = 1.23 \text{ V vs. RHE} \quad \textbf{Eq. 2}$$

The overall equation for the reaction is as follows:

$$2\,H_2 + O_2 \longrightarrow 2\,H_2O \qquad E^\circ = 1.23 \text{ V vs. RHE} \quad \textbf{Eq. 3}$$

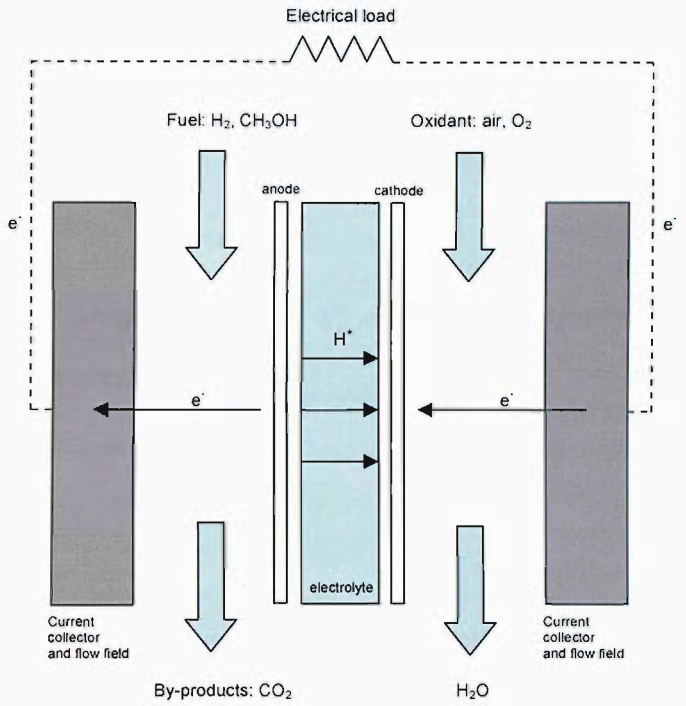

Figure 1 Schematic of a fuel cell.

The maximum electrical energy obtainable is determined by the product of the reversible cell potential, E, and the charge, Q, where $Q = nF$ and is thus given by a change in the Gibbs free energy:

$$\Delta G = -nFE \qquad \textbf{Eq. 4}$$

For materials in the standard state at 25 °C and unit activity, it is written as follows:

$$\Delta G^o = -nFE^o \qquad \textbf{Eq. 5}$$

where n is the number of electrons transferred per mole of reactants, F is the Faraday constant and E is the voltage of the cell [13]. To determine thermodynamic efficiencies, the reaction enthalpy and reaction entropy must also be considered. Using the Gibbs-Helmholtz relation, the functions are connected as follows:

$$\Delta G = \Delta H - T\Delta S \qquad \textbf{Eq. 6}$$

The thermodynamic or ideal efficiency of energy conversion is related to the reaction enthalpy by the following equation:

$$\xi_{th} = \frac{\Delta G}{\Delta H} = 1 - \frac{T\Delta S}{\Delta H} \qquad \textbf{Eq. 7}$$

If the thermal cell voltage is defined as $E_H^o = -\Delta H / nF$, then the thermodynamic efficiency can be expressed as:

$$\xi_{th} = \frac{E^o}{E_H^o} \qquad \textbf{Eq. 8}$$

For example, for the fuel cell reaction shown in equation 3, for standard conditions, $E^o = 1.23\ V$ and E_H^o = 1.48 V, giving ξ_{th} = 0.83 [19].

3 TYPES OF FUEL CELL

Fuel cells are characterised by the type of electrolyte. The five major types of fuel cells are alkaline fuel cell (AFC), phosphoric acid fuel cell (PAFC), molten carbonate fuel cell (MCFC), solid oxide fuel cell (SOFC) and polymer electrolyte membrane fuel cell (PEMFC).

3.1 AFC

The AFC has been used since the mid-1960s by NASA in the Apollo and Space Shuttle programs (section 1.1). As a result, the AFC is one of the most developed technologies. The electrolyte is aqueous potassium hydroxide retained in a porous stabilized matrix. The charge carrier is the hydroxyl ion which migrates from the cathode to the anode where it reacts with hydrogen to produce water and electrons. Water formed at the anode migrates back to the cathode to regenerate hydroxyl ions. Some of the disadvantages of the AFCs have been discussed in section 1.1. An advantage of this cell is that the reduction of oxygen to OH^- is much faster than the acidic equivalent of oxygen to H_2O due to better kinetics [11]. In addition, AFCs

operate at relatively low temperatures (65 °C to 220 °C) and are amongst the most efficient fuel cells.

3.2 PAFC

The PAFCs were the first fuel cells to be commercialised. The ionic conductivity of the phosphoric acid electrolyte is increased by operating in a temperature range of 150 °C to 220 °C. Hydrogen is split at the anode into protons and electrons. The protons migrate through the electrolyte and combine with oxygen at the cathode to form water while the electrons travel round the external circuit. Unlike the AFCs, carbon dioxide does not affect the electrolyte or performance of the cell and can therefore be operated with reformed fossil fuels [20]. PAFCs are usually large and heavy and require warm-up time. As a result, they tend to be limited to stationary applications.

3.3 High Temperature FCs

The MCFC is classed as a high temperature fuel cell and operates at 650 °C. This gives them the advantage of being able to internally reform hydrocarbons such as natural gas and petroleum based fuels. The cells use an electrolyte composed of a molten mixture of carbonate salts. At high temperatures, the salts melt and become conductive to carbonate ions. These ions flow from the cathode to the anode where they combine with hydrogen to give water, carbon dioxide and electrons. The CO_2 evolved at the anode is transferred to the cathode where it reacts with oxygen to reform carbonate ions.

The SOFC comes under the same category of high temperature fuel cell. They are operated over a wide temperature range of 600 °C to 1000 °C. To operate at these temperatures a thin, solid ceramic electrolyte is used that is conductive to oxygen ions. At the cathode, oxygen ions are produced which migrate through the solid oxide electrolyte to the anode where they combine with hydrogen.

The common features of MCFCs and SOFCs are that the high temperature electrochemical reactions are based on fast electrode kinetics, removing the need for precious metals electrodes. The high temperatures also mean that the tolerance of the

electrodes against impurities is high. For example, CO can be used as a fuel unlike low temperature fuel cells where CO rapidly poisons platinum based anodes. A disadvantage of high temperature operation is that the working life is limited by the wearing out of materials. This is particularly true where metallic materials are used as they are not thermodynamically stable in the fuel cell environment [21].

3.4 PEMFC

The PEMFC has received the most attention in recent years, primarily because of its relatively high performance, rapidly advancing technology and system simplicity. They use a proton conducting polymer membrane as the electrolyte and operate within a temperature range of 85 °C to 105 °C. It is possible to distinguish between three types of PEMFCs, the direct H_2-PEMFC, the indirect reformate PEMFC and the direct methanol fuel cell (DMFC). The main difference between them is the fuel and the way the fuel is supplied to the fuel cell system [22].

3.4.1 Hydrogen

Hydrogen is electrochemically oxidised at the anode to give protons. The protons migrate through the membrane while the electrons travel through the external circuit to the cathode where oxygen is reduced to water. As shown in equation 3, the standard reversible cell potential is 1.23 V vs. RHE. For high proton conductivity, the membrane must be well hydrated. This determines the temperature range over which the fuel cell can be operated. Water balance plays a very important role in PEMFCs and must be carefully managed. If this is not done, the water content of the membrane falls resulting in an increase in the cell resistance. The mechanisms of membrane dehydration are (i) electro-osmotic drag pulling water from the anode to the cathode and (ii) loss of water to under-saturated fuel or oxidant gas streams [23]. Depending on operating conditions both anode and cathode gas streams are humidified. However, too much water can also have adverse effects by flooding the catalyst layers. This is a particular problem at the cathode as a result of product water from oxygen reduction.

Unlike the cathode gas which can be taken from the surrounding air, providing hydrogen to the fuel cell is a very challenging task, particularly for mobile applications. At present there are three principal storage technologies, including: high pressure storage, cryogenic storage and hydride storage. The difficulty of storing compressed hydrogen is that the size and mass of the tanks can be a restricting factor. Storing hydrogen as a liquid increases the energy density but the tanks must be extremely well insulated. Another problem with liquid hydrogen is the high amount of energy required to liquefy hydrogen compared to the storage of compressed hydrogen. The formation of metal hydrides is another way to store hydrogen. The main characteristic that affects their use in portable applications is the high specific density of metal hydrides. However, the use of graphite nanostructures for hydrogen storage has been proved to be a possible alternative [24,25].

3.4.2 Reformate

To overcome the problems of storing hydrogen in its pure form or as a hydride, hydrogen can be obtained by reforming hydrocarbons. The advantage of the latter is that liquid fuels have a higher energy density and can be more easily distributed. As a result, providing an infrastructure would be less complicated. However, the difficulty of cold-start capabilities and the additional components required represent obstacles for vehicles and portable applications.

Methanol is a small hydrocarbon and so produces less carbon dioxide and is easier to reform than longer chain molecules. There are two main methods of reforming: partial oxidation and steam reforming. Partial oxidation is an exothermic reaction involving partial burning of the fuel to produce carbon dioxide and hydrogen:

$$CH_3OH + \tfrac{1}{2} O_2 \longrightarrow CO_2 + 2 H_2 \qquad \textbf{Eq. 9}$$

Steam reforming is endothermic and combines the fuel with steam to produce the same products:

$$CH_3OH + H_2O \longrightarrow CO_2 + 3 H_2 \qquad \textbf{Eq. 10}$$

The major problem with using reformate in PEMFCs is that a small amount of CO (0.5 to 2 %) is present as a result of the reverse water gas shift reaction:

$$CO_2 + H_2 \longrightarrow CO + H_2O \qquad \textbf{Eq. 11}$$

CO binds very strongly to platinum based catalysts at the anode, blocking active sites and causing a significant drop in performance. The levels of CO can be reduced to less than 100 ppm using shift reactors and catalytic preferential oxidation reactors (CPOX). However, the additional shift and CPOX reactors complicate the system and add extra cost [26].

3.4.3 Methanol

In theory a DMFC system provides the solution to a number of the problems encountered in the pure hydrogen and reformate PEMFCs. Storing the fuel is no longer an issue and the need for complex reformers is removed. In addition, humidification and heat management hardware modules are not required as this is provided by the dilute methanol-water mixture that circulates around the DMFC [27].

The anode reaction (equation 12) and cathode reactions (equation 13) for a DMFC are as follows:

$$CH_3OH + H_2O \longrightarrow CO_2 + 6H^+ + 6e^- \qquad E^\circ = 0.046 \text{ V vs. RHE} \qquad \textbf{Eq. 12}$$

$$3/2O_2 + 6H^+ \longrightarrow 3H_2O \qquad E^\circ = 1.23 \text{ V vs. RHE} \qquad \textbf{Eq. 13}$$

This gives the following overall reaction with a theoretical efficiency, $\xi_{th} = 0.97$:

$$CH_3OH + H_2O + 3/2O_2 \rightarrow CO_2 + 3H_2O \qquad E^\circ = 1.18 \text{ V vs. RHE} \qquad \textbf{Eq. 14}$$

The thermodynamic potential for methanol oxidation lies very close to the equilibrium potential of hydrogen. However, compared with hydrogen oxidation, the reaction is several orders of magnitude slower. This can be accounted for by the

poor electrochemical activity. The mechanism involves adsorption of methanol onto a catalyst surface (equation 15) followed by sequential stripping of protons and electrons (equations 16-19), leading to the formation of carbon adsorbing species such as $-CO_{ads}$ and $-CHO_{ads}$. Formation of these species during methanol oxidation has been confirmed by IR spectroscopy [28,29].

$$Pt + CH_3OH \longrightarrow Pt - (CH_3OH)_{ads} \quad \textbf{Eq. 15}$$

$$Pt - (CH_3OH)_{ads} \longrightarrow Pt - (CH_3O)_{ads} + H^+ + e^- \quad \textbf{Eq. 16}$$

$$Pt - (CH_3O)_{ads} \longrightarrow Pt - (CH_2O)_{ads} + H^+ + e^- \quad \textbf{Eq. 17}$$

$$Pt - (CH_2O)_{ads} \longrightarrow Pt - (CHO)_{ads} + H^+ + e^- \quad \textbf{Eq. 18}$$

$$Pt - (CHO)_{ads} \longrightarrow Pt - (CO)_{ads} + H^+ + e^- \quad \textbf{Eq. 19}$$

The poor kinetics of methanol oxidation can be explained in two parts. Firstly, the adsorption of methanol requires several neighbouring sites. Therefore, methanol adsorption does not take place until a potential is reached where H atoms are displaced leaving available Pt sites. This occurs at approximately 0.2 V vs. RHE for polycrystalline Pt. Secondly, as with the reformate case (section 3.4.2), CO rapidly poisons the surface of the catalyst. The following reaction has been suggested for the subsequent oxidation of CO:

$$Pt - (CO)_{ads} + OH_{ads} \longrightarrow Pt + CO_2 + H^+ + e^- \quad \textbf{Eq. 20}$$

Oxygen species from the dissociation of water are required for this reaction. The dissociation does not occur on a Pt surface until potentials above 0.4 to 0.45 V vs. RHE are reached [30]. These processes result in the high activation polarisation losses seen at the anode and are one of the limitations of DMFCs.

A further limitation for the DMFC is methanol crossover from the anode to cathode which occurs as a result of diffusion and electro-osmotic drag. This causes a mixed potential, reducing the cell performance. Thicker membranes reduce methanol crossover but also increase the ohmic resistance. A trade-off is required and the development of membranes with low methanol permeability is an important area of research.

4 PEMFC STRUCTURE

The main constituent of a PEMFC is the membrane electrode assembly (MEA). This is a five layer structure consisting of a proton conducting polymer electrolyte positioned between two catalyst layers. A gas diffusion layer is situated on either side to complete the MEA. The MEA is located between two current collector plates which have flow fields machined into them so that fuel and oxidant can be evenly distributed to the anode and cathode, respectively [1]. A unit cell on its own does not provide sufficient voltage for most applications. Therefore, unit cells are connected in series to form a fuel cell stack. Figure 2 shows an expanded diagram of a PEMFC stack and unit cell.

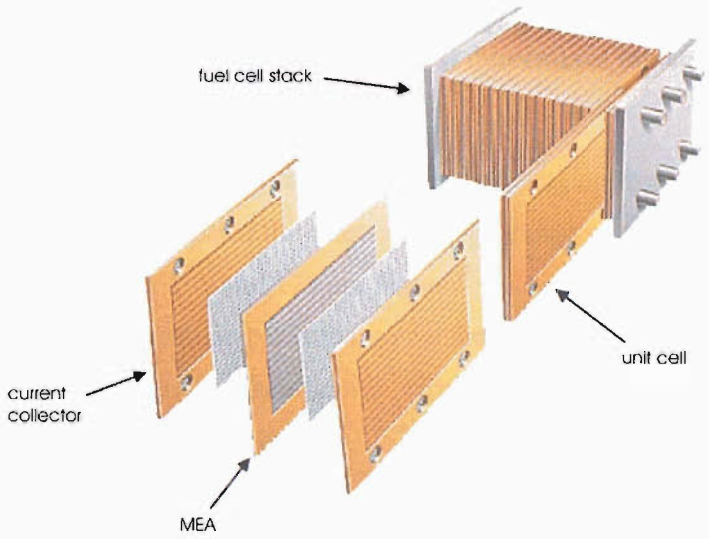

Figure 2 **Expanded view showing the structure of a fuel cell stack and unit cell for a PEMFC [31].**

4.1 Membrane

The membrane allows the transport of protons from the anode to the cathode side of the cell while preventing mixing of reactant gases and electrical shorts. A major breakthrough in PEMFC technology was the development of Nafion® membranes by Dupont. This was for two reasons: firstly, the presence of highly electronegative fluorine atoms bonded to the same carbon atom as the SO_3H group, leads to super acid properties and high proton conductivities. Secondly, the CF_2 groups are very

stable in both reducing and oxidising environments [5]. This is vital for a system where a long operational lifetime is essential.

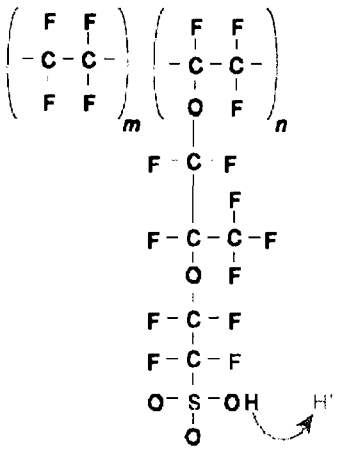

Figure 3 **Chemical structure of Nafion® where the ration *n* to *m* (i.e. active sites to inactive chain monomers) determines the acidity of the electrolyte.**

The membranes can be made with varying thicknesses ranging from 25 to 250 μm. Srinivasan *et al.* [32] investigated the effect of using a range of membrane thicknesses including: 50, 100 and 175 μm Nafion®. They reported lower iR losses and significant improvements in performance for the thinner membranes at high current densities. However, thin membranes can result in increased crossover of reactant gases and the optimum membrane is determined by the operating conditions and requirements of the fuel cell.

These types of membranes require water for proton conductivity therefore, the temperature range over which PEMFCs can operate is limited by the boiling point of water. One area of research is in the development of high-temperature membranes [33]. This can be achieved by introducing a second substance such as SiO_2 into the membrane which can retain water at higher temperatures. The advantage of high temperature operation is the reduced CO coverage leading to improved CO tolerance.

4.2 Gas Diffusion Electrode

Platinum based catalysts have been found to be effective for both anode and cathode reactions. The catalyst is supported on carbon (commonly XC72R) with loadings typically between 10 and 60 wt. % Pt. Using these loadings particle sizes typically between 2 and 6 nm can be achieved. These high catalyst dispersions ensure that there are a large number of active sites and that a high proportion of the platinum is utilised.

The carbon supported catalysts are usually mixed with an ionomeric binder (typically Nafion®) to form an ink. This ensures that when the electrode is pressed onto the membrane there is good contact between the catalyst particles and the membrane via ionomer chains. The ink is then applied to the gas diffusion layer, for example carbon paper, using a number of methods, such as screen printing, manual spreading, painting or rolling. Figure 4 shows an example of this arrangement. The aim is to achieve a three-phase boundary between the supply of gas, the catalyst particle and the ionic conductor.

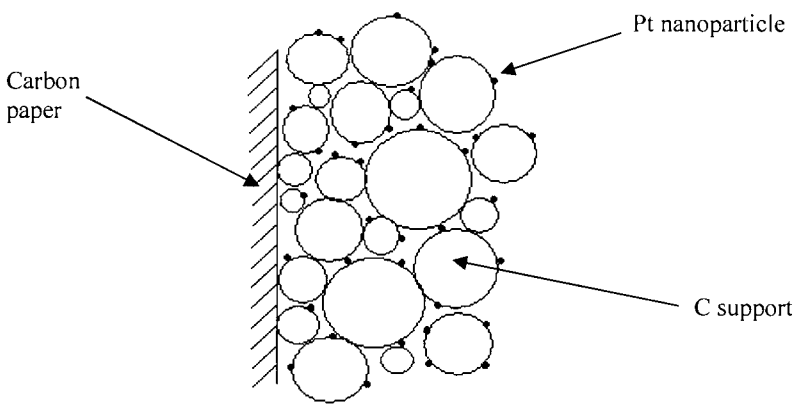

Figure 4 Cross-section through a typical gas diffusion electrode.

4.3 Anode Catalysts

The electrochemical oxidation of hydrogen on platinum is extremely facile. However, CO present in reformate or as an intermediate in methanol oxidation rapidly poisons the platinum surface (sections 3.4.2 and 3.4.3). The CO tolerance can be improved by alloying platinum with a secondary metal. A whole range of secondary metals have been investigated including: Ru, Mo, Sn, Rh, Ge, W, and Sb.

A promoted or bifunctional mechanism to explain the improved CO tolerance was first proposed by Watanabe and Motoo [34]. The mechanism involves water activation on the secondary metal, followed by CO electrooxidation on a neighbouring Pt atom.

$$M + H_2O \longrightarrow M\text{-}OH + H^+ + e^- \qquad \textbf{Eq. 21}$$

$$Pt - CO + M - OH \longrightarrow CO_2 + H^+ + e^- + Pt + M \qquad \textbf{Eq. 22}$$

A second mechanism known as the intrinsic or ligand mechanism has also been proposed. In this case, the secondary metal weakens the Pt – CO bond by reducing the Pt electron density [35,36].

4.4 Cathode Catalysts

Unlike the anode, the kinetics of the oxygen reduction reaction (ORR) on platinum are comparably slow. The high overpotential losses observed at the cathode are one of the major limitations facing PEMFCs. As a result of efforts to improve PEMFC efficiency, an important area of research is the development of catalysts more active than platinum for the ORR. As with the anode catalysts, alloying platinum with a secondary metal has shown improvements in activity for the ORR. Initially, platinum based alloys using secondary metals such as: Co, Cr, Cu, Fe, and Ni were considered for PAFCs in the 1980s. With recent developments in PEMFCs, this technology has been transferred and evaluated. Johnson Matthey investigated a range of cathode catalysts including: PtFe, PtMn, PtNi, PtCr, PtZr and PtTi alloys. Testing showed that leaching of the secondary metal was a problem for the PtFe, PtMn and PtNi alloys [37]. The remaining catalysts showed improved performance relative to platinum and no evidence of leaching into either the membrane or anode layer was found.

5 PROJECT AIMS AND OBJECTIVES

The brief review given is this chapter highlights some of the challenges facing the development of PEMFCs for commercial use. This thesis concentrates on both the anode and cathode catalysts where further development relies on the ability to relate catalyst structure to performance. A range of techniques will be used to determine the catalyst structures including: X-ray absorption spectroscopy (XAS), X-ray diffraction (XRD) and transmission electron microscopy (TEM). Catalyst performance will be assessed using electrochemical techniques such as: Cyclic voltammatry and polarisation measurements carried out under liquid and solid polymer electrolyte environments.

XAS has played an important role in the study of fuel cell catalysts. XAS provides information on the electronic properties and local coordination in terms of the type of neighbour, their number and distance relative to the absorbing atom. A key advantage of XAS over other characterisation methods such as XPS or TEM is the ability to be able to carry out *in situ* experiments in environments closely related to those of a working fuel cell [38]. Chapter three presents the design and operation of a mini-fuel cell for *in situ* XAS studies.

PtRu catalysts have emerged as one of the most promising catalysts showing significant improvements over pure Pt catalysts in terms of CO tolerance. The composition of the catalyst is known to play an important role. Chapter four aims to characterise a series of carbon-supported PtRu catalysts. The catalyst performance with reference to the mechanism for the electro-oxidation of CO will be discussed in terms of the catalysts electronic and structural properties.

PtCr, PtCo and PtTi catalysts have all shown improvements over pure Pt catalysts for the ORR. The electronic, surface and bulk structural properties are all thought to play a role in catalyst performance. Chapter five investigates the extent to which these catalyst properties govern their activity towards the ORR by relating electrochemical and structural data.

6 REFERENCES

1. Hoogers, G.; Thompsett, D. *Cattech* **2000**, *3*, 106.
2. Sandstede, G.; Cairns, E. J.; Bagotsky, V. S.; Wiesener, K. *Handbook of Fuel Cells - Volume 1: Fundamentals and Survey of Systems*; John Wiley and Sons, 2003.
3. Mikkola, M. Experimental Studies on Polymer Electrolyte Membrane Fuel Cell Stacks. MSc, University of Helsinki, 2001.
4. Joon, K. *Journal of Power Sources* **1998**, *71*, 12.
5. Costamagna, P.; Srinivasan, S. *Journal of Power Sources* **2001**, *102*, 242.
6. Ticianelli, E. A.; Derouin, C. R.; Redondo, A.; Srinivasan, S. *Journal of the Electrochemical Society* **1988**, *135*, 2209.
7. Wilson, M. S.; Gottesfeld, S. *Journal of Applied Electrochemistry* **1992**, *22*, 1.
8. Antolini, E. *Journal of Applied Electrochemistry* **2004**, *34*, 563.
9. Acres, G. J. K.; Frost, J. C.; Hards, G. A.; Potter, R. J.; Ralph, T. R.; Thompsett, D.; Burstein, G. T.; Hutchings, G. J. *Catalysis Today* **1997**, *38*, 393.
10. Costamagna, P.; Srinivasan, S. *Journal of Power Sources* **2001**, *102*, 253.
11. Carrette, L.; Friedrich, K. A.; Stimming, U. *chemphyschem* **2000**, *1*, 162.
12. Lloyd, A. C. *Journal of Power Sources* **2000**, *86*, 57.
13. Whittingham, M. S.; Savinell, R. F.; Zawodzinski, T. *Chemical Reviews* **2004**, *104*, 4243.
14. Bossel, U. The Hydrogen 'Illusion'. *Cogeneration and On-Site Power Production* **2004**, March-April, 55.
15. Hart, D. *Journal of Power Sources* **2000**, *86*, 23.
16. http://www.ballard.com/resources/regulatory_filings/doc_uploads/2002-04-30%20AIF.pdf. Annual Information Form, April 30, 2002.
17. http://www.ballard.com/resources/news_releases/21%20London%20Bus.pdf. Ballard Powered Fuel Cell Buses Delivered to the City of London, December 16, 2003.

18. Evers, A. A. *International Journal of Hydrogen Energy* **2003**, *28*, 725.
19. Vielstich, W. *Handbook of Fuel Cells - Volume 1: Fundamentals and Survey of Systems*; John Wiley and Sons, 2003.
20. http://www.fctec.com/fctec_types.asp.
21. Yokokawa, H.; Sakai, N. *Handbook of Fuel Cells - Volume 1: Fundamentals and Survey of Systems*; John Wiley and Sons, 2003.
22. Paulus, U. A. Electrocatalysis for Polymer Electrolyte Fuel Cells: Metal Alloys and Model Systems. PhD, University of Ulm, 2002.
23. Berg, P.; Promislow, K.; St Pierre, J.; Stumper, J.; Wetton, B. *Journal of the Electrochemical Society* **2004**, *151*, A341.
24. Liu, C.; Fan, Y. Y.; Liu, M.; Cong, H. T.; Cheng, H. M.; Dresselhaus, M. S. *Science* **1999**, *286*, 1127.
25. Funck, R. *Handbook of Fuel Cells - Volume 1: Fundamentals and Survey of Systems*; John Wiley and Sons, 2003.
26. Ralph, T. R.; Hogarth, M. P. *Platinum Metals Rev.* **2002**, *46*, 117.
27. Ralph, T. R.; Hogarth, M. P. *Platinum Metals Rev.* **2002**, *46*, 146.
28. Iwasita, T.; Nart, F. C. *Journal of Electroanalytical Chemistry* **1991**, *317*, 291.
29. Wasmus, S.; Kuver, A. *Journal of Electroanalytical Chemistry* **1999**, *461*, 14.
30. Iwasita, T. *Electrochimica Acta* **2002**, *47*, 3663.
31. http://www.xcellsis.com.
32. Srinivasan, S.; Ticianelli, E. A.; Derouin, C. R.; Redondo, A. *Journal of Power Sources* **1988**, *22*, 359.
33. Alberti, G.; Casciola, M. *Solid State Ionics* **2001**, *145*, 3.
34. Watanabe, M.; Motoo, S. *Journal of Electroanalytical Chemistry* **1975**, *60*, 275.
35. Rodriguez, J. A. *Surface Science Reports* **1996**, *24*, 225.
36. Igarashi, H.; Fujino, T.; Zhu, Y. M.; Uchida, H.; Watanabe, M. *Physical Chemistry Chemical Physics* **2001**, *3*, 306.
37. Ralph, T. R.; Hogarth, M. P. *Platinum Metals Rev.* **2002**, *46*, 3.
38. Russell, A. E.; Rose, A. *Chemical Reviews* **2004**, *104*, 4613.

Chapter Two: Experimental Methods and Techniques

A number of electrochemical and spectroscopic methods for the study of fuel cell catalysts have been used in this thesis. These include electrode preparation, cyclic voltammetry, polarisation, single cell testing, X-ray absorption spectroscopy and X-ray diffraction. Both the theory and practical aspects behind these techniques will be covered in this chapter.

1 ELECTRODE PREPARATION

Three main techniques have been used for the preparation of electrodes. In each case the objective was the same, to put an even catalyst layer containing the carbon-supported catalyst and Nafion® onto carbon paper (TGPH-090). The choice of technique is dependent on the size of the electrode and the loading required. The first method involves pasting the catalyst ink onto the carbon paper using a template and spatula. This allows higher loadings to be achieved ranging from 0.5 - 5 mg Pt cm^{-2}. The second method allows far lower loadings to be achieved, 0.1 - 1 mg Pt cm^{-2}, and involves painting the ink onto the carbon paper using a brush. The size of the electrode that can be produced by both of these techniques is limited. When larger electrodes are required, difficulties arise in obtaining even catalyst layers using either a pasting or painting method. In these instances screen printing can be used and this is the final technique covered.

1.1 Reagents and Materials

The catalysts, chemical reagents and materials used in the preparation of electrodes are listed in table 1 along with their respective suppliers. All water used in the fabrication of electrodes and in electrochemical tests was ion exchange treated using a Barnstead Nanopure system giving water with a conductivity of 18 MΩ cm.

Table 1 Reagents and materials.

Reagent / Material		Supplier
Platinum supported on carbon		Johnson Matthey
Palladium supported on carbon		E-TEK, Inc.
Anode catalysts	Platinum-Ruthenium on carbon	Johnson Matthey
Cathode catalysts	Platinum-Chromium on carbon	Johnson Matthey
	Platinum-Cobalt on carbon	Johnson Matthey
	Platinum-Titanium on carbon	Johnson Matthey
Vulcan XC-72R carbon black		Cabot Corporation
Carbon paper TGPH-090		E-TEK, Inc.
Nafion® solution (5 wt. %) in alcohol		Aldrich
Nafion® solution (12.5 wt. %) aqueous		Johnson Matthey
Flemion® SH30 membrane		Asahi Glass, Co.
Concentrated sulphuric acid (98 %)		Aldrich

1.1.1 Catalyst preparation

The catalysts used in this thesis were provided by Johnson Matthey and were prepared according to proprietary methods [1]. This involved mixing the carbon black vigorously with distilled water. In the case of PtRu, chloroplatinic acid (H_2PtCl_6) and ruthenium chloride ($RuCl_3$) dissolved in distilled water were added to the carbon slurry and the pH of the slurry adjusted to the base by the addition of sodium bicarbonate. Hydrazine was then introduced into the slurry to act as a reducing agent for *in situ* liquid phase reduction. The PtRu/carbon slurry was then dried in a vacuum oven.

1.1.2 Nafion®

Nafion® is a polymer based on a PTFE backbone with sulphonated side chains. The fluorinated carbon backbone is strongly electron withdrawing, leading to the super acid properties of the sulphonate groups. The PTFE backbone forms hydrophobic regions and the sulphonated groups form hydrophilic regions. Nafion® has high acidity ensuring fast proton conductivity and hence fast proton conduction between electrodes. In addition, it is chemically inert in both reducing and oxidising environments and is very stable. This is important for a system where a long operational lifetime is essential.

1.2 Pasted Electrodes

A known quantity of catalyst powder giving the required loading was ground with a pestle and mortar until the powder was finely dispersed. A solution was then made up consisting of ~0.5 ml water and Nafion® solution (5 wt. %) in alcohol. This was then added to the catalyst powder. The amount of Nafion® required was calculated to give a 15 wt. % mixture with respect to the catalyst. The mixture was placed in an ultrasonic bath until a thick paste had formed (2-3 hrs). The paste was then spread manually using a spatula onto a weighed carbon sheet in a 3 x 3 cm template ensuring as much of the mixture as possible was used. The amount of unused mixture was weighed and this value taken into account when calculating the Pt loading. The carbon sheet was then hot pressed with a pressure of 10 kg cm^{-2} and a temperature of 100 °C for 3 minutes.

Circular electrodes were cut from the resulting sheet. An electrode area of 0.78 cm^2 and a loading of 0.5 to 1 mg Pt cm^{-2} were used for electrochemical tests in the half-cell. Larger electrodes with an area of 2.5 cm^2 were cut out for use in the *in situ* XAS and XRD electrochemical cells. Higher loadings of 3 – 5 mg Pt cm^{-2} were used for the *in* situ XAS and XRD studies in order to obtain an edge jump in the region of 0.3 – 1 (see section 3.2.3) in XAS and to improve the reflected intensity in XRD. For all flooded half-cell experiments the electrodes were placed in boiling water for approximately 20 minutes to ensure that they were fully hydrated.

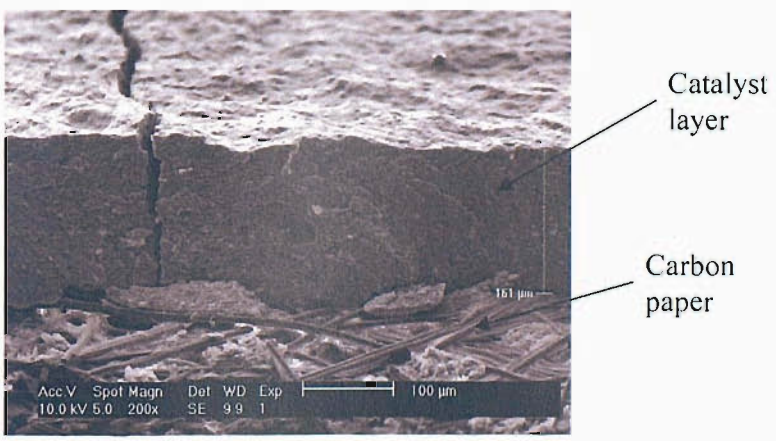

Figure 1 **Cross-sectional SEM image of a Pt/C electrode with a loading of 4 mg Pt cm^{-2} prepared using the pasting method. Magnification x 200.**

An SEM image showing the catalyst layer on the carbon substrate is shown in figure 1. A thickness of 160 μm is found with a platinum loading of 4 mg cm^{-2}. The fibres from the carbon support can clearly be seen.

1.3 Painted Electrodes

Firstly, a known quantity of catalyst was ground with a pestle and mortar until finely dispersed. The amount of 12.5 wt. % aqueous Nafion® added was dependent on whether the electrode was going to be used at the anode or cathode. For the anode, 50 wt. % Nafion® with respect to the total amount of catalyst was used whereas at the cathode 75 wt. % Nafion® with respect to the carbon content was used. It is important that as much of the catalyst is utilised as possible and that the interactions between the metal particles and the Nafion® is maximised. Due to differing environments at the anode and cathode different loadings were used to optimise the electrode performance. The catalyst was added slowly to the Nafion® solution at 70 °C while being stirred constantly and ensuring that the catalyst was thoroughly wetted. Once all the catalyst had been added a Silverson (laboratory stirrer) was used to make sure the ink was completely mixed. If the ink became too thick, water was added. Before painting, to ensure even coverage, IPA was used to wet the carbon paper. After painting each layer, the electrode was dried for 10 to 20 seconds at 120 °C on a hotplate and was weighed. Extra layers of catalyst were added until the correct loading was obtained according to following formula:

$$\text{Pt loading} = \frac{\text{ink weight/ g} \times \%\,\text{catalyst in dried layer} \times \%\,\text{Pt in catalyst}}{\text{electrodearea/ cm}^2} \qquad \textbf{Eq. 1}$$

The electrodes could then be used for making MEAs (section 1.5). For half-cell work, the electrodes were heat treated at 177 °C (above Nafion's® glass transition temperature) for 2 minutes before use.

Figure 2 shows SEM images of electrodes prepared using the painting method. The catalyst layer thickness is approximately 15 μm with a platinum loading of 0.3 mg cm^{-2}.

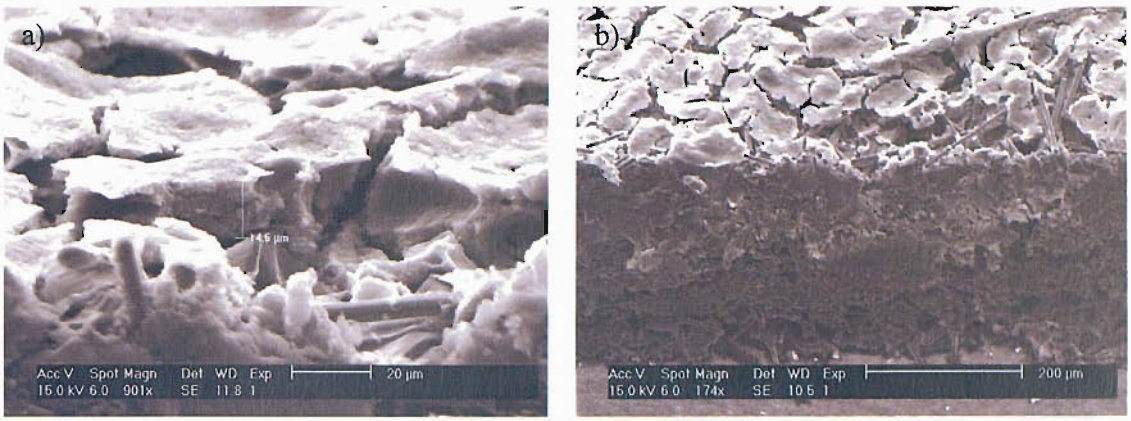

Figure 2 **Cross-sectional SEM images of Pt/C electrode with a loading of 0.3 mg Pt cm^{-2} prepared using the painting method. Magnification (a) x 900, (b) x 174.**

1.4 Screen Printed Electrodes

The ink used in screen printing processing was made in the same way as that for painted electrodes (section 1.3). The ink was smoothly drawn across a screen containing pores covering the carbon paper. The ink passed down through the pores and onto the carbon paper creating thin catalyst layers. Once the electrode was dry it was covered in cling film and pressed at 10 kg cm^{-2} before being weighed and the Pt loading calculated using equation 1. By altering the screen size and the number and size of the pores in the screen, the loading could be controlled so that by trial and error the required loading could be reached. The heat treatment was the same as that used for the painted electrodes (section 1.3).

1.5 MEA preparation

Electrodes with an area of 12.57 cm^2 were cut from the sheet prepared by painting or screen printing. The anode and cathode were positioned either side of a Flemion® SH30 membrane and hot pressed at 150 °C and 230 psi for 2 minutes. A thin sheet of PTFE and paper with a 20 µm thickness was used in the press to ensure even compression (figure 3). It was important to align the anode and cathode accurately to avoid edge effects that result in reduced MEA performance.

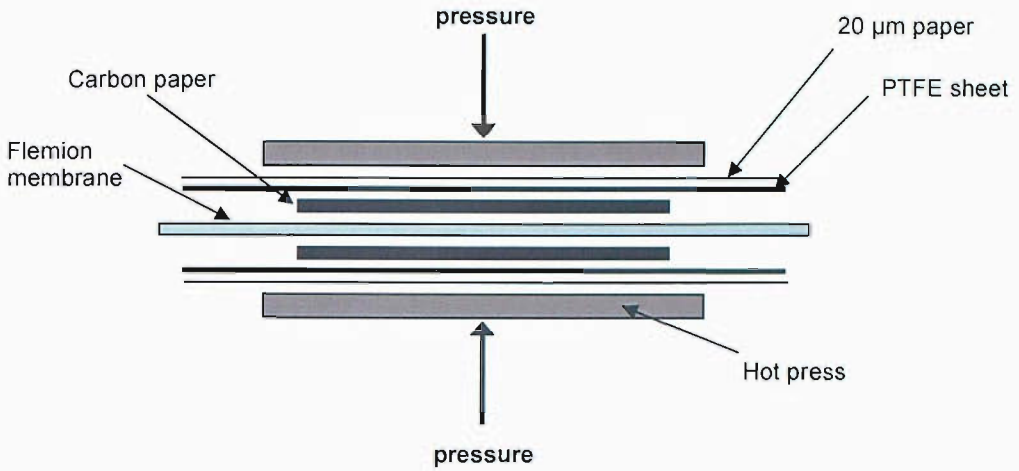

Figure 3 **Arrangement used for hot pressing MEAs showing positioning of PTFE sheet and 20 µm paper used to ensure even compression.**

2 ELECTROCHEMICAL METHODS

Instrumental electrochemistry plays two vital roles in fuel cell research. The first of these is the characterisation of the physical and electronic properties of the catalyst. This involves half-cell measurements which tend to be the first electrochemical tests carried out when presented with a new catalyst and include linear sweep voltammetry and cyclic voltammetry. They are very sensitive techniques and can be used to determine the active electrode area of the catalyst and to carry out quantitative investigation of reactions involving adsorption processes. The second role instrumental electrochemistry plays is in the determination of the performance of the catalyst for hydrogen or methanol oxidation and oxygen reduction. Polarisation curves can give a clear indication of performance and can be carried out potentiostatically by applying a potential to the electrode and measuring the current response.

2.1 Linear Sweep and Cyclic Voltammetry

In linear sweep voltammetry (LSV), the potential scan is applied in only one direction (positive or negative), between two limits at a known sweep rate (v). The cell current is recorded as a function of potential. Figure 4a shows the form of the applied potential between limits 1 and 2 while figure 4b shows a practical example

of the corresponding current response. The form of the current response is dependent on the charge transfer processes taking place at the surface of the working electrode.

Cyclic voltammetry (CV) is an extension of LSV. Again the potential is swept between two potential limits at a known sweep rate (v). On reaching the second limit, the direction of the sweep is reversed and the potential is scanned back to the original value. This gives rise to a triangular potential cycle as shown in figure 5a. The potential limits are selected in such a way that the lower limit corresponds to the start of hydrogen evolution and the upper limit to oxygen evolution. As in LSV the current response is dependent on the charge transfer processes taking place. An example of this is shown in figure 5b. In the reverse sweep the reduction reactions that occur at the working electrode can be studied. The symmetry of the peaks in the forward and reverse sweep suggests whether a reversible or irreversible reaction is taking place and hence the rates of the electron transfer reactions. Symmetrical peaks will be found in reversible cases, but the shape of the cyclic voltammogram changes for the non-Nernstian systems. For the irreversible case the forward peak ceases to be symmetric and the reverse peak is absent. For quasi-reversible reactions there will be a reverse peak, but both peaks will be asymmetric and there will be a separation in peak positions [2].

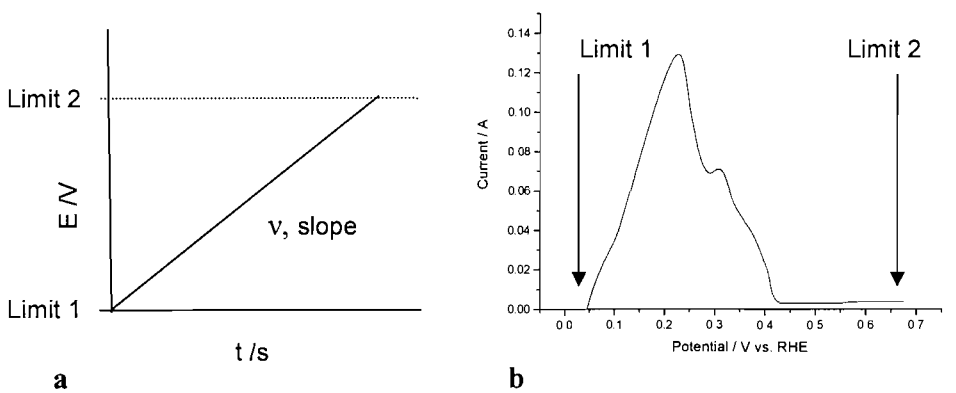

Figure 4 **Applied potential (a) and current response (b) for a linear sweep voltammogram of a Pt/C electrode in 2.5 M H_2SO_4 [3].**

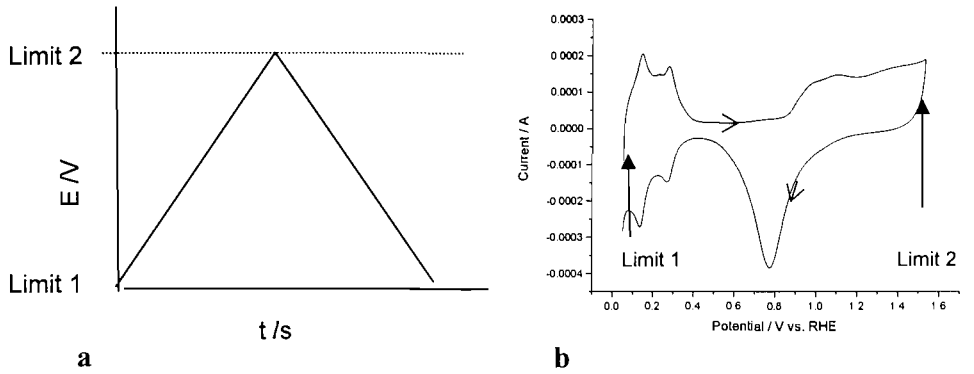

Figure 5 **Applied potential (a) and current response (b) for a cyclic voltammogram of a Pt/C electrode in 2.5 M H_2SO_4.**

One of the main uses of cyclic voltammetry for Pt based anode catalysts was to determine the oxidation potential of carbon monoxide (irreversible reaction) and to evaluate the electrochemical surface area of the catalysts. This will be described in detail in section 2.2.4. However, first the practical procedure used for CV and LSV will be discussed.

2.2 Apparatus and Experimental Procedure

This section will cover cell design and the procedure used for obtaining CVs in a flooded half-cell environment. This thesis concentrates on platinum based catalysts so the features observed in a typical platinum CV will be covered along with the effect of introducing CO to the electrolyte. Methods for determining catalyst surface areas from the CVs will be discussed in section 2.2.4.

2.2.1 Electrochemical cell

Both CV and LSV were carried out in an electrochemical cell comprised of three electrodes (a working electrode (WE), a counter electrode (CE) and a reference electrode (RE)), in an electrolyte, typically 2.5 M H_2SO_4. The electrodes were connected to an Electrochemie Autolab PGSTAT30, which is a combined potentiostat and waveform generator. The electrode potential was controlled by applying a potential difference between the RE and WE. The potentiostat ensured

that current only flowed between the WE and CE, with no current flowing through the reference part of the circuit. This overcame the problem of iR drop in solution and allowed the current to be related directly to the potential drop at the working/solution interface [4]. An example of the electrochemical cell used is shown in figure 6.

The electrode containing the catalyst being studied was held in position at the WE by a screw-on flange. A platinum wire was used as an electrical contact to the back of the WE. The WE holder was mounted in a glass cell with a capacity of 150 cm^3 that had an integrated water jacket for temperature control. A platinum gauze acted as a CE and a mercury mercurous sulphate (MMS), Hg/Hg_2SO_4, reference electrode was used. All potentials measured with respect to a MMS reference electrode have been corrected to the RHE electrode scale, as determined by calibrating with respect to a dynamic hydrogen/Pt electrode (MMS = 0.65 V vs. RHE). A Luggin capillary was used with the reference electrode to reduce errors in the potential due to solution resistance. The electrolyte was purged with nitrogen before use to displace any dissolved oxygen in solution.

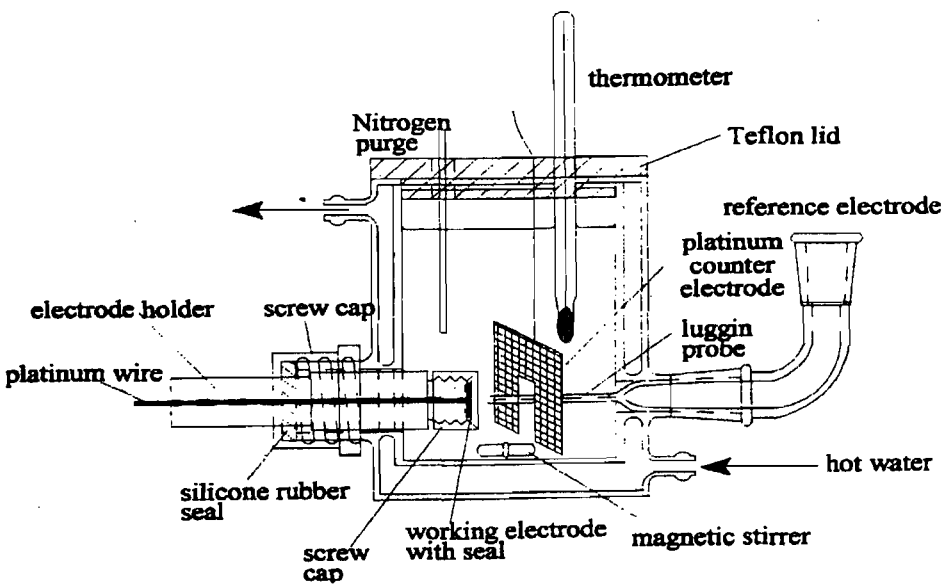

Figure 6 **Example of the three electrode electrochemical cell used to test fuel cell catalysts [5].**

2.2.2 Practical procedure

As mentioned in section 1, carbon-supported electrodes cut out for half-cell experiments were placed in boiling water until they reached a fully flooded state. The electrode was then placed in an electrode holder and a screw-on cap tightened to ensure good contact between the platinum wire and electrode. This assembly was then inserted into the electrochemical cell (figure 6) and 2.5 M H_2SO_4 was then added to the cell and the electrodes were connected to the Autolab potentiostat PGSTAT30. The electrolyte was purged for 20 minutes with nitrogen to remove dissolved oxygen with the stirrer bar rotating ensuring that the electrolyte was well circulated. The stirrer was then turned off and nitrogen was flowed over the surface of the electrolyte. The electrode was cycled between 0.0 V and 1.0 V vs. RHE at 10 mV s^{-1} until a stable CV had been recorded. An example of a platinum CV obtained using this method is shown in figure 7 and discussed in detail in section 2.2.3.

To obtain a CO poisoned platinum CV, a pre-treatment was required and this was programmed into the Autolab software. To ensure complete coverage of CO on the electrode surface, the electrode was held at a potential of 0.05 V vs. RHE for 60 minutes. During this time, CO was bubbled through the solution for 30 minutes followed by nitrogen for a further 30 minutes to remove all dissolved CO in solution. The electrode was then cycled to the upper potential limit of 1.0 V vs. RHE to remove the CO from the surface and then back to a lower limit of 0.0 V vs. RHE at 10 mV s^{-1} (figure 8). A second scan was taken to confirm that all CO had been stripped from the surface.

2.2.3 CV of a platinum surface

Figure 7 gives an example of a typical platinum CV. It contains a number of different features, which can be divided up into three separate regions. An explanation of the processes taking place in each case is given below.

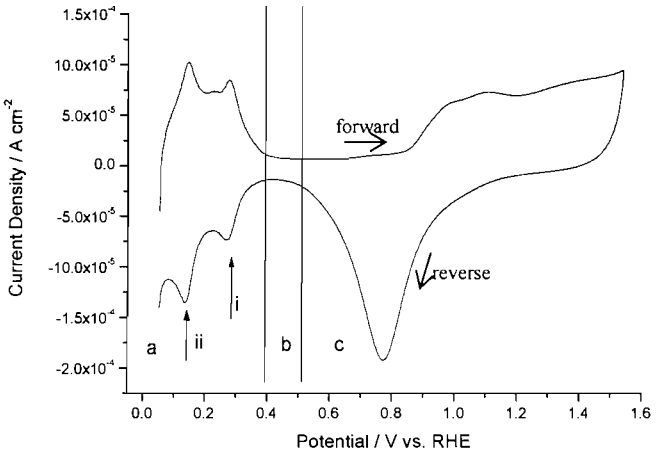

Figure 7 CV of a platinum disc electrode in 1 M H_2SO_4, v = 100 mV s^{-1}.

Region a – Hydrogen region. The peaks seen in the forward scan correspond to desorption of hydrogen from the surface whereas the reverse scan corresponds to adsorption of hydrogen to the surface (equation 2). Moving to more negative potentials marks the start of hydrogen evolution. The strength of the hydrogen adsorption can be determined by the position of the peaks. Peak (i) corresponds to strongly adsorbed hydrogen whereas peak (ii) corresponds to weakly adsorbed hydrogen requiring a smaller overpotential to be desorbed. The area under the hydrogen adsorption peaks can be used to measure the surface area of the platinum (i and ii). The desorption peaks should not be used for high surface area catalysts as hydrogen retained in the structure after hydrogen evolution can be reoxidised giving rise to larger peak areas.

$$Pt + H^+ + e^- \longrightarrow Pt - H_{ads} \qquad \textbf{Eq. 2}$$

Region b – Double layer region. The current flowing in the double layer region is not from chemical reactions but from the charging of the electrochemical double layer by the electrical charges in the electrolyte migrating to the electrode surface. The charging current is proportional to the scan rate, v, and as v is increased the currents are no longer negligible compared to the Faradaic current and as a result distortions appear in the CV. Scan rates in the 10 to 20 mV s^{-1} range were used throughout this work to avoid this.

Region c – Oxide region. An oxide layer begins to form on the platinum surface at around 0.8 – 0.9 V vs. RHE (equations 3 and 4). Once a layer has formed, the oxygen starts to move into the bulk of the metal by a place exchange mechanism. In the reverse sweep a peak is found at 0.78 V vs. RHE corresponding to oxide reduction. The position and area under this peak varies depending on the time spent in the oxide region and the potential to which it was taken. The area of the peak cannot be used to calculate the surface area of the catalyst because the oxide is not confined to the surface.

$$Pt + H_2O \longrightarrow Pt - OH_{ads} + H^+ + e^- \qquad \textbf{Eq. 3}$$

$$Pt - OH_{ads} \longrightarrow PtO + H^+ + e^- \qquad \textbf{Eq. 4}$$

2.2.4 CV of a CO poisoned platinum surface

The effect of introducing CO to the electrolyte is shown clearly in figure 8. The region characteristic of hydrogen desorption is suppressed in the first forward sweep due to the nearly complete CO surface coverage. As the potential is increased an onset potential is reached at 0.43 V vs. RHE when the current begins to rise, indicating CO is being oxidised to CO_2 (equation 5). A peak is reached at 0.73 V vs. RHE, some 0.83 V anodic of the standard reversible potential for the reaction shown in equation 5. This large overpotential demonstrates how strongly CO binds to platinum sites and highlights the problems of having CO present in H_2 as is the case for reformate gases. A clear indication as to whether a catalyst is CO tolerant can be determined by the position of the CO stripping peak. Increased CO tolerance is indicated by a peak shift to more negative potentials. On the reverse sweep no CO reduction peak is seen, indicating that the process is completely irreversible. The removal of the CO from the surface allows the features corresponding to hydrogen adsorption and desorption to reappear in the second scan.

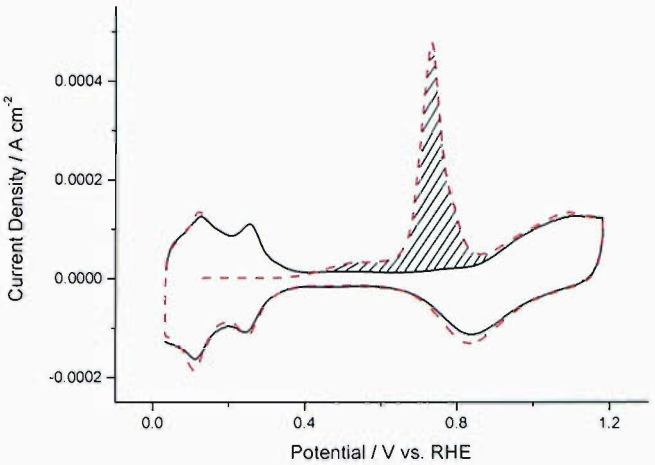

Figure 8 **CV of a platinum surface in 2.5 M H_2SO_4 following a 30 minute CO purge and subsequent 30 minute N_2 purge at 0.05 V vs. RHE. Scan rate = 10 mV s^{-1}. Dotted line: first scan, solid line: second scan.**

$$Pt - CO + H_2O \longrightarrow Pt + CO_2 + 2H^+ + 2e^- \qquad \textbf{Eq. 5}$$

The peak area highlighted in figure 8 and obtained by subtracting the first from the second scan can be used to calculate the catalyst area. The area corresponds to the charge passed during the electro-oxidation of CO. The charge associated with a monolayer of CO is 420 μC cm^{-2} Pt [6]. The active platinum surface area of the catalyst layer (Pt_{area}) can be calculated using this constant as shown in equation 6. To take into account of the amount of platinum present in the catalyst layer, the platinum surface area must be divided by the Pt loading (equation 7) to give the mass normalised area (Pt_{area_m}).

$$Pt_{area} = \frac{\text{Measured CO Charge} / \mu C}{420\ \mu C\ cm^{-2}\ Pt} \qquad \textbf{Eq. 6}$$

$$Pt_{area_m} = \text{mass normalised area} = \frac{Pt_{area} / cm^2\ Pt}{\text{mass of Pt} / mg\ Pt\ cm^{-2}} \qquad \textbf{Eq. 7}$$

2.3 Polarisation

Polarisation refers to the difference between the thermodynamic cell voltage and the measured cell voltage. Throughout this work these measurements will be carried out

potentiostatically as opposed to galvanostatically i.e. a potential will be applied to the electrode and after a steady state condition has been reached the current will be recorded. Steady state polarisation experiments provide a useful way of determining the performance of different catalysts and identifying where inefficiencies arise. A typical polarisation curve for oxygen reduction is shown in figure 9.

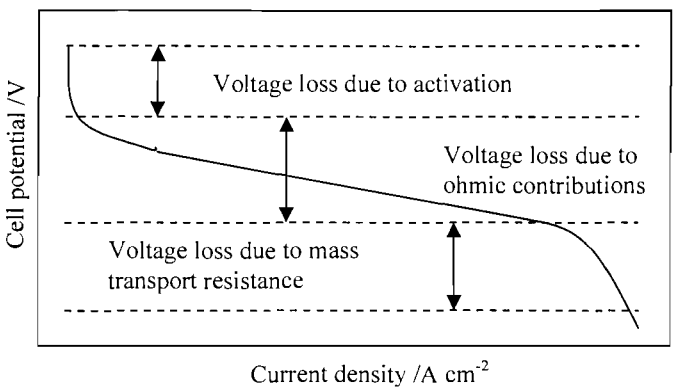

Figure 9 **Polarisation curve identifying the different inefficiencies of a fuel cell.**

The ideal case would give rise to a horizontal line at 1.23 V vs. RHE. However, inefficiencies lead to deviations of the electrode potential from its thermodynamic value. These can be separated into three main categories; the activation overpotential, the ohmic overpotential and the concentration overpotential. This can be expressed in terms of the overpotential of the electrode as follows:

$$\eta = E - E_e$$

where $\eta = \eta_o$ (activation) + η_{iR} (ohmic) + $\eta_{concentration}$ (mass transport)

The activation overpotential is dependent on the rate of reaction at the electrode surface. The extent of the potential loss is determined by the electrocatalyst properties and therefore can be reduced by using electrocatalysts with low activation resistance and by increasing the catalyst surface area available.

The gradual drop in voltage seen in the second region is related to the ohmic overpotential (η_r). η_r is directly proportional to the resistance in the cell ($\eta_r = iR$) arising from the current collectors, electrodes and the electrolyte. Lowering this

resistance will result in a shallower slope in the polarisation curve and consequently higher current densities. The ohmic losses can be accounted for using a current interrupt method and will be discussed in more detail in section 2.3.1.

The sharp potential drop observed in the third region at high current densities results from depletion of the reactant at the reaction interface as mass transport to the reaction sites fails to keep up with the reaction rate. This is a particularly acute problem when oxygen is the reactant. The concentration of oxygen at the surface of the catalyst is not only depleted by the reaction but also by the presence of water, a product of the reaction, creating an additional barrier. Improvements in mass transport allow the ohmic region to be extended, resulting in a fuel cell that can operate at higher current densities.

2.3.1 Methanol oxidation

A three-electrode cell similar to that described in section 2.2.1 was used to study rates of methanol oxidation. The cell was placed in a water bath so that the temperature could be controlled. Firstly, the metal surface area was determined using CO stripping (section 2.2.4) in 1 M H_2SO_4. The electrode was then transferred to a cell containing 2 M methanol, 1 M H_2SO_4 electrolyte. To avoid methanol evaporation, the electrolyte was not purged with nitrogen. The electrode was conditioned by cycling the electrode between 0.05 and 0.8 V vs. RHE with a scan rate of 10 mV s^{-1}. A polarisation experiment was then carried out between 0.05 and 0.8 V vs. RHE using a step potential of 0.05 V and the current was measured after a stabilisation time of 30 seconds. Before the electrode was removed, a current interrupt measurement was taken at three potentials i.e. 0.65, 0.7 and 0.75 V vs. RHE. The values obtained were averaged and used to correct the data for cell resistance.

Current interrupt allows ohmic losses to be accounted for and it can be carried out by the Autolab potentiostat. The technique involves switching off the current and measuring the potential-time curve. As soon as the current is switched off, the potential difference across the ohmic resistance is zero and the charged double layer is discharged. The curve corresponding to the discharge can be extrapolated to the

start, t = 0 seconds, from which the iR drop can be calculated. The current is measured just before the cell is switched off allowing the uncompensated resistance to be calculated.

2.3.2 Oxygen reduction

The electrochemical cell used for oxygen reduction is shown in figure 10 (design provided by Johnson Matthey). It is a three electrode cell made from glass reinforced nylon. The working electrode is held in place on a platinum contact wire with the electrolyte on one side and the gases flowing past the other. The gases were only supplied to the back of the working electrode and not to the electrolyte. In half-cells mentioned previously, the electrode was used in its fully flooded state to ensure fast diffusion rates through the electrode. However, in this case a gas phase is also involved so it is important that the electrode is not flooded as this would immediately reduce the mass transport rates to the catalyst.

The experiments were carried out by first cutting an electrode of diameter 26.5 mm. Excess catalyst was removed using tape leaving the electrode with catalyst covering a geometric area of 2.14 cm^2 corresponding to the size of the seals used. Once the electrode had been mounted in its holder, the half-cell was filled with 2.5 M H_2SO_4. The mass transport rates were much faster because a gas phase is involved and therefore the time required was reduced. CO was flowed to the working electrode for 5 minutes followed by 10 minutes with N_2 while being held at a potential of 0.05 V vs. RHE. O_2 was then connected to the cell and the flow rate set well above the stoichiometric value at 150 cm^3 min^{-1} to ensure that O_2 was always present in excess.

The polarisation experiment was carried out between 0.5 V and 0.96 V vs. RHE. 50 mV steps were used over the ohmic region between 0.5 V and 0.7 V vs. RHE and 20 mV steps were used as the thermodynamic electrode potential is approached between 0.7 V and 0.96 V vs. RHE. A stabilisation time of 60 seconds was used in each case. The currents were iR corrected by taking current interrupt measurements at 0.65 V, 0.75 V and 0.8 V vs. RHE.

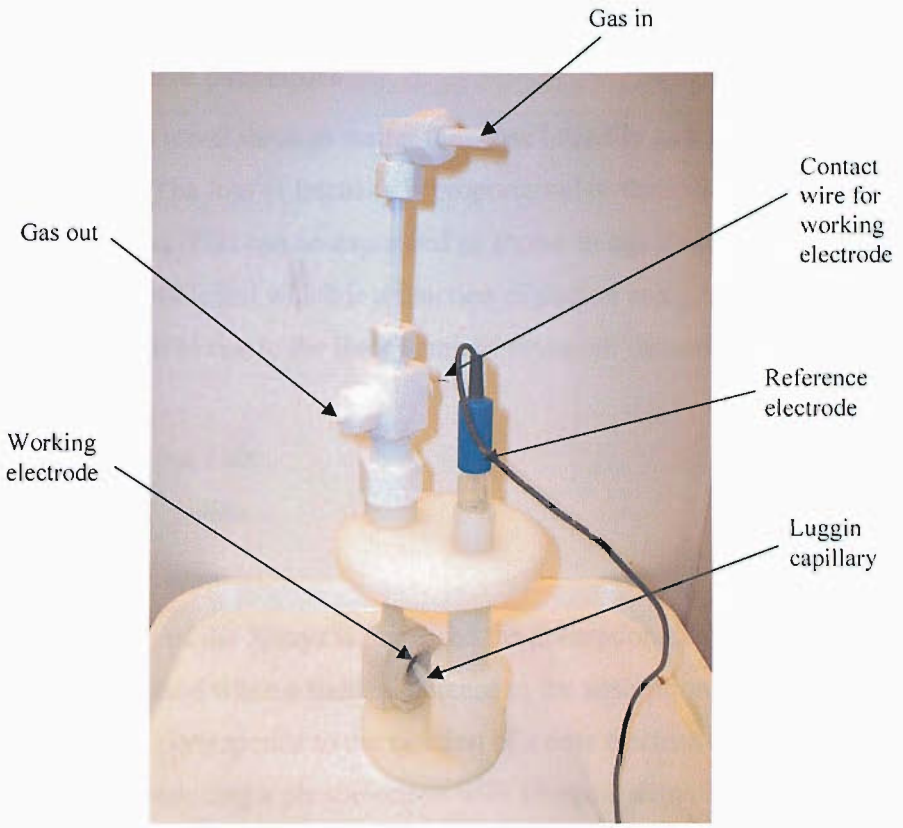

Figure 10 Electrochemical cell design used for oxygen reduction

3 X-RAY ABSORPTION SPECTROSCOPY

X-ray Absorption Spectroscopy (XAS) is a powerful technique that is not limited to materials with long-range order as required by XRD measurements. The spectra consist of two parts, X-ray Absorption Near Edge Structure (XANES) and Extended X-ray Absorption Fine Structure (EXAFS) both of which provide information on the structural properties of electrocatalysts. The X-rays used are high intensity and therefore there is little restriction on the environment of the electrocatalyst. This has allowed XAS experiments to be carried out in a gas cell and under potential control in both half and single cell environments.

3.1 Theoretical Aspects of XAS

3.1.1 General principles

When X-rays travel through matter they lose intensity as a result of interaction with the material. The loss of intensity is proportional to the incident intensity (I_o) and the path length (x). This can be expressed as shown in equation 8 where μ is the linear absorption coefficient which is a function of photon energy, E. Integrating over the path length gives rise to the Beer Lambert equation: (equation 9)

$$dI = -\mu I\, dx \qquad \textbf{Eq. 8}$$

$$I = I_o e^{-\mu(E)x} \qquad \textbf{Eq. 9}$$

As the energy of the X-rays is increased the absorption decreases until a critical energy is reached when a sudden increase in the absorption is observed. This discontinuity corresponds to the ejection of a core electron of the absorber into the continuum producing a photoelectron with kinetic energy, E_k.

$$E_k = h\nu - E_{binding} \qquad \textbf{Eq. 10}$$

Further increase in energy causes the absorption to fall again although at a different rate, until another absorption edge is reached. The absorption edges are labelled in order of increasing energy, K, L_I, L_{II}, L_{III} etc., according to the principle quantum number of the orbital from which the core electron was ejected. For example, K, L_I, L_{II}, L_{III} correspond to the excitation of an electron from the $1s(^2S_{1/2})$, $2s(^2S_{1/2})$, $2p(^2P_{1/2})$, $2p(^2P_{3/2})$ orbitals respectively (figure 11). The intensity of the absorption edge is determined by the X-ray absorption coefficient, μ, which is proportional to the probability of absorption of a photon according to Fermi's Golden Rule (equation 11).

$$\mu(E) = \frac{8\pi e^2 \omega^3 n}{hc^3} \cdot \left|\langle \psi_f \left| \hat{e} \cdot r \right| \psi_i \rangle\right|^2 \cdot \delta(E_f - E_i - h\nu) \qquad \textbf{Eq. 11}$$

This is a function of the initial state $|\psi_i\rangle$ and final state $|\psi_f\rangle$ wavefunctions where ê represents the electric field polarisation vector of the photon and r the coordinate vector of the photon.

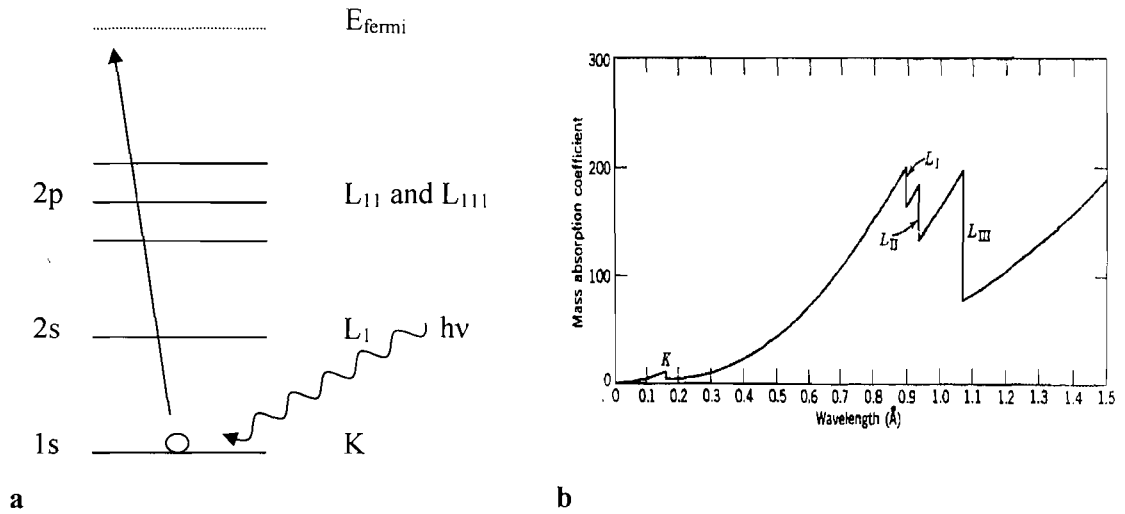

Figure 11 **a) Photoelectric effect – excitation of a core electron giving rise to the K edge. b) Platinum mass absorption coefficients plotted as a function of wavelength showing K and L edges.**

EXAFS is described in k space where the ejected photoelectron can be viewed as a spherical wave with wave vector, k, related to the photon energy, E. This is shown by equation 12 where E_0 is the zero point energy, usually taken as the inflection point of the absorption edge, and m_e is the mass of the electron.

$$k = \sqrt{\left(\frac{8\pi^2 m_e}{h^2}\right)(h\nu - E_0)} \qquad \textbf{Eq. 12}$$

The outgoing photoelectron wave is scattered from the neighbouring atoms producing a backscattered wave which can interfere either constructively or destructively with the outgoing wave. The final state wavefunction $|\psi_f\rangle$ is a superposition of the wavefunctions for the outgoing and back-scattered photoelectron waves. The interference between these two wavefunctions results in

the oscillatory behaviour of the absorption observed above the absorption edge. The absorption coefficient above the absorption edge is defined as,

$$\mu_{tot} = \mu_0 \cdot (1 + \chi) \qquad \textbf{Eq. 13}$$

where μ_0 is the background absorption of a single atom as a result of elastic and inelastic scattering. χ refers to the EXAFS oscillations which can be extracted from the experimental data using the following equation, where the oscillatory behaviour is given as a function of the wavevector, k.

$$\chi(k) = \frac{\mu_{tot}(k) - \mu_0(k)}{\mu_0(k)} \qquad \textbf{Eq. 14}$$

A typical XAS spectrum is shown in figure 12 and is generally divided into three regions. The first, known as the pre-edge region, is where the photon energy is insufficient to excite or ionise the electron of the element of interest ($E < E_0$). The second region is called the X-ray absorption near edge structure (XANES) where E ~ ± 10 eV. Features in the XANES region arise due to electron transitions from the core level to the higher unfilled or half-filled orbitals (e.g. $s \rightarrow p$, or $p \rightarrow d$). Multiple scattering and multi-photon absorptions dominate, making analysis far more difficult than for the EXAFS region. Most studies have been limited to white line analysis, which, in the case of Pt, allows the fractional d-electron occupancy of the Pt atoms in the catalyst to be determined. This will be discussed in detail in chapter 4. The third region is the extended X-ray absorption fine structure (EXAFS) which continues up to 1000 eV past the edge. The ejected photoelectrons in this region have high kinetic energy and single scattering by the nearest neighbour dominates.

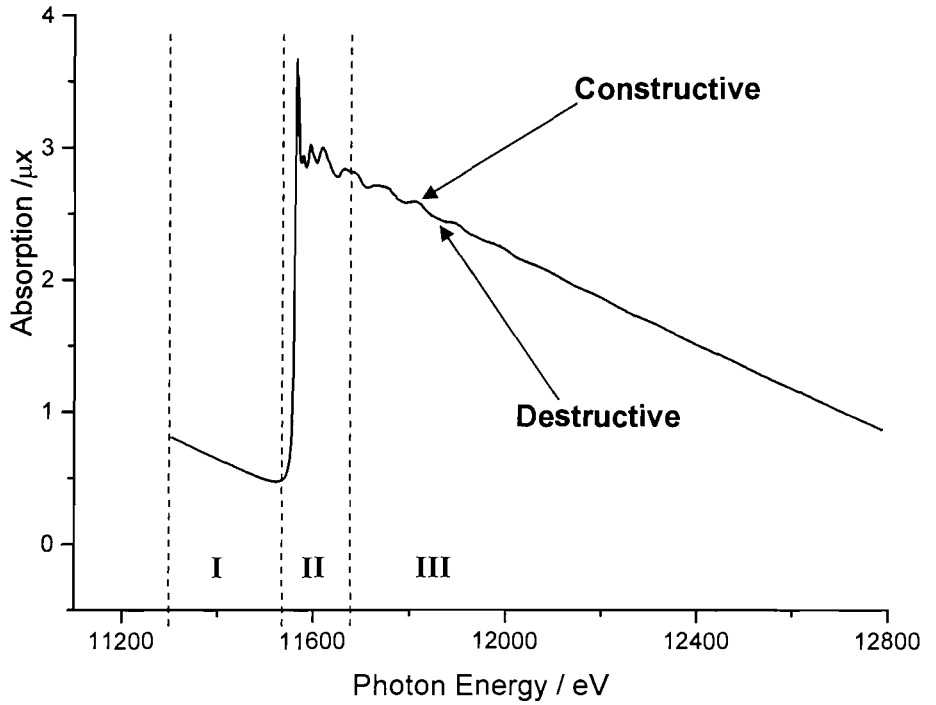

Figure 12 **XAS spectrum of a Pt foil at the Pt L_{III} edge showing: I – pre-edge region, II – edge and XANES region, III – EXAFS region. The inset schematic represents the interference patterns where —— is the maxima in the outgoing electron wave and ---- the maxima in the scattered electron wave.**

3.1.2 The history of EXAFS

EXAFS was first reported by Fricke in 1920 [7], however, it was not until the 1970s that EXAFS became a viable technique for studying materials as a result of work carried out by Sayers *et al.* [8]. Continued work by Lee *et al.* [9] gave rise to point-scattering plane wave approximation, which gave good agreement with experimental data. This is the simplest form of the EXAFS theories and relies on the approximation that the distance to the neighbouring atom is so much larger than the atomic radius of the central atom that the spherical wave may be approximated by a plane wave. However, the approximation breaks down at low values of k (less than 3 $Å^{-1}$) and has led to the development of more accurate EXAFS simulations using spherical or curved wave theory. Another assumption taken is that single scattering is the only important effect, i.e., the photoelectron wave is only scattered once before returning to the central atom. This is a good approximation because the

kinetic energy of the photoelectron in the EXAFS region is very high. An important development in the theory has been the accurate treatment of multiple scattering effects.

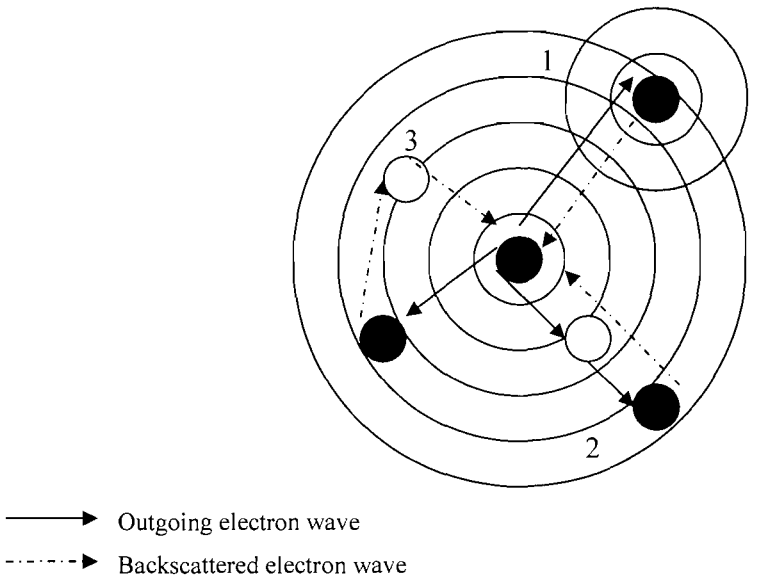

Figure 13 1) single scattering path. 2) and 3) multiple scattering paths.

Figure 13 shows some of the single and multiple scattering paths an outgoing photoelectron can take before returning to the absorbing atom. To be able to extract atomic structure information beyond the nearest neighbour bond distances, it is essential to include the effects of multiple scattering [10]. In particular, multiple scattering by atoms along a linear path, the so-called focussing or shadowing effect (figure 13 (2)) can exceed the single scattering contributions in magnitude. The EXAFS paper by Lee *et al.* [9] gave the first quantitative treatments of multiple scattering effects and more recent work by Zabinsky *et al.* [11] and Rehr and Albers [10] has resulted in the multiple scattering formulation of EXAFS becoming a relatively well understood problem.

3.1.3 EXAFS equations

As mentioned above, quantitative analysis of EXAFS was first carried out by Sayers *et al.* [8] and this work has become the standard for much of the current work. The EXAFS function is a summation of sine waves produced from the

outgoing photoelectron wavefunction, together with the backscattered wavefunction from each co-ordination shell, *j*.

$$\chi(k) = \sum_{j=1}^{shells} A_j(k) \sin \delta_j(k) \qquad \textbf{Eq. 15}$$

The formula contains an amplitude term, A_j, which can be described as follows:

$$A_j(k) = \frac{N_j}{kR_j^2} S_0^2 F_j(k) e^{-2k^2\sigma_j^2} e^{\frac{-2R_j}{\lambda(k)}} \qquad \textbf{Eq. 16}$$

where N_j is the number of atoms of type j at distance R_j from the absorber atom.

S_0 is the amplitude reduction factor reflecting multi-electron effects and central atom shake-up and shake-off due to relaxation processes after photo-ionisation.

F_j is the backscattering amplitude from the jth atom and can be extracted from reference compounds or calculated theoretically [12].

$e^{-2k^2\sigma_j^2}$ is the Debye Waller term. This factor is partly due to thermal effects which cause movement of the atoms from their equilibrium atomic positions. Structural disorder results in a similar effect and contributes to σ_j^2. It is an exponential damping term and, therefore, reduces the amplitude of χ at high k regions more than at low k values.

$e^{\frac{-2R_j}{\lambda(k)}}$ accounts for the decay of the wave due to the mean free path, λ or finite lifetime of the photoelectron and is responsible for the relatively short photoelectron range (few tens of Å) in a material analysed by EXAFS.

The second part of the term (equation 15) [13] is a sine function that reflects the dependence of the oscillatory structure on interatomic distances and energy.

$$\sin \delta(k) = \sin\left(2kR_j + \varphi_j(k)\right) \qquad \textbf{Eq. 17}$$

The sine function consists of the interatomic distance R_j between the absorber atom and the scatterer as well as a phase factor $\varphi_j(k)$ which can be expressed as follows:

$$\varphi_j(k) = 2\varphi_{absorber}(k) + \varphi_{backscatter}(k) \qquad \textbf{Eq. 18}$$

The larger contribution from the absorber to the overall phase factor arises as the photoelectron sees the potential created by this atom twice. The phase shifts account for the difference between the measured and geometric interatomic distances, typically a few tenths of an Å and as in the case of F_j it must be extracted from reference compounds or calculated theoretically.

3.1.4 Data analysis

EXAFS analysis involves fitting data to the EXAFS equation to obtain a structural model. However, before this stage is reached a number of steps have to be carried out. The first of these involves initialising and calibrating the data and the second is to normalise and background subtract the data to extract $\chi(k)$.

The data processing was carried out using the Daresbury suite of programs known as EXCALIB and EXBROOK. The raw data is read into EXCALIB where the energy scale is converted from the position of the monochromator in millidegrees to electronvolts. The program also allows several scans to be summed, thereby reducing noise levels. The first step in EXBROOK is to determine E_0 and subtract the pre-edge background from the data. Unless a sharp feature appears in the pre-edge, E_0 is taken from the maximum in the first derivative. Two quadratics are then used; one is fitted to pre-edge the other to the post-edge. This is then subtracted from the whole spectra and the data is normalised to give an edge jump of one, placing the measured spectrum on a per absorber atom basis (figure 14). The edge jump is defined as the distance between the linear pre-edge and smooth post-edge background extrapolated to E_0.

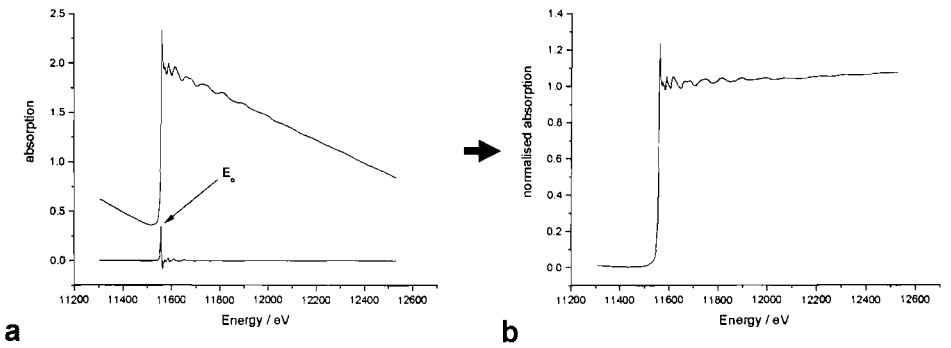

Figure 14 **a) Determining E_0 from first derivative**
b) Pre-edge background subtraction and normalisation

The final step in EXBROOK is background subtraction, isolating the oscillatory EXAFS from the atomic part of the absorption $\mu_0(k)$ (equation 14). The absorption of an isolated atom is unknown; therefore, the background subtraction is carried out by fitting a cubic spline. Care must be taken not to fit the EXAFS too closely as this will result in a loss of data. The start of the background subtraction is set approximately 50 eV above the edge position. The smoothing parameter, *SM*, (equation 19 [14]) is then selected based on changes to the chi and Fourier Transform plots. The weight factor *WE* can be used to enhance the high k part of the spectrum while the smoothing parameter, *SM*, determines the spline function of the background, *BCK*. The aim is to obtain chi data where the amplitude is evenly distributed above and below the axis and where the first peak of the Fourier Transform, usually found from 1.8 to 3 Å, is maximised whilst minimising contributions below 1 Å (figure 15).

$$\sum_{i=1}^{NPTS} \frac{(\mu_i - BCK_i)^2}{e^{-WEk_i^2}} \leq SM \qquad \textbf{Eq. 19}$$

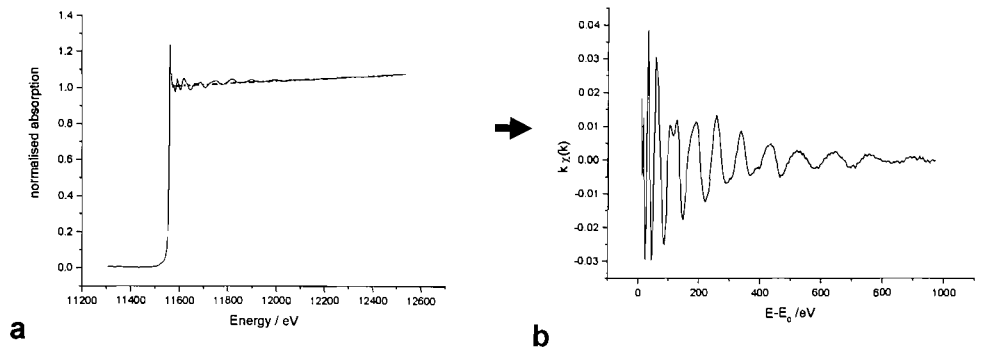

Figure 15 **a) Selection of cubic spline for post edge background removal b) Chi data**

EXCURV98 [15] was used to fit the chi data obtained from EXBROOK. The program simulates EXAFS spectra using rapid curved wave theory [16] and Rehr Albers theory [10,17,18] from the parameters of the radial shells of atoms surrounding the central atom. The EXAFS data is fitted in *k*-space where the coordination number (N), distance to the nearest neighbour (r), the Debye Waller term ($2\sigma^2$) and the shift in Fermi energy (E_f) are all parameters which can be refined. This is carried out using a least-squares minimisation of the fit index. The goodness of fit is determined as follows:

$$R_{exafs} = \sum_i^N 1/\sigma_i \left(\left| \chi_i^{exp}(k) - \chi_i^{th}(k) \right| \right) x\ 100\% \qquad \textbf{Eq. 20}$$

where N is the number of data points, σ_i the standard deviation for each data point, i, and $\chi_i^{exp}(k)$ and $\chi_i^{th}(k)$ the experimental and theoretical EXAFS, respectively. A value between 20 and 30 % is normally considered to be a reasonable fit. Errors in the parameters are estimated from standard deviations. The number of parameters, n, that can be justifiably fit can be estimated from the Nyqvist theorem [19]:

$$n = \frac{2\Delta k \Delta r}{\pi} + 1 \qquad \textbf{Eq. 21}$$

where Δk and Δr are the widths in k- and r- space used in the data analysis and over which the data is substantial.

The data produced from EXCUV98 is shown as chi data and its corresponding Fourier transform (figure 16). The radial distribution function (real part of the Fourier Transform) provides a convenient way of presenting the EXAFS data where the peak positions give the coordination shell radii, peak heights correspond to coordination numbers, and peak widths give an idea of disorder.

$\chi(k)$ decreases in amplitude with k so it is often advantageous to multiply the EXAFS function by k^i, where $i = 1$, 2, or 3. By changing the weighting from 1 to 3 emphasis can be shifted from low to high Z neighbours. In most cases a weighting of 2 is used as a compromise so contributions from both low and high Z neighbours are observed.

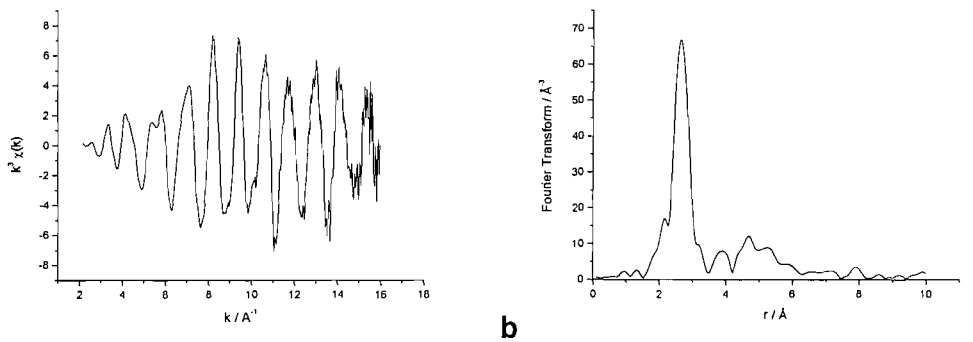

Figure 16 a) chi data and b) corresponding Fourier Transform

3.2 Experimental Aspects of XAS

3.2.1 X-ray source

The X-ray source was the SRS at Daresbury Laboratory, Warrington, UK. The advantage of using Synchrotron radiation is that it is highly collimated, 100 % plane polarised with a continuous energy distribution from infra-red to hard X-rays. The intensity of the radiation is typically 10^6 times greater than conventional sources. This allows EXAFS to be carried out on materials where the element of interest is present at very low concentrations. This is vital for fuel cell electrodes where, for example, platinum loadings are around 0.3 mg cm^{-2}.

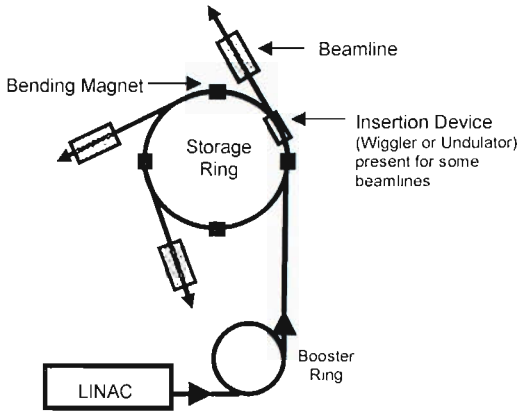

Figure 17 Schematic of the Synchrotron Radiation Source (SRS) [3]. (Not to scale)

The SRS at Daresbury consists of a LINAC (linear accelerator), a booster ring and a storage ring (figure 17). The electron beam is produced by the LINAC and is then accelerated by microwaves produced by a Klystron, which interact with the electrons propelling them along. Once an energy of 12 MeV has been reached the electron beam is injected into the booster ring. The beam is then further accelerated until an energy of 600 MeV is reached at which point the electrons are injected into the main storage ring where microwaves from the Klystron cause the electrons to travel around the storage ring in a series of bunches with a set distance between them and an energy of 2 GeV. Dipole bending magnets are used to bend the beam and it is this acceleration that causes the emission of radiation. The constant supply of energy from the microwaves is required to keep the electrons in orbit.

While the function of the bending magnets is to maintain a circulating beam of electrons, insertion devices such as wigglers and undulators can be included in the straight section of the storage ring to increase the energy distribution of the radiation. A wiggler is a magnetic structure which forces the electron beam to follow a trajectory with a smaller local radius of curvature [20]. The effect on the emitted spectrum is an increase the critical energy and shifting of the overall spectrum to higher energies. An undulator consists of an array of permanent magnets set above and below the electron beam path. As the electron beam passes through the array, its trajectory oscillates in the horizontal plane. Interference effects in undulator

radiation result in resonance peaks in the output spectrum. By varying the distance between the magnets and the electron beam, the position of the harmonics can be modified allowing optimisation for a given experiment. Undulator devices are commonly used for soft X-ray experiments whereas wigglers are used for hard X-ray experiments.

The storage ring is kept under ultra high vacuum, typically 10^{-10} mbar. However, losses still occur due to collisions between the electrons and gas molecules resulting in decay of the beam current. Therefore the beam must be refilled to maintain high currents.

3.2.2 Stations 7.1 and 16.5

Two stations were used at Daresbury laboratory for the EXAFS work presented in this thesis. The station chosen for a particular experiment depended on the energy range required.

Station 7.1 allows EXAFS measurements in the range 4 keV to 10 keV and consists of a harmonic rejecting sagittally focusing double crystal Si (111) monochromator with the first monochromator crystal cooled by circulating water. The sagittal focusing allows the entire X-ray beam to be focused onto the sample. The crystal is dynamically bent during EXAFS scans to maintain a focused spot size and this results in a flux gain and improved signal to noise. The fluorescence detector recently installed on the station consists of a monolithic structure nine-channel array on a germanium wafer with a diameter of 21.8 mm. This has lead to an increase in the total active area of the detector over traditional multi-element assemblies giving a high photon count rate and improved resolution [21]. In addition, the low profile of the detector has made it far easier to incorporate it into the difficult experimental setup required for *in situ* EXAFS work with fuel cells.

Station 16.5 operates at higher energies in the range 7 keV to 40 keV with a multipole wiggler source enhancing the flux and brightness of the light (see section 3.2.1). Vertical collimation is provided with a 1.2 m uncoated plane mirror. The monochromator consists of a water-cooled double crystal Si (220) where the

second crystal is dynamically bent to provide horizontal focus. The fluorescence detector on the station is an Ortec 30-element Ge solid-state detector.

In both cases the monochromators use the double crystal geometry. The aim of the monochromator is to select a well-defined photon energy from the source. This is accomplished using reflections from a crystal planes as a function of the incident angle θ_i according to the Bragg relation:

$$n\lambda = 2d\sin(\theta_i) \qquad \textbf{Eq. 22}$$

Where λ is the wavelength of light, d is the spacing of the atoms in the crystal and θ_i is the angle of incidence. To adjust for the angular deflection a second crystal is positioned at the same angle. However, the reflected beam is not perfectly monochromatic and contains higher harmonics, multiples of the original energy reflected by the first crystal. The harmonic content can be reduced by detuning the second crystal slightly. The higher harmonics have a smaller acceptance angle than the fundamental. This means that while the acceptance angle for the fundamental has a large overlap there is little overlap for the higher harmonics resulting in small reflectivity of the monochromator [22]. Typically, a harmonic rejection of 50 % was used for the Pt L_{III} and L_{II}, Co, Cr, Ti K edges while 70 % was used for higher energy edges such as the Ru K.

3.2.3 Transmission mode

EXAFS spectroscopy can be carried out using a number of different collection modes, the simplest being the transmission mode. The variation in absorption of the X-rays as the energy of the incident photons is increased is measured by a series of ion chambers where the absorption of the sample is obtained by $\ln(I_o / I_t)$. The ion chambers are positioned before and after the sample (figure 18). The first measures I_o to give the incoming intensity and is filled with a mixture of gases to absorb approximately 20 % of the incident flux while a second measures the transmitted intensity; I_t and is filled with a gas mix to absorb 80 %. A third detector I_r is used to calibrate the energy against a metal foil. This is important as the energy calibration

may not be exact and small edge shifts can contain valuable information. A high constant voltage is applied across the ion chambers so that the ions are attracted to the negative side and the electrons to the positive and as a result a current flows directly proportional to the number of photons entering.

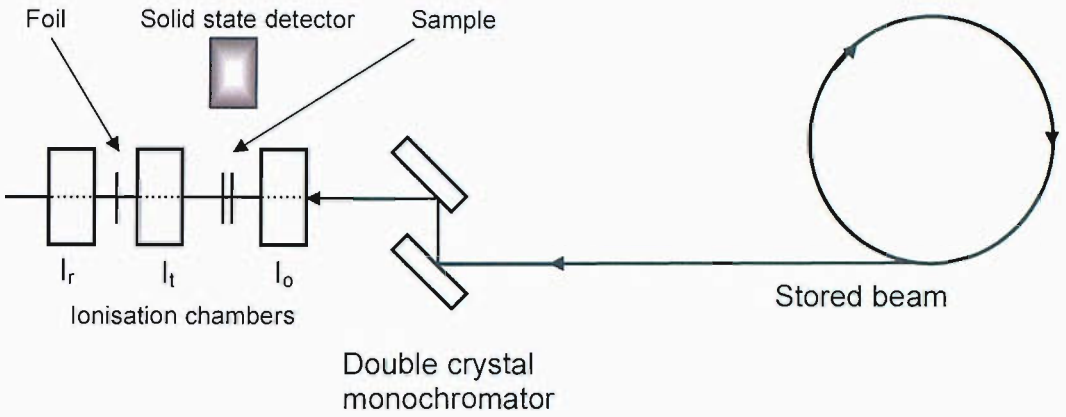

Figure 18 **Schematic of the experimental setup for the transmission mode. The position of the solid state detector is shown for the fluorescence mode.**

The transmission mode is used for the analysis of concentrated samples where there is a significant change in absorption across the edge while still allowing the X-rays through the sample so the change can be observed. This requires careful balance of the concentration and total absorption; an absorption edge (μx) of 0.3 to 1.0 is ideal. The mass of sample required to give this absorption edge can be calculated as follows:

$$mass = \frac{(\mu x)(area)}{(\mu / \rho)} \qquad \textbf{Eq. 23}$$

Where (μ / ρ) is the mass absorption coefficient of a sample with ρ being the density. The mass absorption coefficients were taken from McMaster *et al.* [23] who reported the values for all elements of the periodic table. The mass calculated gives the amount of the element of interest required so must be scaled up to take account of the fraction in the complete sample. The absorption of the other elements in the sample including any additional compounds such as boron nitride or polyethylene

used in the preparation must also be taken into account. The total sample absorption must be kept below 2.5 to prevent self-absorption effects that can lead to errors in coordination numbers.

Transmission is the preferred technique due to its simplicity and the fact that very little statistical noise is introduced through the measurement technique so most noise tends to be sample related. Care must be taken when preparing samples, in particular pellets used in the gas cell (section 3.2.5) to make sure they are completely homogeneous. This helps prevent pin holes in the sample, including areas with less sample than others, through which leakage of incident X-rays can take place. Once the sample becomes too dilute transmission mode can no longer be used as the contrast in absorption before and after the edge becomes indiscernible. In these cases the fluorescence mode can be used.

3.2.4 Fluorescence mode

In the fluorescence mode, the signal is absent before the edge and present after giving a greater contrast for more dilute samples. The experimental setup still uses I_o as a reference (figure 18). The absorption process creates core holes in the atom of the target element. These core holes fill instantaneously with electrons from outer shells and the energy difference between the outer and inner shells is emitted as fluorescent radiation characteristic of the absorbing element. The fluorescence EXAFS signal consists of only a small fraction of the total absorption and is proportional to the incident intensity as follows:

$$\mu(E) = \frac{I_{fluorescence}}{I_o} \qquad \textbf{Eq. 24}$$

The fluorescence photons produced by the sample in the absorption process are detected with a solid-state detector. The detector has a resolution of approximately 100 eV allowing discrimination against other radiative processes, such as elastic scattering, Compton scattering and fluorescence from other elements [22]. The detector is positioned orthogonally to the incident beam with the sample positioned

at 45° to maximise the solid angle. This orientation helps minimise scattering, which is the main source of noise in this technique.

3.2.5 Gas treatment cell

A gas treatment cell was used to analyse the catalysts in pellet form. A picture of the cell is shown in figure 19. The cell was designed to operate in both transmission and fluorescence modes. This was achieved by positioning the cell holder at 45° so that fluorescence could be detected, while an exit window in the cell allows X-rays to pass all the way through the sample. The entrance and exit windows were covered with Kapton film. The pellets were made by first mixing the catalyst with boron nitride using a pestle and mortar and equation 23 to calculate the amounts required before using a die press to form the pellet. Using polyethylene powder instead of boron nitride resulted in poor gas flow through the pellet preventing complete reduction.

Care was taken when setting up the cell to make sure that the X-rays passed through the cell without clipping the sides of the holder. This was done by placing photographic paper before and after the cell. Glitches in the spectra may appear as result of scatter if the X-ray beam does not pass through cleanly. On station 7.1 where lower energy edges were analysed, including Cr, Co and Ti K edges, high-density polyethylene pellet holders were used to reduce scatter and the possibility of contamination.

The gas treatment was carried out away from the beamline for safety reasons. The gas was flowed through the cell at atmospheric pressure for 1 - 2 hours before closing the taps. Once the EXAFS had been collected the cell was purged with nitrogen for approximately 30 minutes before opening to air.

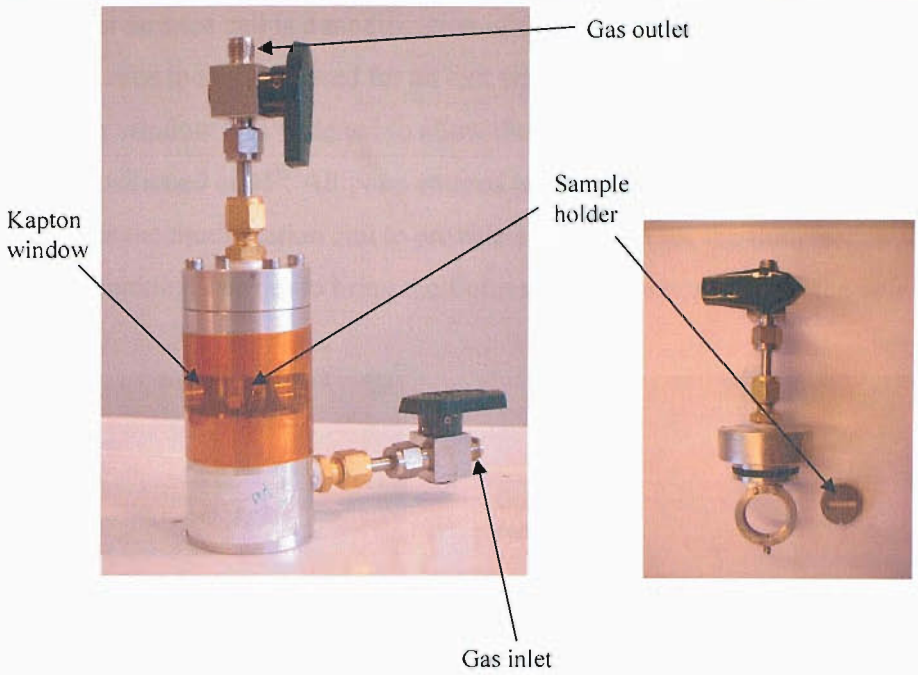

Figure 19 Gas treatment cell showing gas ports, window and sample holder.

3.2.6 Electrochemical cell

The electrochemical cell was based on a design reported by Herron *et al.* [24]. The cell used in this thesis has been reported by Maniguet *et al.* [25]. Two different designs were required to operate the cell in both transmission and fluorescence modes, although the principles are the same in both cases.

In the transmission case (figure 20), the cell consists of two acrylic plates each with circular Kapton windows in the centre. The entrance side of the cell has three ports. One is used for the gold contact wire for the working electrode; the others are empty ports that can be used for gas flow. The exit side of the cell has four ports; the lower of these is used for the MMS reference electrode attached via a salt bridge and one is for the Pt gauze counter electrode. The other two are the electrolyte entry and exit ports.

The cell is assembled by placing the flooded working electrode on the gold contact wire along with four layers of filter paper soaked in 1 M H_2SO_4. The assembly was then sandwiched between the two acrylic plates. A peristaltic pump was used during EXAFS data collection to allow removal of the bubbles from the cell.

The fluorescence cell is a modification of the transmission cell design. In fluorescence there is no need for an exit window so this was removed while the entrance window was widened to allow the X-rays to reach the working electrode while positioned at 45°. All ports entered and exited from the non-window side to allow for the modification and to provide a clear path for the fluorescent photons as well as making it easier to bring the fluorescence detector close to the cell.

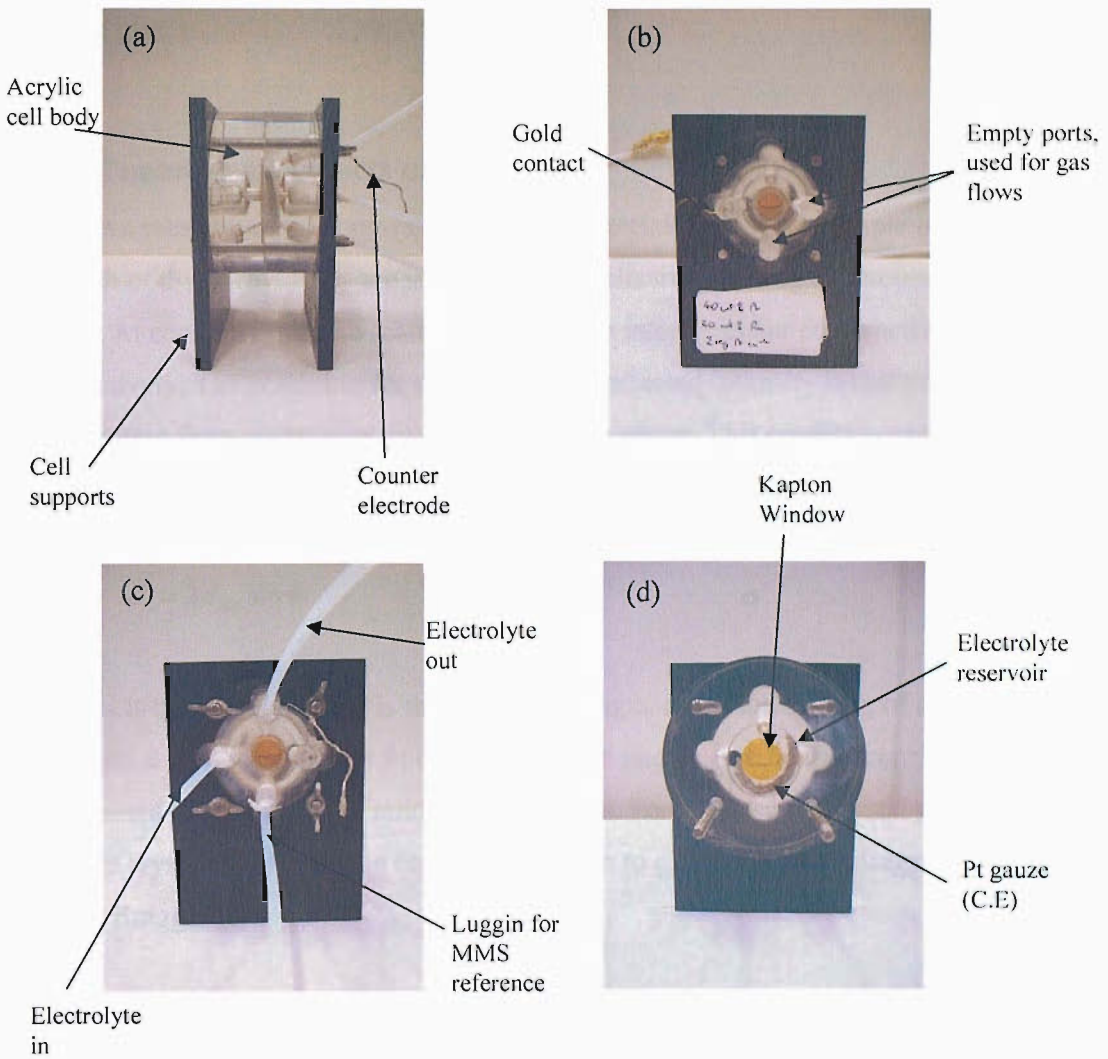

Figure 20 **Annotated pictures of the electrochemical transmission XAS cell. (a) Side view, (b) front view, (c) back view and (d) interior view.**

4 X-RAY DIFFRACTION

Both *ex situ* and *in situ* XRD experiments were carried out on the catalysts. The technique examines the crystalline fraction of the catalyst particle while the amorphous region cannot be detected. XRD provides information on lattice parameters complementing EXAFS data and in addition, peak broadening can be used to give an estimate of particle size.

4.1 Theoretical Aspects of XRD

XRD is a measure of the long-range order of materials. When the sample is put in the path of the X-rays, they are scattered by the electron distribution around the nuclei. At certain angles the scattered X-rays can interact either constructively or destructively. The condition for a maximum of reflected intensity is that the contribution from successive planes should be in phase. This condition can be expressed using Bragg's law:

$$n\lambda = 2d_{hkl}\sin\theta \qquad \textbf{Eq. 25}$$

where λ is the wavelength, θ is the diffraction angle, d_{hkl} is the spacing of the planes (hkl) and n is an integer. The Pt catalysts are not single crystals; they consist of many small crystallites with random orientations. For every set of crystal planes, one or more crystals will be in the correct orientation to give the correct Bragg angle to satisfy Bragg's law.

Given that the intermolecular spacing, d_{hkl}, assuming an fcc structure is as follows:

$$d_{hkl} = \frac{a}{\sqrt{h^2 + k^2 + l^2}} \qquad \textbf{Eq. 26}$$

Bragg's law can be used to determine the lattice parameter, a, once the fcc peak positions, θ_{hkl}, have been identified.

$$\sin^2 \theta_{hkl} = \frac{\lambda^2}{4a^2}(h^2 + k^2 + l^2) \qquad \textbf{Eq. 27}$$

XRD patterns are normally plotted as intensity versus 2θ, an example of which is shown in figure 21. For the fcc structure some values of *hkl* are not possible. The indices must be all odd or all even, thus the first few lines are (111), (200), (220), (311), (222). Four of these diffraction peaks have been assigned in figure 21 for a PtRu catalyst with 54 wt. % Pt and 6 wt. % Ru.

There is a correlation between the peak widths and particle sizes; as the particle size gets smaller, the diffraction peaks become wider. The (220) reflections were analysed to determine the particle size. After subtracting a linear background a Lorentzian function was fitted to determine the FWHM values The inset in figure 20 provides an example of the peak fit for the (220) reflection.

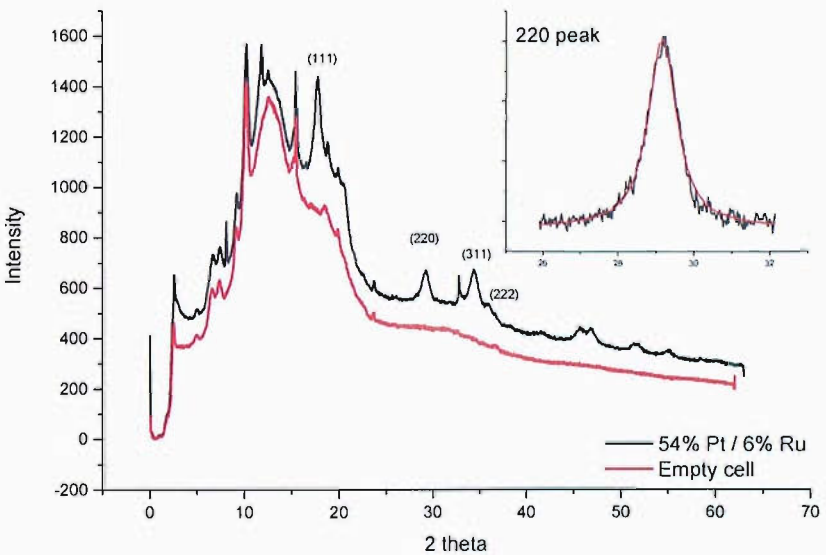

Figure 21 ***In situ*** **XRD at 0.0 V vs. RHE. 54 wt. % Pt 6 wt. % Ru catalyst showing assignment of first four reflections for an fcc structure. Inset shows peak fitting used to calculate particle size.**

From the FWHM value, the average particle size L can be estimated using the Scherrer equation:

$$L = \frac{0.9\,\lambda}{B_{2\theta}\cos\theta_{\max}} \qquad \textbf{Eq. 28}$$

Where λ is the wavelength (0.692 Å) and $B_{2\theta}$ is the measured broadening in radians.

4.2 Experimental Aspects of XRD

The cell setup was very similar to that used for the EXAFS experiments with an enlarged vertical exit window to allow for the X-ray scattering (figure 22(a)). The experiments were carried out using the high-resolution powder diffraction facility at station 9.1 at the Daresbury laboratory. The station can deliver 0.6 mrads of beam to the sample from the 5 Tesla wiggler via a water cooled Si (111) monochromator. A wavelength of 0.692 Å was used for all experiments and the XRD data were collected using a Curved Image Plate (CIP) camera [26] which is shown in figure 22(b). The beam size was reduced to 0.5 mm x 0.5 mm and this was passed down an anti-scatter tube to impinge on the sample.

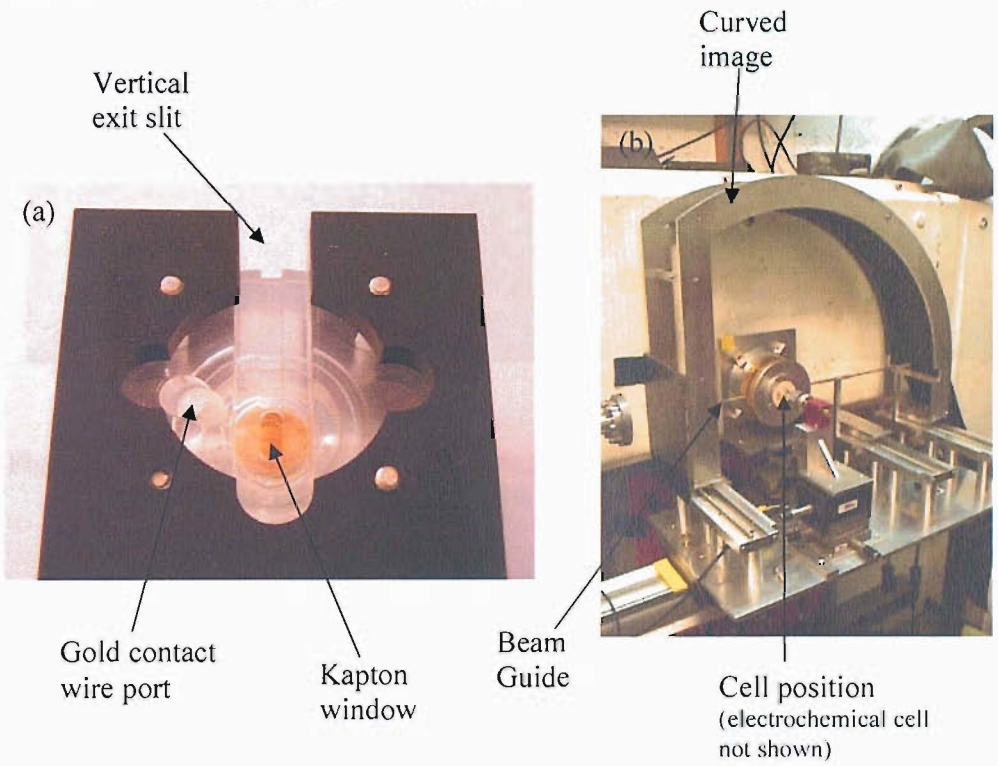

Figure 22 **(a) Electrochemical cell showing enlarged vertical exit window**
(b) Picture of Curved Image Plate camera used on station 9.1.

Before starting, an X-ray diffraction pattern was taken of the electrochemical cell in the absence of catalysts, just containing electrolyte and carbon paper as shown in figure 21. This subsequently allowed the peaks corresponding to the catalyst to be

easily identified. The cell was located at the centre of curvature of the 350 mm radius camera arc. To correct for positional discrepancy, data were collected from a silicon pellet mounted in the same cell. Spatial distortions introduced when reading the image plate were corrected using a grid calibration, which was repeated every 10 images. The film slide is loaded into the CIP in darkness and a scan time of 5 minutes and scan resolution of 176 μm was used.

An example of the scanned image taken using a CIP is shown in figure 23. From this image, the computer calculates the 2θ scattering angle for each pixel and integrates the intensity around the diffraction bands.

Figure 23 **Scanned image taken using a film slide from a Curved Image Plate (CIP) camera. White lines indicate diffraction bands.**

5 REFERENCES

1. Keck, L.; Buchanan, J.; Hards, G. A. *United States Patent*, 1991; Vol. 5 068 161.
2. Pletcher, D.; Greef, R.; Peat, R.; Peter, L. M.; Robinson, J. *Instrumental Methods in Electrochemistry*; Horwood Publishing, 1985.
3. Rose, A. Structural Effects in Fuel Cell Electrocatalysts. PhD, University of Southampton, 2004.
4. Fisher, A. C. *Electrode Dynamics*; Oxford University Press, 1996.
5. Hogarth, M. P. The Development of the Direct Methanol Fuel Cell. PhD, University of Newcastle upon Tyne, 1995.
6. Bett, J.; Kinoshita, K.; Routsis, K.; Stonehart, P. *Journal of Catalysis* **1973**, *29*, 160.
7. Lytle, F. W. *Journal of Synchrotron Radiation* **1999**, *6*, 123.
8. Sayers, D. E.; Stern, E. A. *Physical Review Letters* **1971**, *27*, 1204.
9. Lee, P. A.; Pendry, J. B. *Physical Review B* **1975**, *11*, 2795.
10. Rehr, J. J.; Albers, R. C. *Reviews of Modern Physics* **2000**, *72*, 621.
11. Zabinsky, S. I.; Rehr, J. J.; Ankudinov, A.; Albers, R. C.; Eller, M. J. *Physical Review B* **1995**, *52*, 2995.
12. Russell, A. E.; Rose, A. *Journal of the American Chemical Society* **2004**, *104*, 4613.
13. Mojet, B. L. *Metal-Support Interactions - a step closer to the origin*; Utrecht University, 1997.
14. Cook, J. W.; Sayers, D. E. *Journal of Applied Physics* **1981**, *52*, 5024.
15. Binsted, N. EXCURV98: CCLRC Daresbury Laboratory computer program, 1998.
16. Gurman, S. J.; Binsted, N.; Ross, I. *Journal of Physics C-Solid State Physics* **1984**, *17*, 143.
17. Rehr, J. J.; Albers, R. C. *Physical Review B* **1990**, *41*, 8139.
18. Rehr, J. J.; Albers, R. C.; Zabinsky, S. I. *Physical Review Letters* **1992**, *69*, 3397.

19. Stern, E. A. *Physical Review B* **1993**, *48*, 9825.

20. Koch, E. E. *Handbook on Synchrotron Radiation*; North-Holland Publishing, 1983; Vol. 1A.

21. Derbyshire, G.; Cheung, K. C.; Sangsingkeow, P.; Hasnain, S. S. *Journal of Synchrotron Radiation* **1999**, *6*, 62.

22. Kampers, F. W. H. *EXAFS in Catalysis: Instrumentation and Applications*; Technical University of Eindhoven, 1998.

23. McMaster, W. H. Compilation of X-ray Cross-Sections, National Bureau of Standards, for calculation of X-ray cross sections.

24. Herron, M. E.; Doyle, S. E.; Pizzini, S.; Roberts, K. J.; Robinson, J.; Hards, G.; Walsh, F. C. *Journal of Electroanalytical Chemistry* **1992**, *324*, 243.

25. Maniguet, S.; Mathew, R. J.; Russell, A. E. *Journal of Physical Chemistry B* **2000**, *104*, 1998.

26. Roberts, M. A.; Finney, J. L.; Bushnell-Wye, G. Development of curved image-plate techniques for studies of powder diffraction, liquids and amorphous materials. *Materials Science Forum* **1998**; 278, 318.

Chapter Three: *In-situ* XAS Cell Design and Testing

One of the primary aims of this project was to develop a fuel cell in which catalyst structure could be studied using XAS under the conditions present in a functioning cell. Collecting XAS spectra from an operating fuel cell introduces a number of complications and imposes limitations to the design as well as the experimental setup. This chapter follows the design and development of an *in situ* XAS fuel cell and discusses the problems encountered.

1 INTRODUCTION

XAS studies of fuel cell catalysts have shown that the study of catalysts under operating conditions is of vital importance [1]. Determination of the catalyst structure of prepared samples has little relevance. The first step was the development of transmission *in situ* XAS cells for bound catalyst electrodes [2,3]. McBreen *et al.* [4] developed a cell containing three layers of filter paper soaked in electrolyte as a separator between the working electrode and a Grafoil counter electrode. By compressing the cell, bubble formation that can result in noise in the spectra due to random density fluctuations in the electrolyte was limited. The half-cell used in this thesis relied on electrolyte being continuously flowed through the cell to remove any bubbles that had formed [5]. A modified version of the half-cell was operated in the fluorescence mode for low metal loadings (e.g. Pt loadings less than 1 mg cm^{-2}).

In an effort to move to more realistic environments, the next development was in single cell designs. By using an MEA and hence removing the need for a liquid electrolyte, bubble formation was no longer a concern. However, catalyst utilisation became more of an issue. XAS is an averaging technique so it important that all of the catalyst is in the same electrochemical or chemical state. In half-cells the electrodes are in a flooded environment and the entire catalyst is known to be contacted by liquid electrolyte, eliminating the problem of utilisation. Reports by Bett *et al.* [6] comparing catalyst surface area measurements by a number of

different techniques including XRD, TEM, ECA and CO adsorption confirmed this belief. In a single cell the catalyst particles are located in a gas diffusion electrode in such a way that they form a three-phase boundary. The properties of a gas diffusion electrode must ensure that the catalyst particles are in contact with both the carbon support for electronic conductivity and the ionomer for proton conductivity. In addition, the catalyst layer must be sufficiently porous to allow reactants to reach the catalyst particles and for reaction products to exit. To maximise utilisation, i.e., the fraction of the catalyst that is part of the three-phase boundary, thin film electrodes are used. The consequence of using thin films is that the catalyst loading is reduced.

In XAS experiments using single cells, there is a trade-off between utilisation and the catalyst loading required to make data collection viable. To date there have been only two examples of *in situ* XAS single cells, both of which operated in the transmission mode. The cell designed by Viswanathan *et al.* [7] was based on modification of a single cell. A rectangular hole was milled behind the flow channels leaving only 4 mm of graphite impeding the X-ray beam before it contacted the anode catalyst. To avoid averaging the XAS signal from catalysts on both sides of the MEA, a Pd/C cathode was used. The cell used by Roth *et al.* [8] was a modified commercially available fuel cell. As in the previous case, holes were drilled in the end plates and the graphite plates thinned to 4 mm. This thickness proved to be thin enough to make only small contributions to the spectra while still being sufficiently thick to keep the cell gas tight. To eliminate the problem of monitoring both electrodes in XAS experiments, a small area of cathode catalyst, approximately 0.2 cm^2, was removed in line with the X-ray beam. The removal of the cathode may have resulted in a change to the current distribution on the anode side. This was the area being probed by the X-rays, so the XAS data may be of limited value when correlated to electrochemical measurements [9].

The use of the transmission mode for collection of XAS data, as used by Viswanathan *et al.* and Roth *et al.*, required a minimum thickness of the catalyst layer in the MEA. Viswanathan *et al.* used a loading of 0.6 mg Pt cm^{-2}, whilst Roth *et al.* used 1.2 mg Pt cm^{-2}. For optimal data quality in transmission XAS the change in absorbance at the edge should be at least 0.3, which requires 1.7 mg Pt cm^{-2} and 4.4 mg Ru cm^{-2} at the Pt L_{III} edge and Ru K edges, respectively [10]. The lower

experimental loadings used relative to the ideal case reduces the signal to noise ratio making EXAFS analysis more difficult. Thus, in the case of Viswanathan *et al.* only the XANES region was reported. Higher loadings can be used to improve the signal to noise ratio, however, catalyst utilisation then begins to become an issue. This is a particularly important consideration given that XAS is an averaging technique and therefore all of the catalyst layer must be in the same electrochemical or chemical state to aid the interpretation of the results. Thin film electrodes are used in fuel cells in an effort to maximise utilisation. Typical platinum loadings range from 0.1 to 0.3 mg Pt cm^{-2} and one way to approach these loadings while still maintaining a sufficient signal to noise ratio in the XAS spectra, is to operate the cell in the fluorescence mode.

The objective of the work presented in this chapter was to build a mini-fuel cell which can operate in a fluorescence collection mode, thereby enabling XAS data to be collected from catalyst layers with low metal loadings and high catalyst utilisation.

2 ROOM TEMPERATURE PEMFC

Initially, an *in situ* XAS PEM fuel cell was designed to operate at room temperature. This reduced the complexity of the cell by removing the need for a humidification system. This allowed the emphasis to be placed on addressing the difficulties of collecting XAS data in the fluorescence mode, rather than on performance of the cell itself. The simplicity of the system also allowed modifications to be carried out more easily. By starting the development at this stage, a better understanding was achieved before subsequent more complex designs with humidification systems were attempted, which were more costly and time consuming to build.

2.1 Cell Design

A schematic cross-section of the cell, not to scale, is shown in figure 1a. The MEA (described in section 2.2) was placed between two graphite plate current collectors, into which serpentine flow fields were machined to enable transport of gases to the anode and cathode. The graphite plates were held in position by two Perspex end plates and six threaded screws with two alignment pins to facilitate assembly of the cell and to ensure proper alignment of the seals on the graphite plates.

The window that allowed the X-rays to enter the cell and through which the fluorescence was detected is shown in figure 1b. A region of the graphite plate in line with the window was thinned to further reduce X-ray absorption. The two ports above and below the window were the gas inlet and outlet, which fed into the flow field. Figure 1c shows the side view of the cell and the thickness of the graphite plates and end plates. The copper current collectors were positioned at the top of the cell. The distance between the graphite plates, 0.4 mm, was carefully measured using a feeler gauge to ensure even compression of the MEA. Figure 1d gives the back view of the cell and shows the positioning of four ports. The ports at the top and bottom were the gas inlets and outlets while the ports to the left and right fed into the water channel. The water channel hydrated the membrane which extended into this region.

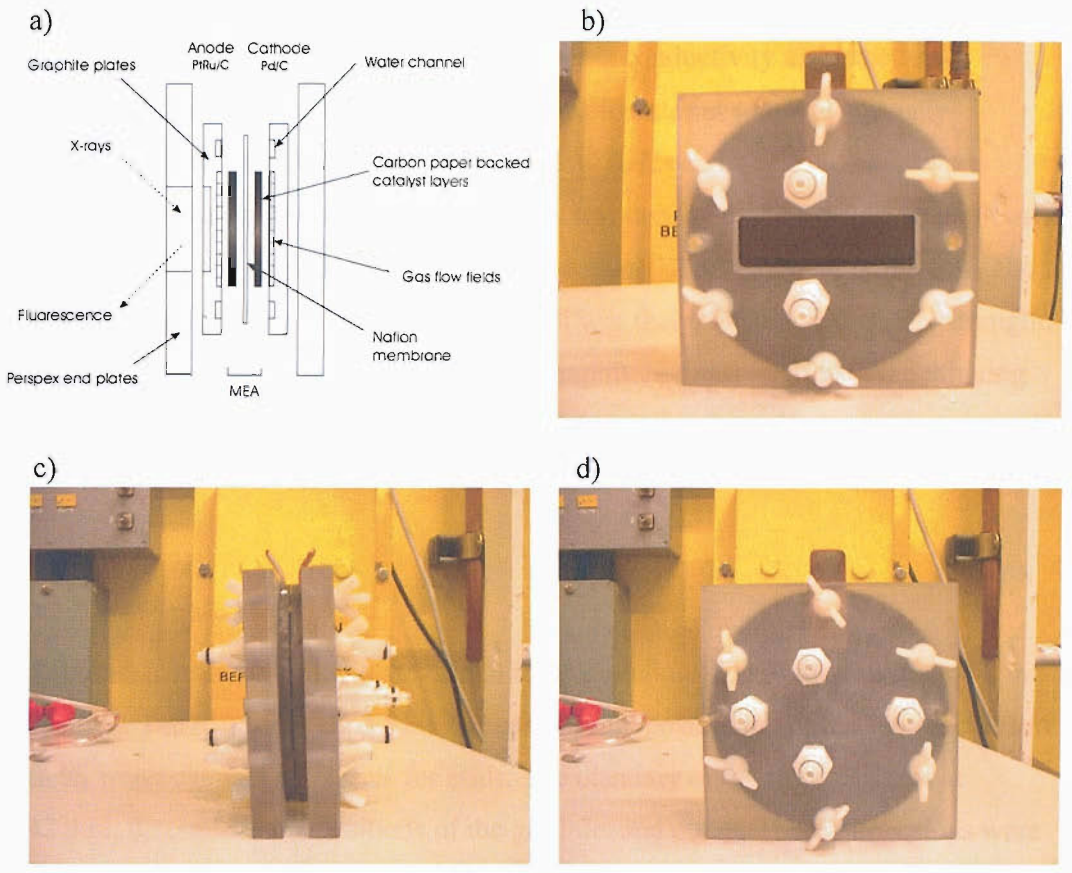

Figure 1 **a) Schematic cross-sectional diagram and pictures of the room temperature cell from various angles. b) front view, c) side view and d) back view.**

The following section covers the design and construction of components for the cell including graphite plates, seals, current collectors and end plates. The materials used and the function of the components will also be covered.

2.1.1 Graphite plates

The graphite plates used in this design fulfilled a number of different roles, including 1) acting as a current collector, 2) providing mechanical support for the electrodes, 3) providing access channels for the fuel and oxidant to the respective anode and cathode surfaces, 4) providing channels for the removal of water formed during the operation of the cell and 5) providing a physical barrier to avoid mixing of oxidant and fuel [11].

The plates were made from Le Carbone graphite grade RF. This material had a number of advantages including good electronic conductivity and excellent resistance to corrosion. It is also a relatively soft material so could be easily machined. This was important as both the flow fields and water channels were milled from the graphite. In addition it has a low density of 1.77 g cm^{-3} so the X-ray absorption of the graphite was minimised, an essential requirement of the cell. The disadvantage of using a low-density material was that it lacked mechanical strength. This placed a limit on the thickness of the graphite, a consideration when thinning the graphite to reduce X-ray absorption further (section 2.1.1.2). A compromise between mechanical strength and low X-ray absorption had to be reached.

2.1.1.1 Plate design

A technical drawing of the plate design for the window side of the cell is shown in figure 2. The plan view shows the dimensions and positioning of the serpentine flow field, water channel and insets for seals. The diameter of the flow field, set at 42 mm, determined the positions of the gas inlet and outlet. These dimensions were set to allow for a cell window and to provide space for the fluorescence detector. A wider flow field was not used as this would have created problems keeping the membrane at the centre of the MEA hydrated. The insets for the two concentric circular seals were positioned either side of the water channel to keep the water separate from the flow fields. The membrane extended beyond the first seal into the water channel to help keep the membrane hydrated. The water channel also provided a method of heating the cell in future designs.

A second plate was made using the same dimensions. The difference from the first plate was that the water entered the cell from the non-window side so extra holes were required to allow for this. Also, because the cell was to be operated in the fluorescence mode it was not necessary to thin the graphite on the second side to reduce X-ray absorption.

The plates were made at Johnson Matthey using a milling machine originally used for making circuit boards. The drawings were put together using a software package called Rhino, which generated the 3D images along with the measurements and

labels. This was then read into TurboCAD, which converted the drawings into 2D images. The path the milling machine was to follow was assigned and the correct tool bit to perform the particular job required was selected. Finally, CircuitCAM was used to control the milling machine and set the origins for the plate centres and pin positions.

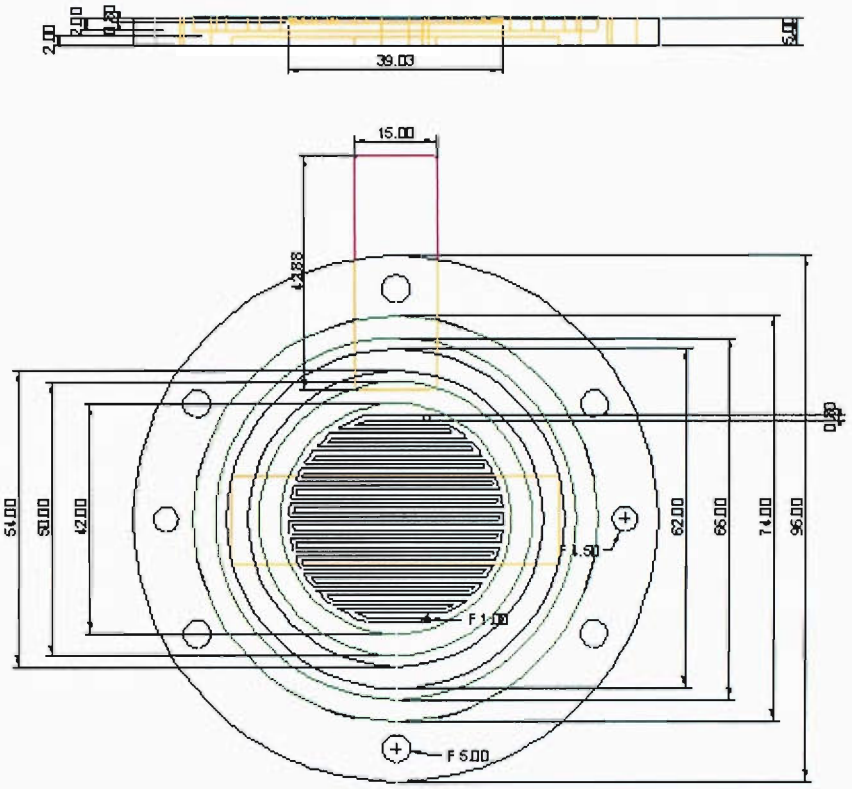

Figure 2 **Plan and side view of the graphite plate for the window side of the cell showing positioning of flow field, water channel and seal insets. Dimensions are given in millimetres.**

2.1.1.2 Cell window

For higher energy edges, Pt L_{III} (11.564 keV) and Ru K (22.117 keV) the X-ray window was made by thinning the graphite to 1.5 mm over an area of 60 x 16 mm (figure 3). The window design for the lower energy edges used for the cathode catalysts will be discussed in section 3.3. The thickness of the window was limited by the structural strength of the graphite. The window was an area of weakness in the cell, as it was not supported by the end plate, yet under compression, the window

region had to be sufficiently strong to resist bending. The thickness was also limited by the precision of the milling machine used. Another reason for not thinning the graphite further was that in subsequent designs where the cell was operated at higher temperatures, heat loss became an issue and it was important to be able to maintain a uniform temperature across the MEA.

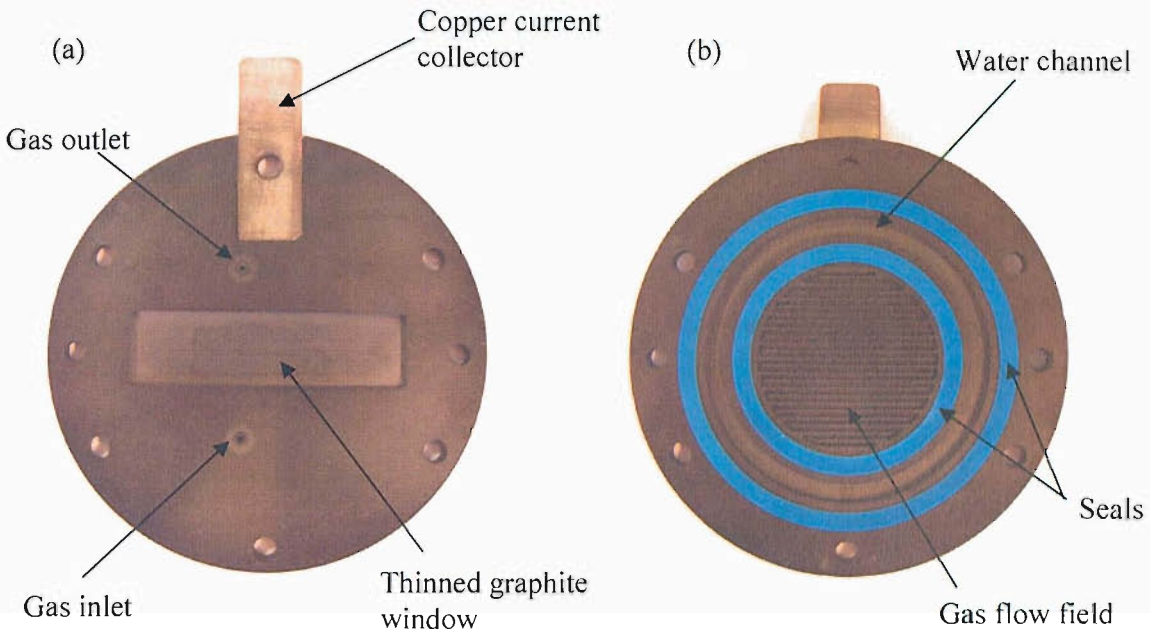

Figure 3 **(a) Graphite plates showing thinned region and (b) interior of the graphite plate.**

2.1.1.3 Absorption tests

Before starting to collect data using the cell, the X-ray absorption of the graphite was investigated in more detail. Consider the case for a typical PtRu anode catalyst with a 40 wt. % Pt / 20 wt. % Ru composition and a loading of 1.0 mg Pt cm^{-2}. The mass absorption coefficient, (μ/ρ) of ruthenium at the Ru K edge is 67.7 $cm^2 g^{-1}$. The μ/ρ value for C at the same energy is 0.39 $cm^2 g^{-1}$. The absorption coefficient (μx) is given by the following equation:

$$\mu x = (\mu/\rho)(\text{mass/area}) \qquad \textbf{Eq. 1}$$

Therefore, for the above mentioned catalyst the ruthenium loading is 0.5 mg cm^{-2} and the absorption coefficient, μx, is 33.9 x 10^{-3}. Compare this with the graphite which has a thickness of 0.15 cm, a density of 1.77 g cm^{-3} and μx of 103.5 x 10^{-3}. The value of μx for the graphite remains small indicating that the window is not opaque. However, this calculation does not give any indication as to whether the experiment is viable in the fluorescence mode. The fluorescence must be able to exit the cell and scattering must be limited.

This was investigated experimentally by positioning a series of PtRu pellets, made using boron nitride with a range of loadings from 1 mg Pt cm^{-2} down to 0.3 mg Pt cm^{-2}. The pellets were positioned behind the graphite plate and at 45° to the detector so as to maximise the solid angle (chapter 2, section 3.2.4) and to minimise the effects of X-ray scatter. The XANES region was collected at the Ru K edge out to 100 eV beyond the edge. This initial test showed that a reasonable edge step could be obtained with these loadings in the fluorescence mode. Scattering was found to cause a problem with lower loadings. The scattering of elastic and Compton radiation is the major source of noise when using fluorescence [12]. A molybdenum filter was found to be an effective way of removing scatter. X-ray filters are effective in removing background scattered radiation because the emission lines are down-shifted in energy just enough so that for the K edges, the Z-1 element (or Z-1 or 2 for Ru and above) will preferentially absorb the scattered component. Once the scattered radiation is absorbed by the filter it is re-emitted in all directions as fluorescent radiation. Therefore, the filter was positioned as close to the cell as possible so as to reduce the amount of fluorescence from the filter that entered the detector.

2.1.2 Seals

The moulds for the seals were made from glass reinforced nylon using the same milling machine as for the graphite plates. The insets in the graphite had a depth of 2 mm while the seals were made with a thickness of 2.4 mm to allow for compression and to provide a water and gas tight seal. The seals were made from silicone rubber obtained from Replication Technologies Limited. The first step was to mix the base polymer (Silastic® M RTV silicone rubber) with a curing agent in a

ratio of 10:1. The silicone rubber remained workable for 1 - 1½ hours in which time it was poured into the seals and placed in a vacuum oven for 10 - 20 min. This removed any trapped air included during mixing. The excess was scrapped off and the seal was cured at 80 °C for 30 minutes.

2.1.3 Current collectors

The current collectors were made from copper and were glued to the graphite plate using a conducting epoxy. Initially, a two electrode setup was tried. However, at higher currents the voltage applied by the potentiostat became significantly different from the potential difference between the two graphite plates. This was due to the potential drop between the copper current collector and graphite plate. To overcome this problem a four electrode setup was used. A hole was drilled in the side of each of the graphite plates into which a gold pin was set. The potential was applied across the two gold pins while the current flowing was measured at the copper current collectors. This ensured that the potential of the graphite plates matched the applied potential, overcoming the problem of potential drop.

2.1.4 End plates

The purpose of the end plates was to hold the cell in place. They provided a way of evenly compressing the cell and feeding the required gases and water to the flow fields in the graphite plate. The technical drawing for the windowed side of the cell is shown in figure 4. Two holes were drilled for alignment pins and a further six for threaded screws. In addition, two ports were needed for the gas inlet and outlet. A window 60 x 16 mm was cut in the end plate to allow X-rays to enter the cell. The end plates were made of Perspex and the milling machine mentioned previously was used to mark the outline and cut out the recesses for the gas seals. The workshop completed the drilling and cut the endplates to size. Valved Swagelok connectors were used for the gas and water connectors.

The non-windowed end plate is shown in figure 5. The only difference from the windowed end plate being the absence of a window and two extra holes for the water inlet and outlet. These were positioned on the non-window side to reduce

obstruction of the fluorescence detector. Plastic threaded screws and wing nuts were used to hold the end plates in place. Plastic threads were used instead of metal to prevent over compression of the MEA and to reduce the risk of putting too much strain on the graphite plates. They also prevented an electrical short between the plates.

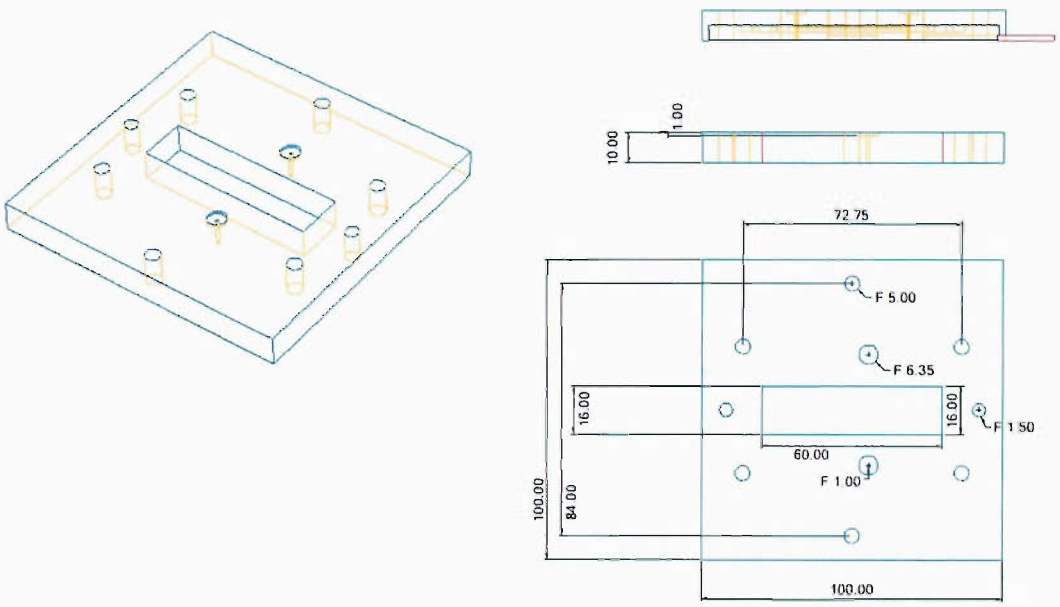

Figure 4 **Design of the end plate for the windowed side of the cell showing dimensions of the window and positioning of the gas ports and holes for screw threads.**

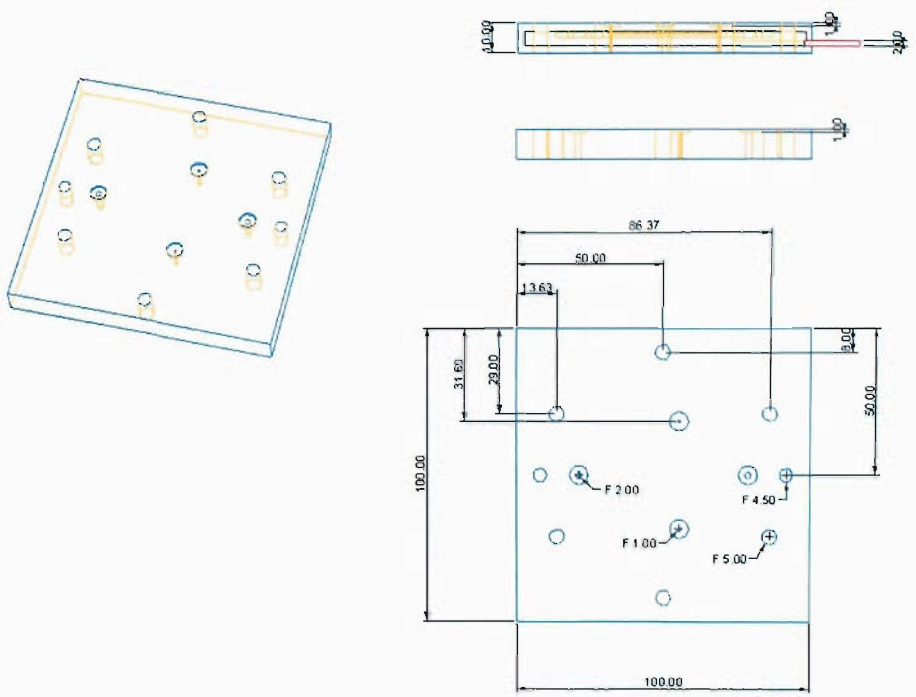

Figure 5 **Design of the end plate for the non-windowed side of the cell showing positioning of the extra ports required for the water channel.**

2.2 Membrane Electrode Assemblies (MEA)

The MEA is the key component of a fuel cell and is located between the graphite plate flow fields. The following section covers some of the principles of the fabrication of MEAs followed by the experimental method used in this thesis.

2.2.1 Components of the MEA

The MEA is a five-layer structure consisting of a proton exchange membrane electrolyte at the centre, separating two electrodes and preventing gas mixing and the formation of an electrical short. The electrodes are composed of a gas diffusion substrate onto which the catalyst is deposited using techniques such as screen printing, painting or rolling (chapter 2, section 1) [13].

The membrane used in this thesis was Flemion® manufactured by Asahi Glass, Co. Flemion® consists of a fluorinated carbon backbone that contains a small number of

carboxylic ionic functional groups. It is similar to Nafion® in nature with the main difference being that Nafion® contains sulphonate functional groups.

The thickness of the membrane affects its performance in a number of ways. For example, voltage loss is greater across thicker membranes and becomes increasingly significant with higher current densities. The advantage of thicker membranes is that they have a lower permeability and reactant crossover resulting in improved cell performance as well as improved durability. A compromise was required between cell performance and low reactant crossover. In this thesis a membrane thickness of 30 μm was used. Yoshida *et al.* [14] investigated the permeability of Flemion® membranes to hydrogen and found that hydrogen cross leakage is less than 1 % of operating current density. However, the permeability to hydrogen varies depending on the parameters of the cell operation such as temperature, humidity, partial pressure and membrane water content so this must be taken into account. Further reports suggest that hydrogen crossover is negligible for membrane thicknesses above 25 μm [15].

The purpose of the gas diffusion layer (GDL) is to distribute the gases and to manage the water content, current collection, mechanical support and heat conduction. One of the common materials used for GDLs is carbon paper due to its high porosity and good electrical conductivity. Water management is controlled by using different treatments and coatings. PTFE is often used to increase the hydrophobicity of the GDL. This helps prevent water accumulation in the region where reactant gases are required. Mass transport limitation is particularly evident at the cathode where water is produced and where catalyst layer flooding is far more apparent. Another way of managing the water content is to put carbon base layers onto the carbon paper before the catalyst layer. The base layers commonly consist of carbon particles mixed with a polymeric binder such as PTFE. The purpose of the base layer is to wick water away from the catalyst layer into the diffusion media. It also reduces the electrical contact resistance of the catalyst layer. For cathode catalyst work carried out in this thesis the gas diffusion layer was made from TGPH-060 with 11 % PTFE and a Shawinigan base layer. For the anode side where water management is not as important, a gas diffusion layer without a base layer was used.

The catalyst layer was made from an ink containing the platinum based catalyst supported on carbon black and aqueous Nafion® (chapter 2, section 1.3). The carbon black support provides electrical and thermal conductivity and gives good reactant gas access to the electrocatalyst. The support must be stable over a potential range from 0 to 1 V under humidified reducing and oxidising gases. A common support is Vulcan XC72R which was used for most of the catalysts in this thesis with the exception of the palladium catalyst where Shawinigan was used.

The variables involved in making an MEA are numerous and each of these can be optimised to give the best possible performance for a given fuel cell design. Though this has not been the aim of the thesis, the performance of the MEA was considered as it reflects the utilisation of the catalyst. In turn, this is important for *in situ* XAS, which as mentioned previously (section 1), is an averaging technique and as such all of the catalyst must all be in the same electrochemical or chemical state.

2.2.2 MEA preparation

The inks consisting of the catalyst and aqueous Nafion® were made up using the method described in chapter 2, section 1.3. Aqueous Nafion® was used instead of an organic solvent to avoid leaving carbon species in the MEA that may poison the catalyst. The anode contained 50 wt. % Nafion® with respect to the total amount of catalyst used, whereas the cathode contained 75 wt. % Nafion® with respect to the carbon content. The inks were painted onto the carbon paper (E-Tek TGPH-090) with an artist's brush. After painting each layer, the electrode was dried for 10 to 20 seconds at 120 °C on a hotplate before weighing. Additional catalyst layers were added until the correct loading was obtained. Circular electrodes with a radius of 2.0 cm were cut from the catalyst-coated carbon papers.

The MEAs were made by positioning the anode and cathode either side of a circular (3 cm radius) 30 μm Flemion® membrane. The membrane and electrodes were then placed between two metal plates with a piece of PTFE and paper on either side to ensure even compression. The MEA was then hot pressed at 150 °C and 230 psi for 2 minutes. The glass transition temperature for Nafion® is approximately 150 °C therefore, hot pressing at this temperature ensures that the Nafion® starts to flow

resulting in a good contact between the membrane and the ionomer content in the catalyst layer. Higher temperatures can result in reduction of the water retention properties of the membrane, degradation of the polymer, and delamination of the electrode from the membrane.

2.3 Cell Operation

The following section describes the setup of the cell, conditioning of the membrane prior to use and some of the electrochemical tests used to assess the performance of the cell. The conditioning step was particularly important for room temperature operation. With no humidification system present, there was no water in the membrane so resistance was very high. This problem became apparent when the cell was operated without oxygen in order to obtain CVs or hydrogen polarisation curves where no product water was produced.

2.3.1 Cell setup

When assembling the cell the first step was to clean the seals and flow field plates using cotton buds and isopropyl alcohol (IPA). After measuring the thickness of the MEA it was placed in the centre of the gas flow field. The thickness of the MEA varied depending on the carbon paper used, with a typical value of 0.6 mm. The MEA was compressed to 70 % of its original thickness between the graphite plates. A feeler gauge was used to aid even compression across the MEA. This kept the contact resistance low while not crushing the carbon paper and ensuring that the same compression was used each time.

Before use, the MEA was conditioned by flowing 40 % methanol through both the anode and cathode flow fields using a peristaltic pump. After approximately 20 minutes the methanol was removed and the flow fields were flushed through with purified water for a further 20 minutes. Throughout the experiment, purified water was kept flowing through the water channel to make sure that the MEA remained hydrated.

An Electrochemie Autolab PGSTAT30, which is a combined potentiostat and waveform generator, was used in conjunction with an Electrochemie Autolab 10 A current booster BSTR10A for electrochemical measurements. This allowed currents up to 10 A to be reached without overloading the potentiostat.

2.3.2 Experimental procedure

Typically the first electrochemical test that was carried out was taking a CV of the catalyst. This was done by passing nitrogen over the electrode of interest with hydrogen flowing to the other side of the MEA. By passing hydrogen over Pt or Pd the potential is brought close to 0 V vs. RHE so that this electrode may act as a reference. A low hydrogen flow rate of 10 to 20 cm^3 min^{-1} was used and this proved sufficient to give a stable reference potential. The potential was then scanned between 0 and 1 V vs. RHE with a scan rate of 20 mV s^{-1}. Repeated scans were performed until a stable CV was obtained. To obtain a CO poisoned CV, to allow the catalyst surface area to be measured, the electrode was held at 0.05 V vs. RHE for 25 minutes. During this time, CO was flowed over the surface at a rate of 30 cm^3 min^{-1} for 5 minutes followed by a 20 minute purge with nitrogen using the same flow rate to remove any CO remaining in the catalyst layer. The electrode was then cycled to the upper potential limit of 1.0 V vs. RHE to remove the CO from the catalyst surface before cycling back to the lower potential limit of 0.0 V vs. RHE. Further scans were taken to ensure complete stripping of CO from the surface.

Hydrogen and oxygen polarisation curves were used to determine the performance of the anode and cathode catalysts, respectively. For hydrogen polarisation measurements, hydrogen was flowed to both sides of the MEA. Again a low flow rate of 10 to 20 cm^3 min^{-1} was used over the cathode while a flow rate of 30 to 40 cm^3 min^{-1} was used at the anode. This was well in excess of the stoichiometric value so that a mass transport limited current was never reached. The anode was then polarised at potentials between 0.0 and 0.3 V vs. RHE and the current recorded after a stabilisation time of approximately 60 seconds. The iR drop accounted for ohmic losses and was measured using the current interrupt method.

For oxygen polarisation curves, oxygen was flowed over the cathode at a flow rate of 60 cm^3 min^{-1}, while hydrogen was flowed to the anode at the same rate. Before starting, a pre-conditioning stage was carried out to help hydrate the membrane using the water produced from oxygen reduction. This involved polarising the cathode to 0.7 V vs. RHE for 300 seconds after which time the open circuit potential was recorded. The cathode was then polarised between 0.95 V and 0.5 V vs. RHE and the current was recorded after a stabilisation time of 60 seconds. Again, the current interrupt method was used to account for ohmic loses.

2.3.3 Cell performance (room temperature)

The following section covers some of the initial electrochemical tests carried out on the cell. This included CVs, hydrogen polarisation and oxygen polarisation. The aim at this stage was to determine how well the cell worked and the extent of catalyst utilisation rather than comparison of catalyst performance.

2.3.3.1 Cyclic voltammetry

After conditioning the cell, a CV for a PtRu (40 wt. % Pt / 20 wt. % Ru) anode with a loading of 1 mg Pt cm^{-2} was taken (figure 6). This provided a way of checking that the cell resistances were not too high. Changes in either the contact resistance or hydration of the membrane would lead to distortions in the CV. The slope in the hydrogen region between 0.0 and 0.1 V vs. RHE provided an indication of the membrane resistance with a steeper gradient indicating a lower resistance. The mass normalised area (Pt_{area_m}) measured from the hydrogen adsorption region gave a value of 47.9 m^2 g^{-1} while a Pt_{area_m} of 70 m^2 g^{-1} was obtained in a flooded environment of 2.5 M H_2SO_4. Comparison of the two values indicates that catalyst utilisation of 68 % was obtained in this single cell.

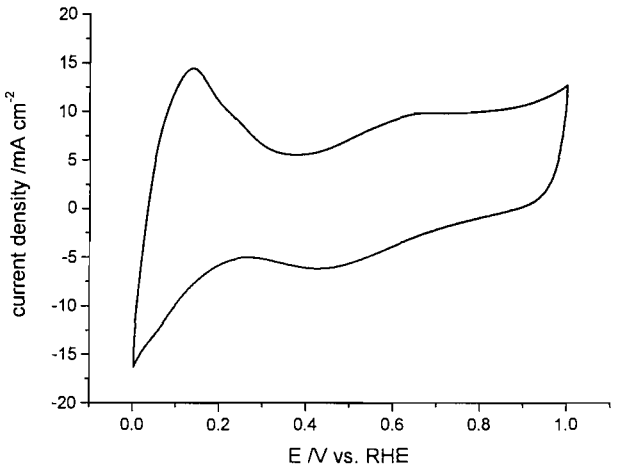

Figure 6 **Cyclic voltammogram of PtRu in a conditioned MEA at 25°C. Anode: 40 wt. % Pt and 20 wt. % Ru, 1.01 mg Pt cm^{-2}. Cathode: 20 wt. % Pd, 023 mg Pd cm^{-2}. Membrane: 30 µm Flemion. Scan rate = 20 mV s^{-1}.**

To obtain a more accurate $Pt_{area_{m}}$ value, a CO stripping experiment was carried out using the mini-cell. However, distortions in the CVs became more pronounced making it difficult to determine the platinum area. This may have been due to dehydration of the membrane as water is required for the oxidation of CO.

2.3.3.2 Hydrogen polarisation

A hydrogen polarisation plot is shown in figure 7 for the PtRu / Pd MEA used above. A linear response was observed with increasing potential. No mass transport limitation was observed within the potential limits chosen. Due to the fast kinetics of the hydrogen oxidation reaction, any performance loss is likely to be a result of membrane resistance. Therefore, the gradient of a hydrogen polarisation plot gives a measure of the membrane resistance and in this case a value of 0.36 Ω cm^2 was found. This is a factor of ten higher than the expected value for a Flemion® membrane [14]. The most likely cause of this high resistance was poor membrane hydration suggesting that the methanol pre-treatment of the MEA was not effective.

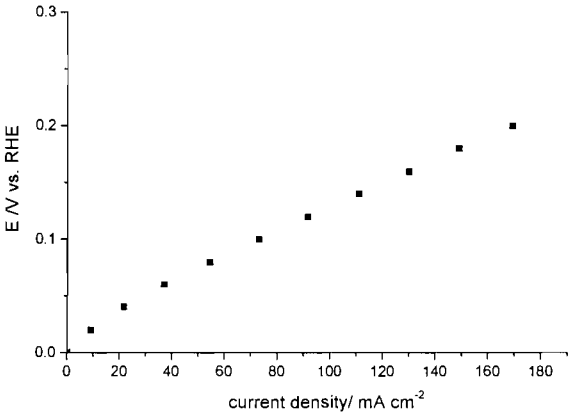

Figure 7 **Hydrogen polarisation curve for PtRu in a conditioned MEA at 25°C. Anode: 40 wt. % Pt and 20 wt. % Ru, 1.01 mg Pt / cm^2. Cathode: 20 wt. % Pd, 0.23 mg Pd / cm^2. Membrane: 30 µm Flemion.**

2.3.3.3 Oxygen polarisation

An oxygen polarisation curve of a PtRu / Pd MEA is shown in figure 8. A stable open circuit potential 0.97 V vs. RHE was determined which was in good agreement with values found by Mukerjee *et al.* [16]. The linear region beyond 0.6 V vs. RHE indicated an ohmic response. A mass transport limited current was never reached even at potentials as low as 0.4 V vs. RHE due to the overriding effect of the ohmic response. This was a further indication of high membrane resistance attributed to partial hydration. Subsequent scans showed a further fall in performance as the benefits of the initial pre-conditioning step wore off. This was due to insufficient product water and the effect of using dry gases that removed water from the MEA while passing through the flow fields.

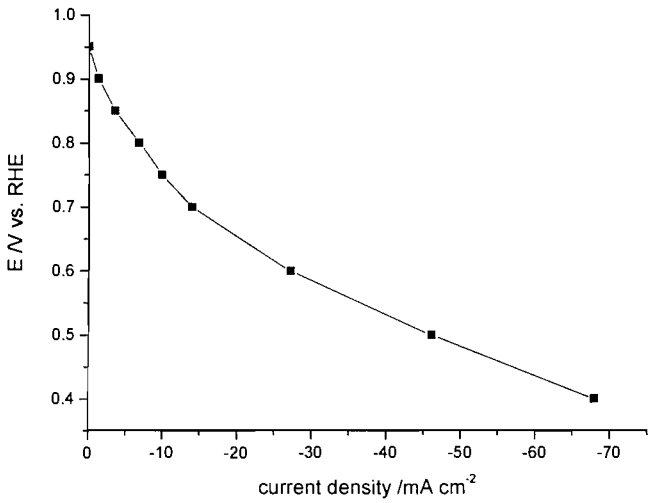

Figure 8 **Oxygen polarisation curve for PtRu in a conditioned MEA at 25°C. Anode: 40 wt. % Pt and 20 wt. % Ru, 1.01 mg Pt / cm^2. Cathode: 20 wt. % Pd, 0.23 mg Pd / cm^2. Membrane: 30 µm Flemion.**

2.3.3.4 Areas of improvement

As mentioned above, (section 2.3.1) 40 % methanol was used to condition the MEA before use. The effectiveness of this method was investigated by using different alcohol solutions in addition to 40 % methanol. For example, soaking the membrane in 10 % isopropyl alcohol (IPA) for 2 to 3 minutes before assembling the cell was tested. After flushing the flow fields with purified water for 20 minutes, the performance of the MEA was tested (figure 9). With H_2 at the anode and O_2 at the cathode, both at flow rates of 60 cm^3 min^{-1}, the potential was stepped down from open circuit (~1.0 V vs. RHE) in 50 mV steps until 400 mV was reached. It was then held at this potential and the current was recorded as a function of time. Both MEAs consisted of a Pt/C anode and cathode with a loading of 0.8 to 1.0 mg Pt cm^{-2}. From figure 9, a slight increase in performance was observed for the IPA conditioned MEA relative to the methanol pre-treatment. In both cases a gradual decay in current was observed until a current of ~ -250 mA cm^{-2} was reached. The fall off in current was a result of the membrane drying out and demonstrates the problem of reproducibility.

The third plot in figure 9 was recorded using a different membrane. In this case Nafion® 115 was used as an alternative to Flemion®. Nafion® 115 is a thicker membrane (125 μm) and as a result holds more water. It was thought that the increased water content of the membrane would help prevent drying out and give a more stable performance. The disadvantage of using Nafion® 115 was that the increased thickness resulted in a higher membrane resistance. The Nafion® 115 MEA was run unconditioned to see if the product water was sufficient to hydrate the membrane. Figure 9 shows an initial increase in the current with time, however, after 1500 seconds the current reached a maximum of -220 mA cm^{-2} beyond which the current fell.

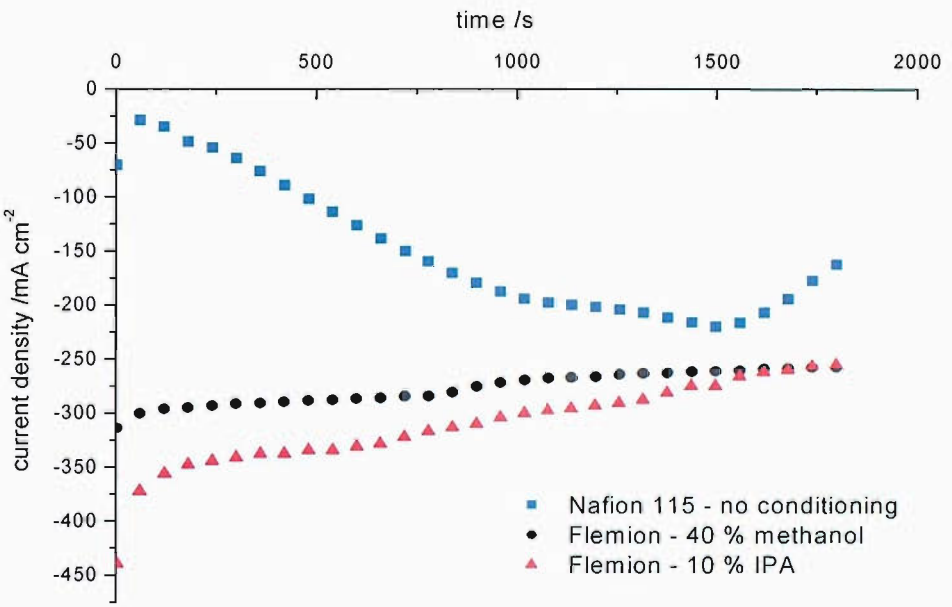

Figure 9 **Cell performances as a function of time for different pre-treatments and membranes. Operating with H_2 at the anode (Pt/C) and O_2 at the cathode (Pt/C) polarised to 400 mV and with a temperature of 25 °C. Flow rates = 60 cm^3 min^{-1}, electrode area = 12.56 cm^2.**

This result confirmed that reproducibility was very difficult to achieve. Drying out of the membrane remained a problem even with different membrane pre-treatments showing that a separate humidification system was required.

The experiments carried out suggested that it was not possible to operate this type of cell effectively at room temperature. For XAS measurements it was important that the poor performance observed was a result of slow kinetics at this temperature rather than due to areas of the catalyst layer being inactive. Typical values for catalyst utilisation in PEMFCs vary from 50 to 80 % [17]. The value obtained at room temperature, 68 %, lies well within this region indicating that slow kinetics and high membrane resistances were the dominating factors.

3 HUMIDIFIED PEMFC

The previous section highlighted the difficulties of operating the cell at room temperature, the main problem being the high membrane resistance that resulted in low currents and distortions in the electrochemical data. Changes in pre-treatment and the type of membrane provided no improvement and confirmed that a separate humidification system was required. The following section covers the various options available for humidification of the gases in a fuel cell. The advantages of the selected method will be discussed along with the humidifier design.

3.1 Methods of Humidification

Humidification of the fuel and oxidant gas is generally required for fuel cells that use solid polymer electrolyte membranes. The membrane requires water to support proton conduction. Despite the production of water at the cathode, it is often not enough to maintain membrane hydration. The initial cell designed to operate at room temperature had a water channel running around the outer membrane. However, the water diffusion rates to the centre of the MEA were too slow to maintain membrane hydration. This lead to poor cell performance and irreproducible results.

One reason for inadequate humidification is that water is drawn away from the anode side of the MEA by electroosmosis as protons diffuse through. A significant amount of water is also removed from the cell by the oxidant gas stream. At high current densities, the product water may be sufficient to hydrate the membrane.

However, as the current density is reduced the membrane can dry out and, as a result of the increase in internal resistance, the cell performance drops [18].

There are a number of ways of overcoming this problem. The simplest is to pass the gas through water as a fine stream of bubbles. Provided that the gas has sufficient contact time with the water, a certain amount of water will be picked up. The amount of water vapour present can be controlled by the temperature. It is important that the contact time is long enough to fully saturate the gas as variable amounts of water will result in irreproducible operation and reduced performance. This can be ensured by using a large water volume and a glass frit to give small diameter bubbles.

Another possibility is to hydrate the gases within the fuel cell stack itself. This involves passing the gas over a water permeable membrane with a water flow field on the opposite side. This arrangement will not work well at room temperature as heat is required to evaporate the water. The advantage is that there is no need for a separate humidification system. However, it is difficult to control the water content of the gases as they are effectively at the same temperature as the fuel cell [19].

Although gas humidification is important, going too far the other way i.e. flooding the catalyst layer will also have a detrimental effect on the cell performance. This can occur if there is excess water in the gas streams or if the product water is not being removed at a sufficient rate. Therefore, a balance is required to maintain high cell performance.

3.1.1 External humidification

External humidification was the first option investigated as it required no modifications to the cell design. A simple bubbler was tried for both the anode and cathode gases. This consisted of a fine glass frit placed at the bottom of a column of purified water. The gases were passed through the frit before travelling up through the water and into the cell. However, at room temperature the gases did not pick up enough water vapour to give any significant improvement in the cell performance. Placing the humidifiers in a water bath at 80 °C increased the water content of the

gases. However, operating the cell at this temperature resulted in any water in the membrane evaporating faster than it could be replaced, resulting in the membrane drying out even more rapidly. The other problem was that a significant amount of water condensed in the tubing before reaching the cell.

The conclusion reached was that bubblers would not work without a more substantial system where the tubing was heated and well lagged to prevent water vapour condensation. This option was rejected because of the bulkiness of the system which would be satisfactory for laboratory operation but not on the beamline stations at Daresbury where space is limited due to the presence of the ion chamber and fluorescence detector. It was decided that use of internal humidification was the best way of solving the problem.

3.1.2 Internal humidification

By using internal humidification the cell is self-contained and no separate humidification system is required. The system uses Membrane Substrate Assemblies (MSAs), which consisted of Nafion® membrane with carbon paper on either side. Unlike the MEAs, the carbon paper was not hot pressed to the Nafion® membrane. As mentioned previously, (section 3.1) the system works by passing heated water over one side of the membrane through a flow field and the reactant or oxidant over the other side. The positioning of the MSA can vary along with the materials used for the flow field plates. One possible design is to position the MSA on either side of the cell and use extra graphite plates for the flow field. The advantage of this is that gases are fed directly from the humidifier to the catalyst layer preventing condensation of water. This is aided by the fact that the cell and humidifier are kept at the same temperature. However, *in situ* XAS experiments would prove very difficult due to the extra graphite plate and MSA in the path of the X-ray beam. This would result in very high X-ray absorption and the fluorescence would be undetectable. Putting both MSAs on the non-window side of the cell was considered though subsequently ruled out because of the problem of porting the gases across the cell to the catalyst layer.

It was decided that the internal humidification system would have to be positioned above the X-ray window and extended above the cell rather than being an integral part of the cell. This ensured that the humidification system did not obstruct the X-ray beam or the positioning of the fluorescence detector.

3.2 Humidifier Design

Pictures of the completed humidifiers are shown in figure 10. The humidifiers were composed of two parts, both machined from glass reinforced nylon with a rectangular serpentine flow field milled into both sides. The flow fields overlay exactly so that water uptake was maximised. The seals enclose the flow field and were made using the method described in section 2.1.2. The two sides of the humidifier system were held together by ten bolts to ensure that even compression was obtained. A further four bolts were used to attach it to the end plates of the cell. The positioning of the humidifier on the mini-cell is shown in figure 11. The gas inlet is positioned at the top of the humidifier; after passing through the flow field the humidified gas enters the mini-cell and leakage was prevented by a small o-ring. Heated water passes through the second flow field in the opposite direction via the inlet and outlet ports.

The MSA was made using two pieces of carbon paper (TGPH-060) with a thickness of 170 μm and a PTFE loading of 10 – 11 % which were soaked in 1 % aqueous Nafion and left to dry. 40 x 20 mm rectangular pieces were then cut from the carbon paper along with a section of Nafion® 115 membrane (thickness = 140 μm) cut slightly larger so that it covered the seals. The carbon paper was placed either side of the membrane and positioned between the two flow fields in the humidification system. Using a feeler gauge, the assembly was tightened to approximately 0.35 mm to give a compression of 80 % of the total thickness.

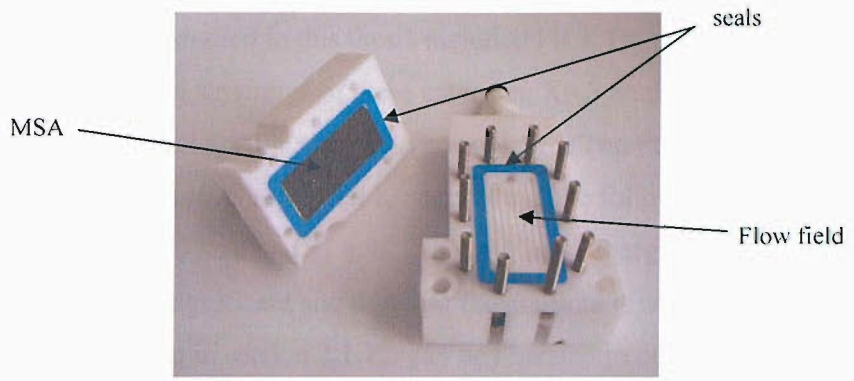

Figure 10 **Interior view of the humidifier system showing positions of the flow field and MSA.**

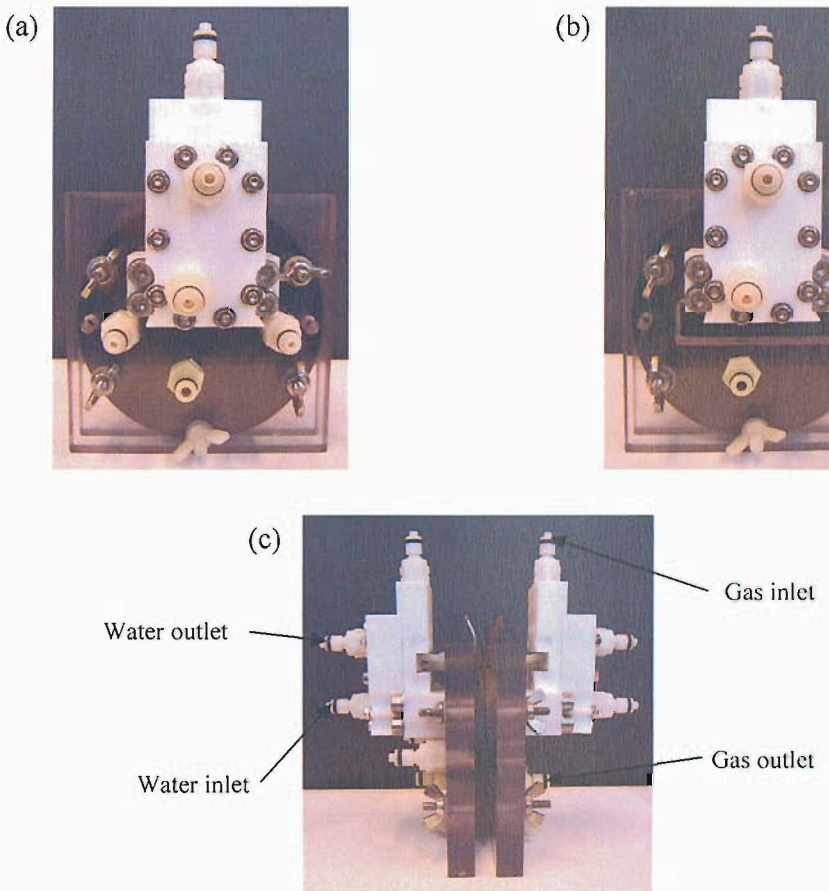

Figure 11 **Pictures of the completed *in situ* XAS cell for operation at elevated temperatures showing positioning of the humidification system above the X-ray window. (a) Back, (b) window and (c) side view.**

3.3 Further Modifications

The cathode catalysts studied in this thesis included PtCr, PtCo, and PtTi. To be able to fully characterise the structures of these catalysts, XAS analysis from both the Pt L_{III} and secondary metal K edge needed to be analysed. The Pt L_{III} edge is at 11.564 keV while the secondary metal K edges are at the following edges: Co 7.709 keV, Cr 5.989 keV and Ti 4.966 keV. At these energies the absorption of the graphite becomes significant and thinning the graphite is no longer sufficient. The calculations shown in section 2.1.1.3 can be repeated to demonstrate this. The Ti K edge is particularly difficult as it is lowest in energy. The mass absorption coefficient (μ/ρ) of Ti at the Ti K edge is 74.6 $cm^2\ g^{-1}$. The μ/ρ value for C at the same energy is 18.8 $cm^2\ g^{-1}$. For a 20 wt. % Pt / 4.9 wt. % Ti with a Pt loading of 1 mg Pt cm^{-2} and hence a loading of 0.25 mg Ti cm^{-2}, $\mu x = 18.7 \times 10^{-3}$. Compare this with the graphite with a thickness of 0.15 cm and a density of 1.77 g cm^{-3}, $\mu x = 4.99$. The absorption coefficient of the graphite is so large that it effectively stops X-rays from reaching the Ti containing catalyst layer. The same problem is found at the Co and Cr K edges although the effect is not as severe.

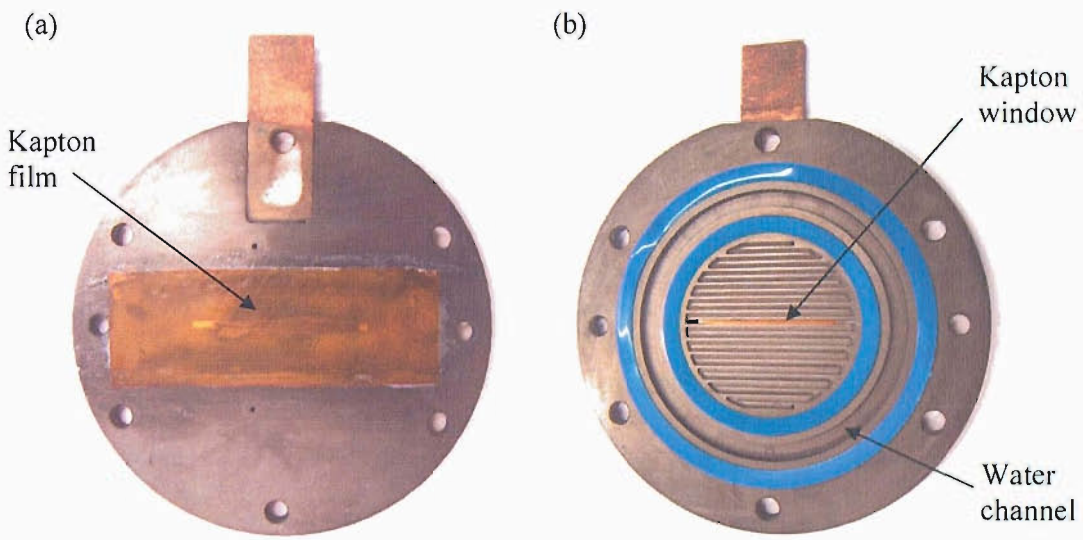

Figure 12 **Picture showing (a) slit with Kapton covering and (b) interior of the graphite plate.**

To overcome the high graphite absorption at low X-ray energies, a new graphite plate was made with a 1 mm slit cut corresponding to the width of one channel of the flow field. This was then covered with a Kapton film which was held in place with silicone rubber sealant (see figure 12). The width of the slit was limited by the flow field. A wider slit would have resulted in disruption of the gas flow to the catalyst layer. This may have changed the environment of the catalyst in the window region making the XAS data less representative of the surrounding catalyst layer. The spot size of the X-ray beam depends on the focussing but was approximately 2 x 0.8 mm in size on station 7.1. Though alignment was difficult, the effect of graphite absorption was significantly reduced.

3.4 Cell Setup

The positioning of the MEA and cell compression was very similar to that described in section 2.3.1 for the room temperature mini-cell. The main difference being that there was no longer a need for a conditioning pre-treatment. A flow diagram showing the direction of gas and water flow can be seen in figure 13. The water passed from the water bath into the water channel to raise the temperature of the graphite plates. From there it flowed through the flow fields in both humidifiers before returning to the water bath. The gases pass through the humidifiers before entering the flow fields in the graphite plates and being vented to air.

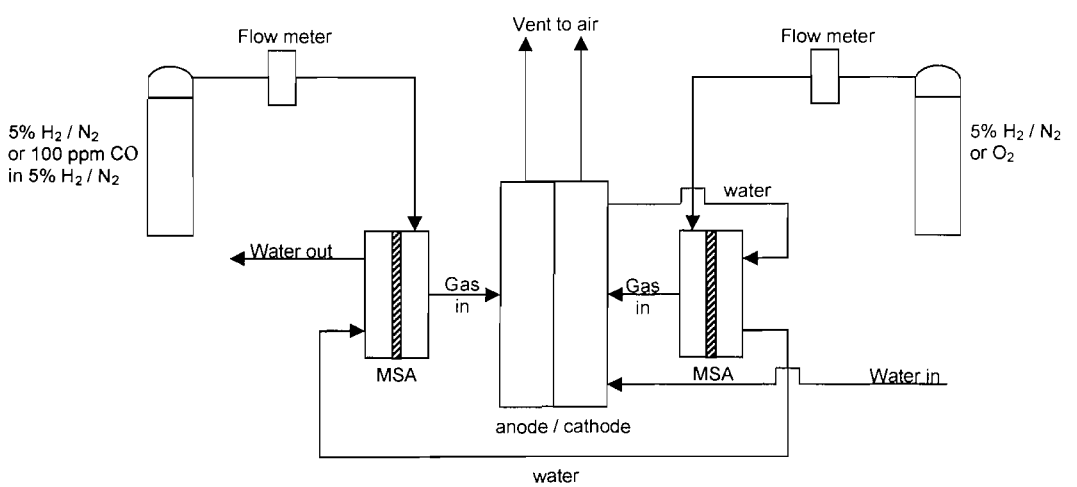

Figure 13 **Schematic flow diagram of the experimental arrangement used showing direction of gas and water flow.**

There is no difference in experimental procedure for the electrochemical measurements using the modified cell compared to the room temperature mini-cell and this has been described previously in section 2.3.2.

3.5 Cell Performance (80 °C)

The aim of the humidification system was to allow higher temperature operation by keeping the membrane hydrated and hence reducing membrane resistance. The following section examines the effectiveness of the humidification system in terms of improved cell performance relative to room temperature operation. So that the performance can be compared to the room temperature case, a similar MEA was used with a PtRu anode (loading = 0.45 mg Pt cm^{-2}) and Pd cathode (loading = 0.25 mg Pd cm^{-2}).

3.5.1 Cyclic voltammetry

A CV for a PtRu / Pd MEA at 80 °C is shown in figure 14. The CV is positioned evenly above and below the zero point on the current density axis. The absence of obvious distortions indicated that the humidifiers were effectively hydrating the membrane. The gradient in the hydrogen region is greater than that obtained at room temperature demonstrating improved membrane resistance.

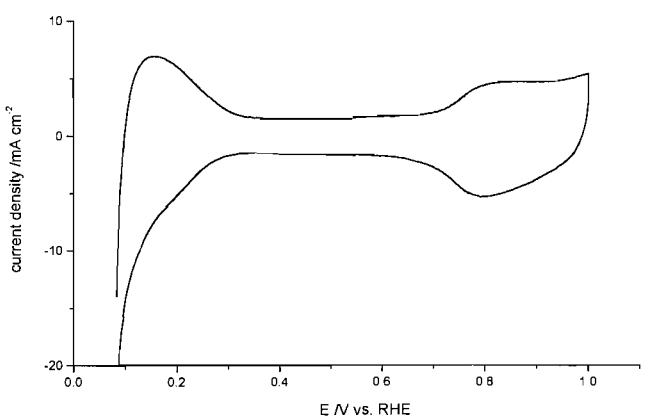

Figure 14 **Cyclic voltammogram of PtRu MEA at 80°C. Anode: 40 wt. % Pt and 20 wt. % Ru, 1.01 mg Pt cm^{-2}. Cathode: 20 wt. % Pd, 023 mg Pd cm^{-2}. Membrane: 30 µm Flemion. Scan rate = 20 mV s^{-1}.**

The Pt_{area_m} measured from the hydrogen adsorption region was 38.8 $m^2 g^{-1}$. When compared with an Pt_{area_m} of 59 $m^2 g^{-1}$ obtained in a flooded environment a catalyst utilisation of 66 % is observed. This is similar to the value obtained at room temperature, 68 %, indicating that temperature has little effect on catalyst utilisation.

3.5.2 Hydrogen polarisation

A hydrogen polarisation curve for a PtRu / Pd MEA at 80 °C is shown in figure 15. A linear potential vs. current density response was observed. The membrane resistance may be estimated from the gradient, yielding a value of 0.04 Ω cm^2, which is in close accord with the expected value for the Flemion® membrane used [14]. This indicated that the response of the PEM mini-cell under humidified conditions was not limited by the contact resistance between the graphite plates and the MEA and that the MEA remained well hydrated during operation.

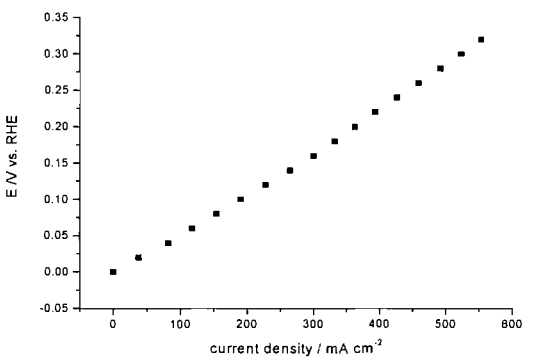

Figure 15 **Hydrogen polarisation curve for PtRu at 80°C. Anode: 40 wt. % Pt and 20 wt. % Ru, 1.01 mg Pt / cm^2. Cathode: 20 wt. % Pd, 0.23 mg Pd cm^{-2}. Membrane: 30 μm Flemion.**

3.5.3 Oxygen polarisation

An oxygen polarisation curve for a PtRu / Pd MEA at 80 °C is shown in figure 16. The measured open circuit potential was 0.997 V vs. RHE. The current density was a factor of 10 higher than at room temperature indicating increased oxygen kinetics of the oxygen reduction reaction (ORR) [20]. A mass transport limited current was not reached using the potential range of 0.95 to 0.55 V vs. RHE.

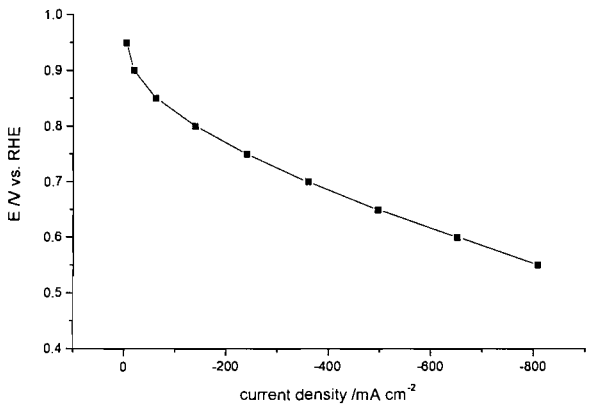

Figure 16 **Oxygen polarisation curve for PtRu in a conditioned MEA at 80°C. Anode: 40 wt. % Pt and 20 wt. % Ru, 1.01 mg Pt / cm^2. Cathode: 20 wt. % Pd, 0.23 mg Pd / cm^2. Membrane: 30 µm Flemion.**

4 *IN SITU* OPERATION

There were a number of factors that needed to be taken into account when moving from the laboratory environment to the beamline for *in situ* operation. The first of these was the safety aspect of the experiment. This was an important issue as it placed limitations on the experimental setup, the most significant being that pure hydrogen could not be used on the beamline. As an alternative, a 5 % hydrogen / nitrogen gas mix was used. The effect of using a diluted gas mix will be discussed in chapter 4 and 5. A second factor was the limited space on the beamline. The X-ray beam must not be obstructed and the fluorescence detector must have a clear path allowing positioning close to the cell window to maximise counts. The experimental setup on the beamline will be discussed in the following section.

4.1 Experimental Setup

Figure 17 shows a picture giving an overview of the experimental setup on station 7.1 at the Daresbury laboratory. The mini-cell was situated between two ionisation chambers, I_0 and I_t. The second ionisation chamber was not used as the XAS were collected in the fluorescence mode. The mini-cell was positioned at 45° to the incident beam while the detector was positioned at 90°. The gases were ported in

from cylinders located outside of the hutch. The outlet gases were bubbled through water so that the flow rate could be monitored. An extraction system was used to remove waste gases from the hutch. The water bath was positioned as close as possible to the mini-cell to reduce heat loss. The mini-cell temperature was monitored using a thermocouple.

Figure 18 shows a close up of the front side of the cell. The Kapton window used for the low energy edges can clearly be seen. The picture also demonstrates the difficulty of preventing obstruction of the fluorescence detector. The metal loading of the catalyst determines the positioning of the detector although in most cases, due to the low loadings used, the detector was positioned as close as possible with no risk of saturation. The picture also demonstrates why scattering from the humidifier was a problem for the mini-cell. Although the humidifier does not obstruct the incident X-ray beam, it does restrict the available solid angle over which the fluorescence can be collected. The resulting fluorescence was admitted at all angles leading to scatter and noise in the XAS data.

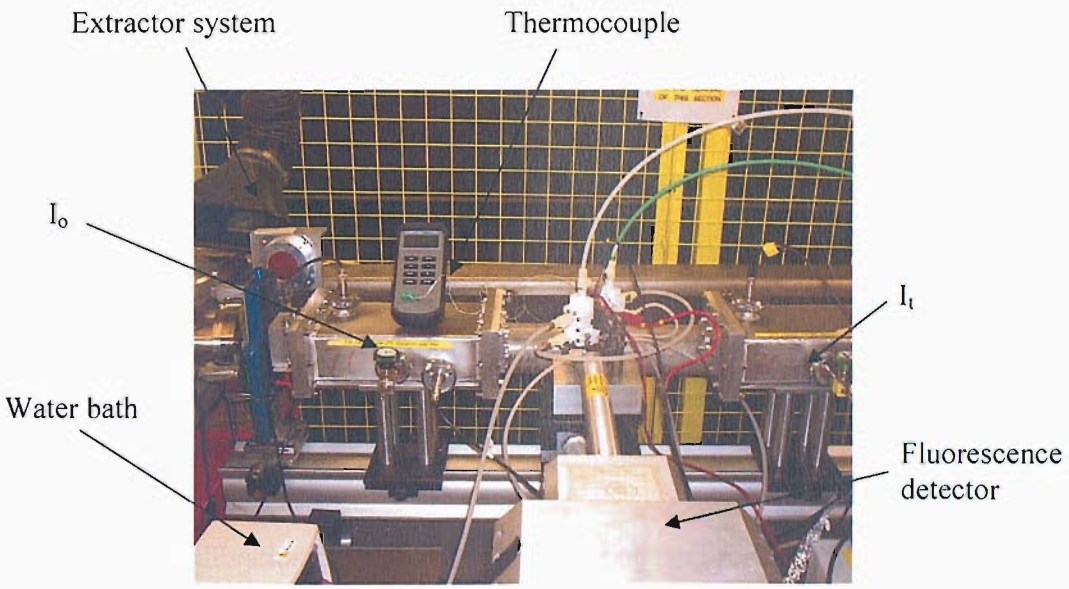

Figure 17 **Picture of the experimental setup used on station 7.1 at the Daresbury laboratory**

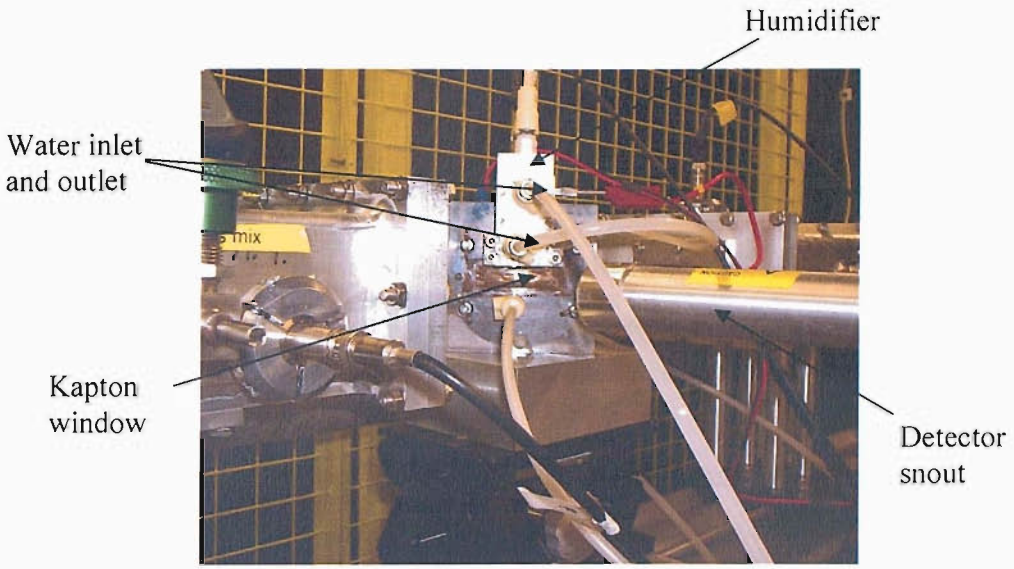

Figure 18 **Close up of the front view of the mini-cell showing positioning of the fluorescence detector**

4.2 Operational Procedure

The cell was used to investigate both anode and cathode catalysts. For anode catalysts, a 5 % hydrogen / nitrogen gas mix was flowed to both sides of the MEA. The anode was then polarised at varying potentials. The effect of using a diluted gas mix was to reduce the amount of reactant gas reaching the catalyst layer. This meant that the onset of mass transport limited currents occurred far sooner than under pure hydrogen.

For the cathode catalysts, oxygen was used at the cathode while 5 % H_2 / N_2 was flowed to the anode. Again, the use of a diluted gas mix meant that mass transport limited currents were observed.

In both cases calibration curves were collected using pure gases with no dilution so that when the electrode was polarised the resulting current could be related to realistic operating conditions. This will be discussed in more detail in subsequent chapters.

5 REFERENCES

1. O'Grady, W. E.; Hagans, P. L.; Pandya, K. I.; Maricle, D. L. *Langmuir* **2001**, *17*, 3047.
2. Herron, M. E.; Doyle, S. E.; Pizzini, S.; Roberts, K. J.; Robinson, J.; Hards, G.; Walsh, F. C. *Journal of Electroanalytical Chemistry* **1992**, *324*, 243.
3. McBreen, J.; Mukerjee, S. *Journal of the Electrochemical Society* **1995**, *142*, 3399.
4. McBreen, J.; O'grady, W. E.; Pandya, K. I.; Hoffman, R. W.; Sayers, D. E. *Langmuir* **1987**, *3*, 428.
5. Maniguet, S.; Mathew, R. J.; Russell, A. E. *Journal of Physical Chemistry B* **2000**, *104*, 1998.
6. Bett, J.; Kinoshita, K.; Routsis, K.; Stonehart, P. *Journal of Catalysis* **1973**, *29*, 160.
7. Viswanathan, R.; Hou, G. Y.; Liu, R. X.; Bare, S. R.; Modica, F.; Mickelson, G.; Segre, C. U.; Leyarovska, N.; Smotkin, E. S. *Journal of Physical Chemistry B* **2002**, *106*, 3458.
8. Roth, C.; Martz, N.; Buhrmester, T.; Scherer, J.; Fuess, H. *Physical Chemistry Chemical Physics* **2002**, *4*, 3555.
9. Russell, A. E.; Rose, A. *Chemical Reviews* **2004**, *104*, 4613.
10. McMaster, W. H. Compilation of X-ray Cross-Sections, National Bureau of Standards, for calculation of X-ray cross sections.
11. Wilkinson, D. P.; Vanderleeden, O. *Handbook of Fuel Cells - Volume 3: Fuel Cell Technology and Applications*; John Wiley and Sons, 2003.
12. Lytle, F. W. *Experimental X-ray Absorption Spectroscopy*; Gordon and Breach, 1988.
13. Ralph, T. R.; Hogarth, M. P. *Platinum Metals Rev.* **2002**, *46*, 3.
14. Yoshida, N.; Ishisaki, T.; Watakabe, A.; Yoshitake, M. *Electrochimica Acta* **1998**, *43*, 3749.
15. Doyle, M.; Rajendran, G. *Handbook of Fuel Cells - Volume 3: Fuel Cell Technology and Applications*; John Wiley and Sons, 2003.

16. Mukerjee, S.; Srinivasan, S.; Soriaga, M. P.; McBreen, J. *Journal of the Electrochemical Society* **1995**, *142*, 1409.

17. Kocha, S. S. *Handbook of Fuel Cells - Volume 3: Fuel Cell Technology and Applications*; John Wiley and Sons, 2003.

18. Andrews, C. C.; Flusche, M. J.; Lyons, D. P. Gas humidification device for operation testing and evaluation of fuel cells. *United States Patent,* 1999; Vol. 6 383 671.

19. Buchi, F. N.; Srinivasan, S. *Journal of the Electrochemical Society* **1997**, *144*, 2767.

20. Stamenkovic, V.; Schmidt, T. J.; Ross, P. N.; Markovic, N. M. *Journal of Physical Chemistry B* **2002**, *106*, 11970.

Chapter Four: Anode Catalyst - PtRu

A number of results presented in this chapter have been submitted for publication [1]

1 INTRODUCTION

The success of low temperature proton exchange membrane fuel cells (PEMFCs) is dependent on the development of efficient catalysts. The simplest and highest performing PEMFC systems employ pure hydrogen as the fuel. For this reason, hydrogen is the preferred choice for transport applications. However, current storage technology means that this is not a viable option for cars where space is limited. In the case of stationary applications, hydrogen is not suitable at present because the infrastructure required to support a hydrogen economy is not in place. An alternative approach is to use a liquid fuel such as methanol with an onboard reformer to obtain the hydrogen. This can be carried out using steam, partial oxidation or autothermal reforming.

In addition to hydrogen, the reformate also contains carbon dioxide, 15-25 % and carbon monoxide 1-2 %. CO is strongly adsorbed to sites on platinum based catalysts preventing the dissociated electrosorption of hydrogen resulting in a significant drop in the cell potential. The CO levels can be reduced to less than 100 ppm using various clean up stages using shift reactors followed by catalytic preferential oxidation reactor [2]. However, even at these levels, the high affinity of platinum to CO can cause deactivation of the catalyst with coverage of CO reaching levels as high as 0.98 [3] resulting in a reduction in the number of sites available for the hydrogen oxidation reaction.

To avoid the need for reformers and clean up stages a liquid fuel, commonly methanol, can be used as in the case of direct methanol fuel cells (DMFCs). This has proved to be an attractive alternative but it is not without its problems. The anode performance of DMFCs is limited by poor electrochemical activity arising due to the

formation of surface bound intermediates including CO. DMFCs generate a lower level of power density compared to reformate fuelled PEMFCs, but the absence of a fuel processing system makes them a viable option for continuing research and development [4].

The lack of tolerance of platinum to even very low levels of CO has led to the development of catalysts with enhanced activity towards CO oxidation and reduced overpotentials at the anode. PtRu has emerged as one of the most promising catalysts showing significant improvements in CO tolerance over pure Pt catalysts. The mechanism was originally put forward by Watanabe *et al.* [5] involving the promotion of CO oxidation by OH species from the activation of water which form at a far lower overpotential over ruthenium compared to platinum. This provides a reactant for the oxidation of CO on a neighbouring Pt atom. The optimum ratio for CO oxidation for both polycrystalline and supported alloys has been shown to be 50:50 [6,7]. This supports the bifunctional mechanism given that maximising the Pt-Ru pair sites results in the most efficient catalyst. Recently, some dispute has arisen over the role of amorphous phases in the bifunctional mechanism. Rolison *et al.* [8] used XPS and thermogravimetric analysis to study the composition of carbon supported PtRu catalysts and identified substantial amounts of hydrous ruthenium oxide present in the catalysts. In contrast, *in situ* XANES studies of PtRu carried out by O'Grady *et al.* [9] indicated that metal oxides present in the as prepared catalyst samples were reduced to the metallic form in the potential region where methanol oxidation occurs. In addition, EXAFS analysis carried out by Maniguet *et al.* [10] showed that for a well mixed PtRu catalyst both Pt and Ru are metallic in nature at potentials at which hydrogen oxidation occurs.

For methanol oxidation Gasteiger *et al.* [11] found that the optimum Pt:Ru ratio on a polycrystalline surfaces was 90:10. The explanation put forward suggests that methanol adsorption occurs on a Pt ensembles and a minimum size is required. The further electro-oxidation of methanol dehydrogenation fragments is then catalysed by oxygen like species adsorbed on adjacent Ru atoms. However, different optimum ratios have been found for carbon supported electrodes. Lizcano-Valbuena *et al.* [12] found that a Pt:Ru ratio of 75:25 gave the largest activity for methanol oxidation. This is in contrast to Dinh *et al.* [13] who in agreement with Johnson Matthey [14]

found that a 50:50 ratio was favourable. Temperature has also been found to play an important role in determining the optimum Pt:Ru ratio. For example, Dickinson *et al.* [15] found that platinum rich 3:2 atomic ratio catalysts perform better than a 1:1 catalyst at 25 °C while the reverse is found at 65 °C. The explanation put forward suggested that methanol dehydrogenation occurs on both Pt and Ru sites at higher temperatures. A similar trend was observed by Gasteiger *et al.* [16] where the optimum surface had an Ru content of 10 atomic percent at 25 °C increasing to a value of 30 atomic percent at 60 °C. The shift in optimum composition with temperature was attributed to a shift in the rate determining step from methanol/dehydrogenation at low temperature to the surface reaction between the dehydrogenated intermediate and surface oxygen at high temperatures.

For these comparisons to be meaningful, the bulk composition of the particle must resemble the surface structure. The results mentioned above show that this is clearly not the case. This highlights the difficulty in comparing results obtained from different preparation methods which range from sputtered polycrystalline bulk alloys, to carbon supported catalysts, to platinum blacks decorated with ruthenium using spontaneous deposition methods [17]. In addition, it has been established that nanoscale materials vary in both physical and chemical properties from those that characterise similar compositions in the bulk due to the large fraction of surface atoms leading to perturbations [18-20].

As mentioned previously, the bulk composition does not necessarily reflect the morphology of the catalyst. Although smooth, polycrystalline surfaces can be accurately characterised using LEIS, LEED and XPS, it is far harder to determine the surface composing of high surface area carbon-supported nanoparticles. The aim of this work is to use a number of techniques, specifically EXAFS and XRD to characterise a series of carbon-supported PtRu nanoparticle catalysts in an effort to study the morphology of the particles as a function of composition and relate this to the electro-oxidation mechanisms taking place on the catalyst surface. This will hopefully bridge the gap between nanoparticle properties and a number of other studies, in particular those by Gasteiger *et al.* [21] who have carried out work on a series with equivalent compositions for well defined PtRu polycrystalline surfaces.

XAS is a powerful tool for characterising fuel cell catalysts and has been used for a large range of studies of fuel cell catalysts [22-26]. EXAFS is element specific so by probing both the Pt L_{III} and Ru K edge, the average environment around each atom type can be determined. From these results, information about the degree of mixing can be obtained. Further information regarding particle size and geometry is reflected in the average first shell coordination number. One of the benefits of EXAFS is that the catalyst can be analysed *in situ* under electrochemical control and there have been a number of examples where XAS has been applied to electrocatalysts in a flooded half-cell environment [10,27-29]. The necessity to carry out *in situ* measurements has been demonstrated by O'Grady *et al.* [9] who found that the as-prepared catalyst bear no resemblance to the catalyst under electrochemical control. This result highlighted the importance of carrying out XAS in realistic environments. Although experiments using half-cells were a step in the right direction, to be able to approach the actual case, the catalyst structure in a working fuel cell must be investigated. Work using single cell designs with MEAs and no aqueous, acidic electrolyte has been confined to only a handful of cases [30,31]. One of the reasons for the limited number of examples is the number of considerations that must be taken into account when designing and operating an *in situ* XAS fuel cell. These include:

- Realistic metal loadings (0.1 to 0.3 mg Pt cm^{-2}) required to ensure high catalyst utilisation.
- Operation in fluorescence mode as opposed to transmission due to low metal loadings.
- Avoiding inclusion of contributions to the XAS from the cathode side of the cell.
- XAS absorption by the graphite flow fields reducing signal intensity.
- Positioning of the gas ports to avoid obstructing the X-ray beam and the fluorescence detector.
- Condensation in the flow fields leading to fluctuations in the X-ray absorption and glitches in the spectra.

The solutions to these difficulties have been discussed in detail in chapter 3 while the *in situ* XAS results for the PtRu catalyst will be presented in this chapter.

Both *ex situ* and *in situ* XRD will be used alongside EXAFS. The nature of the technique relies on the crystalline fraction of the catalyst particle while the amorphous fraction cannot be detected. The XRD provides information on lattice parameters complementing the EXAFS data and in addition, peak broadening can be used to give an estimate of particle size. Discrepancies in particle size between the two techniques are explained in terms of different possible particle geometries.

2 EXPERIMENTAL DETAIL

2.1 Catalysts

The series of five PtRu catalysts supported on XC72R were supplied by Johnson Matthey. The catalyst compositions and corresponding atomic ratios are shown in table 1. The 40 wt. % Pt and 20 wt. % Ru catalysts were used as reference points in the structural analysis.

Table 1 Pt, PtRu and Ru catalyst compositions.

Pt wt. %	Ru wt.%	Atomic Ratio Pt:Ru
40	0	100 : 0
54	6	82.3 : 17.7
48	12	67.4 : 32.6
40	20	50.9 : 49.1
30	30	34.1 : 65.9
17	43	17.0 : 83.0
0	20	0 : 100

2.2 Electrode Preparation

The catalysts were fabricated into electrodes by first making inks using Nafion® as described in chapter 2, section 1.2. For half-cell work, the inks were thickened to give a paste and spread manually onto carbon paper in a 3 x 3 cm template to give a loading of 3 to 5 mg Pt cm^{-2}. For electrochemical testing 1 cm^2 electrodes were cut

from the resulting sheet. For XAS and XRD measurements larger electrodes with an area of 2.54 cm^2 were used. The electrodes were then placed in boiling water for 20 minutes to ensure that they were fully hydrated.

2.3 MEA Preparation

The 40 wt. % Pt / 20 wt. % Ru catalyst was used for the anode while 20 wt. % Pd was used for the cathode. Inks were made using the catalyst and aqueous Nafion® and painted onto the carbon paper using the method described in chapter 2, section 1.3. Electrodes with an area of 12.56 cm^2 were then cut out in preparation for hot pressing. A Flemion® membrane, 30 μm, was used to make the MEA and the procedure has been described in detail in chapter 3, section 2.2.2.

2.4 Electrochemistry

2.4.1 Cyclic voltammetry

For CV experiments, the wetted electrodes were placed in a standard three-electrode cell. A platinum gauze was used for the counter electrode and all potentials were measured with respect to a Hg/Hg_2SO_4 (MMS) reference electrode. The potentials reported have been corrected to the RHE scale, as determined by calibrating with respect to a dynamic hydrogen/Pt electrode. 2.5 M H_2SO_4 prepared from 18 MΩ cm purified water purged with N_2 was used for the electrolyte. A scan rate of 10 mV s^{-1} was used unless otherwise stated.

For CO electro-oxidation experiments, the catalyst electrode was held at 0.15 V vs. RHE while first CO and subsequently N_2 was purged through the electrolyte for 15 and 30 minutes, respectively. The electrode was then cycled to the upper potential limit of 1 V vs. RHE and then back to 0.05 V vs. RHE with a scan rate of 10 mVs^{-1}.

2.4.2 Methanol oxidation

Again a three-electrode cell was used. After determining the metal area using CO stripping in 1 M H_2SO_4, the electrode was transferred to a cell with 2 M methanol in 1 M H_2SO_4. The electrode was then conditioned by cycling between 0.05 and 0.8 V

vs. RHE with a scan rate of 10 mV s^{-1}. The electrode was then polarised using the same potential range and a step potential of 0.05 V. The current was recorded after a stabilisation time of 30 seconds. Current interrupt measurements were taken at 0.65, 0.7 and 0.75 V vs. RHE to correct the data for cell resistance. The temperature was controlled by placing the cell in a water bath and the procedure was carried out at 30 °C and 80 °C.

2.4.3 Mini-cell

Results from both the room temperature and high temperature mini-cell will be presented in this chapter. Although the operation of the cell was the same, the room temperature mini-cell required an extra pre-conditioning stage as the gases were not humidified. This has been described in chapter 3, section 2.3.1 and involved flowing 40 % methanol through both the anode and cathode flow fields for 20 minutes. The flow fields were then flushed through with purified water for a further 20 minutes before use.

For high temperature operation the humidification system removed the need for a conditioning pre-treatment. The cell was operated at 80 °C using the same gas flow rates as those used at room temperature.

Cyclic voltammetry experiments were carried out by passing nitrogen over the PtRu anode with hydrogen flowing to the Pd cathode. Flowing hydrogen over the Pd cathode enabled this electrode to serve as both the cathode and as an RHE reference electrode. A relatively low hydrogen flow rate of 10 to 20 cm^3 min^{-1} was used. This proved sufficient to give a stable reference potential. The potential was then scanned between 0 and 1 V vs. RHE with a scan rate of 20 mV s^{-1}. Repeated scans were taken until a stable CV was obtained.

For hydrogen polarisation measurements, hydrogen was flowed to both sides of the MEA. A low flow rate of 10 to 20 cm^3 min^{-1} was used over the cathode while a flow rate of 60 to70 cm^3 min^{-1} was used at the anode. The anode was then polarised at potentials between 0 and 0.5 V vs. RHE and the current recorded after a stabilisation time of approximately 60 seconds.

2.5 XAS

The following edges were used to carry out the XAS measurements: Pt L_{II} (13.273 keV), Pt L_{III} (11.564 keV) and Ru K (22.117 keV). Station 16.5 of the synchrotron radiation source (SRS) at Daresbury was used to collect all data. The station operates with a multipole wiggler source and double crystal Si (220) monochromator. The second crystal was detuned to give 50 % harmonic rejection at the Pt L_{II} and L_{III} edges while 70 % harmonic rejection was used at the Ru K edge.

2.5.1 Half-cell

The PtRu data were collected in both the transmission (Pt L_{II} and L_{III} edges) and fluorescence (Ru K edge) modes. The cells have been described previously in chapter 2, section 3.2.6. The PtRu electrodes were placed against a gold wire current collector and an electrolyte of 1.0 M H_2SO_4 was flowed through the cell. A platinum gauze was used for the counter electrode and all potentials were measured with respect to a Hg/Hg_2SO_4 (MMS) reference electrode connected via a salt bridge. All potentials shown have been corrected to the RHE scale.

For transmission experiments, three ion chambers were used in series to measure the intensities of the incident beam, I_o, the beam transmitted by the sample, I_t, and the beam subsequently transmitted by a reference foil, I_m. The foil was used as an internal reference, enabling calibration of the X-ray beam energy. For fluorescence experiments, the cell was positioned at 45° with respect to the incident beam and a 30-element solid state detector used to measure the X-ray fluorescence, I_f.

XAS data were collected at three potentials: 0.0, 0.65 and 1.05 V vs. RHE. The electrode was polarised to these potentials and the experiment started once the current had decayed to a constant value.

2.5.2 Mini-cell

In situ mini-cell operation was carried out using 5 % H_2/N_2 for safety reasons at the beamline. The gas mix was flowed to both sides of the MEA and the PtRu anode polarised at potentials between 0 and 0.5 V vs. RHE. As for the half-cell, the

experiment was started once a stable current had been reached. Polarisation measurements were also conducted using a simulated reformate as the fuel, consisting of 100 ppm CO in 5 % H_2/N_2, with all other parameters remaining constant.

The XAS data were collected in the fluorescence mode at both the Ru K and Pt L_{III} absorption edges at open circuit and at anode polarisations up to 0.5 V.

2.6 XRD

XRD data were collected on station 9.1 of the SRS at the Daresbury laboratory. A beam with a spot size of 0.5 mm x 0.5 mm and a wavelength of 0.692 Å was used for all experiments and the XRD data were collected using a curved image plate (CIP) camera. A phosphor based image plate was loaded into the CIP in darkness and an exposure time of five minutes was used after which, the image plate was removed and scanned. A PhosphorImager™ reader was used to scan the film and a .gel file was produced by the Imagequant™ software. The intensity of the Debye-Scherrer rings in the .gel file was integrated to give the 2θ values.

Before commencing experiments the XRD data of the empty electrochemical cell containing just the electrolyte and carbon paper was collected to give a background pattern. With the electrode in the cell, XRD data were collected at O.C., 0.0 and 1.05 V vs. RHE.

3 RESULTS

It is well documented that PtRu anode catalysts have proved to give high CO tolerance relative to pure platinum. The effect of the catalyst composition will be discussed in terms of CO tolerance and methanol oxidation. The catalyst performances will be related to their structure using a number of techniques including TEM, XRD and XAS. *In situ* operation will be used where possible to give the most accurate representation of the catalyst structure.

A miniature PEM fuel cell the design of which was described in the previous chapter will be used to provide realistic environments to study the PtRu catalysts. Results from both room temperature and elevated temperature operation will be discussed.

3.1 Electrochemistry – Half Cell

3.1.1 Cyclic voltammetry

Figure 1 shows the CO oxidative stripping voltammograms for the series of PtRu/C catalysts in addition to a 40 wt. % Pt/C and 20 wt. % Ru/C, included for comparison. In all cases, during the first forward sweep from 0.15 V vs. RHE, the region characteristic of hydrogen desorption is suppressed due to the nearly complete CO surface coverage. After the first forward sweep the hydrogen desorption region returns indicating that the CO has been completely removed from the surface, with the exception of the Ru/C catalyst for which no evidence of hydrogen adsorption or desorption was observed.

As the amount of Ru in the catalyst is increased a change is seen in the hydrogen adsorption/desorption features. Peaks which are clearly visible in the 40 wt. % Pt case at 0.09 and 0.22 V vs. RHE become less pronounced with increasing Ru content. By the 40/20 PtRu catalyst there is complete loss of the adsorption/desorption features and little change is observed as the Ru content is increased further.

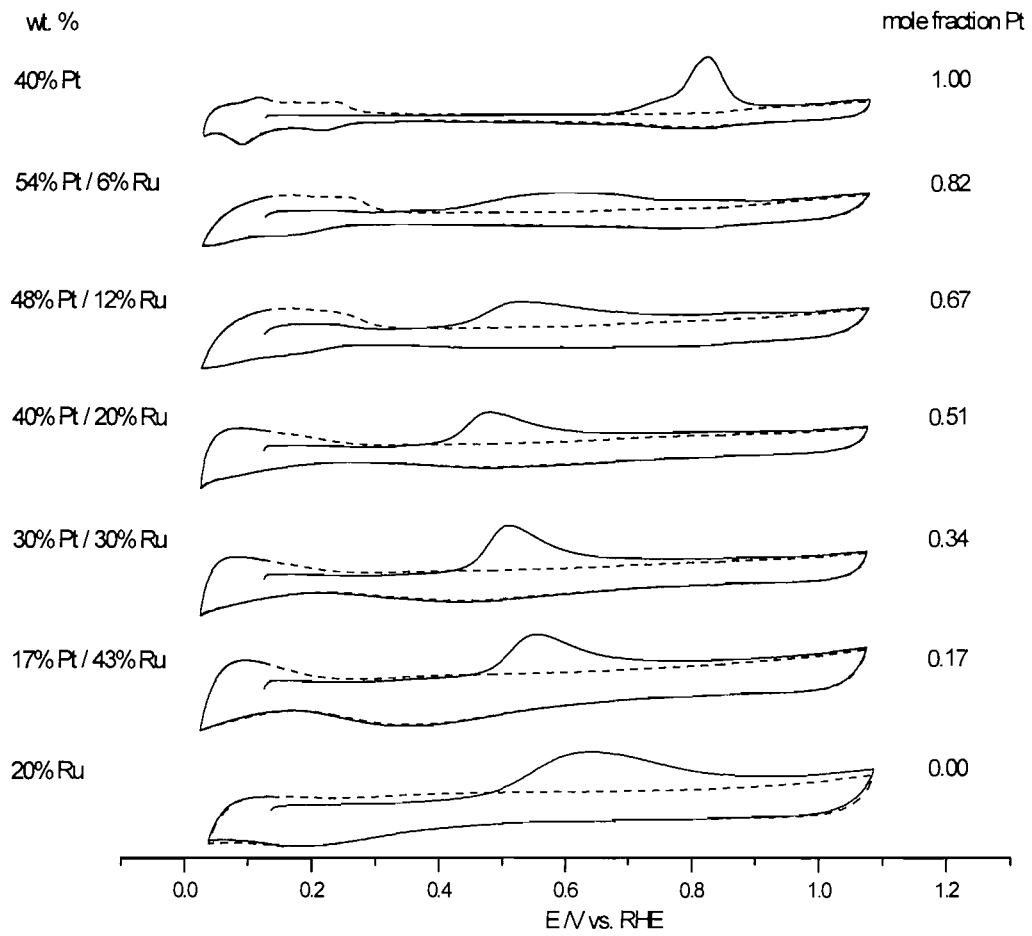

Figure 1 **Cyclic voltammetry of Pt/C, Ru/C and a PtRu/C series of fuel cell catalysts (electrode area 1 cm^2) in 2.5 M H_2SO_4. Compositions are given as wt. % of the dry catalyst powders. Electrode surface exposed to CO saturated solution while the potential was held at 0.05 V vs. RHE. After absorption, CO was displaced from the solution by purging with N_2. Sweep rate 10 mV s^{-1}. Solid line indicates the first cycle; the dotted line indicates the second.**

The presence of Ru leads to a substantial increase in the catalytic activity towards the oxidation of adsorbed CO [5,6,21,32]. This is demonstrated by the shift in the CO peak position to lower potentials relative to the pure Pt case (figure 2). The catalyst composition of 40/20, corresponding to an atomic ratio of 1:1, gives rise to the lowest CO oxidation peak potential at 0.48 V vs. RHE. As the Ru content is increased further, the peak position shifts to more positive values indicating a

decrease in the catalytic activity for CO oxidation. A shift in the oxide reduction peak with varying Ru content is also observed. Figure 2 shows that as the Ru content is increased the oxide reduction peak shifts to lower potentials. This reflects the ability of Ru to form oxide species at lower potentials than Pt. These oxide species are thought to promote the oxidation of adsorbed CO by a bifunctional mechanism and explain the improved CO tolerance when Ru is present.

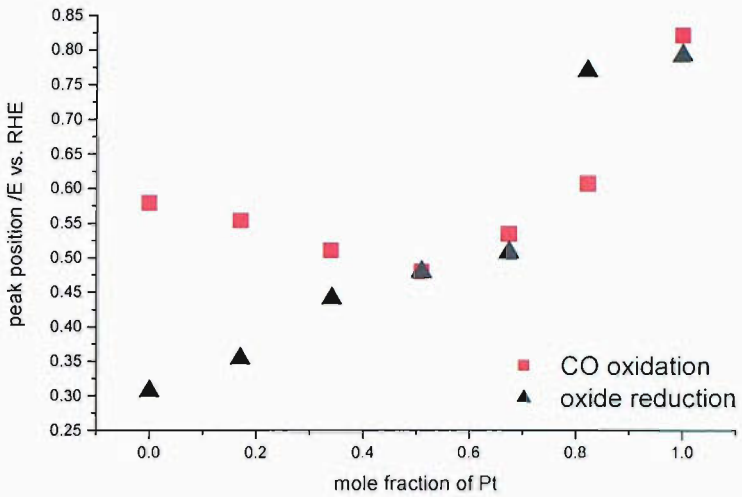

Figure 2 **CO stripping peak and oxygen reduction peak potentials as a function of the atomic ratio of Pt corresponding to only the metal atoms in the catalyst. Conditions: 2.5 M H_2SO_4, 10 mV s^{-1} sweep rate.**

A change in the shape of the CO peak is also observed as the Ru content is varied. At low Ru contents a broad peak is observed with lower peak currents. As the Ru content is increased the peak becomes progressively sharper until pure Ru is reached, at which point the peak begins to broaden. This trend has been observed experimentally by Gasteiger *et al.* [21] on polycrystalline PtRu alloys and predicted theoretically by Koper *et al.* [33] using Monte Carlo simulations.

3.1.2 Methanol oxidation

3.1.2.1 Low temperature methanol oxidation

Figure 3 presents the anode half-cell polarisation data for the series of PtRu catalysts. The specific activities at 30 °C have been plotted against potential to allow

the intrinsic activity of the catalysts to be compared, independent of the surface area of the catalysts. A large improvement is seen in the kinetic performance of the PtRu catalysts over pure Pt for methanol oxidation. A difference of approximately 130 mV is observed in the linear region of the Tafel plot between Pt and the best PtRu catalysts.

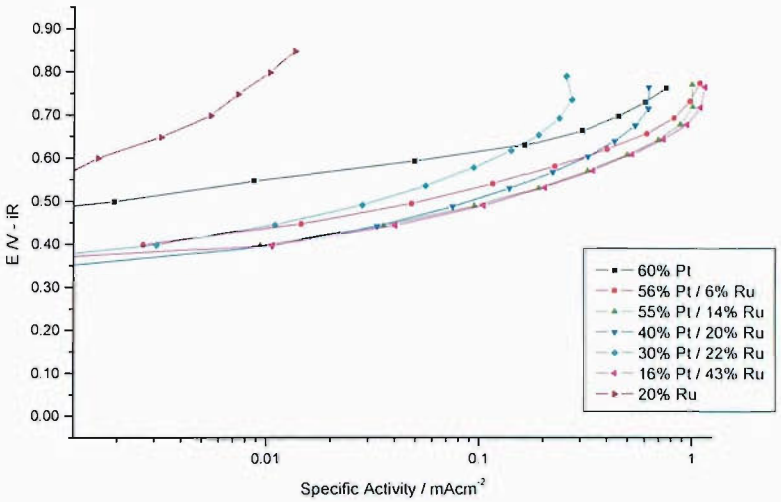

Figure 3 **Comparison of the specific activity of a PtRu series in 2 M MeOH / 1 M H_2SO_4 at 30 °C.**

Comparing the specific activities, a range of catalysts are found to give very similar performances including the following PtRu compositions: 55/14, 40/20 and 16/43. The wide ranging compositions giving comparable activities makes it difficult to determine an optimum ratio from the specific activity at this temperature.

In addition to the Pt and PtRu catalysts the performance of pure Ru for methanol oxidation is shown. Low specific activities indicate that on its own, Ru is a relatively inactive catalyst for methanol oxidation. This is related to the high adsorption strength of OH_{ads}, as indicated by the CV in figure 1, which, at room temperature, prevents the dissociative adsorption of methanol.

Figure 4 shows the mass activities for the PtRu series again at 30 °C. This allows catalyst performances to be compared as a function of the platinum content. The mass activities indicate that the 40/20 catalyst gives the highest performance. This

corresponds to the CVs in figure 1 obtained in a CO saturated 2.5 M H_2SO_4 which show that a 40/20 catalyst is the most CO tolerant catalyst.

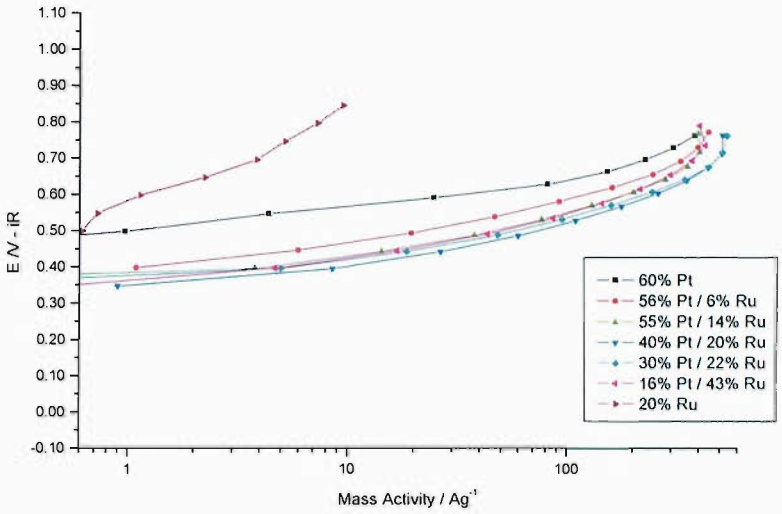

Figure 4 **Comparison of the mass activity of a PtRu series in 2 M MeOH / 1 M H_2SO_4 at 30 °C.**

3.1.2.2 High temperature MeOH oxidation

The importance of temperature effects on the optimum catalyst composition for methanol oxidation has been discussed in the introduction (section 1). The same set of experiments was repeated at 80 °C to see if the 40/20 catalyst gave the highest performance under these conditions.

Figure 5 shows the specific activity for the PtRu series at 80 °C. A marked increase in performance relative to the low temperature case is observed for all catalysts indicated by the improvement in specific activity. For example, for the 40/20 catalyst the specific activity at 0.4 V vs. RHE and 80 °C is 0.51 mA cm^{-2} compared with 0.01 mA cm^{-2} at 30 °C. The difference in potential between the Pt and PtRu catalysts has also increased to 170 mV from 130 mV in the linear region of the Tafel plot. This indicates a larger increase in activity for the PtRu catalysts relative to Pt with increasing temperature.

Again, a large improvement is seen in the kinetic performance of the PtRu catalysts over pure Pt for methanol oxidation. As the Ru content is increased the potential

shifts to lower values indicating an increase in the activity of the electrocatalysts. A maximum activity is reached for the 40/20. However, there is little change in the activities as the ruthenium content is increased further and the performances of the 30/22 and 16/43 are all very similar with little to differentiate between them.

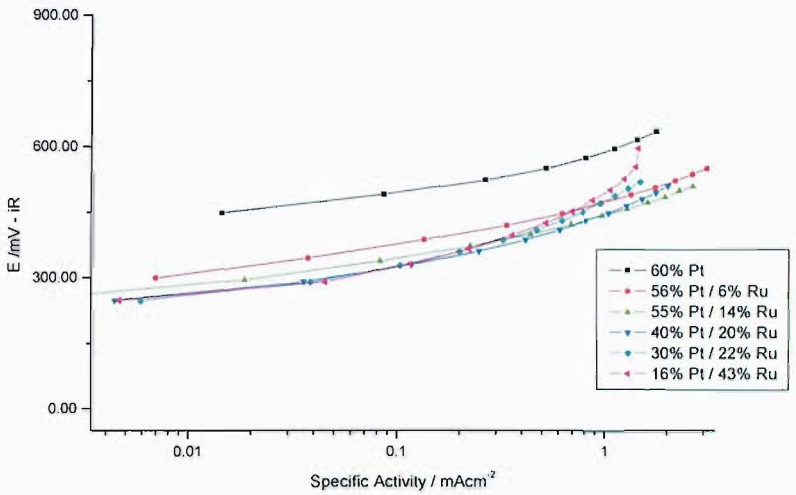

Figure 5 **Comparison of the specific activity of a PtRu series in 2 M MeOH / 1 M H_2SO_4 at 80 °C.**

At high potentials, a non-linear region is reached in the Tafel plot. This is particularly apparent for the 16/43 PtRu catalyst where the activity begins to level off as the potential is increased. It is also beginning to occur in the 30/22 case. The fall in current at high potentials may be due to the formation of a passive oxide film which results in the deactivation of the electrode. This will affect the high Ru content catalysts to a greater extent due to the lower potential for the formation of Ru-OH compares to Pt-OH. Mass transport may also play a part in limiting the current. For example, if the electrode is not completely flooded, the transport of methanol to the catalyst surface is limited. Another possibility is that there is a thickness affect as a result of keeping approximately the same Pt loadings for all the electrodes. This means that for catalysts with high Ru content a thicker catalyst layer must be applied to achieve the same Pt loadings, resulting in slower diffusion rates through the layer.

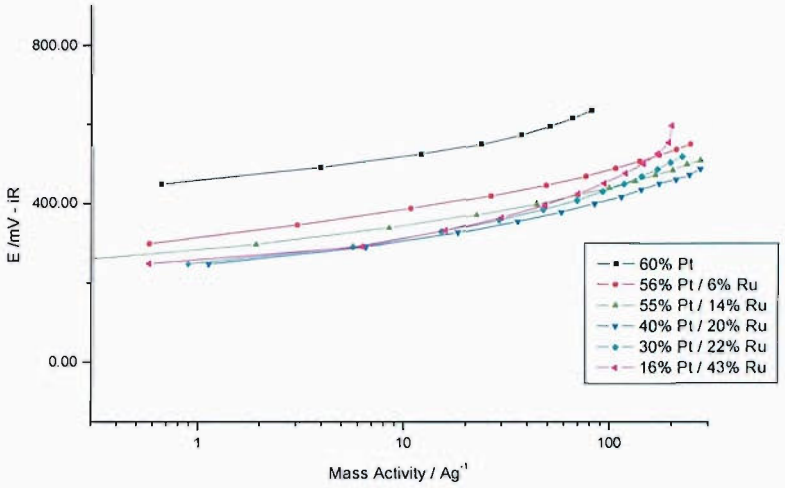

Figure 6 **Comparison of the mass activity of a PtRu series in 2 M MeOH / 1 M H_2SO_4 at 80 °C.**

Figure 6 shows the mass activities for the PtRu series again at 80 °C. A similar pattern to the specific activity is observed. The performance increases dramatically as Ru is introduced to the catalyst and reaches a limit for the 40/20 catalyst. There is little difference in mass activities at low mass activities (>10 A g^{-1}) however, the difference in performance becomes more apparent at high mass activities where a slight fall off in activity is observed as the Ru content is increased further.

3.2 Catalyst Characterisation

3.2.1 Transmission Electron Microscopy – *ex situ*

Transmission electron microscopy images were collected for the 54/6, 40/20, 30/30 and 16/43 PtRu catalysts. The images were obtained by technical staff at Johnson Matthey using a Tecnai F20 TEM at a voltage. The material was suspended in acetone, sonicated and applied to carbon coated copper grid. The images of the catalysts for a range of magnifications are shown below.

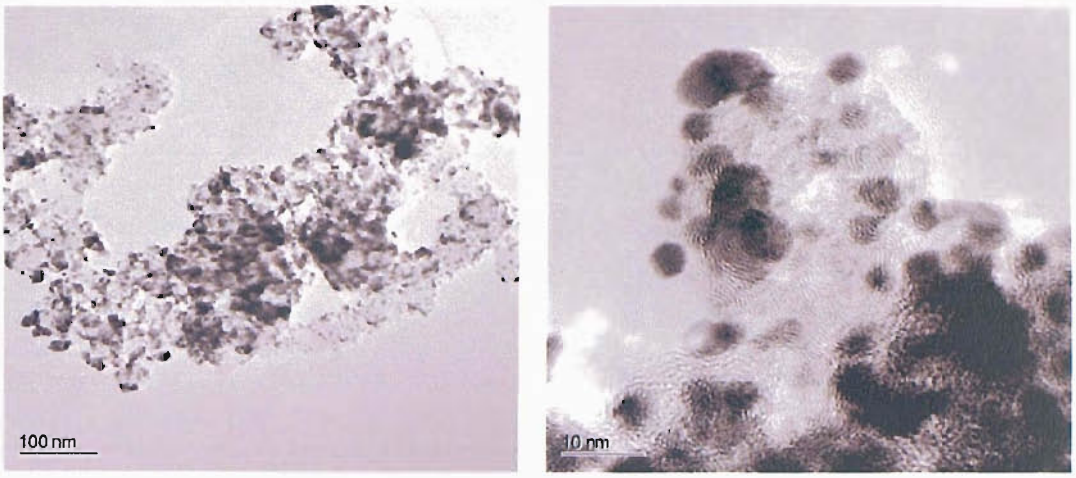

Figure 7 **TEM micrographs of 54 wt. % Pt / 6 wt. % Ru (a) scale bar 100 nm, (b) scale bar 10 nm.**

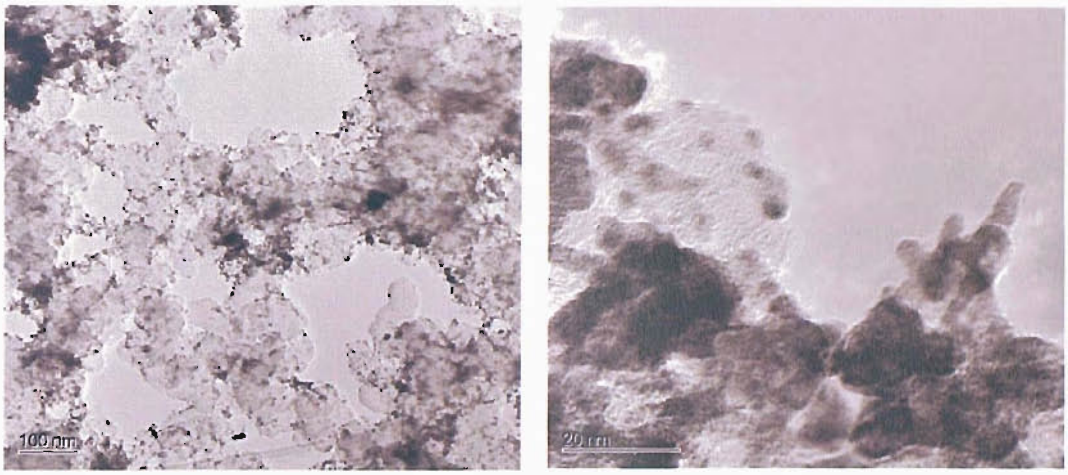

Figure 8 **TEM micrographs of 40 wt. % Pt / 20 wt. % Ru (a) scale bar 100 nm, (b) scale bar 20 nm.**

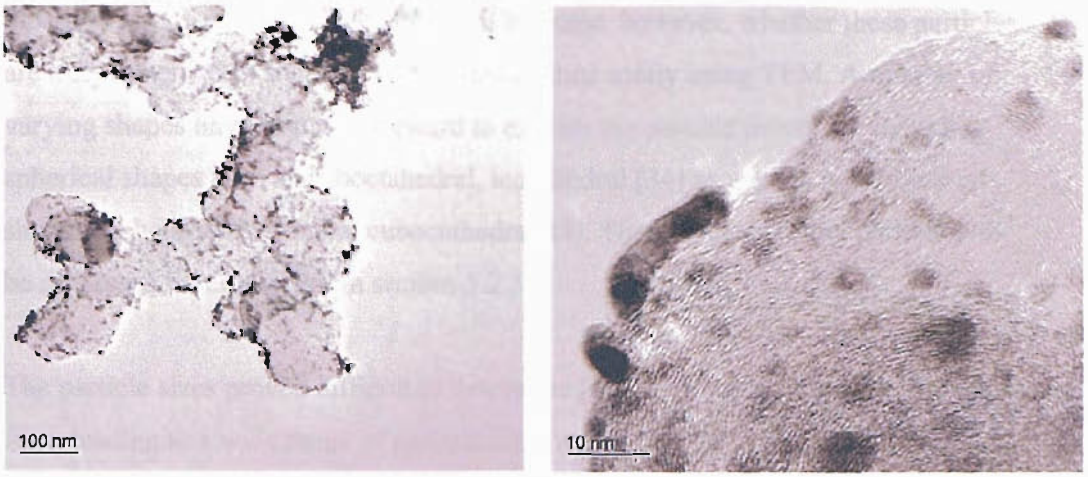

Figure 9 **TEM micrographs of 30 wt. % Pt / 30 wt. % Ru (a) scale bar 100 nm, (b) scale bar 10 nm.**

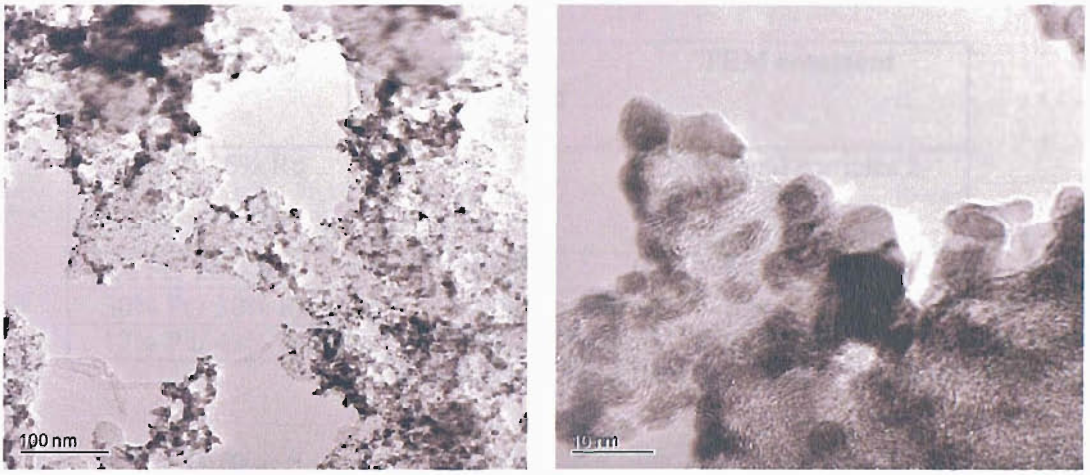

Figure 10 **TEM micrographs of 17 wt. % Pt / 43 wt. % Ru (a) scale bar 100 nm, (b) scale bar 10 nm.**

The low magnification images in Figures 7 to 10 illustrate the dispersion of the catalyst on the carbon support. The metal loading on the carbon support determines the particle size although the alloying element has been shown to play an important role. Hogarth and Ralph [14] have shown that Ru promotes the dispersion of the catalyst. The explanation put forward suggested that unalloyed amorphous material present on or near the surface of the particles may help prevent sintering during the deposition or thermal reduction processes. The high magnification images show that

the particles are approximately spherical in shape, however, whether these particles are truly spherical in shape cannot be determined solely using TEM. A number of varying shapes have been put forward to explain the particle properties including spherical shapes such as cuboctahedral, icosahedral [34] as well as non-spherical shapes such as hemispherical cuboctahedra [18]. The geometry of the particle will be discussed in more detail in section 3.2.3.2.

The particle sizes proved difficult to determine from TEM (table 2). Agglomerates form leading to a wide range of particle sizes ranging from 2 to 20 nm for the 54/6 catalyst and 3 to 14 nm in the case of the high ruthenium content catalysts. In each case the same total metal content is used (60 %). Therefore, changes in particle size and dispersion may be related to the ruthenium content as explained above.

Table 2 Range of particle sizes determined from TEM

Catalyst Assay	Catalysts composition Pt:Ru	TEM comment
54% Pt / 6% Ru	83:17	Individual particles 2-20nm Lots of clusters
40% Pt / 20% Ru	49:51	3-14nm particles
30% Pt / 30% Ru	32:68	3-12nm particles
17% P t/ 43% Ru	17:83	3-13nm particles

3.2.2 X-ray Diffraction

The XRD patterns for the PtRu catalysts collected *in situ* at 0.0 V vs. RHE and with an electrolyte of 1 M H_2SO_4 are shown in figure 11. The scatter generated by an empty cell containing just the electrolyte and carbon paper was collected to act as a background. The lattice parameters were calculated for all of the PtRu catalysts in the series assuming an fcc structure. Table 3 shows the lattice parameters for the PtRu catalysts in 1 M H_2SO_4 at a potential of 0.0 V vs. RHE and the *ex situ* results for comparison.

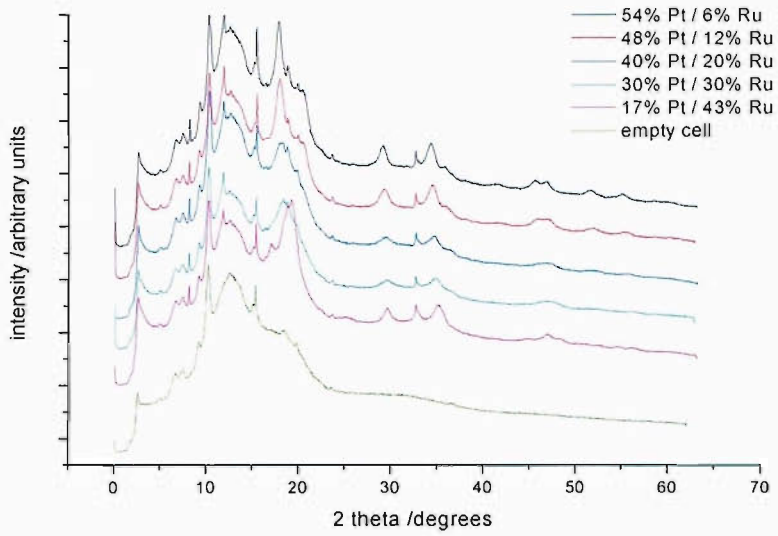

Figure 11 **XRD patterns for the PtRu series of catalysts at 0.0 V vs. RHE in 1 M H_2SO_4 and the empty cell.**

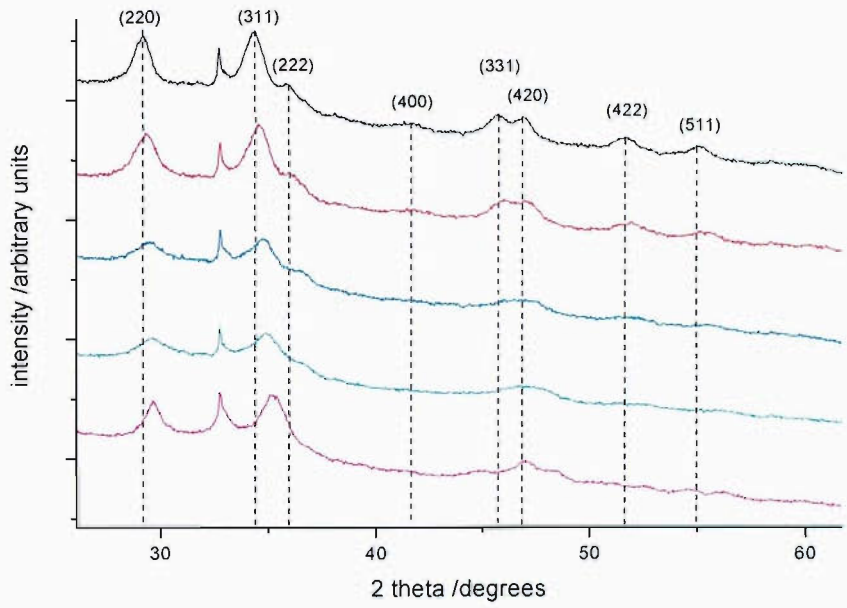

Figure 12 **Rescaled plot of the XRD patterns for the PtRu series (shown above) highlighting reflections in the 2 theta range from 30 to 60. (The colour scheme is the same as that used in figure 11).**

As the Ru content increases, a lattice contraction takes place resulting in shorter Pt-Pt distances. Mukerjee *et al.* [35] observed a strong correlation between bond distances and Pt 5d band character for a range of platinum alloys. Very similar

results are obtained using *in situ* and *ex situ* XRD methods. Thus, there is little effect of the electrode structure and the electrolyte on the bulk structure of the catalyst particles. The XRD patterns were also collected at O.C. and at 1.05 V vs. RHE but no changes in lattice parameter were observed within the error involved.

Table 3 **Lattice parameters and crystallite sizes calculated from XRD. All *in situ* measurements taken at 0.0 V vs. RHE.**

Pt/Ru wt. %	Atomic Ratio Pt:Ru	Lattice Parameter /Å		Crystallite Size /nm	
		ex situ XRD	in situ XRD	ex situ XRD	in situ XRD
54/6	82.3 : 17.7	3.90	3.890 ±0.005	3.8	4.14
48/12	67.4 : 32.6	3.88	3.867 ±0.004	3.2	3.79
40/20	50.9 : 49.1	3.85	3.845 ±0.004	2.4	2.59
30/30	34.1 : 65.9	3.84	3.839 ±0.002	2.3	2.93
17/43	17.0 : 83.0	-	3.830 ± -	3.2	4.83

A rescaled plot showing reflections with 2 theta values ranging from 30 to 60 is shown in figure 12. Less scattering from the cell appears in this region so the peaks corresponding to reflections from the PtRu catalyst can be clearly seen. The peaks corresponding to an fcc lattice have been assigned for the 54/6 case. As the Ru content is increased a shift to higher angles can be seen, corresponding to the lattice contraction. The broadening and merging of the peaks, for example the (331) and (420), arises partly due to a decrease in particle size but also due to a transition from an fcc to hcp lattice. This makes the accuracy of the lattice parameter for the 17/43 catalyst difficult to determine because the reflections corresponding to the fcc reflections become very weak and hcp reflections of either pure Ru or a Ru rich phase dominate the XRD pattern.

The (220) reflections were analysed to determine the particle size. After subtracting a linear background a Lorentzian function was fitted to determine the Full Width Half Maximum (FWHM) values. From this, the average particle size can be estimated using the Scherrer equation (chapter 2, section 4.1). An example of the peak fit for the XRD pattern of the 54/6 PtRu catalyst at 0.0 V vs. RHE in 1 M H_2SO_4 is shown in chapter 2, figure 21. The inset of the figure provides an example of the peak fit for the (220) reflection used to determine the particle size. Table 3

shows the particle sizes determined from the peak broadening for both the *in situ* and *ex situ* environments, with the *in situ* particle size being larger. This may reflect the reduction of an amorphous surface oxide on the crystalline particles under potential control making the crystalline size appear larger. XRD is only sensitive to the crystalline fraction of the catalyst. Therefore, any oxide present on the surface of the particle will not contribute to the diffraction peaks and will not be accounted for in the particle size determined from peak widths.

3.2.3 XAS – Half Cell

3.2.3.1 XANES

The XANES region allows the fractional d-electron vacancies of the Pt atoms in the catalyst to be determined. The d-band vacancies are derived from analysis of the Pt L_{II} and Pt L_{III} white lines. The L_{II} and L_{III} edges arise due to excitations of the $2p_{1/2}$ and $2p_{3/2}$ electrons, respectively, to empty states in the vicinity of the Fermi level. The dipole selection rules, $\Delta L = \pm 1$ and $\Delta J = 0, \pm 1$, restrict transitions so that excitation to the d-orbitals is the most favoured. Brown *et al.* [36] showed that the final Pt d-states are predominately those with total angular momentum J = 5/2, they contribute about 14 times more to the final d-states than those with a total angular momentum J = 3/2. This explains the difference in intensity of the white lines, with the L_{III} edge ($2p_{3/2}$ to $5d_{5/2}$) giving a more intense peak than the L_{II} edge ($2p_{1/2}$ to $5d_{5/2}$).

The d-band vacancies relative to a reference material can be quantified from the difference in areas under the Pt L_{III} and L_{II} absorption edges, between the sample and a pure Pt reference foil [37]. The fractional change, f_d, in the number of d-band vacancies relative to the reference material can be expressed using the following equation:

$$f_d = \frac{\Delta A_3 + 1.11\Delta A_2}{A_{3,r} + 1.11A_{2,r}} \qquad \textbf{Eq. 1}$$

Where $\Delta A_3 = (A_{3s} - A_{3r})$ and $\Delta A_2 = (A_{2s} - A_{2r})$ with s indicating sample and r the reference. The terms A_2 and A_3 represent the areas under the L_{II} and L_{III} absorption edges respectively and were determined by integration of the normalised spectra from 10 eV below the edge to 40 eV above the absorption edge. The quantity $A_{3,r} + 1.11A_{2,r}$ is the combined area per unoccupied d-electron and is a constant for the element being studied and has been determined according to the procedure of Brown *et al.* [36]. The $A_{3,r}$ and $A_{2,r}$ areas were determined by first calculating the difference in areas under the L_{III} and L_{II} edges. The difference in areas was then multiplied by a correction term specific to the edge to account for the white line weight.

The f_d value (equation 1) can then be used to calculate the total number of unoccupied d-states per Pt atom in the samples as follows:

$$(h_J)_{t,s} = \frac{(1.0 + f_d)}{(h_J)_{t,r}} \qquad \textbf{Eq. 2}$$

Where $(h_J)_{t,r}$ for Pt has been shown to be 0.3 [36]. A large value of $(h_J)_{t,s}$ indicates a smaller d-electron density and an increased d-band vacancy as compared to those for bulk Pt.

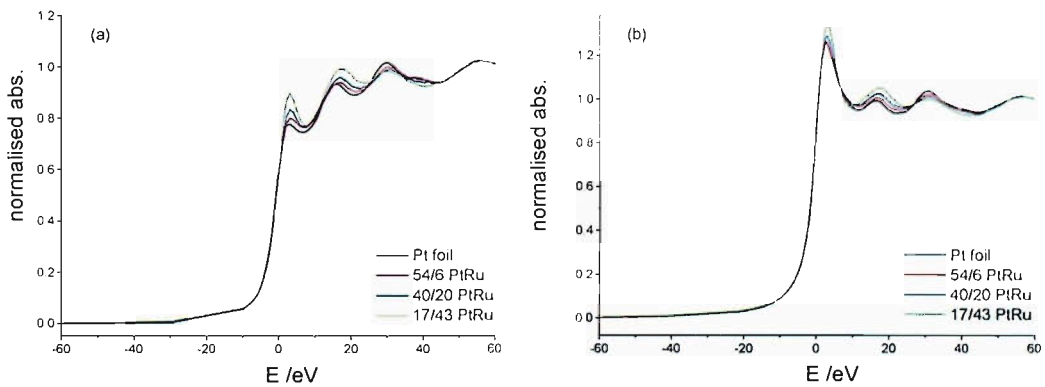

Figure 13 **XANES region for a 54/6, 40/20 and 17/43 PtRu catalyst at 0.0 V vs. RHE in 1 M H_2SO_4 and Pt foil at the (a) Pt L_{II} and (b) Pt L_{III} edges.**

The XANES spectra at both the Pt L_{II} and L_{III} edges for a selected number of PtRu compositions and a platinum foil are shown in figure 13. The spectra were collected

with the PtRu electrodes at 0.0 V vs. RHE and with a 1 M H_2SO_4 electrolyte. As the ruthenium content increases, the intensity of the white line region at both edges increases, indicating that there is an increase in d-band vacancy of Pt as the amount of ruthenium increases. The calculated $(h_J)_{t,s}$ values are given in table 4.

Table 4 Pt d-band vacancies for Pt and a series of PtRu catalysts

Electrocatalyst	$(h_J)_{t,s}$
60 % Pt	0.307
54 % Pt / 6 % Ru	0.311
48 % Pt / 12 % Ru	0.323
40 % Pt / 20 % Ru	0.325
30 % Pt / 30 % Ru	0.336
17 % Pt / 43 % Ru	0.348

The potential of 0.0 V vs. RHE was chosen so that contributions from surface oxides present on the catalyst surface (see EXAFS, section 3.2.3.2) were minimised. This indicates that enhancement in the white line intensity of PtRu/C relative to Pt/C is largely a result of the amount of Ru present. The electron withdrawing effect of Ru is therefore causing an emptying of the 5d band of the Pt. The continuing increase in d-band vacancies with Ru content (table 4) implies that the Ru is well alloyed even for the 17/43 case. If the additional Ru was present as an oxide or as separate particles a plateau in the $(h_J)_{t,s}$ / d-band vacancy would have been expected.

3.2.3.2 EXAFS

EXAFS data were collected for each of the PtRu catalysts in the series. Figure 14 shows the k^2 weighted raw EXAFS data at 0.0 V vs. RHE in 1 M H_2SO_4 for the PtRu catalysts at both the Pt L_{III} and Ru K edges. The solid lines represent the raw data and the dotted/red lines represent the fit. At both edges a region of low amplitude oscillation can be seen in the chi data at approximately 6 $Å^{-1}$. This is an area of destructive interference between the backscattered photoelectron wave from

the Pt and Ru neighbours. For this to occur the backscattering must be 180° out of phase [29,38].

A phase shift can be observed in the chi data as the ruthenium content is decreased. For example, the chi data at the Pt L_{III} edge for the 17/43 catalyst shows a peak at 10 $Å^{-1}$, which undergoes a phase shift as ruthenium is added so that by the time the 54/6 catalyst is reached a complete reversal of phase is observed. Similar examples can be seen at the Ru K edge.

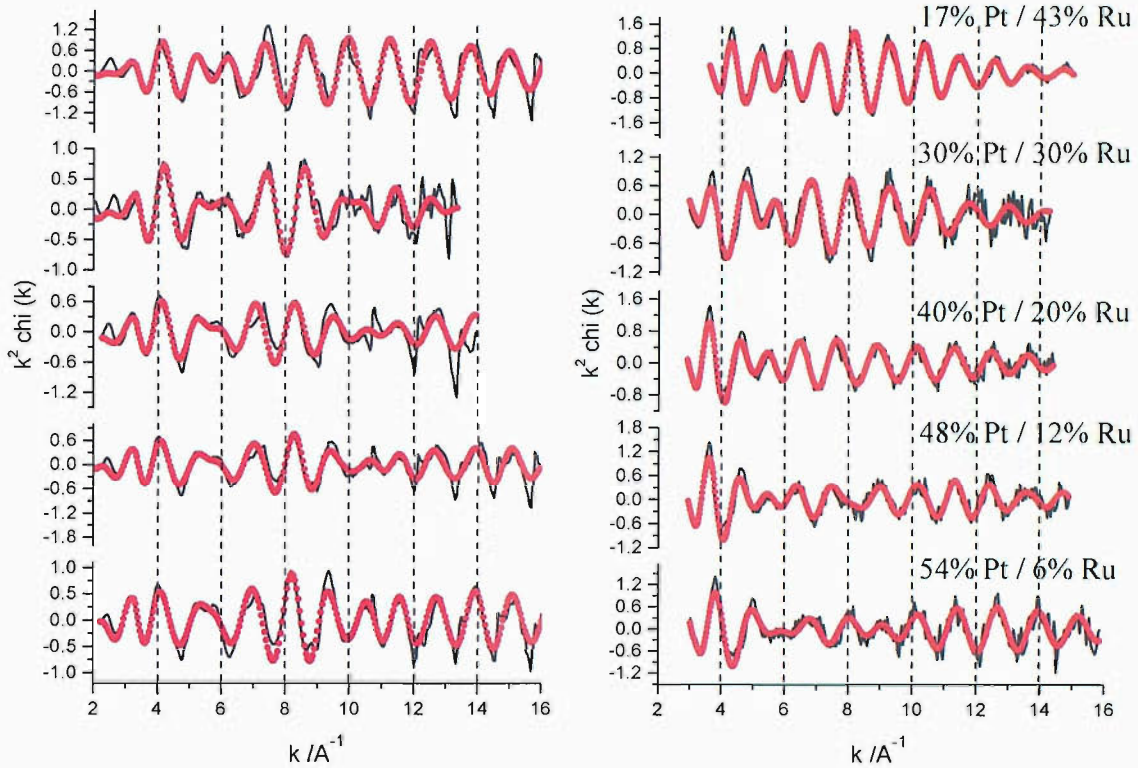

Figure 14 **k^2 weighted EXAFS data (solid lines) and fits (dotted lines) at 0.0 V vs. RHE for the series of five PtRu catalysts (60 wt. % total metal content) at the Pt L_{III} edge (left) and the Ru K edge (right).**

The Fourier transforms of the chi data (figure 15) show that the environment around each metal absorber includes both Pt and Ru for all metal ratios of the bimetallic catalysts. At the Pt edge this results in a splitting in the first shell peak which is particularly pronounced for the 40/20 and 48/12 catalysts. The peak splitting is less evident from the Ru K edge although it can be seen for the 48/12 and 54/6 catalysts. The origin of the peak splitting is a result of backscattering from the Pt and Ru neighbours being 180° out of phase causing beats in the chi data. The parameters

obtained from fitting the data at the Pt L_{III} and Ru K edges are shown in tables 5 and 6 respectively.

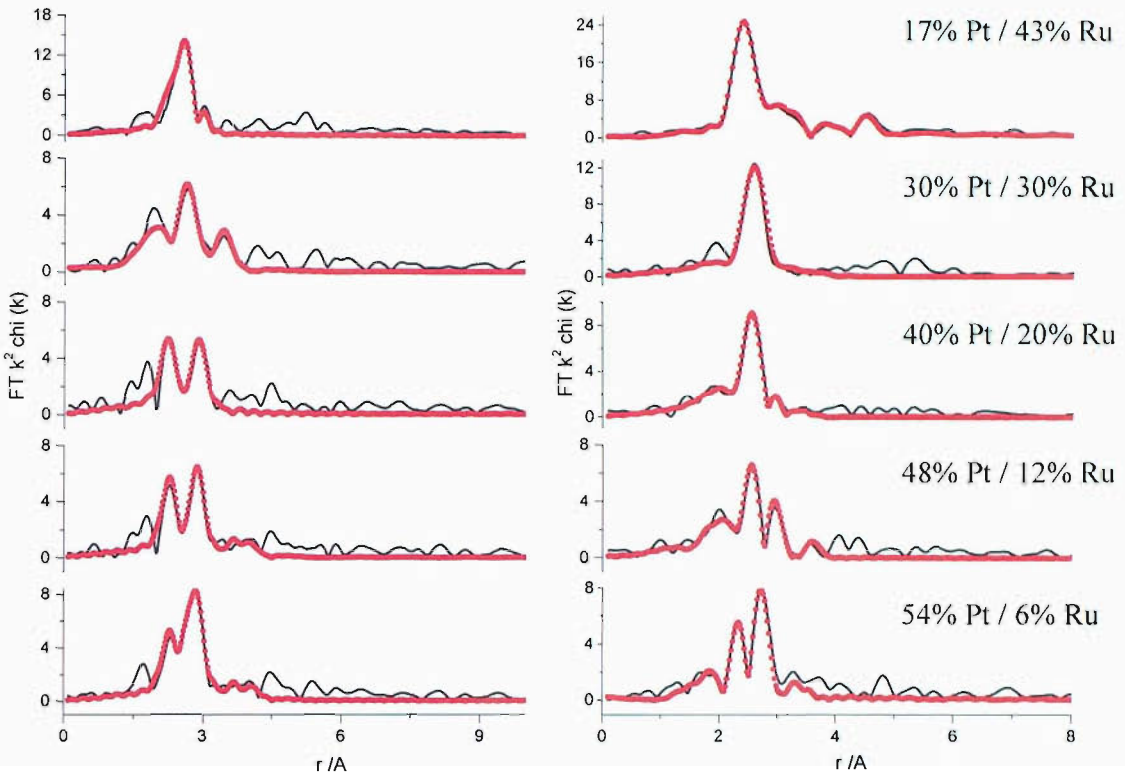

Figure 15 **k^2 weighted Fourier transforms at 0.0 V vs. RHE of the data (solid line) and fits (dotted lines) for the series of five PtRu catalysts (60 wt. % total metal content) at the Pt L_{III} edge (left) and the Ru K edge (right).**

Table 5 Structural parameters for the PtRu catalysts. Taken from the Pt L_{III} edge, 0.0 V vs. RHE.

Catalyst	Shell	Calculated parameters (Pt L_{III} edge)				
		N	*R* /Å	$2\sigma^2$ /Å^2	E_f /eV	R_{exafs}
54/6	Pt-Ru	1.2 ±0.2	2.79 ±0.01	0.006 ±0.002	-13.6 ±0.7	40.91
	Pt-Pt	6.0 ±0.4	2.79 ±0.004	0.009 ±0.001		
	Pt-Pt	3.2 ±1.2	3.90 ±0.02	0.016 ±0.004		
48/12	Pt-Ru	2.1 ±0.3	2.77 ±0.009	0.010 ±0.01	-13.4 ±0.8	49.98
	Pt-Pt	5.2 ±0.4	2.78 ±0.005	0.010 ±0.001		
	Pt-Pt	2.7 ±1.1	3.88 ±0.03	0.015 ±0.005		
40/20	Pt-Ru	2.3 ±0.4	2.77 ±0.01	0.010 ±0.002	-12.9 ±1.2	59.48
	Pt-Pt	4.9 ±0.6	2.78 ±0.01	0.010 ±0.002		
30/30	Pt-Ru	3.4 ±0.4	2.70 ±0.009	0.014 ±0.002	-9.9 ±1.0	50.88
	Pt-Pt	3.7 ±0.7	2.70 ±0.02	0.016 ±0.003		
17/43	Pt-Ru	5.6 ±0.6	2.74 ±0.008	0.011 ±0.009	-14.5 ±2.2	44.19
	Pt-Pt	3.2 ±0.7	2.80 ±0.008	0.009 ±0.001		

Table 6 Structural parameters for the PtRu catalysts. Taken from the Ru K edge, 0.0 V vs. RHE.

Catalyst	Shell	Calculated parameters (Ru K edge)				
		N	*R* /Å	$2\sigma^2$ /Å^2	E_f /eV	R_{exafs}
54/6	Ru-Ru	5.9 ±0.4	2.65 ±0.007	0.012 ±0.001	-0.4 ±0.5	51.59
	Ru-Pt	2.4 ±0.3	2.72 ±0.005	0.012 ±0.001		
48/12	Ru-Ru	3.4 ±0.2	2.65 ±0.005	0.013 ±0.001	0.1 ±0.4	44.81
	Ru-Pt	4.7 ±0.4	2.71 ±0.006	0.014 ±0.001		
	Ru-Pt	0.6 ±0.3	3.45 ±0.02	0.006 ±0.003		
40/20	Ru-Ru	4.4 ±0.2	2.65 ±0.004	0.013 ±0.0006	1.9 ±0.4	37.90
	Ru-Pt	3.0 ±0.3	2.69 ±0.008	0.013 ±0.001		
30/30	Ru-Ru	5.3 ±0.3	2.66 ±0.005	0.012 ±0.0007	0.3 ±0.5	41.34
	Ru-Pt	2.3 ±0.4	2.69 ±0.01	0.012 ±0.002		
17/43	Ru-Ru	6.8 ±0.2	2.67 ±0.002	0.012 ±0.0002	-0.4 ±0.5	20.12
	Ru-Pt	1.1 ±0.2	2.68 ±0.008	0.010 ±0.001		

The results from the EXAFS analysis can be compared with those obtained from the *ex situ* and *in situ* XRD (table 3) by comparison of the Pt-Pt lattice parameter

(table 7), which corresponds to the second shell Pt-Pt distance. In agreement with the XRD results, a lattice contraction is observed with increasing Ru content. For the 40/20, 30/30 and 17/43 catalysts a second shell Pt-Pt distance was not fitted, as the effects of the interference between the backscattering from the Pt and Ru neighbours are more severe at this distance, effectively cancelling the contributions in the EXAFS data. In these cases, the distances were calculated from the first shell assuming an fcc lattice. The fact that the 17/43 catalyst does not follow the trend provided additional evidence of the presence of the hcp structure observed in the XRD data.

Table 7 **Lattice parameter and crystallite size (using the Benfield model [39]) calculated from EXAFS. Measurements taken at 0.0 V vs. RHE. EXAFS lattice parameters taken from the Pt L_{III} edge and calculated from the 2nd shell distance. * Calculated from 1st shell distance.**

Pt/Ru wt. %	Atomic Ratio Pt:Ru	Lattice Parameter /Å	Particle Size /nm
54/6	82.3 : 17.7	3.94 ±0.01	1.30
48/12	67.4 : 32.6	3.93 ±0.01	1.33
40/20	50.9 : 49.1	3.93* ±0.01	1.31
30/30	34.1 : 65.9	3.82* ±0.02	1.24
17/43	17.0 : 83.0	3.97* ±0.01	1.86

EXAFS can also be used to gain information regarding the catalyst particle size, as this is reflected in the coordination numbers. For example, a bulk platinum foil has an fcc lattice and hence a first shell coordination number of 12. The PtRu nanoparticle catalysts have been shown by XRD to resemble an fcc lattice except in the case of the high ruthenium content catalysts. However, the average first shell coordination number is reduced, as the atoms on the particle surface do not have the full complement of neighbours. As a result of this, it is possible to relate the size of the nanoparticles to the first nearest neighbour coordination number. Benfield [39] has derived equations by modelling the nanopaticles using icosahedral and cuboctahedral geometries (figure 16). The icosahedron and cuboctahedron are made up of concentric shells of atoms where the central atom is counted as the first shell and a cluster of *m* complete shells has an edge length of *m* atoms. Equations 3 and 4

show the relationship between the coordination number, *N* and the number of complete shells, *m* for the icosahedral and cuboctahedral cases, respectively.

$$N_{total} = \frac{6(m-1)(20m^2 - 25m + 12)}{(2m-1)(5m^2 - 5m + 3)} \qquad \textbf{Eq. 3}$$

$$N_{total} = \frac{12(m-1)(10m^2 - 14m + 6)}{(2m-1)(5m^2 - 5m + 3)} \qquad \textbf{Eq. 4}$$

The correct choice of geometric model is difficult to determine. The cuboctahedron is the most widely used cluster model [40]. However, it is found that the icosahedron has a higher value of *N* for a particle the same size because of the higher coordination of some of the surface atoms (figure 16 (a) and (b)). Therefore the icosahedron will be favoured thermodynamically as the number of interatomic interactions are maximised. As the particle size increases, the benefits of the icosahedral geometry become smaller as the differences in *N* for the same particle size decrease. The values of *N* found in the PtRu cases were all relatively small giving *m* values of around 3. Therefore, an icosahedral geometry was used throughout.

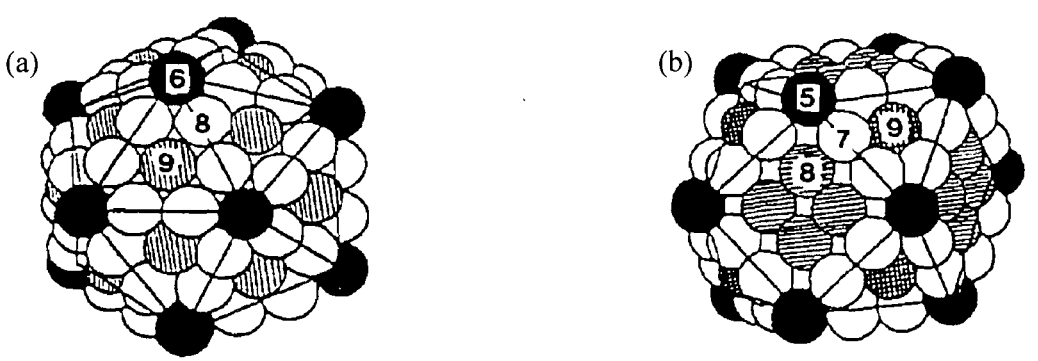

Figure 16 **Particle geometries for a) icosahedron and b) cuboctahedron using 147 atoms corresponding to four complete shells. Numbers on surface atoms indicate varying coordination numbers [39].**

An estimation of the particle sizes from the total number of atoms in the first shell is shown in table 7. Using data from the Pt L_{III} edge, a distribution of particle size

between 1 and 2 nm was observed, assuming an icosahedral model. Within the errors involved, the particle sizes determined from EXAFS remained fairly constant with the exception of the 17/43 catalyst, which has a slightly larger particle size of 1.86 nm.

The particle size results from EXAFS are far lower than those determined by XRD or TEM. This can be attributed to the fact that the EXAFS results include contributions from all of the Pt atoms, even those in particles too small to be detected by XRD or TEM. Interpretation of these results must also take into account the limitations of assuming an icosahedral particle shape. In addition, it is important to look at how the coordination number might vary as atoms are added. The outer shell of the particle is only complete for certain numbers of atoms: 1, 13, 55, 147 etc. For example, an *m* value of 2 corresponds to a particle of 13 atoms. If one atom is added to this cluster to begin the next shell, then the average coordination number drops. The coordination will not start rising again until the atoms in the new shell are coordinated to each other. This effect suggests that the structure of the nanoparticle plays an important role and that the difference between the EXAFS and XRD or TEM results are not simply an averaging effect due to a large number of very small particles.

Since particle size and lattice parameters follow the same trend, there is also the possibility that the lattice contraction is a result of particle size, in addition to the electron affinity of the Ru. Small particles often have very different properties to those of the bulk metal [18]. For example, platinum metal atoms in the bulk metal generally have more d-band character than atomic platinum [41]. Evidence for this is shown in table 4 where the value of $(h_J)_{t,s}$ is 0.307 for the 60 wt. % Pt catalyst. This is greater than the value of 0.3 for bulk platinum indicating increased d-band vacancies for small particle sizes. The change in the d-band vacancies could lead to the contraction observed in the lattice parameter as the particle size decreases.

3.3 Electrochemistry – Mini-Cell

3.3.1 Hydrogen polarisation

The 40 wt. % Pt / 20 wt. % Ru catalyst was used at the anode of the MEA while 20 wt. % Pt was used for the cathode. The electrochemical performance of the PEM mini-cell fitted with the MSA gas humidifiers was assessed via the collection of anode steady-state polarisation curves for the MEA. The results obtained with pure hydrogen, 5 % H_2/N_2, and 100 ppm CO in 5 % H_2/N_2 used as the anode fuel gases are shown in figure 17. The flow rate was kept constant throughout at 60 to 70 cm^3 min^{-1} and the cell was operated at 80 °C.

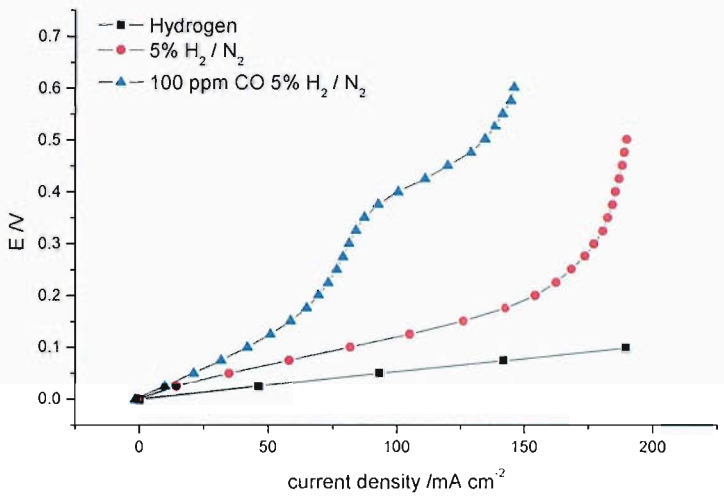

Figure 17 **Comparison of hydrogen polarisation curves using different gas mixes. Demonstrates performance under pure hydrogen (squares), 5 % hydrogen balance nitrogen (circles) and 100 ppm CO reformate (triangles). Anode: 40 wt. % Pt / 20 wt. % Ru, 0.8 mg Pt cm^{-2}. Cathode: 20 wt. % Pd, 0.25 mg Pd cm^{-2}. Cell temperature = 80 °C.**

Under pure hydrogen, a linear potential vs. current density response was observed. The membrane resistance may be estimated from the gradient, yielding a value of 0.04 Ω cm^2, which is in close accord with the expected value for the Flemion membrane used [42]. This indicates that the response of the PEM mini-cell is not limited by the contact resistance between the graphite plates and the MEA and that the MEA remains well hydrated during operation.

As discussed in chapter 3, section 4, pure H_2 could not be used on the beamline for safety reasons and, therefore, 5 % H_2/N_2 was used. The effect of the dilution on the cell performance can clearly be seen in figure 17 (circles) as a decrease in the current density at which mass transport limitations dominate the response to 155 mA cm^{-2} (anode polarisation of approximately 0.2 V), observed as a sharp increase in the potential for a small increase in the current density.

The presence of 100 ppm CO in the simulated reformate gas mix reduces the performance of the fuel cell further; as shown by the triangular data points in figure 17, the anode is polarised to a greater extent even at the lowest current densities. This change in response is attributed to poisoning of the surface of the PtRu catalyst particles by adsorbed CO. At anode polarisations above 0.38 V, corresponding to current densities > 90 mA cm^{-2}, the slope of the polarisation curve decreases. Above this onset potential, adsorbed CO is being oxidised increasing the number of free sites available on the surface of the catalyst particles available for H absorption, providing the slight improvement in the polarisation response. For current densities greater than 125 mA cm^{-2}, dilution effects can again be seen as mass transport limitations begin to dominate the response.

3.4 XAS – Mini Cell

3.4.1 XANES

The effects of the composition of the anode fuel on the chemical state of the PtRu/C catalyst particles may be initially assessed by comparison of the near edge region (XANES) of the XAS data collected at both the Ru K and Pt L_{III} absorption edges, as previously reported by O'Grady *et al.* for an unsupported PtRu catalyst electrode [9]. The results for the carbon supported catalyst MEA used in the present study are summarised in figure 18. The XANES of the as prepared MEA in air collected at both edges show that in the initial state, prior to exposure to the fuel, the catalyst is somewhat oxidised. This is evidenced by the broad first peak in the XANES at the Ru K edge and the more intense white line at the Pt L_{III} edge. Upon exposure of the anode catalyst to the 5 % H_2/N_2 fuel, the XANES data more closely resembles that of metallic Ru and Pt, in good agreement with the results reported by O'Grady *et al.*

[9] and those for an MEA containing 1:1 PtRu/C collected using transmission XAS reported by Viswanathan *et al.* [30]. No further change was observed in the XANES region following a subsequent increase in the temperature of the PEM mini-cell or upon changing the anode fuel to the synthetic reformate, as shown by the fact that the dashed (80 °C) and dot-dashed lines (synthetic reformate) overlap with the dotted line (room temperature) in figure 18.

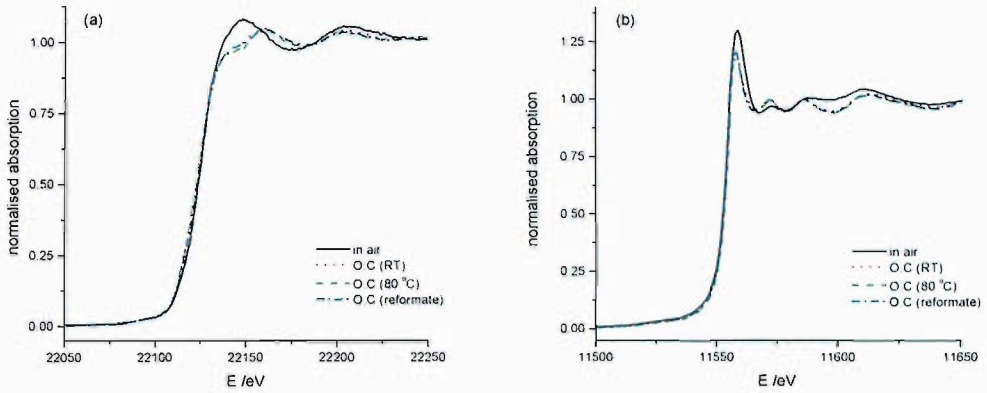

Figure 18 **XANES spectra at (a) Ru K edge and (b) Pt $_{LIII}$ edge for the PtRu MEA as a function of the anode fuel composition. As prepared MEA in air (solid), 5 % H_2 / N_2 at 25 °C (dots) and 80 °C (dashes), and 100 ppm CO in 5 % H_2 / N_2 (dot-dash).**

3.4.2 EXAFS

A more detailed analysis of the effects of cell temperature, anode fuel composition and anode polarisation on the structure of the PtRu/C catalyst particles is provided by analysing the EXAFS region of the spectra obtained at both the Ru K and Pt L_{III} edges. The following sections describe the findings at room temperature and subsequently at 80 °C under humidified conditions.

3.4.2.1 Room temperature

As in the XANES analysis, the as prepared MEA in air was used as a reference point. The *k* weighted EXAFS data with the corresponding Fourier transform obtained at the Ru K edge and k^2 weighted EXAFS data and Fourier transform obtained at the Pt L_{III} edge are shown in figures 19 (a, b) and (c, d), respectively.

The solid lines represent the raw data and the dots represent the fit. The parameters obtained by fitting the data at the Ru K and Pt L_{III} edges are shown in tables 8 and 9, respectively. The EXAFS spectra at both edges decay rapidly indicating the presence of low Z neighbours in the first coordination shell [43], with the amplitude decreasing to the noise level of the data at $k = 9$ Å^{-1} and $k = 10.5$ Å^{-1} at the Ru K and Pt L_{III} edges, respectively. Similarly, the peaks in the Fourier transforms at $r < 2.0$ Å, provide evidence of bonds which can not be accounted for by the inclusion of only metal-metal interactions. The fits required 1.1 and 1.5 O neighbours at approximately 2 Å in the first coordination shell at the Ru K and Pt L_{III} edges, respectively, in addition to Pt and Ru neighbours. Thus, the EXAFS analysis at both edges is in good agreement with the XANES and indicates that the PtRu bimetallic particles are oxidised in the as prepared MEA.

XAS data at the Ru K and Pt L_{III} edges were collected at room temperature and open circuit, using the PEM mini-cell without the MSA humidifiers, and 5 % H_2/N_2 fed to both the anode and cathode sides of the cell. The measured open circuit potential was 0.0 V. The k^2 weighted EXAFS data and corresponding Fourier transforms are shown in figure 20 and the fit parameters are summarised in tables 8 and 9 for the Ru K and Pt L_{III} edges, respectively. In agreement with the XANES results described above, the effect of exposing the anode catalyst to the hydrogen containing fuel is to decrease the relative contributions of low Z neighbours, i.e. O, to the EXAFS at both edges, and to increase the contributions of high Z neighbours, i.e. Pt and/or Ru, as evidenced by the increase in the amplitude of the EXAFS at higher k. At the Pt L_{III} edge the reduction in the number of O neighbours is complete, from 1.1 to 0. This is accompanied by an increase in the total number of metal neighbours in the first shell, $N_{Pt} + N_{Ru}$, from 4.2 to 6.7, indicating that the average first shell coordination environment of the Pt atoms may be described by only metal neighbours. In contrast, the reduction in the O coordination number at the Ru K edge was smaller; a decrease from 1.5 to 0.7 was observed, which was also accompanied by an increase in the number of metal neighbours in the first coordination shell.

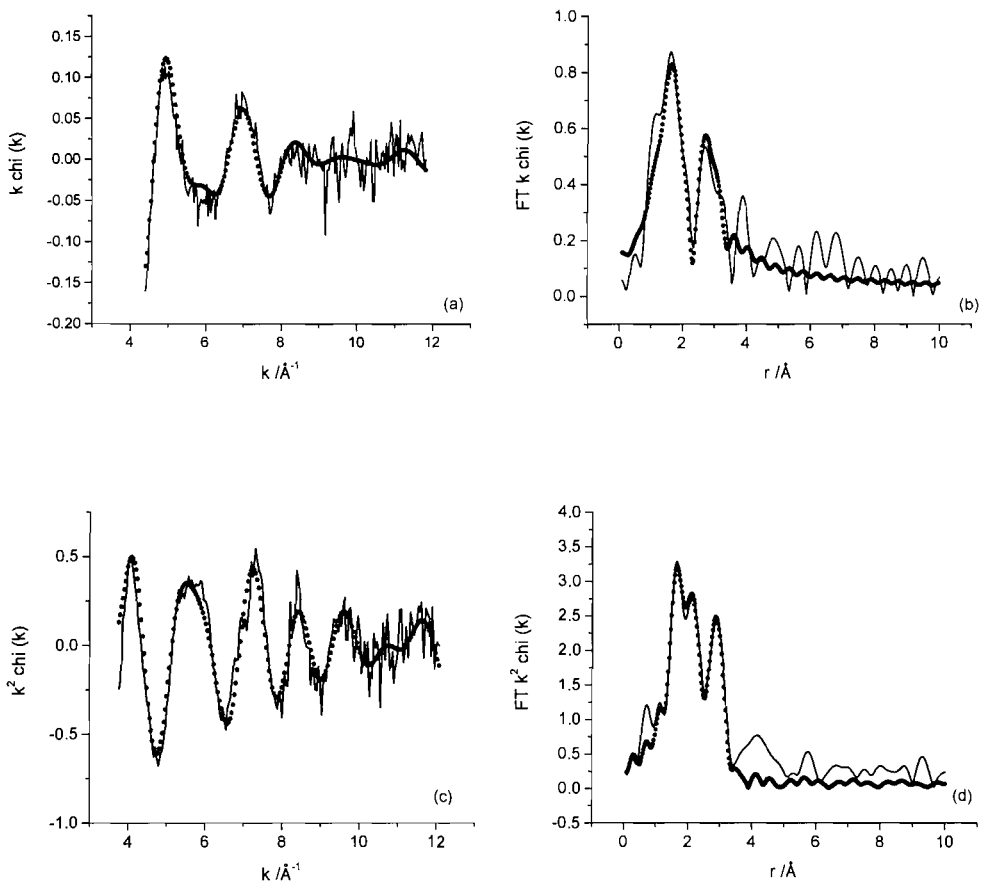

Figure 19 **EXAFS for a 40 wt. % Pt / 20 wt. % Ru catalyst MEA in air at (a and b) the Ru K edge, (c and d) the Pt L_{III} edge. (a) *k* weighted and (c) k^2 weighted experimental data (solid line) and fit (dots). (b and d), the corresponding Fourier transforms, phase corrected for backscattering from Ru.**

The EXAFS results at the Ru K edge indicate that the PtRu bimetallic particles are not fully reduced under these conditions, with the residual oxide being associated with the Ru component of particles. The results presented here may be compared with the analysis of the EXAFS data collected for a similar 1:1 PtRu/C catalyst under gas-treatment [44] and flooded half-cell conditions [45]. The gas treatment conditions consisted of preparing a self-supporting pellet of the PtRu/C catalyst with BN as a diluent, and exposure of the catalyst pellet to pure H_2 gas at room temperature. Analysis of the EXAFS data at the Pt L_{III} edge showed no evidence of O neighbours, whilst O neighbours were retained at the Ru K edge. Thus, while the

chemical reduction of the Pt component of the catalyst at room temperature by H_2 is relatively facile, reduction of the Ru component is not. In contrast, at 0.05 V vs. RHE in 1 mol dm^{-3} H_2SO_4, no remaining O neighbours were observed at either the Ru K or Pt L_{III} edges, indicating full reduction of the particles under flooded half-cell conditions, at a similar potential to that present in the PEM mini-cell results reported above.

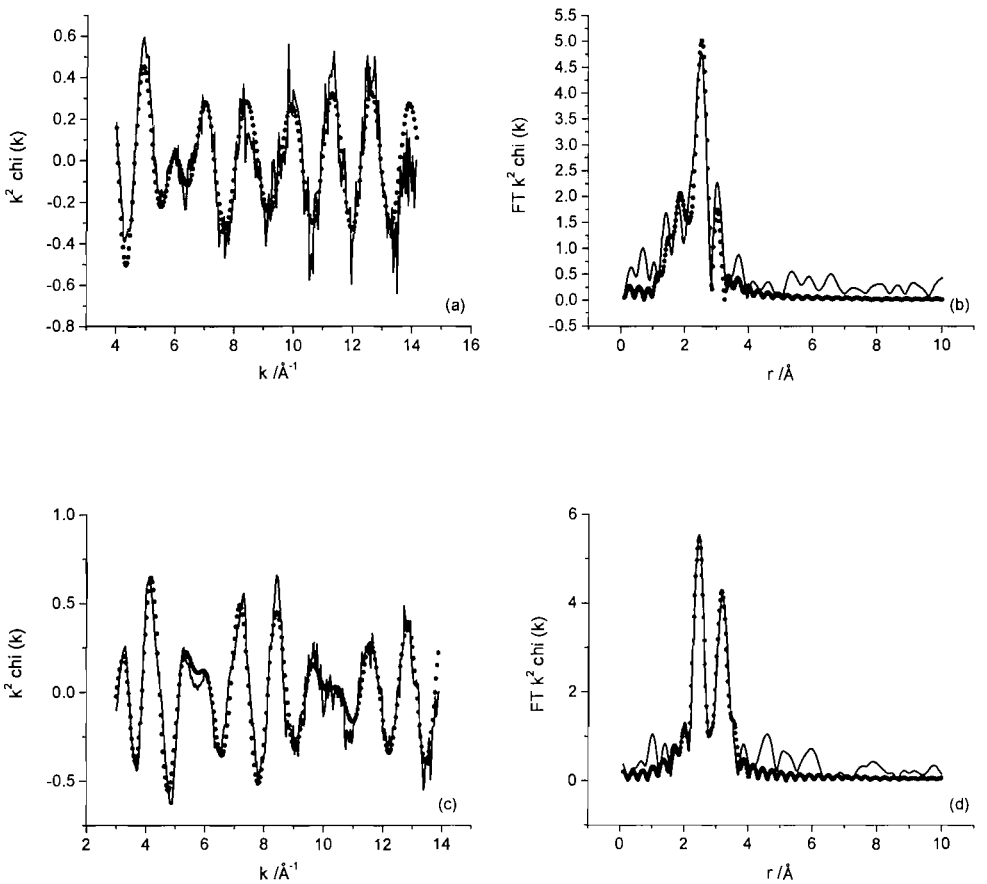

Figure 20 **(a and c) k^2 weighted experimental data at open circuit (solid line) and fit (dots). (b and d), the corresponding Fourier transforms (solid line) and fit (dots) phase corrected for backscattering from Ru. (a and b) Ru K edge, (c and d) Pt L_{III} edge. Anode: 40 wt. % Pt / 20 wt. % Ru, 0.8 mg Pt cm^{-2}. Cathode: 20 wt. % Pd, 0.25 mg Pd cm^{-2}. Cell operating at 25 °C with 5 % hydrogen / nitrogen.**

This comparison raises the concern that the retention of Ru-O neighbours may be attributed to a lack of electrochemical contact to the PtRu particles in the room temperature PEM mini-cell, which may be caused by slow dehydration of the catalyst layer under the operating conditions of this cell.

Table 8 **Structural parameters for the 40 wt. % Pt / 20 wt. % Ru anode catalyst as a function of the composition of the gas fed to the anode and cell temperature obtained by fitting the Ru K edge EXAFS data.**

PEM cell conditions	Absorber - Neighbour	N	R / Å	$2\sigma^2$ / Å^2	E_f / eV	R_{exafs} / %
MEA in air	Ru-Ru	1.2 (±0.2)	2.66 (±0.01)	0.011	-6.4 (±1.2)	45.8
	Ru-Pt	1.9 (±0.3)	2.70 (±0.01)	0.013		
	Ru-O	1.5 (±0.1)	2.01 (±0.01)	0.008		
Open circuit 5% H_2 / N_2 (25 °C)	Ru-Ru	2.1 (±0.2)	2.65 (±0.006)	0.010	-7.5 (±1.1)	46.1
	Ru-Pt	2.5 (±0.3)	2.70 (±0.009)	0.013		
	Ru-O	0.7 (±0.3)	2.09 (±0.03)	0.021		
Open circuit 5% H_2 / N_2 (80 °C)	Ru-Ru	3.1 (±0.2)	2.65 (±0.006)	0.012	-2.2 (±0.6)	40.0
	Ru-Pt	3.1 (±0.3)	2.69 (±0.009)	0.013		
	Ru-O	0	-	-		
Open circuit 100 ppm CO in 5% H_2 / N_2 (80 °C)	Ru-Ru	3.3 (±0.2)	2.66 (±0.005)	0.012	-2.2 (±0.5)	35.5
	Ru-Pt	3.4 (±0.3)	2.70 (±0.007)	0.012		
	Ru-O	0	-	-		

Table 9 **Structural parameters for the 40 wt. % Pt / 20 wt. % Ru anode catalyst as a function of the composition of the gas fed to the anode and cell temperature obtained by fitting the Pt L_{III} edge EXAFS data.**

PEM cell conditions	Absorber - Neighbour	N	R / Å	$2\sigma^2$ / Å^2	E_f / eV	R_{exafs} / %
MEA in air	Pt-Ru	1.3 (±0.2)	2.71 (±0.01)	0.011	-11.6 (±1.2)	39.4
	Pt-Pt	2.9 (±0.3)	2.73 (±0.01)	0.011		
	Pt-O	1.1 (±0.1)	2.01 (±0.01)	0.008		
Open circuit 5% H_2 / N_2 (25 °C)	Pt-Ru	2.0 (±0.2)	2.71 (±0.006)	0.011	-10.0 (±0.6)	35.5
	Pt-Pt	4.7 (±0.2)	2.73 (±0.004)	0.011		
	Pt-O	0	-	-		
Open circuit 5% H_2 / N_2 (80 °C)	Pt-Ru	2.3 (±0.2)	2.71 (±0.007)	0.011	-12.2 (±0.9)	44.7
	Pt-Pt	4.4 (±0.3)	2.73 (±0.007)	0.012		
	Pt-O	0	-	-		
Open circuit 100 ppm CO in 5% H_2 / N_2 (80 °C)	Pt-Ru	2.6 (±0.2)	2.71 (±0.005)	0.009	-12.1 (±0.7)	39.1
	Pt-Pt	4.8 (±0.2)	2.74 (±0.005)	0.010		
	Pt-O	0	-	-		

3.4.2.2 Elevated temperature

The improvements in the cell design described in chapter 3, section 3, enabled XAS data to be collected with humidified gases at elevated temperatures. The k^2 weighted EXAFS data and Fourier transforms for the PtRu/C catalyst at open circuit at 80 °C with humidified 5 % H_2/N_2 fed to both the anode and cathode sides of the cell are shown in figure 21 (a and b) and (c and d) for the Ru K and Pt L_{III} edges, respectively. The parameters obtained by fitting the EXAFS data are shown in tables

8 and 9. For the EXAFS data collected at the Pt L_{III} edge no change was observed in the fit parameters within the error of the fitting upon increasing the cell temperature at open circuit. However, at the Ru K edge changes in the coordination numbers are observed relative to the room temperature case. The number of oxygen neighbours falls to 0 under humidified conditions and an increase in the number of metal neighbours is observed from 4.6 to 6.2, thus indicating that under these conditions the Ru component of the PtRu bimetallic particles is reduced to a more metallic state.

The effect of anode polarisation was investigated by setting the cell potential to 0.05 V and 0.1 V using the humidified cell at 80 °C and feeding 5 % H_2/N_2 to both the anode and cathode sides of the cell. The upper limit was selected by referring to the work of Ralph *et al.* [2] who have reported that the typical anode potential of a PEM fuel cell using H_2 as the fuel is less than 0.1 V vs. RHE. The XAS data were collected at both the Ru K and Pt L_{III} absorption edges. Analysis of the EXAFS data (not shown) yielded fit parameters that did not deviate from those obtained under open circuit reported above.

Finally, the effect of using a synthetic reformate, 100 ppm CO in 5 % H_2/N_2, as the anode fuel was assessed. EXAFS data (not shown) was collected using the humidified PEM mini-cell at 80 °C and under open circuit conditions (0.0 V) with synthetic reformate fuel being fed to the anode and 5 % H_2/N_2 to the cathode. The fit parameters obtained for the EXAFS data collected at the Ru K and Pt L_{III} edge are shown in tables 8 and 9, respectively. No evidence of CO neighbours was found at either absorption edge, with the coordination numbers remaining the same as those obtained when 5 % H_2/N_2 was used as the anode fuel.

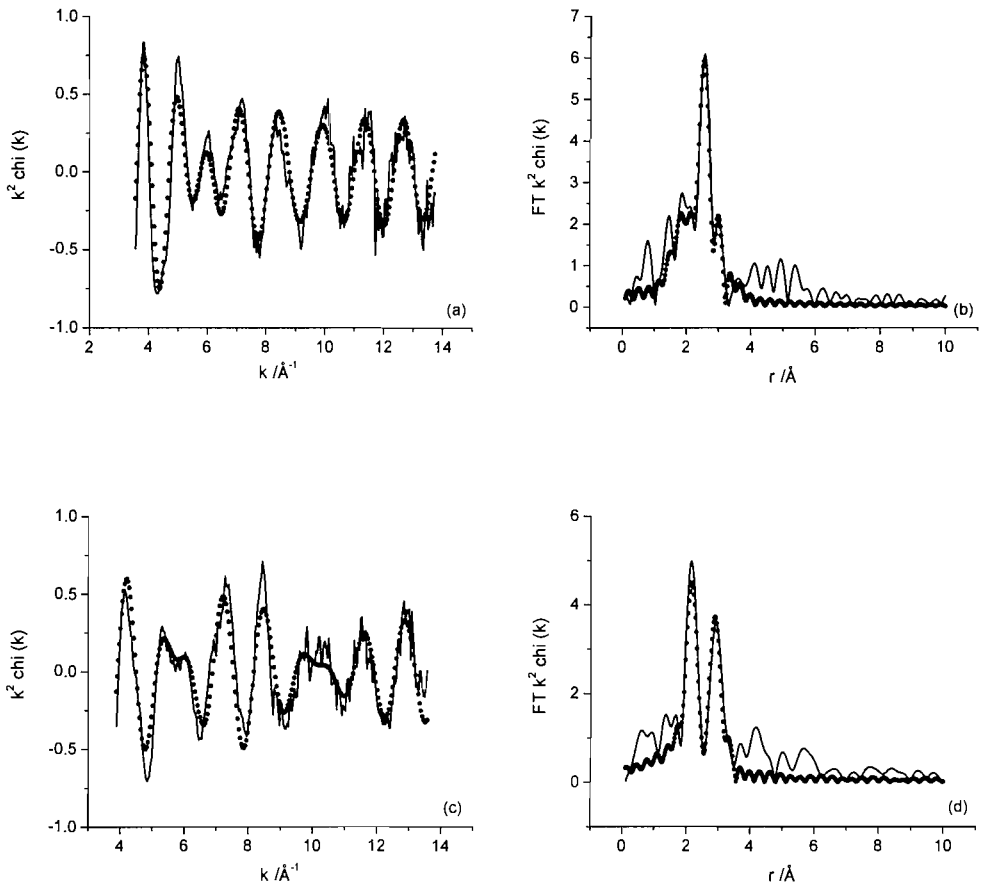

Figure 21 **(a and c) k^2 weighted experimental data at open circuit (solid line) and fit (dots). (b and d) the corresponding Fourier transforms (solid line) and fit (dots) phase corrected for backscattering from Ru. (a and b) Ru K edge, (c and d) Pt L_{III} edge. Anode: 40 wt. % Pt / 20 wt. % Ru, 0.8 mg Pt cm^{-2}. Cathode: 20 wt. % Pd, 0.25 mg Pd cm^{-2}. Cell operating at 80 °C with 5 % hydrogen / nitrogen.**

4 DISCUSSION

The first part of the following discussion will aim to bring together the key findings from the XRD, EXAFS and electrochemical results. XRD and EXAFS will be used to explain the morphology of the particle in terms of segregation of metal atoms within the particle and the possibilities for particle shape will be discussed. The implications of the CO stripping voltammetry and methanol oxidation will then be considered. The second part of the discussion will concentrate on results from the *in situ* mini-cell with the aim of demonstrating the importance of *in situ* studies under realistic environments.

4.1 Particle Structure

The first shell coordination numbers taken from the EXAFS data at both the Pt L_{III} and Ru K edge give the local environment around the central atom. By comparing the ratio of the coordination numbers at the Pt L_{III} and Ru K edges with the atomic ratio the extent of mixing within the particle can be determined (figure 22). For particles with high ruthenium content the ratio of Pt to Ru closely resembles the atomic ratio. As more platinum is introduced to the particle the experimentally determined ratio moves further away from the theoretical case of complete mixing. By the time a platinum rich system is reached, atomic ratio 82.3:17.7, the environment from the ruthenium perspective is Ru rich beyond the error in the measurement. At this point and for the 67.4:32.6 sample, the number of metal neighbours in the first coordination shell in the Pt EXAFS fit is less than that for the Ru EXAFS fit. Together the relative and total first shell coordination numbers indicate that for these compositions, the particle may be described as having a Ru rich core and a Pt rich surface composition compared to the bulk composition.

DFT calculations have been carried out by Christoffersen *et al.* [46] to construct a database of segregation energies of binary transition metal alloys investigating the effect of alloying Pt with other metals. For the PtRu system a positive segregation energy of 0.7 eV was found indicating a situation where the impurity, in this case Ru, prefers to remain in the interior of the host, Pt. Experimentally this situation has

been investigated by Nashner *et al.* [47]. Bimetallic nanoparticles were made with a small size and composition distribution from cluster precursors. Pt atoms in the particle showed a pronounced tendency to self segregate to surface sites. EXAFS results showed preferential Pt-Pt, Ru-Ru bonding at the expense of heterometallic bonding.

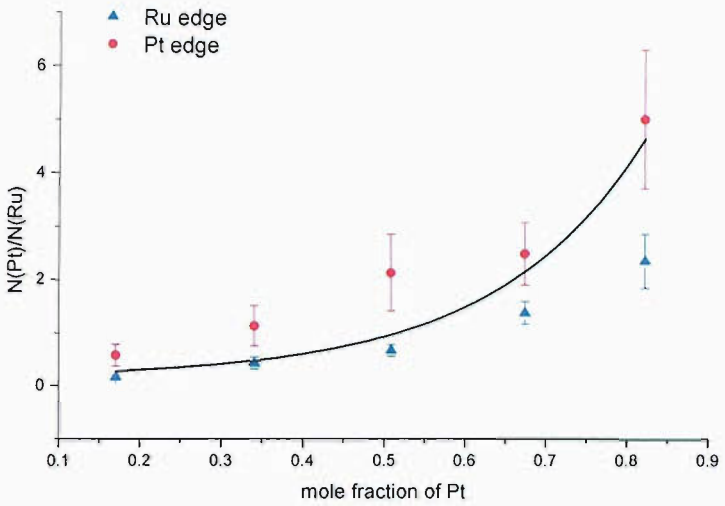

Figure 22 **Ratio of the Pt to Ru first shell coordination numbers as a function of the percentage of platinum atoms in the catalyst for the Pt L_{III} (●), Ru K (▲) edges. The predicted ratio based on an ideal mixture at each composition is shown as a line.**

XRD can provide a limited level of information regarding the segregation of Pt and Ru within the particle. In all but the Ru rich catalyst, diffraction peaks characteristic of an fcc Pt-Ru bulk alloy predominate indicating no pure Ru or Ru rich phase is present [48]. For the 17:83 PtRu catalyst, an hcp phase is found. This transition from fcc to hcp has been studied by Hills *et al.* [20] who found that no clear phase boundary exists for bimetallic nanoparticles. Examples of strongly persistent metastable structures were found that were not present in the bulk alloy case.

Very differing values were obtained using XRD and EXAFS for the particle size. In all cases the size determined by EXAFS was far smaller. As mentioned previously, (section 3.2.3.2) the size was calculated from first shell coordination numbers assuming an icosahedral shape. This geometry was favoured over cuboctahedral as it gives the highest coordination number for particles the same size due to the higher

coordination number of some of the surface atoms, therefore maximising the number of interatomic interactions [39]. However, the systematic difference in size observed when the EXAFS and XRD are compared suggests that this assumption may not be correct. One possibility is that the particles adopt a hemispherical cuboctahedral shape. The same number of atoms arranged in this way would lead to particle sizes approaching that obtained by XRD. For example, the two model particles shown in figure 23 have the same average first shell coordination number of approximately 8 for a 55 atom spherical cuboctahedral and a 92 atom hemispherical cluster. Despite the difference in particle shape and size, it is not possible to distinguish between the two models based on a first shell analysis of the EXAFS data. The more distant shells are far more sensitive to particle shape so a multiple shell analysis is required [18]. However, in the work presented in this chapter the EXAFS data quality prevented analysis over a large k region so higher coordination shells could not be fitted. The decrease in the data quality may be attributed to the interference observed in the backscattering from the Pt and Ru neighbours.

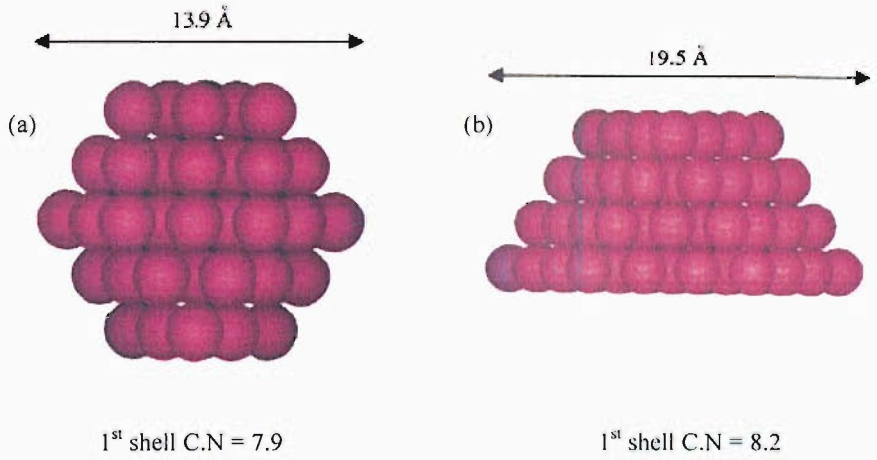

Figure 23 **Model of a (a) 55 atom spherical and (b) 92 atom hemispherical cuboctahedral particle with comparable first shell coordination numbers [18].**

4.2 CO Oxidation on PtRu

A number of studies, both experimental and theoretical have been carried out on the electro-catalytic activities of PtRu. Gasteiger *et al.* [21] made measurements on the electrocatalytic activity of well characterised PtRu alloy electrodes toward the electro-oxidation of CO. Sputtered electrodes were used where the surface

composition reflects the bulk arrangement of atoms in the alloy. The surface compositions were determined using Low Energy Ion Scattering (LEIS). CO stripping voltammetry was presented for a range of surface compositions from a Ru surface concentration of ~7 atom % to complete Ru coverage. When compared with results obtained in this study a strong correlation is observed in terms of both peak position and shape. This finding is of importance because it suggests that the surface composition of the nanoparticles resembles that found in the polycrystalline alloys. Annealed PtRu electrodes where equilibration of the surface concentration has taken place showed a marked difference in electrochemical characteristics suggesting cluster formation at the surface. The peak shape of the sputtered electrodes were explained in terms of the diffusional path length for the surface migration of CO bound to Pt atoms in order to reach oxygen containing species adsorbed on Ru atoms.

Koper *et al.* [33] used dynamic Monte Carlo simulations to reproduce qualitatively the stripping experiments by Gasteiger *et al.* [21]. The reactions taken into account reflect the generally accepted mechanism for the bifunctional model (equations 5 to 6), in which the OH with which CO reacts is preferentially formed on the Ru surface sites:

$$H_2O + *_{Ru} \longleftrightarrow OH_{Ru} + H^+ + e^- \quad \textbf{Eq. 5}$$

$$CO_{Ru} + OH_{Ru} \longleftrightarrow CO_2 + H^+ + 2*_{Ru} + e^- \quad \textbf{Eq. 6}$$

$$CO_{Pt} + OH_{Ru} \longleftrightarrow CO_2 + H^+ + *_{Pt} + *_{Ru} + e^- \quad \textbf{Eq. 7}$$

For the simulations to give good agreement with experimental results, in particular the changes in peak shape, very mobile CO on the PtRu surfaces was required. The bifunctional mechanism was found not to work for completely immobilized CO. A number of studies have also been carried out on Pt(111) surfaces covered with Ru islands. Davies *et al.* [49] observed two stripping peaks in the voltammetry and assigned one to the oxidation of CO from Ru islands and neighbouring sites and the other to Pt(111) sites. This result suggests slow CO mobility between sites. There are two possible explanations for the conflicting results. Either the presence of sulphate ions may reduce the CO mobility in Davies experiments or the second peak may be associated with spill-over and diffusion of the oxidant produced at Ru sites

to Pt(111) sites rather than a mobile CO species. Support for this explanation comes from work by Desai *et al.* [50] who carried out *ab initio* DFT calculations to examine the effects of an aqueous environment on the dissociation of water over a PtRu alloy. The simulations showed that water dissociates over Ru and that the hydroxyl intermediate that first forms over Ru rapidly diffuses along the metal surface, migrating over Pt as well as Ru sites.

The results obtained in this study confirm that the electro-oxidation of CO is dependent on mobile species at the surface of the catalyst particle. However, whether CO or the oxidant is the mobile species cannot be determined from this study. Assuming that CO mobility is low in the presence of sulphate ions, as shown by Davies *et al.* [49], the CO stripping peak position and shape can be explained. On pure Pt, a relatively sharp CO stripping peak is observed at very positive potentials, 0.82 V vs. RHE. This can be related to the difficulty with which OH is formed on Pt. When a small amount of Ru is added to the catalyst (54/6 PtRu), a very broad CO peak is observed at less positive potentials relative to platinum, 0.61 V vs. RHE. The adsorption of oxygen species on Ru commences at potentials as low as ~0.2 V vs. RHE compared with ~0.7 V vs. RHE for Pt [21] and explains the observed peak shift for the 54/6 PtRu. The broad CO peak reflects the long diffusional path length between oxygen species adsorbed on Ru atoms and CO bound to Pt atoms. The lowest peak position is observed for the 40/20 PtRu catalyst indicating that the number of Pt and Ru neighbouring sites has been maximised. This is supported by the sharp peak shape which suggests short diffusional path lengths. As the Ru content is increased further, the CO peak shifts to more positive potentials. This reflects the slower electro-oxidation rate of CO adsorbed on Ru compared with Pt [33]. This is demonstrated by the broad CO peak observed for pure Ru in contrast to the sharp peak for pure Pt.

4.3 Methanol Oxidation on PtRu

The results for the specific activities (section 3.1.2, figures 3 and 5) indicate an optimum composition of 40/20 beyond which the performance levels out with increasing Ru content. This is particularly apparent at 80 °C but also to a certain degree at the lower temperature of 30 °C. Examples from the literature [15,16]

suggest that high ruthenium content catalysts are poor at room temperature due to the high surface coverage of OH_{ads} limiting the number of sites available for dissociative adsorption of methanol. At increased temperatures the effectiveness of the high ruthenium content catalysts can be explained due to the reduction in the adsorption strength of OH_{ads} and that methanol oxidation is no longer solely taking place on the platinum. This can also explain the changes in activity with temperature for Pt relative to PtRu. A 130 mV kinetic performance increase is observed at 30 °C whereas a 170 mV is observed at 80 °C. In the case of Pt the adsorption and subsequent oxidation occurs by the same process independent of temperature. The improved performance is most likely to be related to the enhancement in the nucleation of OH_{ads} [51]. For PtRu the more significant enhancement observed with increasing temperature is related to the availability of Ru sites for methanol oxidation as OH_{ads} coverage decreases. Methanol oxidation is no longer limited to Pt ensembles.

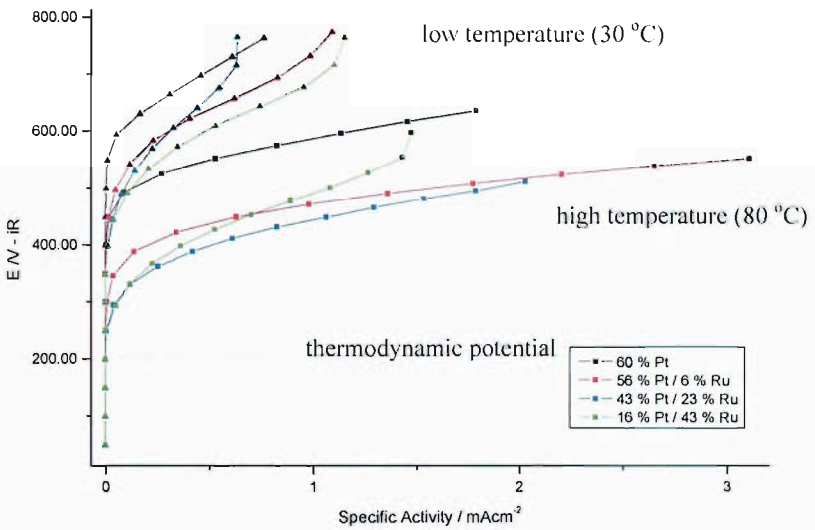

Figure 24 Comparison of specific activities for a range of catalysts at high and low temperatures in 2 M MeOH / 1 M H_2SO_4 at 30 °C

A comparison of the specific activities at 30 °C and 80 °C for a range of catalysts including Pt and 56/6, 43/23, 16/43 PtRu is shown in figure 24. The onset potential for all catalysts shifts in a negative direction with increasing temperature. This is thought to relate directly to the difference in potentials for the formation of Ru-OH at the PtRu electrodes and Pt-OH at the Pt electrodes [52].

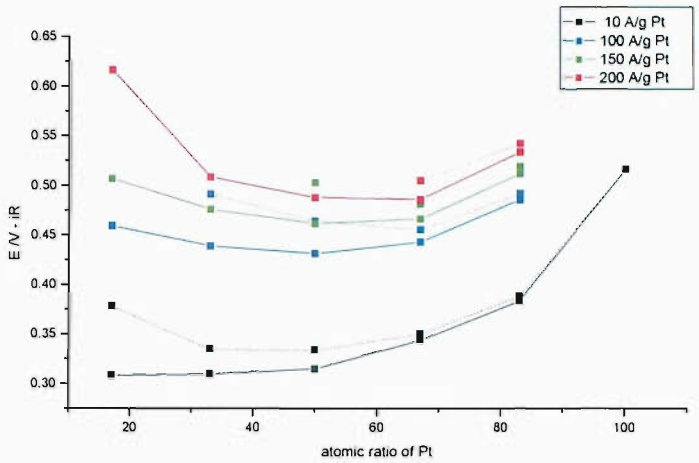

Figure 25 **Mass activity analysis of PtRu series in 2 M MeOH / 1 M H_2SO_4 at 80 °C. Solid lines indicate mass activity in terms of Pt content. Dotted lines are for the total metal content (Pt + Ru).**

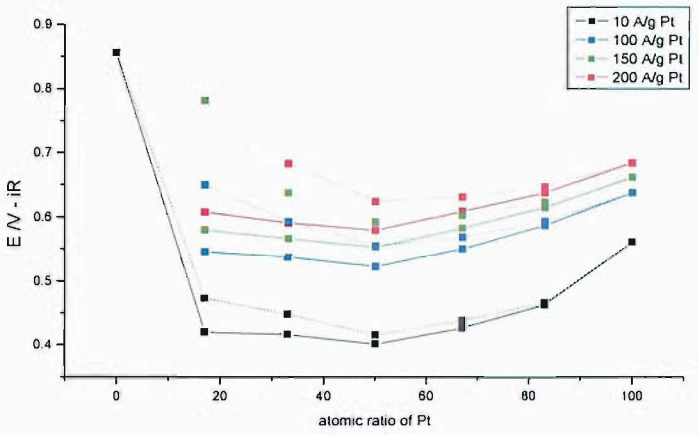

Figure 26 **Mass activity analysis of PtRu series in 2 M MeOH / 1 M H_2SO_4 at 30 °C. Solid lines indicate mass activity in terms of Pt content. Dotted lines are for the total metal content (Pt + Ru).**

The potentials at set mass activities were taken from figures 4 and 6 (section 3.1.2) and plotted against the atomic ratio of Pt in figures 25 and 26 for the high and low temperatures, respectively. Similar trends are found at both temperatures. In both cases an optimum performance is reached with a PtRu atomic ratio of approximately 50:50 although it is less clear cut at higher temperatures.

This does not agree with the finding of Gasteiger *et al.* [16]. They observed variation in the optimum composition with temperature and found that the optimum Ru

content shifted from close to ~10 atomic percent at 25 °C to a value of ~30 atomic percent at 60 °C. However, Gasteiger *et al.* carried out their experiments on circular, smooth bulk alloy surfaces with a diameter of 6.35 mm whereas high surface area nanoparticle catalysts were used for these studies. Particle size effects and metal-support interactions both absent for smooth surface electrodes may contribute to the differences observed. Another reason that makes the two sets of results difficult to compare is that the bulk composition of the nanoparticle catalysts does not necessarily reflect the surface composition. As discussed previously, surface segregation in PtRu nanoparticles has been observed experimentally by a number of groups [53] using EXAFS. Theoretical work by Norskov *et al.* on surface segregation energies [54] and adsorption induced segregation [55] confirm that there is a driving force for an uneven distribution of Pt and Ru within the nanoparticle.

4.4 Comparison of Electrochemical and EXAFS Results

The close agreement between the CO oxidation results and those obtained by Gasteiger *et al.* [21] suggest that the properties of the surfaces are very similar. This allows for a better understanding of the surface composition of the nanoparticle catalysts i.e. the bulk composition resembles the surface. However, this does not agree with the EXAFS (figure 22) which show that surface and bulk compositions may not be the same for the platinum rich nanoparticles (67.4:32.6 and 82.3:17.7 catalysts). One possible reason is that the deviation of the surface composition from the atomic ratio may be too small to be observed electrochemically.

A second possible reason is that the presence of an adsorbate can change the surface composition of an alloy significantly. Monte Carlo simulations carried out by Norksov *et al.* [46,55] found that in the presence of CO some segregation of Ru to the surface takes place with all Ru sites at the surface covered by CO. This means that CO is not probing the true unperturbed surface structure.

A number of groups have used XRD to gauge the degree of particle segregation [14]. Gurau *et al.* [56] compared lattice parameters of arc-melted PtRu alloys and as prepared unsupported nanoparticle catalysts. They found that for the arc-melted alloys, the lattice parameter decreases smoothly with decreasing Pt content.

However, for the high surface area, nanoparticle catalysts, the lattice parameters for the fcc phase in the catalysts are found at values larger than the corresponding arc-melted alloy. This was explained in terms of Pt enrichment of the fcc phase relative to the overall composition of the catalyst. The same analysis was carried out on the PtRu series of catalysts. Figure 27 shows the comparison of lattice parameters for arc-welded PtRu alloys reported by Gasteiger *et al.* [11] and values obtained from XRD and EXAFS (2nd shell) of the PtRu catalysts. The XRD lattice parameters were found to be smaller than the arc-melted case except for the 100 and 17 at. % Pt cases. The contraction in Pt-Pt distance suggests that the particles are well alloyed with very little Pt enrichment of the fcc phase. However, the results must be interpreted cautiously as XRD only detects the crystalline fraction of the catalyst. Lattice parameters determined from the 2nd shell fit of the EXAFS data have also been included to overcome this problem. However, as mentioned in section 3.2.3.2, the effects of the interference between the backscattering from the Pt and Ru neighbours cancel out contributions at this distance in the EXAFS data. This resulted in large errors and no data points for the 40/20, 30/30 and 17/43 catalysts.

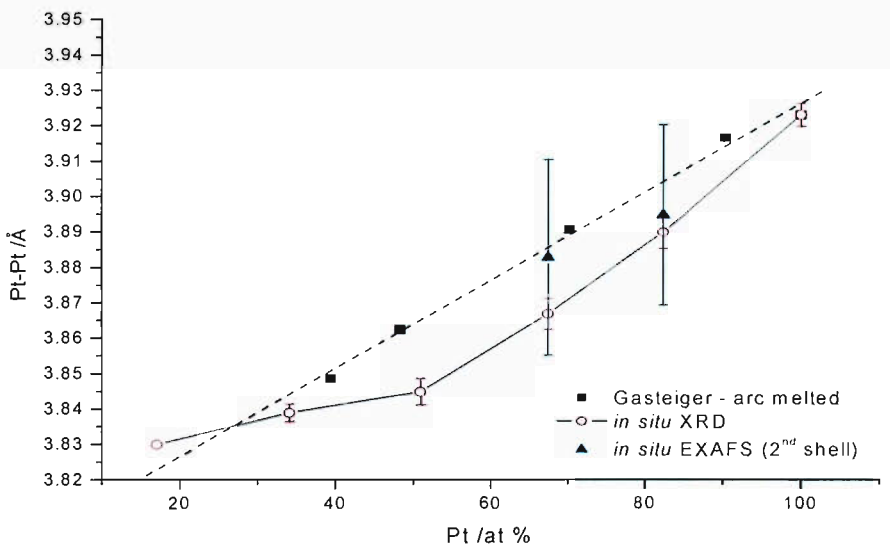

Figure 27 **Comparison of lattice parameters for arc-welded PtRu alloys [11] (dotted line indicates linear fit) and values obtained from XRD and EXAFS (2nd shell) for the PtRu high surface area catalysts.**

The trend observed in figure 27 is the reverse of the findings by Gurau *et al.* [56]. A possibly explanation is that Gurau *et al.* used unsupported catalysts whereas the

catalysts used here are all carbon supported. Another possible explanation is that the particle size is having an effect on the degree of contraction. As mentioned previously (section 3.2.2), the particle size and lattice contraction follow the same trend.

4.5 Optimal Composition for Performance

The optimal composition of the catalyst for various performance criteria can be examined by the construction of so called volcano plots [57]. The variation in the CO peak position with Ru content has been shown to have a minimum value for the 40/20 PtRu catalyst or 50 Pt at. %. This is plotted in figure 28 (a) along with the change in Pt d-band vacancy which increases linearly with increasing Ru content. This result shows that the CO tolerance of PtRu is not simply an electronic effect. If this were the case, no minimum would be observed in the CO peak position with increasing Ru content.

Volcano plots can also be used to correlate electrocatalytic ability with geometric or electronic properties. A volcano plot based on the Pt d-orbital vacancies and Pt-Pt distance as a function of the CO peak position is shown in figure 28 (b). The Pt-Pt distance and Pt d-orbital vacancy found to give the optimum performance is 3.85 Å and 0.325, respectively. The strength of the Pt-CO bond has been shown to decrease as the Pt electron density is reduced [58-60]. However, weakening of the Pt-CO bond is not the only mechanism taking place resulting in improved CO tolerance. The adsorption of the oxygen containing species, OH, must also play an important role. Figure 28 (b) provides no information on the electronic properties of the Ru component of the catalyst. Hammer *et al.* [59] have shown using DFT calculations that as the Pt d-orbital vacancy increases an electron flow from Pt to Ru occurs resulting in reduced d-orbital vacancy and enhanced bonding to the Ru sites. These sites with a high affinity for CO are also found to have a high OH binding energy. Accordingly, sites that show a weaker CO binding energy are found to bind OH weakly, for example, Pt sites [61]. For an effective CO tolerant catalyst, a balance is required of both Pt and Ru sites at the surface to give a volcano type response.

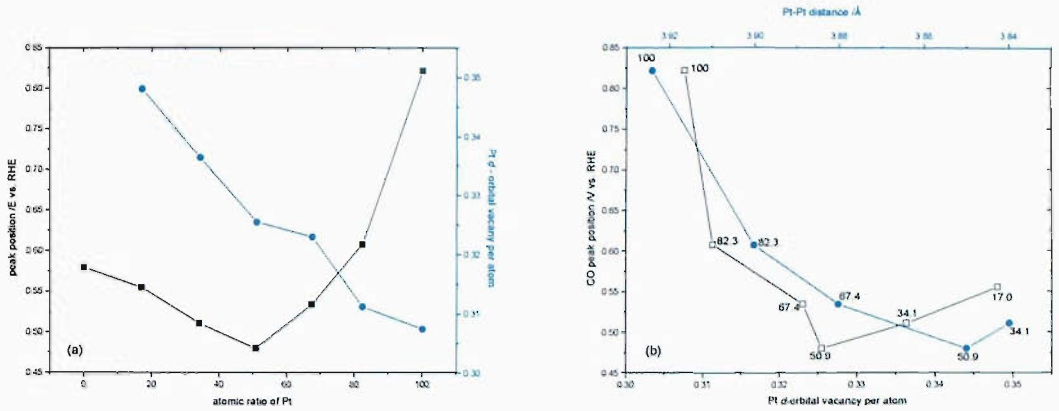

Figure 28 **(a) Variation in CO peak position and Pt d-orbital vacancy as a function of the Pt atomic ratio. (b) A volcano plot for CO peak position versus measured physical properties. □ d-orbital vacancy and ● Pt-Pt bond distance. Symbol labels correspond to the atomic ratio of Pt.**

A similar volcano plot analysis can be used for the methanol data. In figure 29 the potential for a mass activity of 100 A g^{-1} Pt has been plotted versus the d-orbital vacancy and the Pt-Pt bond distance where (a) corresponds to the activity at 30 °C and (b) 80 °C. Very similar trends are observed at both temperatures with the same d-orbital vacancy and Pt-Pt distance giving the optimum performance. This suggests that similar mechanisms are involved in both cases.

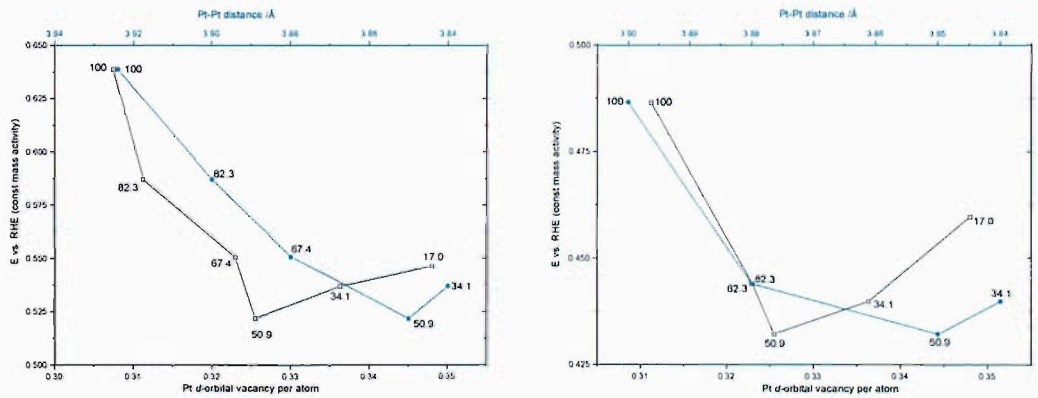

Figure 29 **Volcano plot showing methanol oxidation performance at 100 A g^{-1} Pt as a function of □ d-orbital vacancy and ● Pt-Pt bond distance. Potential measured at (a) 30 °C and (b) 80 °C) in 2 M MeOH / 1 M H_2SO_4. Symbol labels correspond to the atomic ratio of Pt.**

Similarities are also found with the volcano plot in figure 28 (b) where CO peak position has been used as a measure of performance. A possible reason for this is that CO oxidation is the rate determining step for methanol oxidation so the same 50.9 at. % Pt catalyst will give the best performance. The result suggests that provided sufficient Pt sites are available for dehydrogenation of the methanol, ensemble effects [11] will not govern the performance of the catalyst and oxidation of CO will be the dominating factor.

4.6 Mini Cell

At increased polarisation, when synthetic reformate is used as the anode fuel, the polarisation curves shown in figure 17 clearly demonstrate that CO was present on the surface blocking sites for hydrogen oxidation resulting in a drop in performance. EXAFS data were collected at both absorption edges at an anode polarisation of 0.5 V vs. RHE, which is a sufficiently high potential that at least some of the adsorbed CO is oxidatively removed from the surface of the PtRu bimetallic particles. The oxidation of adsorbed CO on PtRu catalysts is thought to occur by a bifunctional mechanism (section 4.2), proposed by Watanabe and Motoo [5]; the presence of the Ru in the catalyst particles serves to both decrease the Pt-CO bond strength and to provide a source of adsorbed oxygen containing species at lower potentials. Thus, the Ru atoms at the surface of the bimetallic particles are expected to be oxidised at potentials at which CO oxidation is occurring. However, the fitting parameters obtained for the EXAFS data at both edges did not show any deviation from those obtained at open circuit presented in tables 8 and 9.

The lack of observation of C neighbours under open circuit conditions and O neighbours at an anode potential where CO is oxidised when synthetic reformate was used as the fuel, reflects the limitations in the sensitivity of the EXAFS technique. The parameters obtained by analysing EXAFS provide the average, per atom, coordination environment of the atoms of the absorbing species, in this case Ru and Pt. As such EXAFS does not provide sufficient surface sensitivity to detect submonolayer quantities of adsorbed OH species. The dispersion of the 40 wt. % Pt, 20 wt. % Ru catalyst used in this study is approximately 0.5, based on TEM and XRD measurements of the particle size as well as electrochemical measurements of

the accessible surface area of the catalyst. Thus, a full monolayer of carbon monoxide would provide a maximum of 0.5 C neighbours, assuming linearly bound CO and that surface layer of the catalyst particles only contained the absorber element, i.e. only Pt or Ru, not a mixture. If the surface composition reflected the bulk 1:1 composition of the PtRu catalyst, a maximum of 0.25 C neighbours would be expected, such a value is below the detection limit of the EXAFS analysis method used in this study. Maniguet *et al.* [10] have shown that a monolayer of CO adsorbed on a Pt/C catalyst can be observed in the Pt L_{III} EXAFS by using a difference file technique, in which the dominant Pt-Pt contributions are fitted and then removed from the data, leaving the contributions from the other neighbours which may then be fitted separately. However, the complication introduced by the interference in the backscattering between Pt and Ru neighbours makes such an analysis very difficult for PtRu alloy particles.

The lack of O neighbours in the fitting of the Ru EXAFS data obtained at 0.5 V with reformate as the anode fuel must, therefore, be interpreted under the constraints of the sensitivity limits discussed above. The results do not indicate that the coverage of oxygen containing species at the Ru surface sites zero, thereby calling into question the bifunctional mechanism. Rather, they indicate that (i) the coverage is below that which can be observed using a conventional EXAFS analysis method and (ii) at anode potentials as high as 0.5 V, the catalyst particles do not undergo a significant restructuring to return the state of the catalyst to the initial oxidised condition found for the as prepared MEA.

5 CONCLUSIONS

Detailed studies, both experimental and theoretical, have been carried out previously on well characterised PtRu surfaces. This is the first example where comprehensive structural and electrochemical data have been collected for a series of commercial carbon supported PtRu fuel cell catalysts.

Strong correlation in terms of peak shape and position were observed between CO stripping voltammetry obtained in this study and experimental and theoretical results carried out by Gasteiger *et al.* [21] and Koper *et al.* [33], respectively. The composition of the PtRu catalysts had a considerable effect on performance with the 1:1 catalyst giving the highest CO tolerance. This was attributed to a combination of (i) maximising the pairing of Pt and Ru sites at the surface of the nanoparticle and (ii) the electron withdrawing properties of Ru, reducing the Pt d-band vacancy and weakening the Pt-CO bond.

In terms of methanol activity, the 1:1 catalyst again gave the highest performance at both low and high temperatures. This suggested that similar mechanisms were involved over the temperature range. No evidence of methanol ensemble effects were observed and the rate of CO removal from surface sites was found to be the dominating factor.

EXAFS provided evidence that the surface and bulk compositions may not be the same for the nanoparticles used in this study. This was particularly apparent for catalysts with high Pt content. These particles were described in terms of a Ru rich core and a Pt rich surface composition compared to the bulk composition. The fact that evidence of the segregation was not observed electrochemically was attributed to the small deviations from the theoretical case of complete mixing and that adsorbed CO can cause changes to the surface composition.

In situ XAS experiments were successfully performed at both the Pt L_{III} and Ru K absorption edges using a miniaturised PEM fuel cell operating under varying conditions. While the catalyst particles in the as prepared MEA showed evidence of oxidation, under realistic operating conditions the coordination environment of both the Pt and Ru components of the bimetallic catalyst particles could best be described as metallic in nature. The results obtained reflected the requirement for both good mass transport and electrochemical contact to ensure full utilisation of the catalyst layer under investigation as well as the limitations in sensitivity of EXAFS towards surface species present on the supported nanoparticles.

6 REFERENCES

1. Wiltshire, R. J. K.; King, C. R.; Rose, A.; Wells, P. P.; Hogarth, M. P.; Thompsett, D.; Russell, A. E. *Electrochimica Acta, submitted* **2004**.
2. Ralph, T. R.; Hogarth, M. P. *Platinum Metals Rev.* **2002**, *46*, 117.
3. Papageorgopoulos, D. C.; de Bruijn, F. A. *Journal of the Electrochemical Society* **2002**, *149*, A140.
4. Hoogers, G.; Thompsett, D. *Cattech* **2000**, *3*, 106.
5. Watanabe, M.; Motoo, S. *Journal of Electroanalytical Chemistry* **1975**, *60*, 275.
6. Gasteiger, H. A.; Markovic, N. M.; Ross, P. N. *Journal of Physical Chemistry* **1995**, *99*, 8290.
7. Ianniello, R.; Schmidt, V. M.; Stimming, U.; Stumper, J.; Wallau, A. *Electrochimica Acta* **1994**, *39*, 1863.
8. Rolison, D. R.; Hagans, P. L.; Swider, K. E.; Long, J. W. *Langmuir* **1999**, *15*, 774.
9. O'Grady, W. E.; Hagans, P. L.; Pandya, K. I.; Maricle, D. L. *Langmuir* **2001**, *17*, 3047.
10. Maniguet, S.; Mathew, R. J.; Russell, A. E. *Journal of Physical Chemistry B* **2000**, *104*, 1998.
11. Gasteiger, H. A.; Markovic, N.; Ross, P. N.; Cairns, E. J. *Journal of Physical Chemistry* **1993**, *97*, 12020.
12. Lizcano-Valbuena, W. H.; Paganin, V. A.; Gonzalez, E. R. *Electrochimica Acta* **2002**, *47*, 3715.
13. Dinh, H. N.; Ren, X. M.; Garzon, F. H.; Zelenay, P.; Gottesfeld, S. *Journal of Electroanalytical Chemistry* **2000**, *491*, 222.
14. Ralph, T. R.; Hogarth, M. P. *Platinum Metals Rev.* **2002**, *46*, 146.
15. Dickinson, A. J.; Carrette, L. P. L.; Collins, J. A.; Friedrich, K. A.; Stimming, U. *Journal of Applied Electrochemistry* **2004**, *34*, 975.
16. Gasteiger, H. A.; Markovic, N.; Ross, P. N.; Cairns, E. J. *Journal of the Electrochemical Society* **1994**, *141*, 1795.

17. Waszczuk, P.; Solla-Gullon, J.; Kim, H. S.; Tong, Y. Y.; Montiel, V.; Aldaz, A.; Wieckowski, A. *Journal of Catalysis* **2001**, *203*, 1.
18. Frenkel, A. I.; Hills, C. W.; Nuzzo, R., G. *Journal of Physical Chemistry B* **2001**, *105*, 12689.
19. Christensen, P. A.; Stoltze, P.; Norskov, J. K. *Journal of Physics: Condensed Matter* **1995**, *7*, 1047.
20. Hills, C. W.; Mack, N. H.; Nuzzo, R. G. *Journal of Physical Chemistry B* **2003**, *107*, 2626.
21. Gasteiger, H. A.; Markovic, N.; Ross, P. N.; Cairns, E. J. *Journal of Physical Chemistry* **1994**, *98*, 617.
22. Richard, D.; Couves, J. W.; Thomas, J. M. *Faraday Discussions* **1991**, 109.
23. Yoshitake, H.; Yamazaki, O.; Ota, K. *Journal of the Electrochemical Society* **1994**, *141*, 2516.
24. Allen, P. G.; Conradson, S. D.; Wilson, M. S.; Gottesfeld, S.; Raistrick, I. D.; Valerio, J.; Lovato, M. *Journal of Electroanalytical Chemistry* **1995**, *384*, 99.
25. Lin, S. D.; Hsiao, T. C.; Chang, J. R.; Lin, A. S. *Journal of Physical Chemistry B* **1999**, *103*, 97.
26. Camara, G. A.; Giz, M. J.; Paganin, V. A.; Ticianelli, E. A. *Journal of Electroanalytical Chemistry* **2002**, *537*, 21.
27. McBreen, J.; Ogrady, W. E.; Pandya, K. I.; Hoffman, R. W.; Sayers, D. E. *Langmuir* **1987**, *3*, 428.
28. Herron, M. E.; Doyle, S. E.; Pizzini, S.; Roberts, K. J.; Robinson, J.; Hards, G.; Walsh, F. C. *Journal of Electroanalytical Chemistry* **1992**, *324*, 243.
29. McBreen, J.; Mukerjee, S. *Journal of the Electrochemical Society* **1995**, *142*, 3399.
30. Viswanathan, R.; Hou, G. Y.; Liu, R. X.; Bare, S. R.; Modica, F.; Mickelson, G.; Segre, C. U.; Leyarovska, N.; Smotkin, E. S. *Journal of Physical Chemistry B* **2002**, *106*, 3458.
31. Roth, C.; Martz, N.; Buhrmester, T.; Scherer, J.; Fuess, H. *Physical Chemistry Chemical Physics* **2002**, *4*, 3555.
32. Friedrich, K. A.; Geyzers, K. P.; Linke, U.; Stimming, U.; Stumper, J. *Journal of Electroanalytical Chemistry* **1996**, *402*, 123.

33. Koper, M. T. M.; Lukkien, J. J.; Jansen, A. P. J.; van Santen, R. A. *Journal of Physical Chemistry B* **1999**, *103*, 5522.
34. Montejano-Carrizales, J. M.; Moran-Lopez, J. L. *Nanostructured Materials* **1992**, *1*, 397.
35. Mukerjee, S.; Srinivasan, S.; Soriaga, M. P.; McBreen, J. *Journal of the Electrochemical Society* **1995**, *142*, 1409.
36. Brown, M.; Peierls, R. E.; Stern, E. A. *Physical Review B* **1977**, *15*, 738.
37. Mansour, A. N.; Cook, J. W.; Sayers, D. E. *Journal of Physical Chemistry* **1984**, *88*, 2330.
38. Russell, A. E.; Maniguet, S.; Mathew, R. J.; Yao, J.; Roberts, M. A.; Thompsett, D. *Journal of Power Sources* **2001**, *96*, 226.
39. Benfield, R. E. *Journal of the Chemical Society-Faraday Transactions* **1992**, *88*, 1107.
40. Mukerjee, S.; McBreen, J. *Journal of Electroanalytical Chemistry* **1998**, *448*, 163.
41. Walker, A. P.; Rayment, T.; Lambert, R. M.; Oldman, R. J. *Journal of Catalysis* **1990**, *125*, 67.
42. Yoshida, N.; Ishisaki, T.; Watakabe, A.; Yoshitake, M. *Electrochimica Acta* **1998**, *43*, 3749.
43. Russell, A. E.; Rose, A. *Chemical Reviews* **2004**, *104*, 4613.
44. Rose, A. Structural Effects in Fuel Cell Electrocatalysts. PhD, University of Southampton, 2004.
45. Maniguet, S. EXAFS Studies of Carbon Supported Fuel Cell Electrocatalysts. PhD, University of Southampton, 2002.
46. Christoffersen, E.; Liu, P.; Ruban, A.; Skriver, H. L.; Norskov, J. K. *Journal of Catalysis* **2001**, *199*, 123.
47. Nashner, M. S.; Frenkel, A. I.; Adler, D. L.; Shapley, J. R.; Nuzzo, R. G. *Journal of the American Chemical Society* **1997**, *119*, 7760.
48. Radmilovic, V.; Gasteiger, H. A.; Ross, P. N. *Journal of Catalysis* **1995**, *154*, 98.
49. Davies, J. C.; Hayden, B. E.; Pegg, D. J.; Rendall, M. E. *Surface Science* **2002**, *496*, 110.
50. Desai, S. K.; Neurock, M. *Physical Review B* **2003**, *68*, art. no. 075420.

51. Raicheva, S. N.; Christov, M. V.; Sokolova, E. I. *Electrochimica Acta* **1981**, *26*, 1669.

52. Wakabayashi, N.; Uchida, H.; Watanabe, M. *Electrochemical and Solid State Letters* **2002**, *5*, E62.

53. Nashner, M. S.; Frenkel, A. I.; Somerville, D.; Hills, C. W.; Shapley, J. R.; Nuzzo, R. G. *Journal of the American Chemical Society* **1998**, *120*, 8093.

54. Ruban, A. V.; Skriver, H. L.; Norskov, J. K. *Physical Review B* **1999**, *59*, 15990.

55. Christoffersen, E.; Stoltze, P.; Norskov, J. K. *Surface Science* **2002**, *505*, 200.

56. Gurau, B.; Viswanathan, R.; Liu, R. X.; Lafrenz, T. J.; Ley, K. L.; Smotkin, E. S.; Reddington, E.; Sapienza, A.; Chan, B. C.; Mallouk, T. E.; Sarangapani, S. *Journal of Physical Chemistry B* **1998**, *102*, 9997.

57. Trasatti, S. *Journal of Electroanalytical Chemistry* **1972**, *39*, 163.

58. Rodriguez, J. A. *Surface Science Reports* **1996**, *24*, 225.

59. Hammer, B.; Morikawa, Y.; Norskov, J. K. *Physical Review Letters* **1996**, *76*, 2141.

60. Igarashi, H.; Fujino, T.; Zhu, Y. M.; Uchida, H.; Watanabe, M. *Physical Chemistry Chemical Physics* **2001**, *3*, 306.

61. Koper, M. T. M.; Shubina, T. E.; van Santen, R. A. *Journal of Physical Chemistry B* **2002**, *106*, 686.

Chapter Five: Cathode Catalysts – Pt:Cr, Co, Ti

1 INTRODUCTION

In proton exchange membrane fuel cells (PEMFCs) a major loss of performance occurs at the cathode. Typically, in excess of 300 mV are lost from the thermodynamic potential for the oxygen reduction reaction (ORR) at low current densities compared with only 10 – 20 mV at the anode when operating under pure hydrogen [1]. The mechanism of oxygen reduction in acidic surroundings is assumed to follow one of two reaction paths: direct reduction to water (equation 1) or indirect reduction (equation 2). The indirect pathway involves the formation of hydrogen peroxide which can then be further reduced to water (equation 3) or undergo chemical decomposition (equation 4).

$O_2 + 4H^+ + 4e^- \longrightarrow 2H_2O$ $\quad E^0_{O_2/H_2O} = 1.23\ V$ **Eq. 1**

$O_2 + 2H^+ + 2e^- \longrightarrow H_2O_2$ $\quad E^0_{O_2/H_2O_2} = 0.682\ V$ **Eq. 2**

followed by a further reduction via

$H_2O_2 + 2H^+ + 2e^- \longrightarrow 2H_2O$ $\quad E^0_{H_2O_2/H_2O} = 1.77\ V$ **Eq. 3**

or a chemical decomposition via

$2H_2O_2 \longrightarrow 2H_2O + O_2$ **Eq. 4**

The electrical efficiency of the PEMFC is maximised if the reaction proceeds via the direct four electron pathway. However, a detailed mechanism for this reaction pathway has not yet been resolved. The pathway is dependent on the oxygen adsorption state of the cathode for which three models have been proposed. The first involves molecular edge-wise adsorption without the splitting of the O-O bond (Griffiths model). The second involves end on adsorption through a single bond (Pauling model) while the third, is a bridge model, where the oxygen is adsorbed

across two sites to give two bonds as proposed by Yeager *et al.* [2]. The proposed pathways that result as a consequence of the initial adsorption step are shown in figure 1.

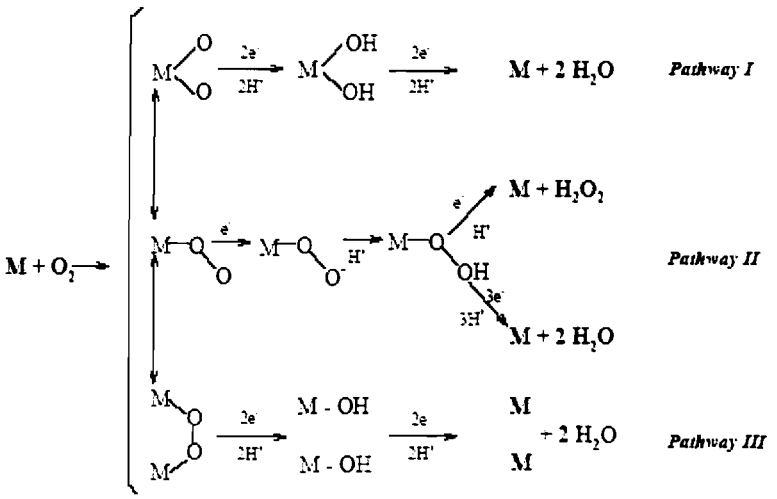

Figure 1 **Reaction pathways resulting from three proposed models for intermediate adsorption states in the ORR [3].**

End on adsorption (Pauling model) avoids the breaking of the O-O bond and pathway II results in the formation of hydrogen peroxide. The subsequent steps in pathway II have been described by Damjanovic *et al.* [4] as the series mechanism with water and peroxide as products. Dissociative chemisorption of oxygen across two adjacent metal sites via a bridging model results in the four electron reduction to water according to pathway III. Pathway I follows a similar route to III, but in this case a single metal site is involved (Griffths model) resulting in the same products.

Unlike the anode, the cathode catalyst is not required to be selective. Any improvements in activity can be broken down into two components, i.e., the number of active sites, and the turnover frequency of each site. Among the noble metals, platinum shows the highest activity in terms of turnover frequency. The reaction proceeds mainly via a four electron pathway and has a comparatively small overpotential [5]. To increase the number of active sites and therefore maximise platinum utilisation, it is generally dispersed as small particles on a conductive support such as high surface area carbon powders. The highest possible dispersion will maximise the number of platinum surface sites for a given platinum content.

However, this does not necessarily give the most active catalyst or highest specific activity (rate per unit area), as shown in studies by Kinoshita [6]. In these studies it was demonstrated that a particle size effect was involved for the ORR. Platinum particles consist of a distribution of surface sites including (111) and (100) crystal faces in addition to corner and edge sites. Kinoshita noted that oxygen reduction is a structure-sensitive reaction and that the distribution of surface sites changes with particle size. For example, edge and corner sites were found to have a less favourable geometric arrangement of surface atoms for the ORR. The specific activity was found to increase with increasing particle size as the ratio of corner and edge site to (111) and (100) crystal faces decreased. The mass activity (rate per unit mass) however, was found to reach a maximum at ~3.5 nm, beyond which it decreased as the ratio of surface to bulk atoms decreased. Markovic *et al.* [7] investigated oxygen activity with varying crystal faces in a number of electrolytes. They found that the electrolyte played an important role in activity. In sulphuric acid, the following order was found (111)<<(100)<(110). These findings, when applied to models of the variation in particle shape with size, fully explained the particle size effect.

As mentioned previously, ORR suffers from poor kinetics and as a result, the search for improved ORR catalysts has been ongoing for the last twenty years. The research has been centred on the development of catalysts which retain the advantageous properties of platinum such as high stability and relatively low overpotential, while reducing the platinum content and increasing the activity. One of the ways this has been achieved, which was first considered for use in phosphoric acid fuel cells (PAFCs), is to alloy platinum with a second metal. Using PtCoCr and PtCr catalysts, Luczak *et al.* [8,9] claimed an increase of a factor of 1.5 to 2.5 in mass activity relative to pure platinum. However, Beard and Ross [10] demonstrated no significant improvement in activity for a PtCo catalyst and observed a loss of cobalt in the phosphoric acid environment, the rate of which was dependent on the degree of alloying. A similar result was obtained by Glass *et al.* [11] using PtCr alloys. Again no improvement was observed relative to platinum, and high Cr concentrations led to the formation of chromium oxide, passivating the surface to the ORR. More recent studies in phosphoric acid by Min *et al.* [12] using PtCo, PtCr and PtNi all showed higher specific activities than Pt catalysts with the same surface

area. Based on the cathode studies in PAFCs the findings were applied to PEMFCs to see if improvements could be observed. Mukerjee *et al.* [13,14] observed a two to threefold increase in the exchange current densities and the current density at 900 mV when studying PtCr, PtMn, PtFe, PtCo and PtNi alloys.

The above studies have all been carried out using carbon supported catalysts. Toda *et al.* [15] determined activities of Pt alloyed with Ni, Co and Fe formed by sputtering of bulk alloys, and observed current densities 10 to 20 times larger than pure platinum. Other studies on bulk alloy systems by Paulus *et al.* [16] showed that improvements were observed for model bulk alloys such as Pt_3Ni and Pt_3Co.

The variation in activities of platinum alloys highlights the difficulty of comparing catalysts that have been prepared using a wide number of techniques. Comparisons between supported and non-supported catalysts with very different structures introduce a degree of uncertainty. As mentioned above, the activity is dependent on both size and shape so normalising the activity as a function of mass or surface area is not sufficient [17].

XAS has played an important role in understanding the observed enhancement for the ORR using platinum alloys. Using XAS a number of possible factors that contribute to the improved activity have been established. These include:

(i) Changes in the electronic structure of the catalyst. The XANES region of the XAS spectra can be used to identify modifications to the platinum electronic structure. Mukerjee *et al.* [13,14] observed changes in the platinum d-band vacancies for the alloy catalysts which may modify the reactivity of the platinum atoms by changing the adsorption strength of reaction intermediates such as $Pt\text{-}OH_{ads}$.

(ii) Change in the physical structure of the catalyst. EXAFS provides information on both bond distances and coordination numbers. A number of groups have observed contractions in the Pt-Pt distance when an alloying metal is introduced [12-14]. They proposed that the reduced Pt-Pt distance was more favourable for oxygen adsorption. EXAFS can also be used to determine the

distribution of the alloying atoms within the particle [18-20]. There remain some questions on the true extent of mixing of the alloys and the stability of the alloy composition. This may affect the distribution of platinum ensembles at the surface of the particle.

(iii) Adsorption of oxygen containing species from the electrolyte onto the platinum or alloying element. The formation of platinum oxides at high cell potentials (equation 5) limits the number of free sites for molecular oxygen adsorption. The presence of the alloying element is thought to play an important role, inhibiting the formation of surface oxides at 0.8 to 0.9 V vs. RHE [21]. *In situ* EXAFS can be used to monitor the surface oxide coverage as a function of potential.

$$Pt + H_2O \longrightarrow Pt\text{-}O + 2H^+ + 2e^- \qquad E^0 = 1.23\ V \qquad \textbf{Eq. 5}$$

(iv) Redox type processes involving the alloying element. Pre-edge features often appear in the XANES region of the secondary element when the alloyed catalyst is analysed from the perspective of the secondary elements. In the case of first row transition metals these are due to transitions from the 1s to 3d orbitals, although the intensity of the peak is dependent on selection rules and symmetry. Changes in the pre-edge feature as well as the intensity of the white line region can be used to determine whether redox behaviour of the secondary element is playing a part in the ORR [14].

Initially, XAS was used as an *ex situ* technique to study cathode catalysts [10,22]. This can provide information on the structure of the as prepared catalyst and the effect of different methods of preparation and heat treatment but is limited in its usefulness when applied to a fuel cell environment. A step towards a more realistic environment was *in situ* analysis using a flooded half-cell environment. This can provide information of the possible mechanism for the ORR in a liquid electrolyte. However, the presence of the electrolyte has been show to play a very important role [7]. For example, in sulphuric acid the highly structure specific adsorption of sulphate anions has a strongly inhibiting effect on a Pt (111) surface. To date, all *in situ* XAS analysis of cathode catalysts have been confined to a flooded half-cell

environment whereas the ideal case would be to study the catalysts in a fuel cell environment under gaseous oxygen.

In this chapter, results from *in situ* XAS investigations carried out using a humidified mini-cell will be presented for a number of cathode catalysts including: PtCr, PtCo and PtTi. Data were also collected in a flooded half-cell environment of 1 M H_2SO_4 for comparison with the mini-cell data to investigate the effect of the electrolyte on particle structure. As mentioned previously, PtCr and PtCo have been studied by a number of groups and have shown improvements over platinum. Only one EXAFS study of PtTi electrocatalysts has been reported by Beard *et al.* [22]. The study concentrated on the *ex situ* characterisation of PtTi after undergoing different heat treatments. EXAFS was only used as a qualitative tool and no fits were made of the data collected. The electrochemical benefits of PtTi for the ORR have been studied by a number of groups [1,23] all of whom have shown an improvement over platinum.

XAS data from both the platinum and secondary metal edge will be used to determine the structure of the catalyst and the extent of mixing in both half-cell and mini-cell environments under varying applied potentials. Information on particle structure, changes in coordination number and the electronic effect of the secondary element will be related to the performance of the catalyst for the ORR.

2 EXPERIMENTAL DETAIL

2.1 Catalysts

Four cathode catalysts supported on either XC72R or Ketjen black carbons were supplied by Johnson Matthey. These included PtCo, PtTi, and a PtCr catalyst which had undergone two different heat treatments at 900 and 1200 °C. The catalyst compositions and corresponding atomic ratios are shown in table 1. 40 and 60 wt. % Pt catalysts were used as reference points in the electrochemical analysis. The particle sizes of the catalysts were determined by XRD and are also shown in table 1.

Table 1 **Pt, PtCr, PtCo and PtTi catalyst compositions and corresponding particle size as determined by XRD.**

Catalyst	Heat Treatment /°C	Carbon Support	Pt wt. %	M wt. %	Atomic Ratio Pt:M	Particle Size /nm
PtCr	900	XC72R	40	3.6	75:25	6.0
PtCr	1200	XC72R	40	10.7	50:50	8.5
PtCo	600	Ketjen	60	6.0	75:25	4.7
PtTi	930	XC72R	20	4.9	50:50	5.0
Pt	-	XC72R	40	0	100:0	4.0
Pt	-	XC72R	60	0	100:0	5.7

2.2 Reference Compounds

A number of reference compounds were used to aid analysis of the Ti K edge XANES region. These included *r*-TiO_2 and a series of TiO_x compounds where x ranges from 1.70 to 1.89. These phases are grouped under the trade name Ebonex and they all contain a different number of oxygen vacancies due to the reduction from TiO_2. The Ebonex phases can also be considered as consisting of different percentages of members of a homologous series with a Ti_nO_{2n-1} structural formula with n an integer between 4 and 10.

2.3 Electrode Preparation

The catalysts were fabricated into electrodes by methods described in chapter 2, section 1.2. Prior to use, the electrodes were placed in boiling water for 20 minutes to ensure that they were fully hydrated.

2.4 MEA Preparation

All cathode catalysts were incorporated into MEAs with either a 20 wt. % Pd or 40 wt. % Pt anode depending on the absorption edge being analysed. The platinum loading at the cathode was approximately 1 mg cm^{-2} while at the anode a metal loading (Pt or Pd) of 0.25 to 0.30 mg cm^{-2} was used. A 30 μm thick Flemion® membrane was used to make the MEA and the procedure has been described in detail in chapter 3, section 2.2.2.

2.5 Electrochemistry

2.5.1 Cyclic voltammetry

CVs were carried out on all cathode catalysts in 2.5 M H_2SO_4. CO electro-oxidation experiments were also performed to determine the catalyst surface area. The methods for both procedures has been described in detail in chapter 2, section 2.2.2.

2.5.2 Half-cell (ORR)

The three electrode cell used to determine oxygen reduction activity in a half-cell environment of 2.5 M H_2SO_4 has been described in chapter 2, section 2.3.2. An oxygen flow rate of 150 cm^3 min^{-1} was used and the electrode was polarised between 0.5 V and 0.96 V vs. RHE. A stabilisation time of 60 seconds was used after which time the current was recorded

2.5.3 Mini-cell (ORR)

In all cases the mini-cell was operated at 80 °C using the membrane substrate assemblies (MSA) to hydrate the gases. The method for obtaining CVs and oxygen polarisation curves has been described in chapter 3, section 2.3.2. The cathode was

polarised between 0.95 V and 0.5 V vs. RHE and the current was recorded after a stabilisation time of 60 seconds.

2.6 XAS

Analysis of the Pt L_{III} edge was carried out on station 16.5 of the synchrotron radiation source (SRS) at Daresbury operating with 50 % harmonic rejection. The following edges were used to determine the environment of the secondary element in the cathode catalysts: Co K (7.709 keV), Cr K (5.989 keV) and Ti K (4.966 keV). These experiments were carried out on station 7.1 which operates in the range 4 keV to 10 keV and consists of a harmonic rejecting, sagittally focussing double crystal Si (111) monochromator. The second crystal was detuned to 80 % to provide harmonic rejection.

2.7 Reference Compounds

A number of Ti based reference compounds were used in the analysis of the XANES data collected for the PtTi catalyst. Pellets were made by mixing the reference compound with boronitride using a pestle and mortar before using a die press to form the pellet. The pellet was mounted in the gas treatment cell (chapter 2, section 3.2.5) and the XAS collected in air.

2.7.1 Half-cell

The XAS data were collected using the *in situ* fluorescence half-cell which has been described previously in chapter 2, section 3.2.6. The electrodes were placed in 1.0 M H_2SO_4 and XAS data were collected at three potentials: 0.0, 1.05 V vs. RHE and open circuit. When the electrode was polarised, the experiment was started once the current had decayed to a constant value (typically after five minutes).

2.7.2 Mini-cell

In situ mini-cell operation was carried out with oxygen flowing over the cathode and 5 % H_2/N_2 at the anode. XAS data were collected in the fluorescence mode at open circuit and 0.7 V vs. RHE.

3 RESULTS

3.1 Cyclic Voltammetry – Half-cell

Figures 2 (a) and (b) show the CVs of two PtCr catalysts heat treated at 900 °C (3:1) and 1200 °C (1:1), PtCo (3:1), PtTi (1:1) along with a 40 and 60 wt. % Pt/C catalyst for comparison. The voltammetry was carried out in 1 M H_2SO_4 with a scan rate of 10 mV s^{-1}. The currents were normalised against the platinum surface area, determined by CO stripping voltammetry (figure 2(a)) and against the platinum loading (figure 2(b)). Table 2 summarises the main electrochemical parameters obtained from the CVs including: peak positions, active Pt surface area (Ptarea) and the mass normalised area ($Ptarea_m$). The onset of oxide formation observed in the forward scan is also included. Murthi *et al.* [21] described the onset as the potential of Pt-OH formation but made no mention as to how to determine its value. In this case, the onset is taken as the value at which the first increase in current is observed after the double layer region in the forward scan. It is difficult to accurately determine and has been included in table 2 only as a guide.

Table 2 **Electrochemical parameters taken from CVs in figures 2 and 3. Ptarea and $Ptarea_m$ has been defined previously in chapter 2, section 2.2.4.**

Catalyst Pt:M	Pt loading mg cm^{-2}	Oxide reduction /V vs. RHE	Oxide onset /V vs. RHE	Ptarea /cm^2 Pt	$Ptarea_m$ /cm^2 Pt g^{-1} Pt
PtCr 3:1	0.796	0.793	0.79	663.9	83.4
PtCr 1:1	0.832	0.809	0.80	143.3	17.2
PtCo 3:1	0.83	0.769	0.81	806.2	97.1
PtTi 1:1	0.6	0.772	0.80	455.0	75.8
--------	--	--	--	--	--
Pt 40%	0.515	0.789	0.79	455.0	88.3
Pt 60%	1.072	0.802	--	466.2	43.5

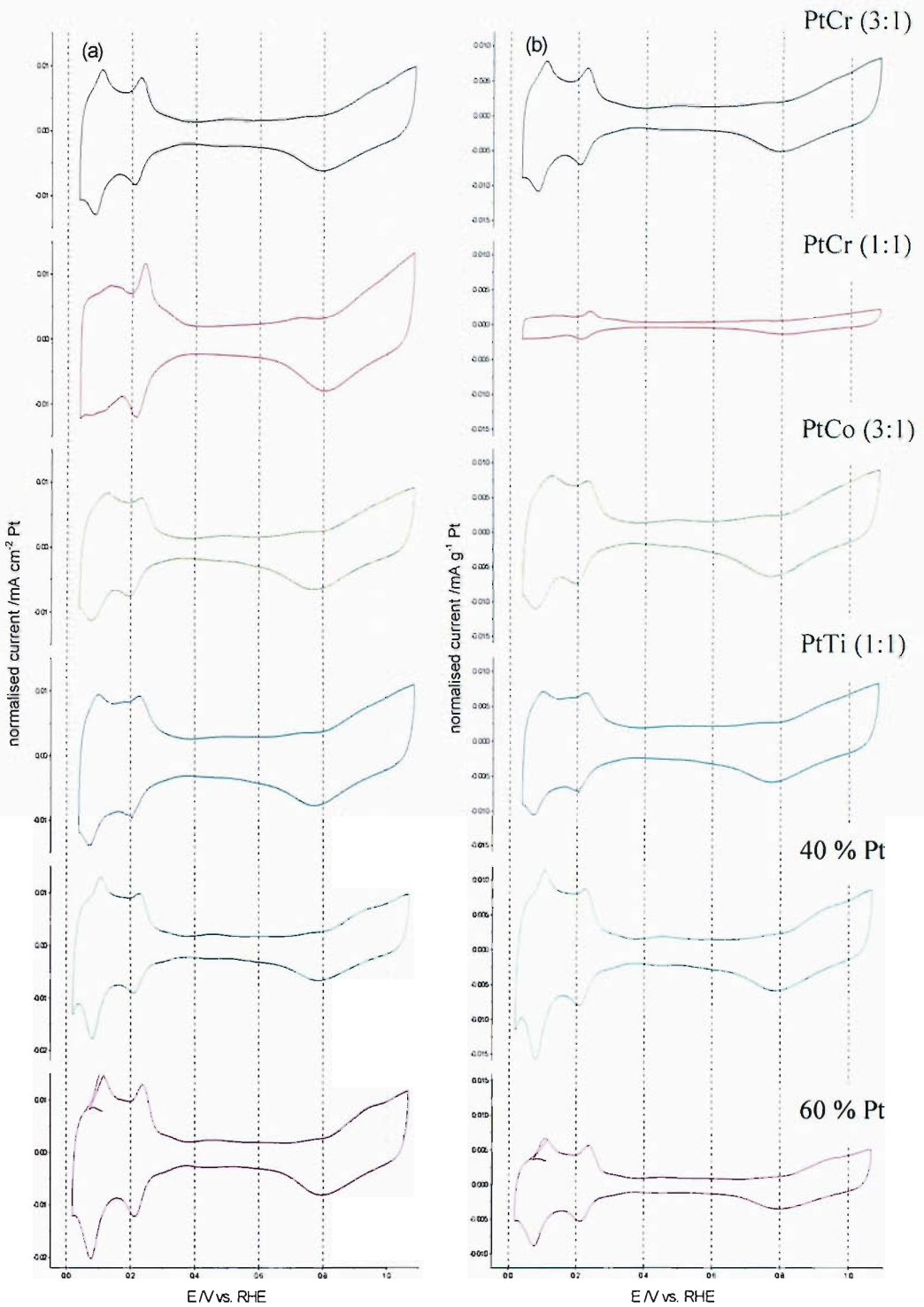

Figure 2 **Cyclic voltammograms for two PtCr catalysts heat treated at 900 °C (3:1) and 1200 °C (1:1), PtCo (3:1), PtTi (1:1) along with a 40 and 60 wt. % Pt/C catalyst for comparison. Carried out in 1 M H_2SO_4 with a scan rate of 10 mV s^{-1}. Currents normalised to (a) the platinum surface area determined by CO stripping voltammetry and (b) the platinum loading.**

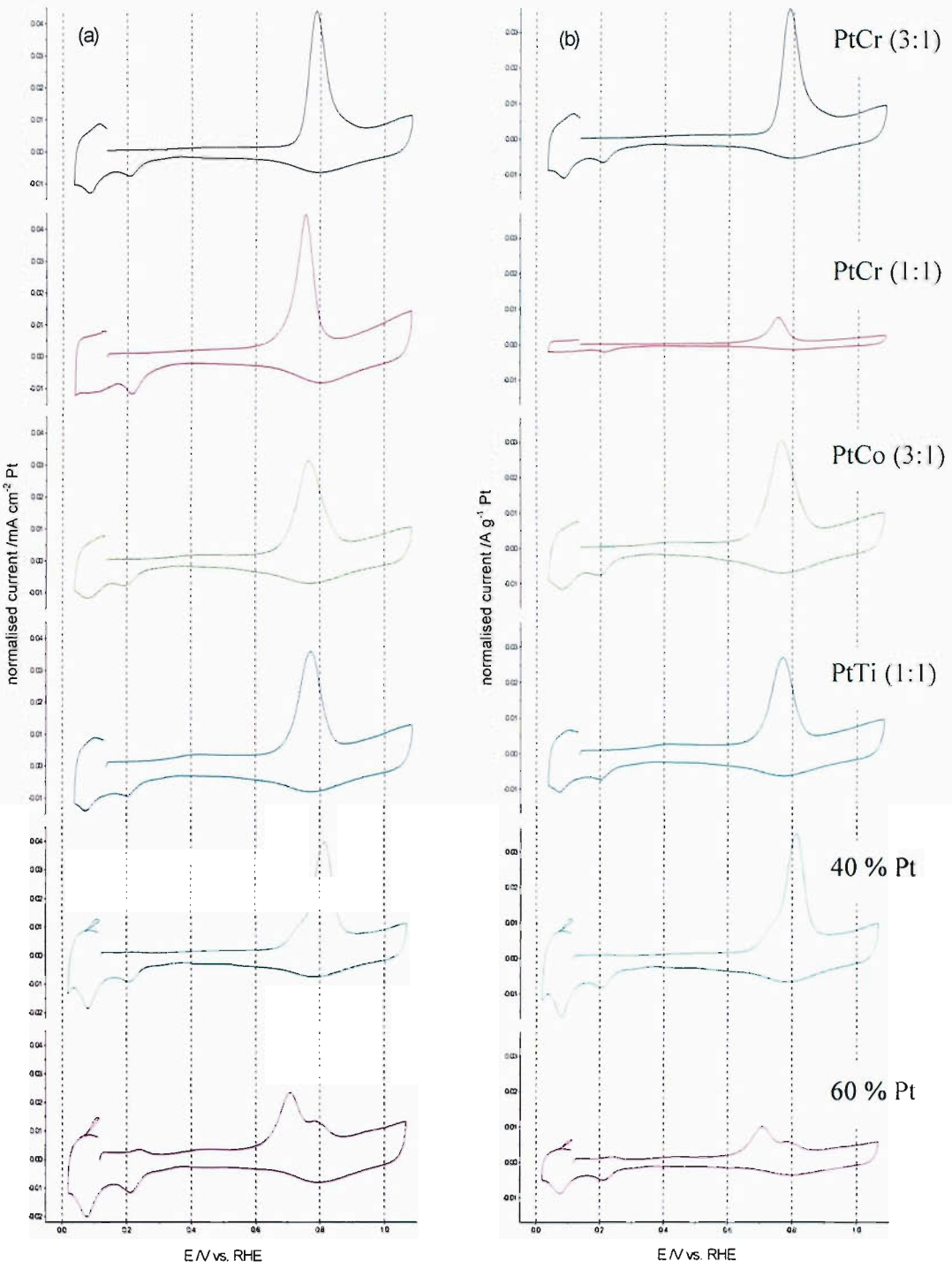

Figure 3 **CO stripping voltammetry for two PtCr catalysts heat treated at 900 °C (3:1) and 1200 °C (1:1), PtCo (3:1), PtTi (1:1) along with a 40 and 60 wt. % Pt/C catalyst for comparison. Carried out in a 1 M H_2SO_4 CO saturated solution with a scan rate of 10 mV s^{-1}. Currents normalised to (a) the platinum surface area determined by CO stripping voltammetry and (b) the platinum loading.**

From the CV of the 40 wt. % Pt/C catalyst, two well defined peaks occur in the hydrogen adsorption/desorption region indicating the presence of polycrystalline Pt. The onset for oxide formation occurs at approximately 0.79 V vs. RHE while the oxide reduction peak occurs at 0.78 V vs. RHE (table 2). More pronounced hydrogen adsorption/desorption features are observed for the 60 wt. % Pt/C catalyst suggesting more extended lattice plane features. This arises due to the larger crystallite size for the 60 wt. % Pt as demonstrated by the smaller currents observed when normalised to the Pt loading. Both the onset for oxide formation and the corresponding oxide reduction peak occur at similar positions to the 40 wt. % Pt/C catalyst.

The PtCr (3:1) catalyst also shows well pronounced hydrogen adsorption/desorption peaks suggesting that the surface closely resembles platinum crystallites. Further evidence comes from comparisons with the Pt/C catalysts in the double layer region where a similar double layer capacitance is observed. Relative to Pt/C, very little shift occurs in the onset of the oxide formation (0.79 V vs. RHE) and the peak potential of oxide reduction (0.81 V vs. RHE). Heat treatment of the PtCr catalyst to 1200 °C (1:1) results in a change in the hydrogen adsorption/desorption features. Only one clearly defined peak remains at 0.24 V vs. RHE (forward scan), 0.21 V vs. RHE (backward scan), with increased intensity relative to the PtCr (3:1) catalyst. This suggests a change in the surface structure of the catalyst. The CV normalised to the Pt loading shows small currents indicating that the heat treatment has resulted in a significant increase in particle size. Reports by Paulus *et al.* [16] have shown that alloy particles contain mainly (111) and (100) facets. A change in particle size alters the ratio of (111) and (100) facets [6] and this may be the cause of the change in the hydrogen adsorption/desorption features.

The CVs for PtCo show less pronounced features in the hydrogen adsorption/desorption region relative to both the 40 and 60 wt. % Pt catalysts. This suggests that the surface is not as well ordered and that the catalyst particles have a higher dispersion. The oxide reduction peak is observed at 0.77 V vs. RHE, a shift to less positive potentials relative to the PtCr and Pt catalysts. This indicates that oxide formation taking place at the surface and bulk in the forward sweep requires a larger driving force, more reducing potentials, before it is removed.

The oxygen reduction peak for the PtTi catalyst occurs at the same potential as PtCo suggesting similar oxygen reduction characteristics. Again, two peaks are observed in the hydrogen adsorption/desorption region for the forward and backward sweep. Comparing the CVs normalised to the CO area (figure 2 (a)) larger currents are observed for PtTi in the double layer region relative to the PtCr, PtCo and Pt. A possible explanation for this is that oxide species such as titanium oxide are present at the surface of the catalyst changing the current response at the double layer when compared to a metal surface.

Figure 3 (a) and (b) show the CO stripping voltammetry for the PtCr (3:1), (1:1), PtCo, PtTi and Pt (40, 60 wt. %) catalysts normalised to the platinum surface area and loading, respectively. The platinum surface area was calculated from the CO peak area. The CO peak position was found to vary depending on particle size and secondary alloying element. The effect of particle size can be seen by comparing the 40 and 60 wt. % Pt catalysts where a peak shift from 0.81 to 0.71 V vs. RHE is observed with increasing particle size. The shoulder in the CO peak for 60 wt. % case suggests that the crystal facets are larger and that the relative contribution of the edge sites is less significant. The CVs for PtCo and PtTi catalysts resemble 40 wt. % Pt in nature as they have similar particle sizes ranging from 4 to 5 nm. The PtCr catalysts have a larger particle size of 6 and 8.5 nm for the (3:1) and (1:1) catalysts, respectively. A narrower CO peak is observed relative to the PtCo and PtTi catalysts which shift to less positive potentials, 0.79 to 0.75 V vs. RHE, with the higher heat treatment of 1200 °C.

3.2 Dispersion

The dispersion can be calculated in a number of ways and is defined as the percentage of surface atoms relative to the total number of atoms in the catalyst. It can be determined experimentally using cyclic voltammetry and theoretically based on models of the catalyst particle structure. A 40 wt. % Pt catalyst has been used as an example for the following calculations.

3.2.1 Experimental calculation

The total number of atoms in the catalyst layer can be determined from the platinum loading. For example, in the above case (section 3.1) the electrode for the 40 wt. % Pt had a loading of 0.52 mg Pt cm^{-2} corresponding to 1.6 x 10^{18} platinum atoms over 1 cm^2. The number of surface atoms can be calculated from the charge transferred when the CO was stripped from the surface i.e. the area under the CO stripping peak which in this case corresponds to 0.182 C over 1 cm^2. Once converted to moles assuming a two electron oxidation, the number of surface atoms can be calculated, 5.7 x 10^{17}, giving a dispersion of 36 %.

3.2.2 Theoretical calculation

To carry out a theoretical calculation of the dispersion, assumptions have to be made about the particle geometry. The cuboctahedral geometry described in chapter 4, section 3.2.3.2, is the shape most commonly associated with platinum alloy particles with sizes ranging from 5 to 8 nm [16,24]. The particle is described by Benfield *et al.* [25] as a series of concentric shells of atoms with the single central atom counted as the first shell. The number of concentric shells, m, can be determined provided both the particle size and Pt-Pt distance is known. The following equations can then be used to obtain the total number of atoms (equation 6) and the number of surface atoms (equation 7) from which the dispersion can be calculated.

$$\text{Total number of atoms} = \frac{1}{3}(2m-1)(5m^2-5m+3) \qquad \textbf{Eq. 6}$$

$$\text{Number of surface atoms} = 10m^2 - 20m + 12 \qquad \textbf{Eq. 7}$$

For example, the 40 wt. % Pt particle has a particle size of 4.0 nm and a Pt-Pt distance of 0.2772 nm. This corresponds to an m value of 7 giving 923 as the total number of atoms, 362 for the number of surface atoms and hence a dispersion of 39 %.

3.2.3 Comparison of calculated values

To confirm the accuracy of the theoretical calculations, the dispersions were calculated experimentally for a series of platinum catalysts with varying particle size (table 3). As expected, the dispersion increases as the wt. % of Pt falls.

Table 3 Comparison of experimentally calculated dispersions for a range of platinum particles with varying wt. %.

wt. % Pt	Pt loading mg cm^{-2}	Q transfer /C cm^{-1}	Number of Pt surface atoms	Total number of Pt atoms	Dispersion /%
10.0	0.09	0.08	2.6×10^{17}	2.7×10^{17}	93
20.0	0.19	0.11	3.3×10^{17}	6.0×10^{17}	56
38.1	0.51	0.18	5.8×10^{17}	1.6×10^{18}	36
50.0	0.77	0.21	6.5×10^{17}	2.4×10^{18}	27
58.5	1.07	0.19	5.9×10^{17}	3.3×10^{18}	18

From XRD measurements of the catalysts, both the particle size and Pt-Pt lattice parameter were calculated. Assuming that the Pt-Pt lattice parameter remained constant at 0.277 nm, the theoretical dispersions were calculated using equations 6 and 7 as shown in table 4. The dispersions from both the experimental (squares) and theoretical (circles) calculations are plotted in figure 4 as a function of the platinum wt. %. With the exception of 10 wt. % Pt catalyst, relatively good agreement is observed between the experimental and theoretical dispersions, considering the assumptions involved. There are a number of possible explanations why discrepancies arise for the 10 wt. % Pt catalyst. The first of these is the assumption that a cuboctahedral structure is present for all particles. As suggested by Benfield *et al.* [25] an icosahedral geometry may dominate in the case of very small particles. The second assumption is that XRD is giving an accurate value for the particle size. Both the 10 and 20 wt. % Pt have similar particle sizes according to XRD however, very different dispersions of 93 % and 53 %, respectively, were calculated from the electrochemical data. XRD is only sensitive to the crystalline fraction of the catalyst and, therefore, atomically dispersed platinum or very small particles will be undetected. The very high experimentally determined dispersion for the 10 wt. % Pt suggests that there are a high percentage of particles smaller than the value of

1.9 nm determined by XRD. This makes modelling the particle and calculating a theoretical dispersion very difficult.

Table 4 **Comparison of theoretically dispersions for a range of platinum particles with varying wt. %. Calculated using equations by Benfield *et al.* [25]**

wt. % Pt	Particle size /nm	Number of complete shells, *m*	Pt atoms at surface, eq. 6	Total Pt atoms, eq 5	Dispersion /%
10.0	1.9	3	42	55	76
20.0	2.1	4	92	147	63
38.1	4.0	7	362	923	39
50.0	4.0	7	362	923	39
58.5	5.7	12	1212	5083	24

For the 20, 38.1, 50 and 58.5 wt. % Pt catalysts, the theoretically calculated dispersions give a higher value than the experimental value. The particles are all supported on carbon which may block a number of surface metal atoms, rendering them inaccessible to gas adsorption [26]. The cuboctahedral structure (chapter 4, section 3.2.3.2, figure 16) has two faces, a square face with a (100) plane consisting of $(m-2)^2$ atoms and a triangular face with a (111) plane and $\frac{1}{2}(m-3)(m-2)$ atoms. Figure 4 shows that removing the atoms in the (100) or (111) plane assumed to be blocked by the carbon support brings the dispersion closer to the experimental value. Removing the (100) plane has a more significant effect, reducing the theoretical dispersion by ~7 % as there are more atoms in this plane relative to the (111) plane.

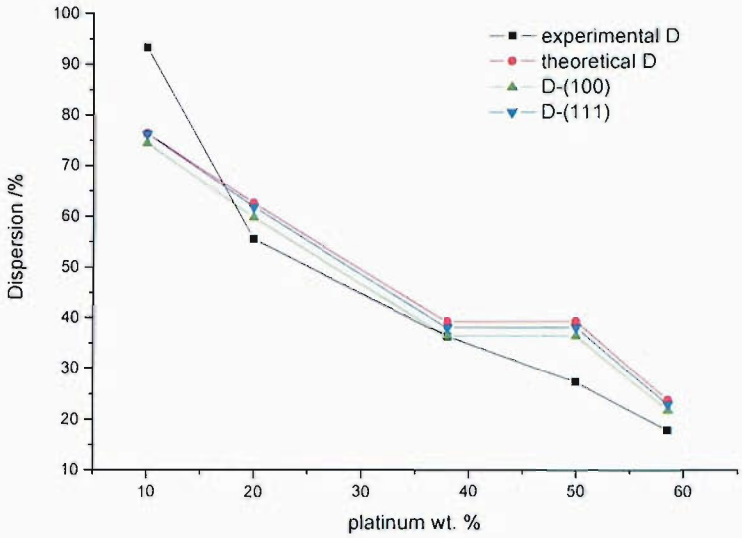

Figure 4 **Comparison of experimentally (squares) and theoretically (circles) calculated dispersions for a range of platinum particles with varying wt. %. The effect on the theoretical dispersion of binding the (100) face (triangles) and (111) face (diamonds) is also shown.**

3.3 Surface Composition

The surface composition plays an important role in the electrocatalytic properties for the ORR. Having established reasonable agreement between theoretical and experimental dispersions for the series of Pt catalysts (section 3.2.3), the same calculations were applied to the PtCr, PtCo and PtTi catalysts to determine their dispersion (table 5).

Table 5 **Theoretical dispersions, D, for cathode catalyst assuming that the (100) face is blocked by the carbon support.**

Catalyst Pt:M	Particle size /nm	Number of complete shells, *m*	Pt atoms at surface, eq. 6	Total Pt atoms, eq 5	Atoms in (100) face	D /%
PtCr 3:1	6	11	1002	3871	81	24
PtCr 1:1	8.5	16	2252	12431	196	17
PtCo 3:1	4.7	9	642	2057	49	28
PtTi 1:1	5	9	642	2057	49	28

From the area of the hydrogen adsorption peak, assuming that Cr, Co and Ti are not active sites for the adsorption of hydrogen and do not affect the adsorption of hydrogen on Pt sites, [27] the number of Pt atoms at the surface of the catalyst could be calculated (table 6). Using the theoretical dispersion to determine the total number of surface atoms, the composition of the surface could be calculated.

Table 6 **Estimation of surface composition for cathode catalysts based on theoretical dispersion and experimentally determined active surface area.**

Catalyst Pt:M	Pt loading mg cm^{-2}	Q transfer (H) /C cm^{-1}	Estimated surface composition Pt:M
PtCr 3:1	0.79	0.131	100:0
PtCr 1:1	0.83	0.030	22:78
PtCo 3:1	0.83	0.165	100:0
PtTi 1:1	0.6	0.094	55:45

Care must be taken when interpreting this result as a number of assumptions are made in determining the surface composition. The error in the dispersion has been demonstrated in section 3.2.3 for the platinum series. Comparing experimental and theoretical values for the range of particle size, 2 to 6 nm, a maximum variation of approximately 30 % is observed. Despite the errors involved, the calculations can provide a semi-quantitative estimation of surface composition.

Both the PtCr and PtCo (3:1) catalysts have a very high percentage, ~100 %, of platinum at the surface of the catalyst particle suggesting that the alloying element remains in the bulk of the particle. The PtCr (1:1) catalyst has only ~22 % platinum at the surface, well below the atomic ratio of (1:1). This suggests that a fraction of Cr remains at the surface of the particle. The value for the PtTi catalyst shows that ~55 % of the particle surface consists of platinum. This is close to the atomic ratio of (1:1) and indicates that the surface sites are blocked by Ti species.

The changes in the CVs (figure 2) with the secondary element and heat treatment correlate well with the estimated surface composition. Both CVs for the PtCr (3:1) and PtCo (3:1) catalysts closely resemble the 40 wt. % Pt catalyst in agreement with surface compositions close to 100 %. The change in the hydrogen

adsorption/desorption region for the PtCr (1:1) relative to the (3:1) catalyst suggests Cr species are present at the surface of the catalyst in agreement with the surface composition of ~22 %. The CV for Pt:Ti (1:1) has Pt characteristics in the hydrogen adsorption/desorption region. However, as discussed in section 3.1, an increase in the double layer currents relative to PtCr, PtCo is observed. This suggests that oxide species such as titanium oxide are present at the surface correlating with the platinum surface composition of 55 %.

3.4 Catalyst Activity

Two methods were used to determine the activity of the cathode catalysts for the ORR. The first method involved a half-cell setup where the cathode electrode was positioned so that one face was in contact with the liquid electrolyte (1 M H_2SO_4) while oxygen was fed to the other side. The performance was measured relative to a MMS reference electrode. The electrolyte can adsorb strongly to catalyst surfaces and therefore, affect the rate of the ORR. To overcome this, the activity was also measured in a PEMFC where no liquid electrolyte is required.

3.4.1 Activity in liquid electrolyte

After deoxygenating the electrolyte with nitrogen, a CV was obtained between the potential limits 0.05 and 1.1 V vs. RHE with a scan rate of 10 mV s^{-1}. An example CV for a PtCr 3:1 electrode with a loading of 0.5 mg cm^{-2} is shown in figure 5 and was used to determine the active Pt surface area of the catalyst layer. Oxygen was then flowed to the back of the electrode with a flow rate of 150 cm^3 min^{-1} and a polarisation experiment was carried out between 0.5 V and 0.96 V vs. RHE. 10 mV steps were used in each case with a stabilisation time of 60 seconds. The first four polarisation curves for the PtCr 3:1 electrode are shown in figure 6.

The poor reproducibility of repeated scans highlights the difficulty in obtaining accurate oxygen activity data in a liquid electrolyte. The highest performance is observed in the first scan where the mass transport rates are at their highest. The product water from the oxygen reduction accumulates in the catalyst layer and carbon paper. For subsequent scans, the presence of water reduces the mass

transport rates to the catalyst resulting in lower performances. Recent studies in the literature have used thin catalyst layers to overcome the problem of mass transport [16,28]. For example, combinatorial screening carried out by Guerin *et al.* [29] used Pt loadings ranging from 2.5 to 35 μg deposited onto glassy carbon rod electrodes with a 3 mm diameter. This allowed accurate and reproducible activities to be achieved across a 64-element half-cell array.

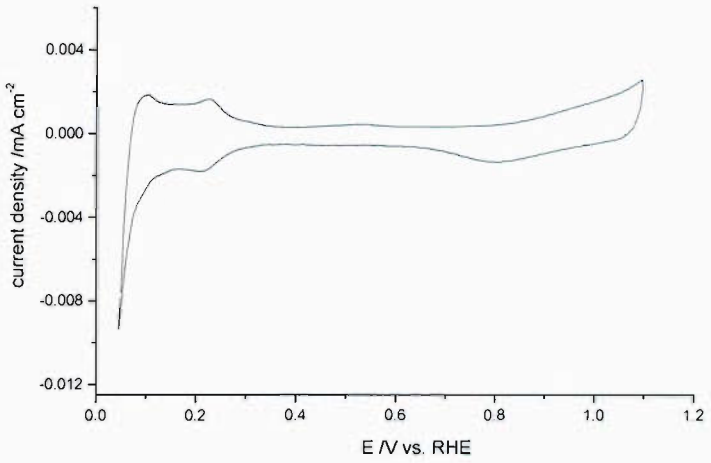

Figure 5 **Cyclic voltammetry of a PtCr (3:1) electrode with a 0.5 mg Pt cm^{-2} loading in nitrogen purged 1 M H_2SO_4. Obtained using a gas half-cell with nitrogen flowing to the back of the electrode and a scan rate of 10 mV s^{-1}.**

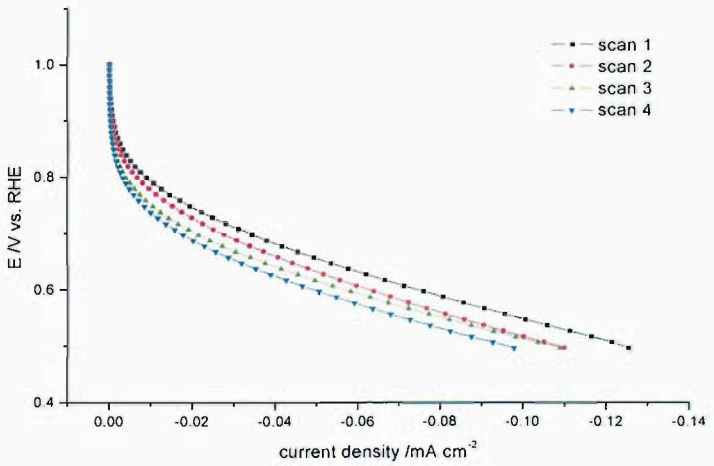

Figure 6 **Oxygen polarisation scans 1 to 4 for a PtCr (3:1) electrode with a 0.5 mg Pt cm^{-2} loading. Obtained using a gas half-cell with oxygen flowing to the back of the electrode (150 cm^3 min^{-1}).**

3.4.2 Activity in a PEMFC

To overcome the problems of flooding in a half-cell environment, the catalysts were tested in an MEA using H_2/O_2 at 80 °C and with high reactant stoichiometries. An oxygen flow rate of 150 cm^3 min^{-1} was used at the cathode while a hydrogen flow rate of 60 cm^3 min^{-1} was used at the anode. Figure 7 shows the polarisation curves for the PtCr (3:1), PtCr (1:1), PtCo (3:1) and PtTi (1:1) catalysts with a 40 wt. % Pt catalyst for comparison. Reproducible currents were observed over four repeated scans and these were averaged and divided by the geometric area of the electrode, 12.56 cm^{-2}, to give the current density.

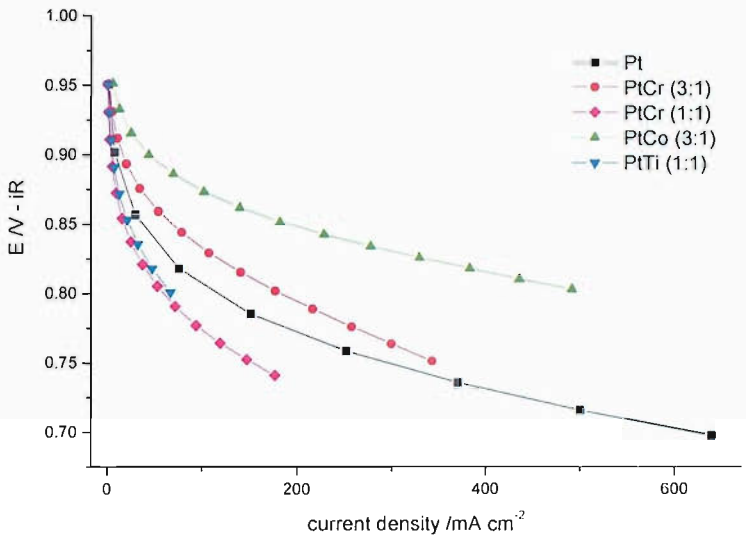

Figure 7 **iR-corrected polarisation curves for 40 wt. % Pt, and Pt alloys cathodes with 40 wt. % Pt anodes in Flemion® bonded MEAs. Cathode loading 0.4 to 0.9 mg Pt cm^{-2}, anode loading 0.57 mg Pt cm^{-2}. Operated with an oxygen flow rate of 150 cm^3 min^{-1}, hydrogen flow rate of 60 cm^3 min^{-1}, cell temperature 80 °C.**

The polarisation data were normalised by the *in situ* platinum surface area as determined by the CO stripping charge (figure 8) and also by the Pt loading (figure 9). The electrochemical and electrokinetic properties of the catalysts are shown in table 7. Currents were measured at 900 mV vs. RHE to avoid mass transport affects.

Comparing specific activities, all alloys apart from PtTi show a clear improvement over Pt with the activities decreasing in the following order: PtCo > PtCr (3:1) > PtCr (1:1) > Pt > PtTi. In the linear region of the Tafel plot, the performance

improvement for the PtCo catalyst is in the order of 35 mV higher than the Pt case. The PtCr activities demonstrate the effect of varying heat treatments. In contrast to results found by Thompsett *et al.* [30] reduced activity was observed with higher temperatures of heat treatment. The PtCr (1:1) heat treated at 1200 °C shows a 16 mV drop in performance in the linear region of the Tafel plot relative to the PtCr (3:1), 900 °C case. Similar Tafel slopes are observed for the PtCo and PtCr catalysts with values in the region of 60 to 70 mV decade^{-1} while PtTi and Pt have a Tafel slope close to 90 mV decade^{-1}. This may indicate a variation in the mechanism taking place which is dependent on the alloying element.

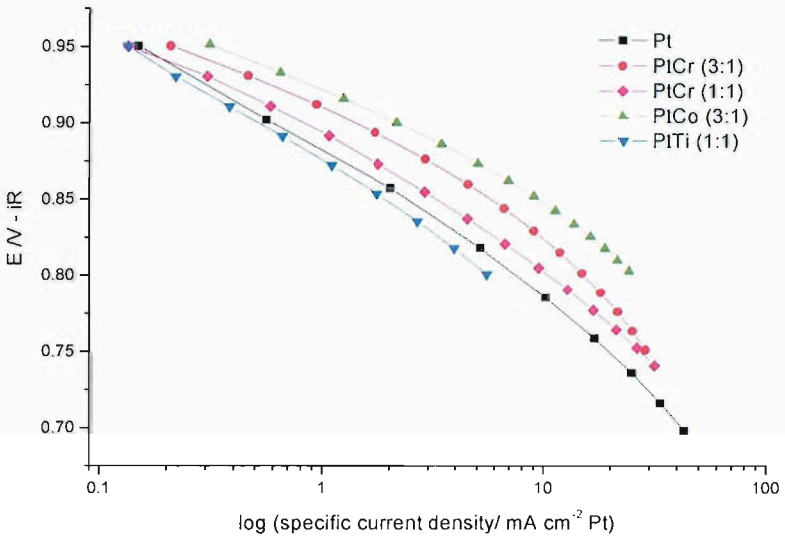

Figure 8 **iR-corrected polarisation curves for 40 wt. % Pt, and Pt alloys cathodes with 40 wt. % Pt anodes in Flemion bonded MEAs. Currents normalised by the *in situ* platinum area as determined by the CO stripping charge.**

The mass activities are an important consideration in terms of cost when new catalysts are being considered for commercial use. Figure 9 clearly shows that the large particle size of the PtCr (1:1) catalyst as a result of the heat treatment at 1200 °C leads to low mass activities, well below the pure Pt case. With the exception of the PtCr (1:1) catalyst, the order remains unchanged when compared to the specific activities: PtCo > PtCr (3:1) > Pt > PtTi > PtCr (1:1).

Table 7 **Electrochemical and electrokinetic properties of carbon-supported Pt and Pt alloys, conditions as Figure 7.**

Catalyst Pt:M	Pt loading mg cm^{-2}	In situ Ptarea (cm^2 Pt cm^{-2} geometric)[a]	In situ $Ptarea_m$ (cm^2 Pt g^{-1} Pt)	% utilisation[b]	O.C. /V vs. RHE	Current density at 900 mV (mA cm^{-2})[c]	Specific activity at 900 mV (mA cm^{-2} Pt)[d]	Mass activity at 900 mV (mA g^{-1} Pt)	Tafel slope (mV $decade^{-1}$)
PtCr 3:1	0.49	12.0	30.9	37	0.992	17.5	1.46	36.0	62
PtCr 1:1	0.95	5.6	7.4	43	1.001	4.8	0.867	5.14	69
PtCo 3:1	0.65	20.4	39.4	41	1.005	44.8	2.20	68.8	62
PtTi 1:1	0.35	12.1	43.1	58	0.984	6.6	0.542	18.5	85
Pt 40%	0.43	14.9	43.2	37	0.987	9.4	0.631	21.7	82

a Calculated from *in situ* CO stripping experiment – cm^2 of Pt surface area per geometric electrode area (12.56 cm^2).

b Based on ex situ calculations of $Ptarea_m$ using cyclic voltammetry in 1 M H_2SO_4 (see table 2).

c Based on geometric electrode area.

d Normalised to *in situ* Pt surface area

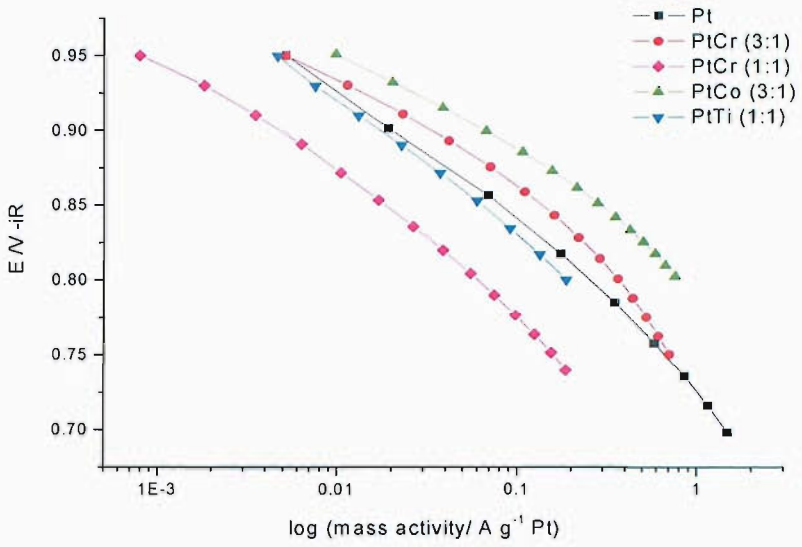

Figure 9 **iR-corrected polarisation curves for 40 wt. % Pt, and Pt alloys cathodes with 40 wt. % Pt anodes in Flemion bonded MEAs. Currents normalised by the platinum loading.**

A linear region is observed for potentials greater than 0.8 V vs. RHE. which can be represented using the semi-empirical equation proposed by Srinivasan *et al.* [31,32] (equation 8 and 9).

$$E = E_o - b \log i - Ri \qquad \textbf{Eq. 8}$$

where $E_o = E_r + b \log i_o$ **Eq. 9**

In these equations, E_r is the reversible potential for the cell, b and i_o are the Tafel slope and exchange current densities, respectively, and R represents the resistance. However, equation 8 does not include diffusion limitations other than linear combinations. For potentials below 0.8 V vs. RHE non-linear contributions become more significant [33]. As a result of this, only the region with potentials greater than 0.8 V vs. RHE were considered in this analysis [34].

3.4.3 Dilution effects

As mentioned in chapter 3, section 4, *in situ* mini-cell operation was carried out using 5 % H_2/N_2 at the anode for safety reasons on the beamline. An example of the

dilution effect is shown clearly in figure 10 using an MEA with a PtCo cathode catalyst (1.1 mg Pt cm^{-2}) and Pd anode (0.3 mg Pd cm^{-2}). The MEA performance with oxygen at the cathode using a flow rate of 150 cm^3 min^{-1} and pure hydrogen at the anode with a flow rate of 60 cm^3 min^{-1} is included for comparison (squares). Using the same flow rates and replacing H_2 with 5 % H_2/N_2 (circles) results in a significant drop in performance. In addition, mass transport limiting currents are rapidly reached at approximate 0.7 V vs. RHE and current densities of 55 mA cm^{-2}. Increasing the anode flow rate to 80 (triangles) and 100 cm^3 min^{-1} (diamonds) extends the linear region of the polarisation curve but limiting currents are still reached at 86 and 126 mA cm^{-2}, respectively.

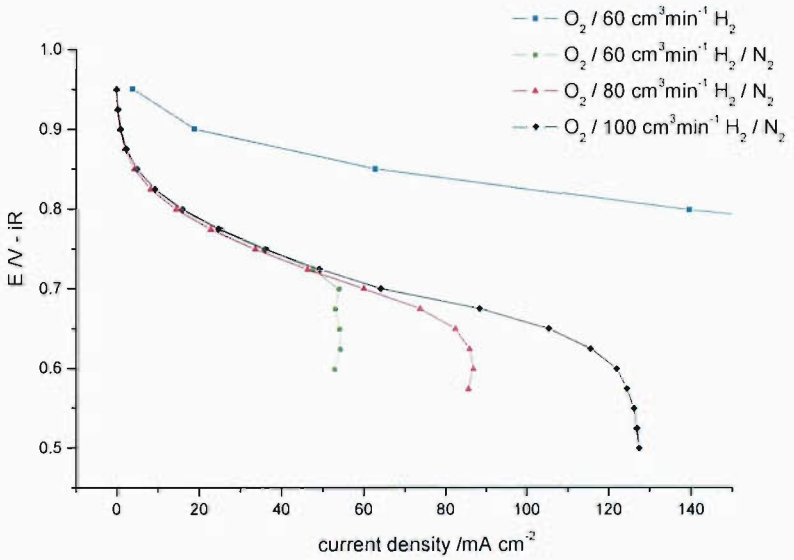

Figure 10 **Comparison of oxygen polarisation curves using different gas mixes at the anode. Demonstrates performance using pure hydrogen, 60 cm^3 min^{-1} (squares), 5 % hydrogen balance nitrogen, 60 cm^3 min^{-1} (circles), 80 cm^3 min^{-1} (triangles) and 100 cm^3 min^{-1} (diamonds). Oxygen flow rate constant at 150 cm^3 min^{-1}. Cathode: 60 wt. % Pt / 6 wt. % Co, 1.1 mg Pt cm^{-2}. Anode: 20 wt. % Pd, 0.3 mg Pd cm^{-2}. Cell temperature = 80 °C.**

3.5 *In situ* XAS

The following section presents the *in situ* XAS results carried out with the aim of gaining an understanding of the varying electrochemical activities observed for the cathode catalysts. The XANES and EXAFS were analysed at both the Pt L_{III} edge and secondary metal K edges providing electronic and structural information for the

cathode catalysts. The XAS data were collected in a half-cell and also in a mini-cell environment to provide more realistic operating conditions.

3.5.1 XANES - Pt L_{III} edge

Analysis of the XANES can provide information regarding the electronic properties of the catalyst. The area under the white line region provides information on the Pt d-band vacancies. Although data were not collected at the Pt L_{II} edge preventing quantitative analysis of the d-band vacancies, the Pt L_{III} edge can still be used as a guide. Table 8 shows the integrated areas measured from 11544 eV (-10 eV before the edge) to 11581 eV (27 eV after the edge) relative to a platinum foil. This was carried out for the PtCr (3:1), Pt (1:1), PtCo and PtTi catalysts as shown in figure 11 (a and b) and figure 12 (a and b), respectively. For comparison, a 40 wt. % Pt catalyst was used. The half-cell studies were carried out at room temperature with the electrode in a flooded environment of 1 M H_2SO_4. XANES were collected at O.C., with no pre-treatment or electrochemical cycling, and under reducing conditions, 0.0 V vs. RHE. This allowed the affect of the alloying element to be analysed without electronic contributions from any oxides present. The mini-cell was operated at 80 °C with oxygen to the cathode at a flow rate of 150 cm^3 min^{-1} and with 5 % H_2 / N_2 to the anode with a high flow rate of 100 cm^3 min^{-1} to prevent reaching mass transport limited currents, ensuring that the cell was operating under reproducible conditions (figure 10).

Table 8 **Relative integrated areas taken from the XANES at the Pt L_{III} edge for Pt alloy and Pt catalysts normalised to that of a Pt foil from 11544 eV to 11581 eV.**

Catalyst	In air	Half-cell		Mini-cell	
		O.C.	0.0 V vs. RHE	O.C.	0.7 V vs. RHE
Pt 40%	-	1.02	0.87	-	-
PtCr (3:1)	1.71	1.28	1.47	2.17	2.37
PtCr (1:1)	2.36	1.69	1.53	2.49	2.53
PtCo	2.66	2.06	1.39	2.94	2.92
PtTi	2.38	1.60	1.12	1.99	1.98

The variation in the white line area as shown in table 8 for the as prepared catalyst is as follows, in order of decreasing area: PtCo > PtTi > PtCr (1:1) > PtCr (3:1). In air, all the catalysts are significantly oxidised in nature. This is indicated by a broad white line region for PtCr (3:1) and PtTi catalysts (figures 11a and 12b) and an increase in peak intensity in the case of the PtCr (1:1) and PtCo catalysts (figures 11b and 12a). A reduction in the white line area is observed when the cell is in a flooded environment as indicated by the values at O.C. in the half-cell (table 8). The order of decreasing area changes, indicating that the catalysts are affected to varying degrees, the most significant change is observed in the PtTi case. As mentioned previously, no pre-treatment or electrochemical cycling was involved in this step so any electronic changes are solely due to the presence of the electrolyte, 1 M H_2SO_4. HSO_4^- adsorbs strongly to platinum and has been shown to alter the white line region [13]. At 0.0 V vs. RHE in the half-cell, the area decreases in the following order: PtCr (1:1) > PtCr (3:1) > PtCo > PtTi > Pt. In all cases the secondary metal causes an increase in the d-band vacancy of Pt relative to the 40 wt. % Pt catalyst as evidenced by the increased white line area. Very little change in area is observed for both the PtCr catalysts when going from O.C. to 0.0 V vs. RHE. Larger changes are observed for the PtCo and PtTi catalysts with the PtTi catalyst having a significantly lower white line area when compared to the rest.

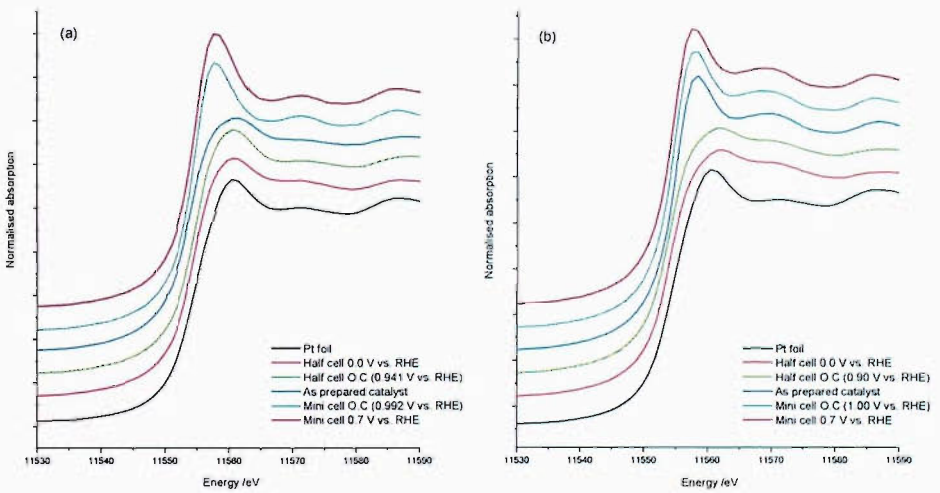

Figure 11 **XANES spectra at the Pt L_{III} edge for (a) PtCr (3:1) and (b) PtCr (1:1) catalysts in both half-cell and mini-cell environments. (The as prepared catalyst and Pt foil have been included for comparison).**

To be able to gain a better understanding of the activities for the ORR observed in section 3.4.2, the XANES collected using the mini-cell must also be considered. For all catalysts, a sharper, more intense peak is observed in the white line region relative to the half-cell case (figures 11 and 12). The areas at O.C. in the mini-cell as shown in table 8 with the exception of PtTi, are significantly larger than those in air. This indicates that the mini-cell presents a very oxidising environment. The area decreases as follows: PtCo > PtCr (1:1) > PtCr (3:1) > PtTi. Polarising the electrode at 0.7 V vs. RHE does not affect the order and no significant change in area is observed within experimental error.

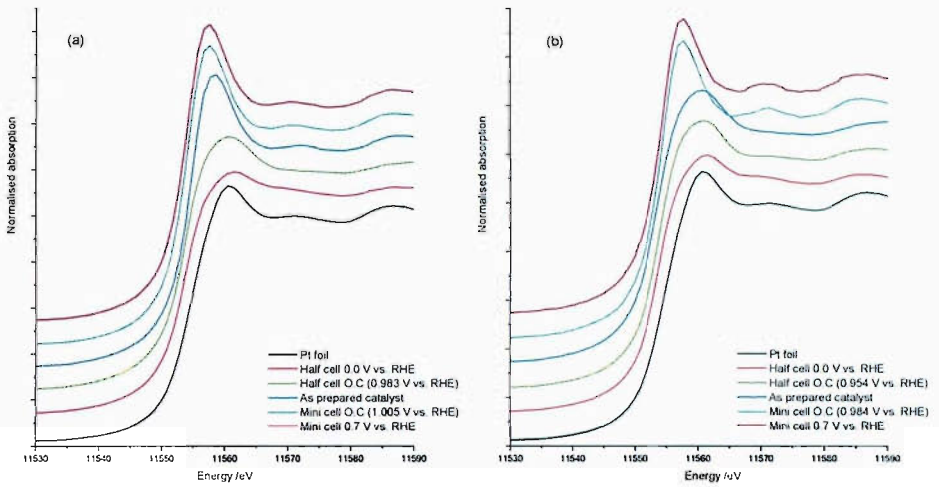

Figure 12 **XANES spectra at the Pt L_{III} edge for (a) PtCo and (b) PtTi catalysts in both half-cell and mini-cell environments. (The as prepared catalyst and Pt foil have been included for comparison).**

3.5.2 XANES – 2nd metal K edge

The XANES were also collected at the corresponding secondary metal K edge under the same electrode conditions. Figures 13 a and b show the XANES region at the Cr K edge for the PtCr (3:1) and PtCr (1:1) catalysts, respectively. Unlike the Pt L_{III} edge XANES, a pre-edge feature is present at approximately 5986 eV which is related to the dipole forbidden 1s to 3d transition. The occurrence of the pre-edge feature is strongly dependent on the coordination geometry. For example, an octahedral geometry such as Cr_2O_3 has no pre-edge feature while a tetrahedral geometry coordinated compound such as CrO_3 has an intense pre-edge. Based on

XANES studies by Pantelouris *et al.* [35] the Cr K edge XANES shown in figure 13 bares little resemblance to a number of oxides including: Cr_2O_3, CrO_2 and CrO_3. This suggests that the Cr present in the catalyst consists of a mixed phase containing both Cr metal and a form of the oxide. The absence of an intense pre-edge feature rules out the presence of CrO_3 with tetrahedral geometry.

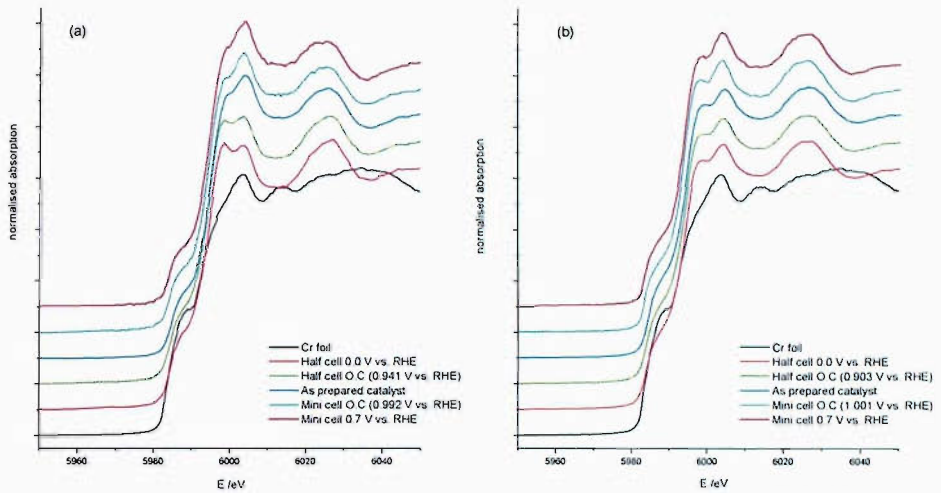

Figure 13 **XANES spectra at the Cr K edge for (a) PtCr (3:1) and (b) PtCr (1:1) catalysts in both half-cell and mini-cell environments. (The as prepared catalyst and Cr foil have been included for comparison).**

The XANES spectra for the PtCo catalyst at the Co K edge also show signs of a pre-edge feature (figure 14a). Again this arises from 1s to 3d transition in the case of tetrahedral Co environments but is forbidden for an octahedral environment [36]. The white line region is characteristic of both Co_3O_4 and CoO while the absence of an intense pre-edge feature suggests that the majority of the Co is in the form CoO due to its octahedral geometry. Co_3O_4 has a pre-edge feature due to its spinel structure with one third cobalt (II) in tetrahedral sites contributing strongly and two-thirds Co (III) in octahedral sites contributing very weakly to the pre-edge. As in the Cr (3:1) case, an increase in intensity of the white line region is observed in the mini-cell relative to the half-cell environment. This indicates that the catalyst is more oxidised in the mini-cell environment.

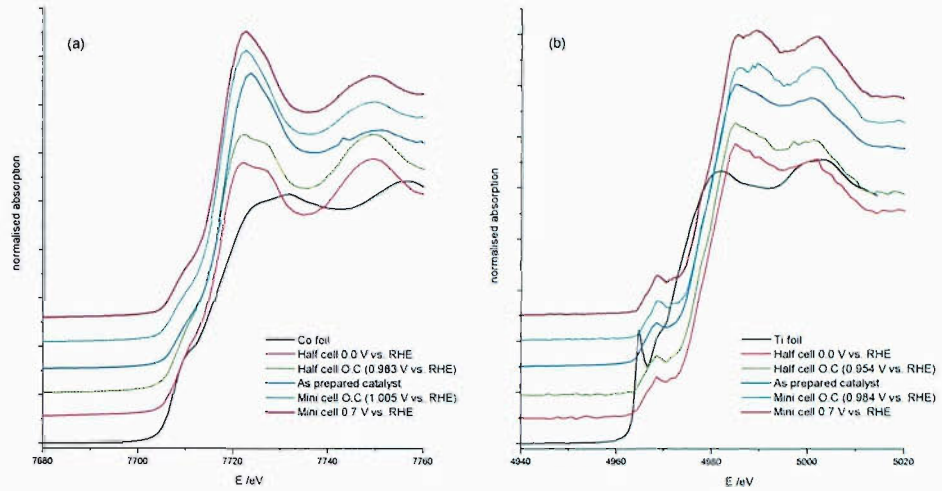

Figure 14 **XANES spectra at the Co and Ti K edge for (a) PtCo and (b) PtTi catalysts, respectively, in both half-cell and mini-cell environments. (The as prepared catalyst and corresponding metal foils have been included for comparison).**

The PtTi XANES (figure 14b) at the Ti K edge has a pre-edge feature occurring at approximately 4969 eV. No significant variation occurs in the white line region under changing conditions suggesting that the Ti phase is remaining largely unchanged. The very distinctive nature of the pre-edge makes it easier to determine which Ti species are present and can be separated out using a base line subtraction. The base line is a spline drawn through manually adjusted knots and can be carried out using a program called Xanda [37].

Figure 15a shows the subtracted pre-edge feature for a Ti foil, the mini-cell at O.C. and 0.7 V vs. RHE, a series of Ebonex TiO_x compounds and *r*-TiO_2. The Ti in the PtTi catalyst under operating conditions resembles more closely the *r*-TiO_2 pre-edge feature. As mentioned above, polarising the electrode at 0.7 V vs. RHE has no effect on the shape of the pre-edge feature. The pre-edge feature of the Ebonex TiO_x compounds of which only one is shown (x = 1.74) consists of only a single peak suggesting that there are no mixed phase oxides present in the catalyst under operating conditions.

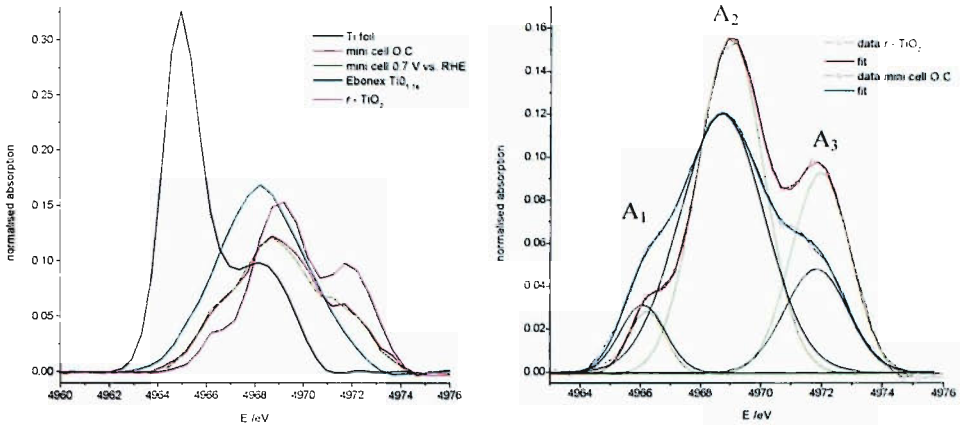

Figure 15 **(a) Subtracted pre-edge feature at the Ti K edge for a Ti foil, mini-cell at O.C. and 0.7 V vs. RHE, Ebonex compound $TiO_{1.74}$ and *r*-TiO_2. (b) Peak fit using three Gaussian curves for the *r*-TiO_2 and mini-cell at O.C.**

Figure 15b shows the analysis of the pre-peak region for the *r*-TiO_2 reference compound and the PtTi electrode at 0.7 V vs. RHE in more detail. Three Gaussian curves were fitted to the pre-edge feature. A_1 was assigned as a weak transition to a t_{2g} orbital. The A_2 and A_3 peaks are due to transitions from 1s to 3d involving the $2t_{2g}$ and $3e_g$ molecular orbitals, respectively [38,39]. The peaks are less well defined for the catalyst in the MEA. This could be because the system is more disordered resulting in changes to the symmetry which may make some transitions less favorable when compared to the *r*-TiO_2 case. Another possibility is that the presence of Ti in a reduced state may distort the pre-edge region. However, no evidence of the pronounced peak at 4964.9 eV seen in the Ti foil case is present in the PtTi electrode.

The normalised height of the pre-edge feature is strongly correlated to both peak position and coordination number. To try to help gauge whether Ti is in a number of different forms, data for a series of reference compounds with varying coordination numbers, taken from work carried out by Farges *et al.* [40] were plotted in addition to the PtTi catalyst data (figure 16). The point for the PtTi catalyst lies in the region of six-fold coordinated Ti. The points for the Ebonex compounds are positioned closer to five-fold coordinated Ti. The small normalised height observed for the Ebonex compounds may be the effect of a disordered structure leading to

broadening of the pre-edge peak. However, one of the problems of using XANES in this way is that there is no simple trend when mixed phases are involved. For example, peak positions or heights do not vary consistently when mixtures are present [40]. Investigations looking into the effects on the pre-edge feature of mixing *r*-TiO_2 with Ti, TiO_x would be required to take this further.

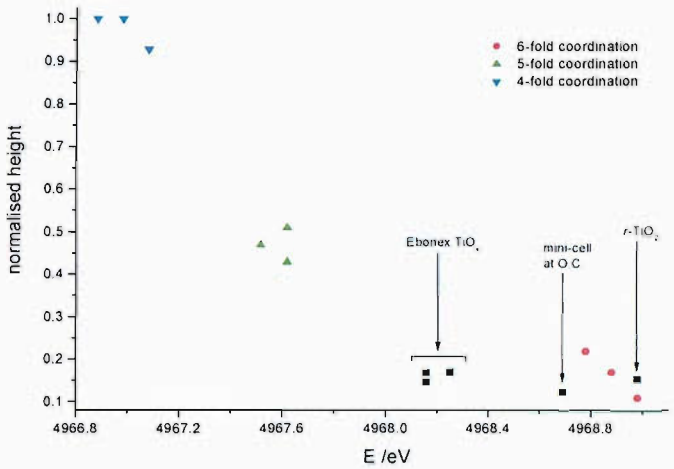

Figure 16 **Plot of normalised height vs. energy for the Ti pre-edge features. ●, ▲, and ▼ represent reference compounds with 4, 5 and 6 fold coordinated Ti, respectively [40]. ■ shows values for the mini-cell at O.C. and reference compounds including Ebonex and *r*-TiO_2.**

3.5.3 EXAFS

EXAFS data were collected at the secondary metal K edge and Pt L_{III} edge for the as prepared catalyst, under flooded half-cell conditions and in the mini-cell. During interpretation of the results of the fits of the EXAFS data, close attention will be paid to the following features:

- The presence of oxygen neighbours in the first coordination shell of the secondary element, giving evidence of an unalloyed oxide component.
- The ratio of Pt and secondary element neighbours in the first coordination shell, giving evidence of the degree of intermixing of the components.
- The Pt-Pt first shell distance, giving evidence of a lattice contraction.
- The contributions for multiple scattering pathways, giving evidence of intermixing and long range order.

3.5.3.1 PtCr (3:1) and (1:1)

The k^2 weighted EXAFS data with the corresponding Fourier transform obtained at the Cr K and Pt L_{III} edges for the PtCr (3:1) and PtCr (1:1) catalysts are presented in figures 17 and 18, and figures 19 and 20, respectively. Data were collected under the following conditions: as prepared catalyst in air, O.C. and 0.0 V vs. RHE in the half-cell, and O.C. and 0.7 V vs. RHE in the mini-cell. The parameters obtained by fitting the data at the Cr K and Pt L_{III} edges for the PtCr (3:1) and PtCr (1:1) catalysts are shown in tables 9 and 10 and tables 11 and 12, respectively.

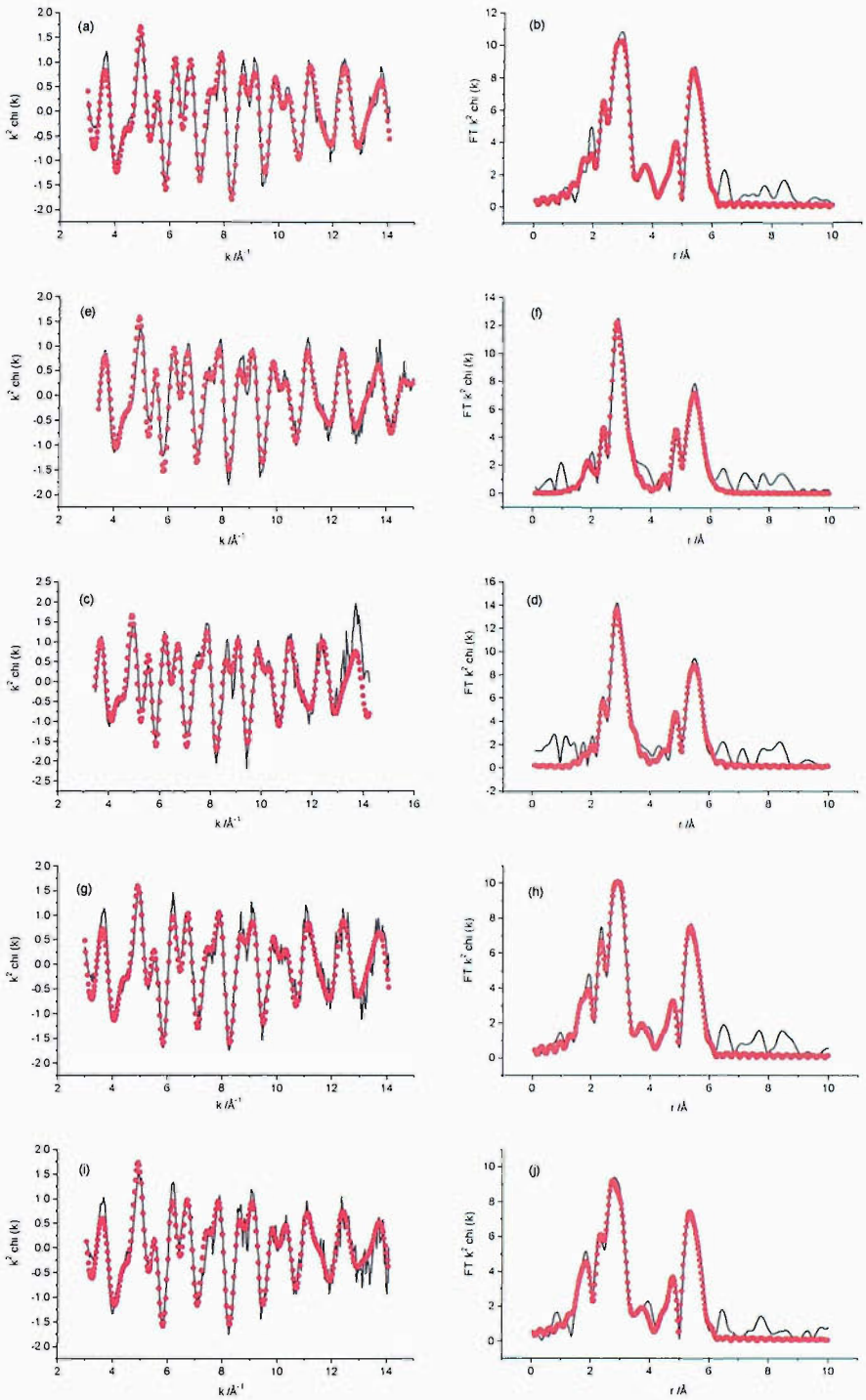

Figure 17 **k^2 weighted Cr K edge experimental data and fit (left) and corresponding Fourier transform (right) phase corrected for backscattering from O. PtCr 3:1 catalyst, (a & b): as prepared, (c & d): half-cell O.C., (e & f): half-cell 0.0 V vs. RHE, (g & h): mini-cell O.C., (i & j): mini-cell 0.7 V vs. RHE.**

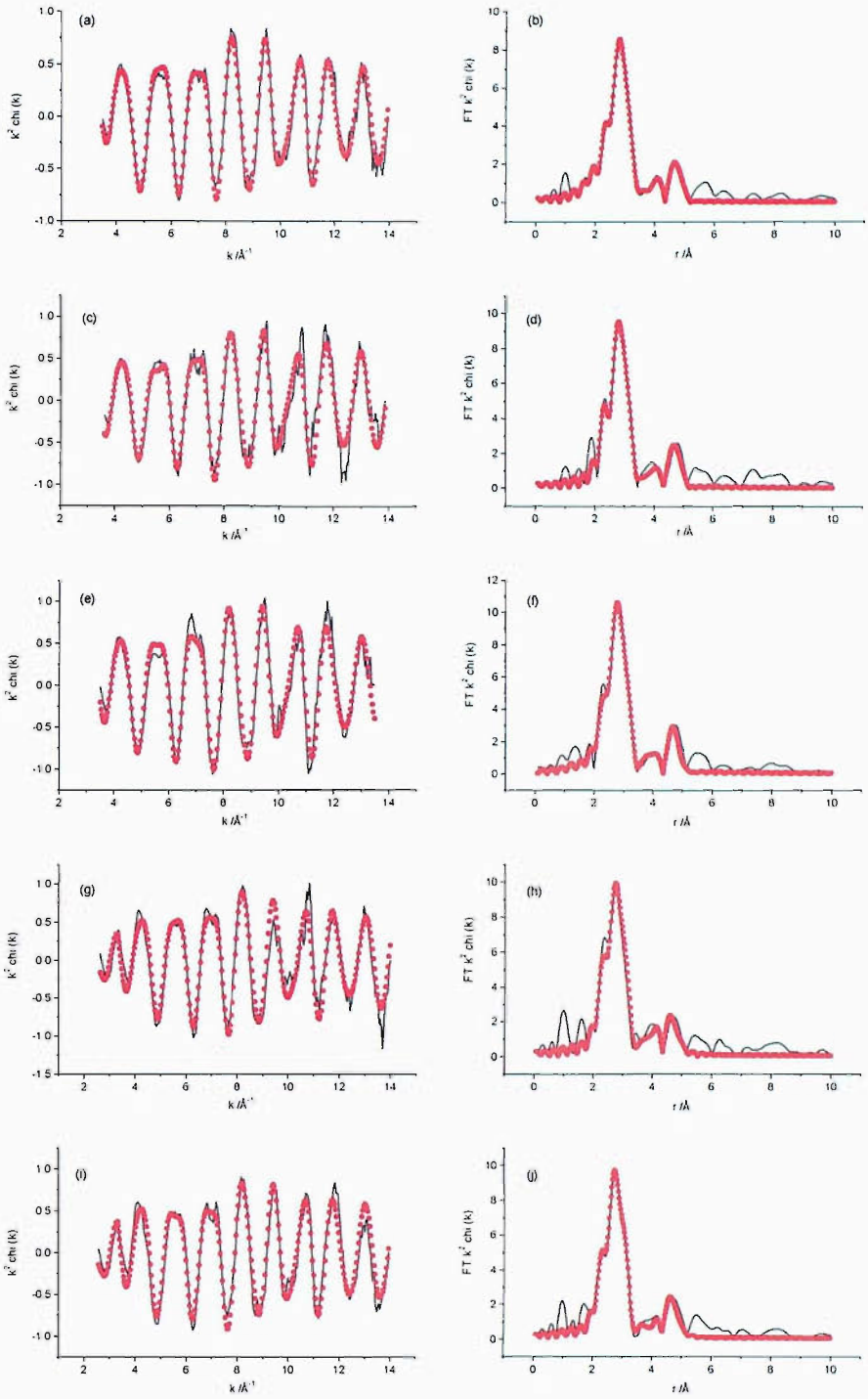

Figure 18 **k^2 weighted Pt L_{III} edge experimental data and fit (left) and corresponding Fourier transform (right) phase corrected for backscattering from Pt. PtCr 3:1 catalyst, (a & b): as prepared, (c & d): half-cell O.C., (e & f): half-cell 0.0 V vs. RHE, (g & h): mini-cell O.C., (i & j): mini-cell 0.7 V vs. RHE.**

Table 9 **Structural parameters for the PtCr (3:1) catalyst under varying conditions obtained by fitting the Cr K edge EXAFS data.**

Condition	Shell	Calculated parameters (Cr K edge)				
		N	*R* /Å	$2\sigma^2$ /Å^2	E_f /eV	R_{exafs}
As prepared	Cr-O	1.3 ±0.2	1.92 ±0.02	0.015 ±0.01	-3.0 ±0.4	27.46
	Cr-Pt unit 1	6.3 ±0.3	2.72 ±0.003	0.010 ±0.0005		
	Cr-Cr	2.1 ±0.5	3.83 ±0.02	0.012 ±0.004		
	Cr-Pt	6.0 ±1.0	4.74 ±0.009	0.009 ±0.008		
	Cr-Pt-Cr	unit 1	5.47 ±0.007	0.019 ±0.001		
Half-cell O.C. (0.941 V vs. RHE)	Cr-O	0.9 ±0.3	1.94 ±0.02	0.012 ±0.006	-1.9 ±0.5	34.22
	Cr-Pt unit 1	6.4 ±0.6	2.73 ±0.004	0.011 ±0.005		
	Cr-Pt	7.4 ±1.1	4.75 ±0.008	0.010 ±0.001		
	Cr-Pt-Cr	unit 1	5.48 ±0.01	0.021 ±0.002		
Half-cell (0.0 V vs. RHE)	Cr-O	0.6 ±0.3	1.95 ±0.06	0.024 ±0.02	-4.1 ±0.7	37.88
	Cr-Pt unit 1	7.3 ±0.8	2.72 ±0.005	0.011 ±0.0008		
	Cr-Pt	9.1 ±2.1	4.74 ±0.06	0.011 ±0.002		
	Cr-Pt-Cr	unit 1	5.48 ±0.01	0.021 ±0.002		
Mini-cell O.C. (0.992 V vs. RHE)	Cr-O	1.2 ±0.3	1.95 ±0.02	0.008 ±0.004	-1.0 ±0.8	34.68
	Cr-Pt unit 1	5.9 ±0.3	2.72 ±0.004	0.010 ±0.0005		
	Cr-Cr	2.1 ±1.1	3.81 ±0.03	0.019 ±0.01		
	Cr-Pt	5.7 ±1.3	4.74 ±0.01	0.011 ±0.002		
	Cr-Pt-Cr	unit 1	5.46 ±0.01	0.017 ±0.002		
Mini-cell (0.7 V vs. RHE)	Cr-O	1.3 ±0.2	1.93 ±0.01	0.008 ±0.003	-2.6 ±0.5	34.32
	Cr-Pt unit 1	5.4 ±0.5	2.72 ±0.005	0.011 ±0.0008		
	Cr-Cr	1.7 ±0.5	3.83 ±0.03	0.014 ±0.006		
	Cr-Pt	5.8 ±1.3	4.75 ±0.01	0.009 ±0.002		
	Cr-Pt-Cr	unit 1	5.48 ±0.009	0.018 ±0.002		

Table 10 Structural parameters for the PtCr (3:1) catalyst under varying conditions obtained by fitting the Pt L_{III} edge EXAFS data.

Condition	Shell	Calculated parameters (Pt L_{III} edge)				
		N	R /Å	$2\sigma^2$ /Å^2	E_f /eV	R_{exafs}
As prepared	Pt-O	0.4 ±0.1	2.01 ±0.03	0.016 ±0.009	-14.7 ±0.7	20.05
	Pt-Cr	1.2 ±0.2	2.73 ±0.009	0.010 ±0.002		
	Pt-Pt	4.7 ±0.2	2.74 ±0.003	0.010 ±0.0004		
	Pt-Cr	2.3 ±0.5	3.87 ±0.01	0.012 ±0.002		
	Pt-Pt	3.8 ±0.6	4.73 ±0.01	0.010 ±0.002		
Half-cell O.C. (0.941 V vs. RHE)	Pt-Cr	1.1 ±0.3	2.72 ±0.02	0.013 ±0.004	-13.4 ±1.1	27.34
	Pt-Pt	5.9 ±0.4	2.74 ±0.004	0.010 ±0.0005		
	Pt-Pt	2.4 ±0.8	3.84 ±0.02	0.012 ±0.004		
	Pt-Cr	4.5 ±0.9	4.72 ±0.02	0.010 ±0.003		
Half-cell (0.0 V vs. RHE)	Pt-Cr	1.6 ±0.2	2.73 ±0.01	0.009 ±0.002	-13.9 ±0.8	26.34
	Pt-Pt	6.1 ±0.4	2.74 ±0.004	0.010 ±0.0007		
	Pt-Pt	2.5 ±0.7	3.85 ±0.02	0.010 ±0.003		
	Pt-Cr	4.7 ±0.8	4.73 ±0.01	0.0.13 ±0.009		
Mini-cell O.C. (0.992 V vs. RHE)	Pt-Cr	2.0 ±0.3	2.71 ±0.01	0.015 ±0.003	-11.0 ±0.7	31.06
	Pt-Pt	5.2 ±0.4	2.74 ±0.004	0.009 ±0.0006		
	Pt-Pt	2.2 ±0.7	3.86 ±0.02	0.008 ±0.003		
	Pt-Cr	4.5 ±1.1	4.72 ±0.02	0.012 ±0.004		
Mini-cell (0.7 V vs. RHE)	Pt-Cr	1.6 ±0.3	2.74 ±0.01	0.013 ±0.003	-13.2 ±0.6	27.80
	Pt-Pt	5.9 ±0.4	2.74 ±0.003	0.010 ±0.0006		
	Pt-Pt	1.9 ±0.7	3.87 ±0.02	0.012 ±0.004		
	Pt-Cr	4.8 ±0.9	4.73 ±0.01	0.012 ±0.003		

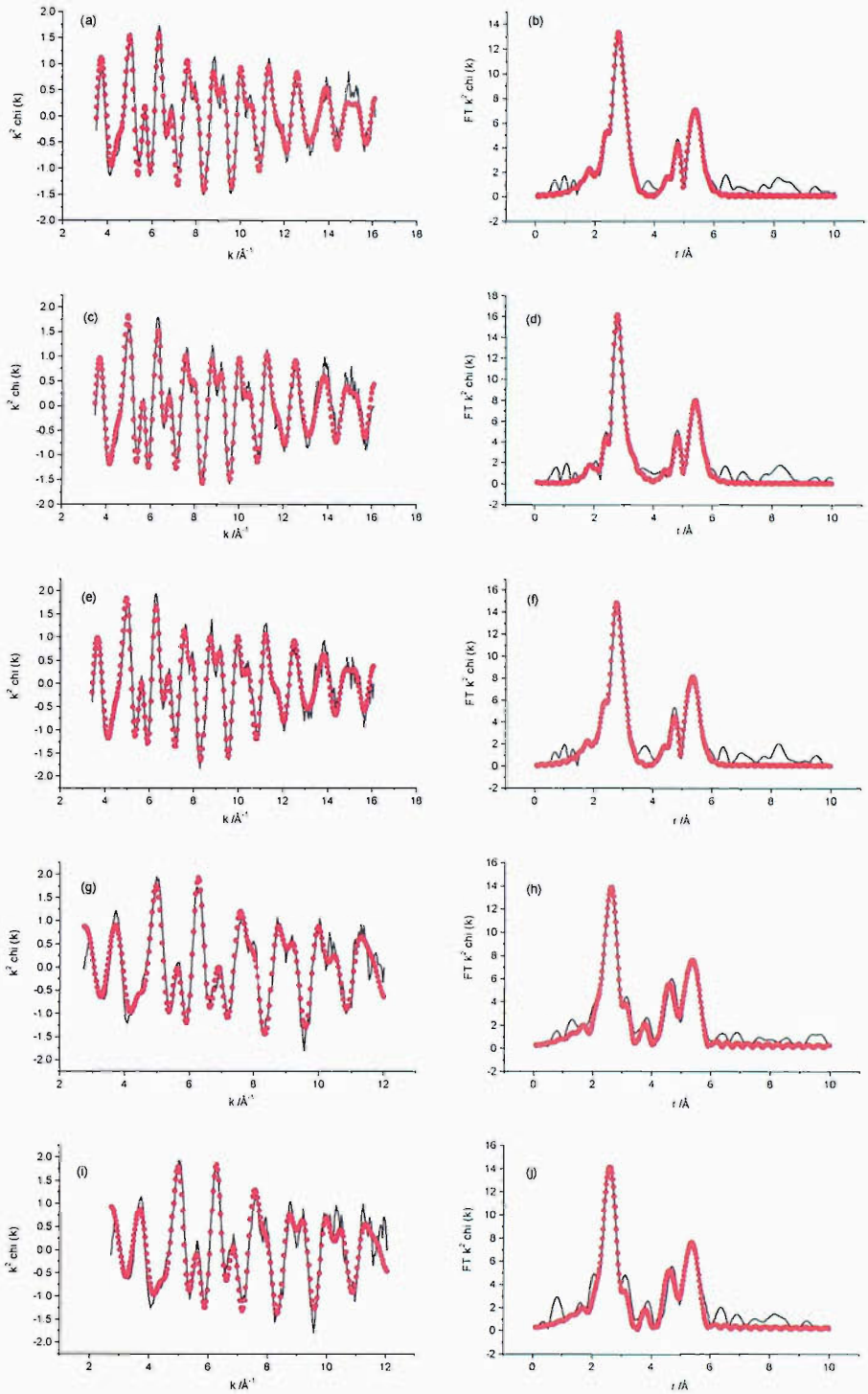

Figure 19 **k^2 weighted Cr K edge experimental data and fit (left) and corresponding Fourier transform (right) phase corrected for backscattering from Cr. PtCr 1:1 catalyst, (a & b): as prepared, (c & d): half-cell O.C., (e & f): half-cell 0.0 V vs. RHE, (g & h): mini-cell O.C., (i & j): mini-cell 0.7 V vs. RHE.**

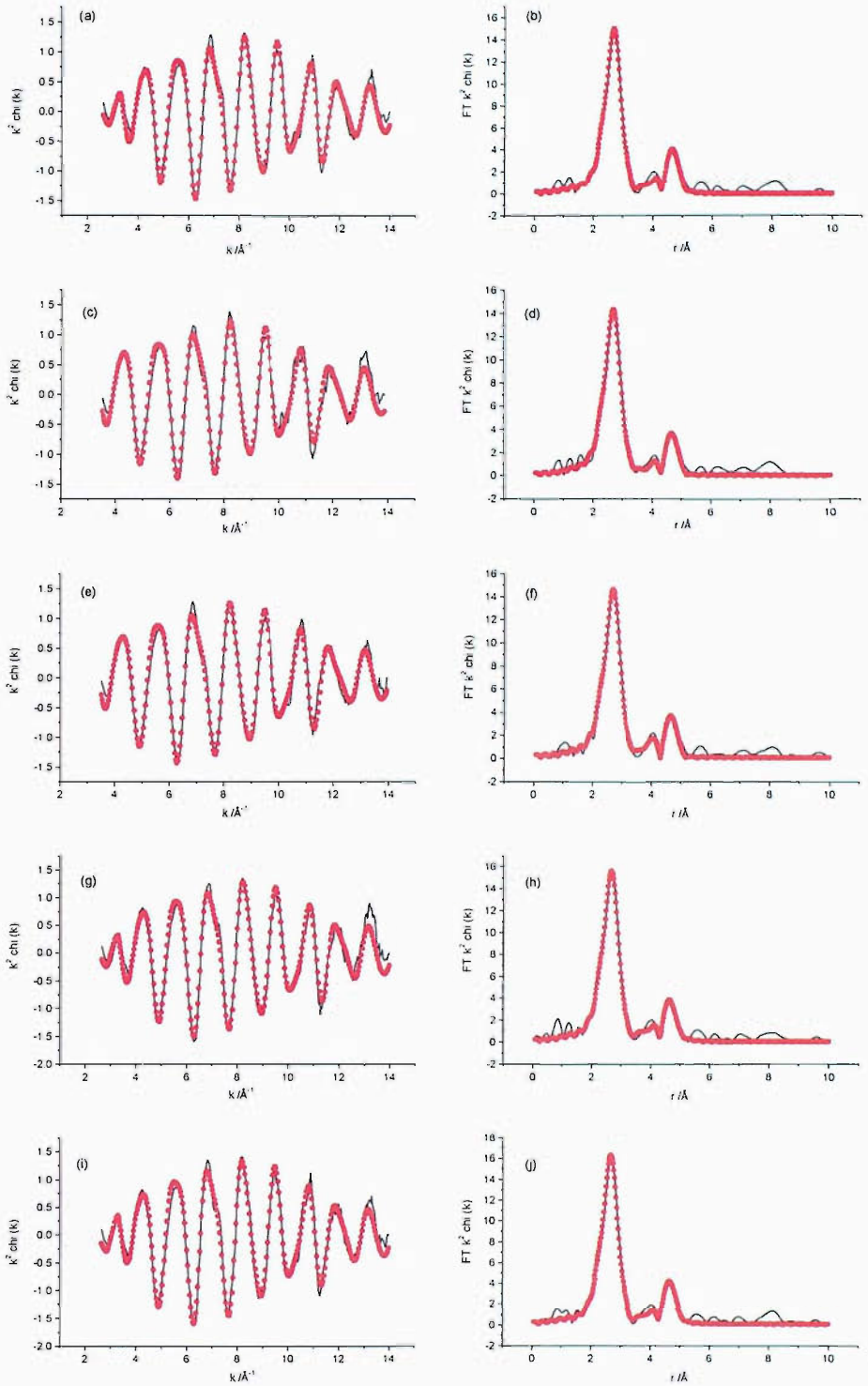

Figure 20 **k^2 weighted Pt L_{III} edge experimental data and fit (left) and corresponding Fourier transform (right) phase corrected for backscattering from Pt. PtCr 1:1 catalyst, (a & b): as prepared, (c & d): half-cell O.C., (e & f): half-cell 0.0 V vs. RHE, (g & h): mini-cell O.C., (i & j): mini-cell 0.7 V vs. RHE.**

Table 11 Structural parameters for the PtCr (1:1) catalyst under varying conditions obtained by fitting the Cr K edge EXAFS data.

Condition	Shell	Calculated parameters (Cr K edge)				
		N	*R* /Å	$2\sigma^2$ /Å^2	E_f /eV	R_{exafs}
As prepared	Cr-O	0.6 ±0.3	1.92 ±0.02	0.012 ±0.007	-2.1 ±0.4	26.36
	Cr-Pt unit 1	5.3 ±0.3	2.70 ±0.003	0.011 ±0.0006		
	Cr-Cr unit 2	1.7 ±0.2	2.71 ±0.009	0.011 ±0.002		
	Cr-Pt	7.4 ±1.0	4.70 ±0.008	0.011 ±0.001		
	Cr-Cr-Pt	unit 2	5.18 ±0.04	0.009 ±0.006		
	Cr-Pt-Cr	unit 1	5.39 ±0.009	0.019 ±0.002		
Half-cell O.C. (0.903 V vs. RHE)	Cr-O	0.6 ±0.3	1.92 ±0.02	0.012 ±0.008	-4.3 ±0.5	27.26
	Cr-Pt unit 1	5.3 ±0.6	2.69 ±0.003	0.010 ±0.0005		
	Cr-Cr unit 2	1.9 ±0.4	2.71 ±0.008	0.011 ±0.002		
	Cr-Pt	8.5 ±1.1	4.70 ±0.008	0.012 ±0.001		
	Cr-Cr-Pt	unit 2	5.18 ±0.04	0.008 ±0.004		
	Cr-Pt-Cr	unit 1	5.40 ±0.008	0.017 ±0.001		
Half-cell (0.0 V vs. RHE)	Cr-O	0.7 ±0.3	1.92 ±0.02	0.014 ±0.009	-4.2 ±0.5	26.77
	Cr-Pt unit 1	5.4 ±0.7	2.70 ±0.003	0.010 ±0.0006		
	Cr-Cr unit 2	2.0 ±0.4	2.71 ±0.008	0.010 ±0.002		
	Cr-Pt	8.9 ±1.2	4.70 ±0.008	0.011 ±0.001		
	Cr-Cr-Pt	unit 2	5.18 ±0.04	0.014 ±0.006		
	Cr-Pt-Cr	unit 1	5.39 ±0.009	0.017 ±0.002		
Mini-cell O.C. (1.001 V vs. RHE)	Cr-O	0.3 ±0.1	1.83 ±0.04	0.012 ±0.01	-1.3 ±0.4	27.62
	Cr-Pt unit 1	3.4 ±0.4	2.69 ±0.01	0.011 ±0.002		
	Cr-Cr	2.6 ±0.3	2.69 ±0.008	0.010 ±0.002		
	Cr-Cr	1.1 ±0.5	3.77 ±0.04	0.010 ±0.009		
	Cr-Cr	5.0 ±0.9	4.66 ±0.01	0.011 ±0.003		
	Cr-Pt-Cr	unit 1	5.40 ±0.009	0.010 ±0.002		
Mini-cell (0.7 V vs. RHE)	Cr-O	0.4 ±0.2	1.84 ±0.05	0.018 ±0.01	-1.7 ±0.5	32.61
	Cr-Pt unit 1	3.5 ±0.3	2.69 ±0.01	0.014 ±0.003		
	Cr-Cr	2.6 ±0.3	2.68 ±0.009	0.009 ±0.002		
	Cr-Cr	3.8 ±1.0	4.66 ±0.02	0.008 ±0.004		
	Cr-Pt-Cr	unit 1	5.40 ±0.01	0.010 ±0.002		

Table 12 Structural parameters for the PtCr (1:1) catalyst under varying conditions obtained by fitting the Pt L_{III} edge EXAFS data.

Condition	Shell	Calculated parameters (Pt L_{III} edge)				
		N	*R* /Å	$2\sigma^2$ /Å^2	E_f /eV	R_{exafs}
As prepared	Pt-Cr	4.0 ±0.2	2.70 ±0.004	0.010 ±0.0006	-11.2 ±0.5	19.80
	Pt-Pt	4.2 ±0.3	2.72 ±0.004	0.010 ±0.0006		
	Pt-Pt	2.3 ±0.5	3.83 ±0.01	0.010 ±0.002		
	Pt-Cr	6.9 ±0.7	4.70 ±0.007	0.010 ±0.001		
Half-cell O.C. (0.903 V vs. RHE)	Pt-Cr	3.9 ±0.2	2.70 ±0.005	0.010 ±0.0008	-13.6 ±0.6	20.10
	Pt-Pt	4.5 ±0.4	2.72 ±0.005	0.011 ±0.0007		
	Pt-Pt	2.0 ±0.7	3.83 ±0.02	0.013 ±0.004		
	Pt-Cr	6.0 ±0.8	4.69 ±0.009	0.009 ±0.002		
Half-cell (0.0 V vs. RHE)	Pt-Cr	4.0 ±0.2	2.70 ±0.004	0.010 ±0.0006	-13.7 ±0.5	
	Pt-Pt	4.5 ±0.4	2.72 ±0.004	0.010 ±0.0006		
	Pt-Pt	2.9 ±0.6	3.83 ±0.01	0.012 ±0.002		
	Pt-Cr	5.6 ±0.6	4.69 ±0.008	0.008 ±0.001		
Mini-cell O.C. (1.001 V vs. RHE)	Pt-Cr	4.4 ±0.2	2.70 ±0.005	0.011 ±0.0008	-11.1 ±0.5	21.91
	Pt-Pt	4.5 ±0.4	2.72 ±0.005	0.010 ±0.0008		
	Pt-Pt	2.7 ±0.8	3.84 ±0.02	0.012 ±0.003		
	Pt-Cr	6.1 ±0.8	4.70 ±0.009	0.009 ±0.002		
Mini-cell (0.7 V vs. RHE)	Pt-Cr	4.5 ±0.2	2.71 ±0.004	0.011 ±0.0007	-11.5 ±0.5	19.49
	Pt-Pt	5.0 ±0.4	2.72 ±0.004	0.011 ±0.0007		
	Pt-Pt	2.0 ±0.6	3.83 ±0.02	0.010 ±0.003		
	Pt-Cr	7.3 ±0.8	4.70 ±0.008	0.010 ±0.002		

For both the PtCr (3:1) and (1:1) catalysts, analysis from the chromium perspective (tables 9 and 11) show that O neighbours were present in the first shell under all conditions. Even under reducing conditions such as 0.0 V vs. RHE in a half-cell environment, O neighbours were observed at a distance of 1.92 Å indicating that a fraction of Cr remains oxidised. This can either be Cr at the surface of the particle or a separate Cr oxide phase on the C support. However, the XRD data (section 3.6) does not support the latter as no evidence of a Cr oxide phase was found. Comparing the levels of oxide present, larger numbers of O neighbours (0.6 to 1.3) were present in the PtCr (3:1) case. The fit showed that there were 1.3 O neighbours for the as prepared catalyst, closely resembling the catalyst in the mini-cell environment. A drop to 0.9 was observed for the half-cell at O.C. which dropped further to 0.6 at 0.0 V vs. RHE. The decrease in O neighbours was accompanied by an increase in

metal neighbours with a maximum value of 7.3 at 0.0 V vs. RHE. An increase in metal neighbours was also observed in the second and third coordination shells indicating that the particles formed a more ordered, extended structure under reducing conditions. The mini-cell was found to be a more oxidising environment for the catalyst relative to the half-cell. The O and Pt first shell coordination numbers at O.C. were found to be 1.2 and 5.9, respectively. These values were comparable to the as prepared catalyst and within error no change was observed when the electrode was polarised to 0.7 V vs. RHE.

At the Pt L_{III} edge, fits of the chi data (tables 10 and 12) showed evidence of very few O neighbours in the first shell. For the PtCr (3:1) catalyst, 0.4 O neighbours were observed for the as prepared catalyst at a distance of 2.01 Å. In the half-cell and mini-cell environments and in all cases for the PtCr (1:1) catalyst, no O neighbours were found. However, this may be a result of the number of O neighbours falling below the detection limit for EXAFS. This will be particularly apparent for larger particles in the PtCr (1:1) catalyst where the fraction of platinum atoms at the surface of the particle will be smaller.

The coordination numbers of the metal neighbours provides useful information when considering the degree of segregation within the particle. For a completely mixed particle with no segregation, the ratio of Pt to Cr coordination numbers ($N_{Pt/Cr}$) would be equal to the atomic ratio. Tables 13 and 14 summarise values for $N_{Pt/Cr}$ and also the total number of metal neighbours in the first shell (N_{Pt+Cr}) for both the PtCr (3:1) and (1:1) catalysts, respectively, across the range of conditions.

Table 13 Summary of N_{Pt+Cr} and $N_{Pt/Cr}$ values for PtCr (3:1) at both the Cr K and Pt L_{III} edges under a range of conditions.

Condition	Cr K		Pt L_{III}	
	N_{Pt+Cr}	$N_{Pt/Cr}$	N_{Pt+Cr}	$N_{Pt/Cr}$
As prepared	6.3 ±0.3	-	6.1 ±0.4	3.9 ±0.8
Half-cell O.C.	6.4 ±0.6	-	7.0 ±0.7	5.5 ±2.0
Half-cell 0.0 V	7.3 ±0.8	-	7.2 ±0.6	3.8 ±0.7
Mini-cell O.C.	5.9 ±0.3	-	6.7 ±0.7	2.6 ±0.6
Mini-cell 0.7 V	5.4 ±0.5	-	6.7 ±0.7	3.7 ±1.0

Table 14 **Summary of N_{Pt+Cr} and $N_{Pt/Cr}$ values for PtCr (1:1) at both the Cr K and Pt L_{III} edges under a range of conditions.**

Condition	Cr K		Pt L_{III}	
	N_{Pt+Cr}	$N_{Pt/Cr}$	N_{Pt+Cr}	$N_{Pt/Cr}$
As prepared	7.1 ±0.5	3.1 ±0.5	8.2 ±0.5	1.1 ±0.1
Half-cell O.C.	7.2 ±1.0	2.7 ±0.9	8.4 ±0.6	1.2 ±0.2
Half-cell 0.0 V	7.4 ±1.1	2.7 ±0.9	8.4 ±0.6	1.1 ±0.2
Mini-cell O.C.	6.0 ±0.6	1.3 ±0.3	8.8 ±0.6	1.0 ±0.1
Mini-cell 0.7 V	6.1 ±0.6	1.4 ±0.2	9.5 ±0.6	1.1 ±0.1

Fits at the Cr K edge for the PtCr (3:1) catalyst showed no sign of Cr neighbours in the first shell suggesting that non-oxidised Cr was well distributed in the bulk of the particle. This was confirmed by the value of $N_{Pt/Cr}$ at the Pt L_{III} edge which was close to the atomic ratio of 3, within error. Values of N_{Pt+Cr} gave good agreement when comparing the two edges in the half-cell and in the as prepared catalyst. Smaller values for the mini-cell at the Cr K edge can be accounted for by the increase in O neighbours as a result of the more oxidising conditions. For the PtCr (1:1) catalyst, the most apparent change compared to the PtCr (3:1) catalyst was the presence of Cr neighbours in the first shell with coordination numbers ranging from 1.7 to 2.6. This change arose due to the increase in the Cr content of the catalyst. At the Pt L_{III} edge, values of $N_{Pt/Cr}$ very close to the atomic ratio of 1 were found. Deviations from this were found at the Cr K edge for the as prepared catalyst and under half-cell conditions when values of approximately 3 were obtained. This indicates an uneven distribution of metal atoms within the particle and may be explained by the proportion of Cr atoms that are at the surface of the particle.

The value of N_{Pt+Cr} for the PtCr (1:1) catalyst at the Pt L_{III} remains constant, within error, across the range of conditions. The increase in value relative to the PtCr (3:1) catalyst can be explained in terms of particle sizes. The PtCr (1:1) catalyst has a larger particle size of 8.5 nm (section 3.3) compared to 6.0 nm for the PtCr (3:1) catalyst. This reduces the fraction of surface atoms resulting in an increase in coordination numbers. For both catalysts, in contrast to the Pt L_{III} edge, smaller values of N_{Pt+Cr} were observed at the Cr K edge. This can be accounted for if Cr atoms reside at the surface of the particle and by the fact that oxygen neighbours in

the first shell have not been included. The value of N_{Pt+Cr} in the PtCr (1:1) case does not remain constant over all conditions and a drop from approximately 7 to 6 is observed in the mini-cell. This is accompanied by a change in the distribution of Pt to Cr neighbours with an increase in Cr neighbours and corresponding decrease in Pt and O neighbours in the first shell. This suggests a structural change to the catalyst taking place under the oxidising conditions of the mini-cell.

For the (3:1) catalyst at the Cr K edge, a pronounced peak was observed between 5.46 and 5.48 Å in the Fourier transforms (figure 17). The size of the peak was attributed to multiple scattering as the peak position was approximately double the Pt first shell distance of 2.72 to 2.73 Å. This suggests that the multiple scattering follows a linear path consisting of: Cr – Pt – Cr. This arrangement was used to fit the data and corresponds to unit 1 in table 9. As the multiple scattering shell is modelled as part of a unit of three atoms, it is dependent on the Pt first shell coordination number and cannot be altered independently. The lack of Cr in the first shell and the order of metal atoms in the multiple scattering unit provides evidence that very little Cr clustering is taking place in the (3:1) catalyst.

The presence of Cr in the first shell of the (1:1) catalyst means that there were two possible multiple scattering paths. Using multiple scattering peaks at 5.2 and 5.4 Å gave the best fit to the EXAFS data. Unit 1 comprised of Cr – Pt – Cr while unit 2, included to account for the Cr neighbours in the first shell, was set as Cr – Cr – Pt. Other multiple scattering including Cr – Pt – Pt and Cr - Cr – Cr were possible but both resulted in increased R_{exafs} values and were discounted. The absence of a Cr - Cr – Cr multiple scattering path indicates that no detectable Cr phase was present and that the catalyst was well mixed.

The first shell Pt-Pt distance for the as prepared 40 wt. % Pt catalyst was approximately 2.76 Å [41]. The Pt-Pt distance for the (3:1) catalyst was 2.74 Å while a value of 2.72 Å was found for the (1:1) catalyst. No changes in the Pt-Pt distance were observed across the range of conditions. The lattice contractions can be related to the Pt electronic properties determined by the XANES in section 3.5.1 with the larger d-band vacancy of the (1:1) catalyst corresponding to the shortest Pt-Pt distances. This is a good indication that the increased Cr content of the (1:1)

catalyst relative to the (3:1) catalyst is well mixed with the Pt and incorporated into the bulk of the particle.

3.5.3.2 PtCo (3:1)

The k^2 weighted EXAFS data with the corresponding Fourier transform obtained at the Co K and Pt L_{III} edges for the PtCo (3:1) catalyst are shown in figures 21 and 22, respectively. Data were collected under the following conditions: as prepared catalyst in air, O.C. and 0.0 V vs. RHE in the half-cell, O.C. and 0.7 V vs. RHE in the mini-cell. The parameters obtained by fitting the data at the Co K and Pt L_{III} edges are shown in tables 15 and 16, respectively.

Analysis of the Co K edge data (table 15) showed that the number of O neighbours varied considerably depending on conditions. The as prepared catalyst has 1.1 O neighbours decreasing to 0.3 at O.C. in the half-cell and this change was accompanied by an increase in Pt neighbours from 3.0 to 5.8. Given that the electrode has not undergone any electrochemical process, the change could be linked to the dissolution of cobalt oxide. The oxide layer has been found to dissolve in phosphoric acid, leaving a dealloyed pure Pt surface region on top of the bulk alloy [10,42]. Even in dilute acid solutions, dissolution of Co from surface layers has been observed [43]. Further evidence of changes to the surface layers come from the O.C. potentials. A lower value of 0.983 V vs. RHE is observed in the half-cell relative to 1.005 V vs. RHE in the mini-cell which could be accounted for by a loss of surface oxides. Unlike the PtCr catalysts where oxide is present under all conditions, the remaining oxide can be fully reduced at 0.0 V vs. RHE under half-cell conditions. In the mini-cell 1.0 O neighbours were observed at O.C. decreasing to 0.8 at 0.7 V vs. RHE. This closely resembles the values found for the as prepared catalyst indicating that in the mini-cell under non-flooded conditions stable cobalt oxide remains at the surface of the particle or on the C support. From the Pt perspective (table 16), when compared with the PtCr catalysts, more O neighbours were required in the fits over a greater range of conditions. Values between 0.7 and 0.9 were observed for the as prepared and mini-cell environments. Analysis of the data showed 0.5 O neighbours for the catalyst at O.C. in the half-cell while complete reduction of Pt occurs at 0.0 V vs. RHE.

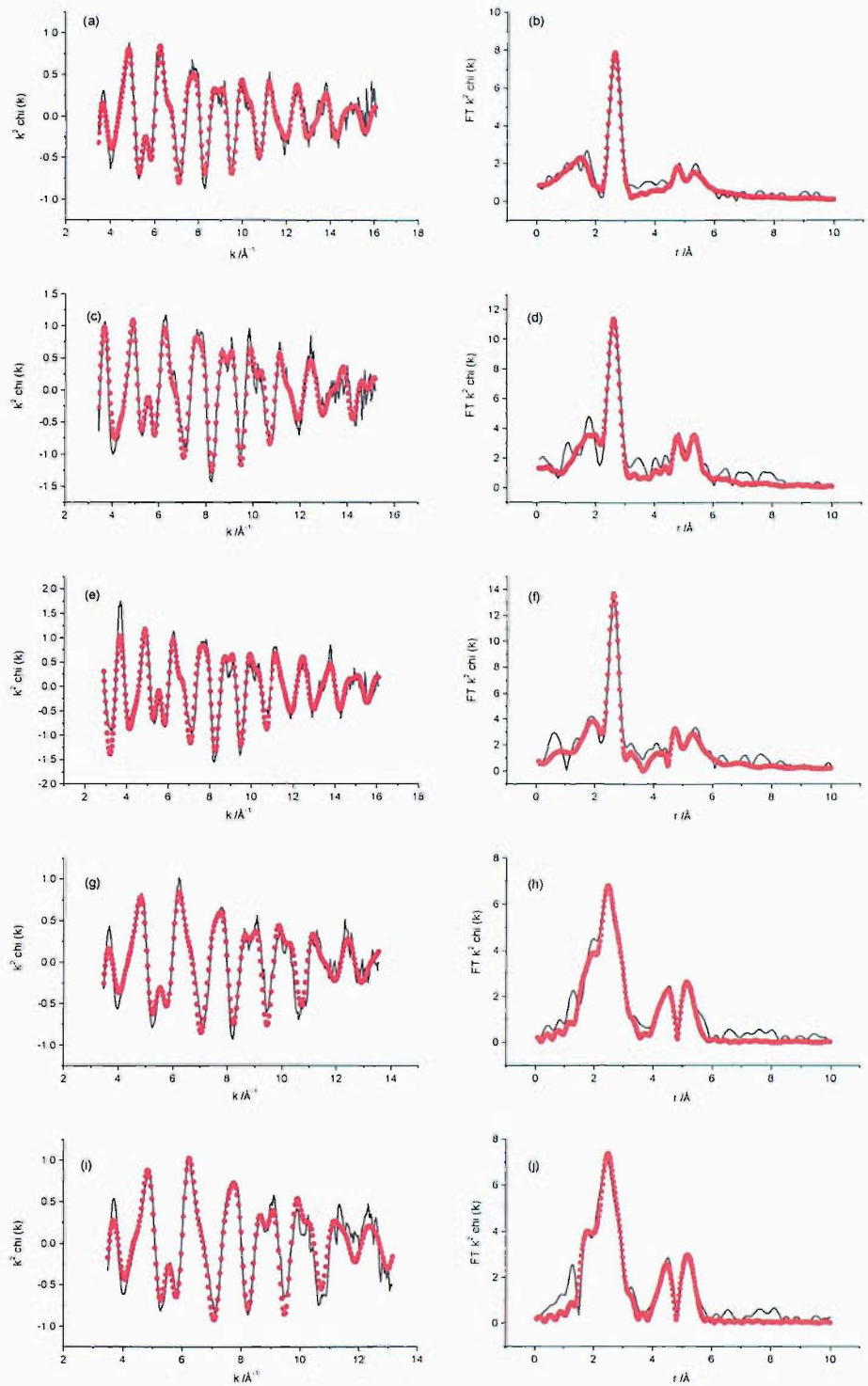

Figure 21 **k^2 weighted Co K edge experimental data and fit (left) and corresponding Fourier transform (right) phase corrected for backscattering from Co. PtCo 3:1 catalyst, (a & b): as prepared, (c & d): half-cell O.C., (e & f): half-cell 0.0 V vs. RHE, (g & h): mini-cell O.C., (i & j): mini-cell 0.7 V vs. RHE.**

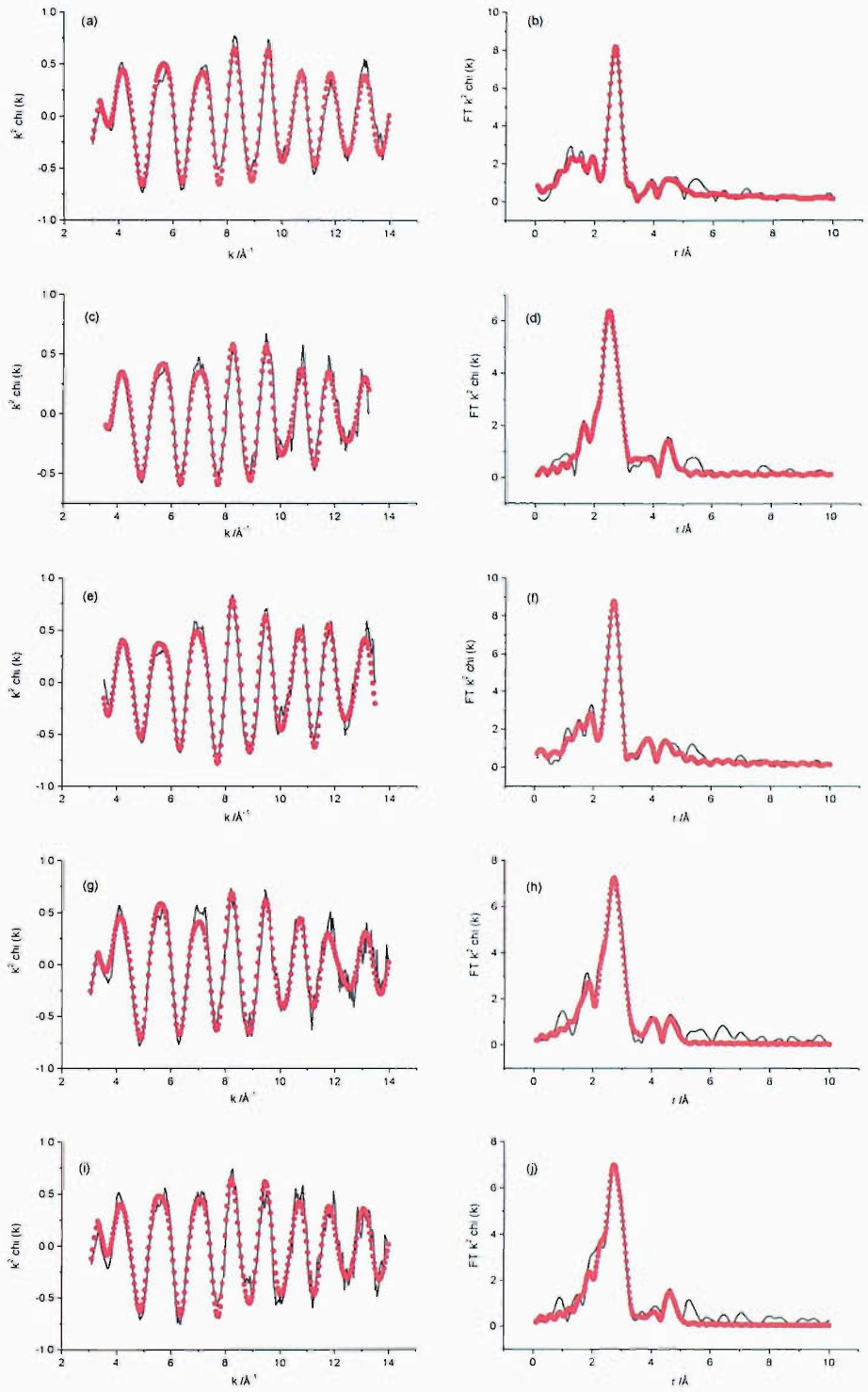

Figure 22 **k^2 weighted Pt L_{III} edge experimental data and fit (left) and corresponding Fourier transform (right) phase corrected for backscattering from Pt. PtCo 3:1 catalyst, (a & b): as prepared, (c & d): half-cell O.C., (e & f): half-cell 0.0 V vs. RHE, (g & h): mini-cell O.C., (i & j): mini-cell 0.7 V vs. RHE.**

Table 15 Structural parameters for the PtCo (3:1) catalyst under varying conditions obtained by fitting the Co K edge EXAFS data.

Condition	Shell	Calculated parameters (Co K edge)				
		N	*R* /Å	$2\sigma^2$ /Å^2	E_f /eV	R_{exafs}
As prepared	Co-O	1.1 ±0.1	2.03 ±0.01	0.014 ±0.005	-4.3 ±1.5	43.56
	Co-Co	1.0 ±0.2	2.64 ±0.02	0.016 ±0.004		
	Co-Pt unit 1	3.0 ±0.4	2.69 ±0.006	0.012 ±0.0007		
	Co-Pt	4.0 ±1.2	4.71 ±0.01	0.013 ±0.002		
	Co-Pt-Qa	unit 1	5.41 ±0.02	0.014 ±0.003		
	where Qa = 0.5Pt : 0.5Co ±0.1					
Half-cell O.C. (0.983 V vs. RHE)	Co-O	0.3 ±0.1	1.86 ±0.06	0.013 ±0.02	-4.6 ±0.5	31.65
	Co-Co	1.0 ±0.3	2.65 ±0.01	0.011 ±0.003		
	Co-Pt unit 1	5.8 ±0.6	2.69 ±0.005	0.014 ±0.0008		
	Co-Pt	6.1 ±1.1	4.71 ±0.009	0.011 ±0.002		
	Co-Pt-Qa	unit 1	5.42 ±0.01	0.016 ±0.002		
	where Qa = 0.6Pt : 0.4Co ±0.07					
Half-cell (0.0 V vs. RHE)	Co-Co	1.1 ±0.2	2.65 ±0.02	0.011 ±0.003	-4.5 ±0.3	30.27
	Co-Pt unit 1	6.4 ±0.3	2.70 ±0.006	0.013 ±0.001		
	Co-Pt	5.7 ±0.9	4.71 ±0.01	0.012 ±0.002		
	Co-Pt-Qa	unit 1	5.43 ±0.01	0.017 ±0.003		
	where Qa = 0.6Pt : 0.4Co ±0.08					
Mini-cell O.C. (1.005 V vs. RHE)	Co-O	1.0 ±0.1	2.04 ±0.01	0.010 ±0.004	-4.6 ±0.8	29.59
	Co-Co	0.6 ±0.2	2.63 ±0.01	0.009 ±0.003		
	Co-Pt unit 1	3.9 ±0.3	2.70 ±0.006	0.013 ±0.0009		
	Co-Pt	5.3 ±1.0	4.72 ±0.01	0.014 ±0.002		
	Co-Pt-Qa	unit 1	5.43 ±0.02	0.020 ±0.003		
	where Qa = 0.5Pt : 0.5Co ±0.08					
Mini-cell (0.7 V vs. RHE)	Co-O	0.8 ±0.1	2.04 ±0.01	0.002 ±0.001	-3.8 ±0.8	30.74
	Co-Co	0.9 ±0.2	2.62 ±0.02	0.013 ±0.0003		
	Co-Pt unit 1	4.0 ±0.3	2.70 ±0.007	0.013 ±0.0009		
	Co-Pt	2.5 ±1.2	4.71 ±0.02	0.011 ±0.004		
	Co-Pt-Qa	unit 1	5.43 ±0.02	0.015 ±0.003		
	where Qa = 0.5Pt : 0.5Co ±0.1					

Table 16 Structural parameters for the PtCo (3:1) catalyst under varying conditions obtained by fitting the Pt L_{III} edge EXAFS data.

Condition	Shell	Calculated parameters (Pt L_{III} edge)				
		N	R /Å	$\Delta\sigma^2$ /Å	ΔE_f /eV	R_{exafs}
As prepared	Pt-O	0.8 ±0.1	2.00 ±0.01	0.013 ±0.004	-12.0 ±0.5	22.24
	Pt-Co	1.1 ±0.1	2.68 ±0.008	0.012 ±0.002		
	Pt-Pt	4.4 ±0.2	2.73 ±0.003	0.011 ±0.0004		
	Pt-Pt	1.5 ±0.5	3.86 ±0.02	0.014 ±0.004		
	Pt-Co	2.7 ±0.5	4.7 ±0.01	0.014 ±0.003		
Half-cell O.C. (0.983 V vs. RHE)	Pt-O	0.5 ±0.1	2.00 ±0.02	0.006 ±0.004	-14.1 ±0.9	21.79
	Pt-Co	0.9 ±0.1	2.67 ±0.009	0.010 ±0.002		
	Pt-Pt	3.8 ±0.3	2.73 ±0.005	0.011 ±0.0006		
	Pt-Pt	1.5 ±0.4	3.85 ±0.01	0.010 ±0.002		
	Pt-Co	2.1 ±0.4	4.68 ±0.01	0.010 ±0.003		
Half-cell (0.0 V vs. RHE)	Pt-Co	1.0 ±0.2	2.69 ±0.01	0.013 ±0.002	-13.1 ±0.7	20.84
	Pt-Pt	5.2 ±0.3	2.73 ±0.004	0.011 ±0.0005		
	Pt-Pt	1.9 ±0.4	3.85 ±0.01	0.009 ±0.002		
	Pt-Co	2.9 ±0.6	4.7 ±0.02	0.014 ±0.003		
Mini-cell O.C. (1.005 V vs. RHE)	Pt-O	0.9 ±0.1	2.00 ±0.01	0.009 ±0.003	-13.1 ±0.7	25.93
	Pt-Co	1.3 ±0.2	2.68 ±0.009	0.010 ±0.001		
	Pt-Pt	4.1 ±0.3	2.73 ±0.005	0.012 ±0.0007		
	Pt-Pt	1.7 ±0.5	3.87 ±0.01	0.010 ±0.003		
	Pt-Co	2.5 ±0.7	4.69 ±0.02	0.015 ±0.005		
Mini-cell (0.7 V vs. RHE)	Pt-O	0.7 ±0.1	2.04 ±0.02	0.013 ±0.006	-13.5 ±0.7	28.86
	Pt-Co	1.0 ±0.2	2.69 ±0.01	0.011 ±0.002		
	Pt-Pt	4.9 ±0.3	2.73 ±0.004	0.012 ±0.0006		
	Pt-Pt	1.4 ±0.7	3.87 ±0.03	0.015 ±0.006		
	Pt-Co	2.8 ±0.7	4.67 ±0.02	0.014 ±0.004		

As mentioned previously, the value of $N_{Pt/Co}$ gives an idea of the segregation within the catalyst (table 17). The simplest catalyst condition to analyse is where no O neighbours are present as is the case in the half-cell at 0.0 V vs. RHE. Values of 6.1 and 5.0 for $N_{Pt/Co}$ were found at the Co K and Pt L_{III} edges, respectively, both larger than the expected atomic ratio for a perfectly mixed catalyst. This indicates a degree of segregation within the particle or a significant loss of Co from the particle compared to the prepared composition. In all other cases oxides are present at the surface making it difficult to make comparisons especially given the large errors involved. The values of N_{Pt+Co} at the Co K edge show the effect of varying the

conditions. In the half-cell values of approximately 7 were reached but for the as prepared catalyst and for the catalyst under mini-cell conditions, smaller values ranging from 4 to 5 were found. Within error the number of Co neighbours remains constant across all conditions. Therefore, the large coordination numbers found in the half-cell may reflect the dissolution of Co oxide and the movement of the remaining Co metal into the bulk giving rise to increased Pt neighbours. These changes in coordination numbers at the Co K edge are represented in figure 23. At the Pt L_{III} edge, much less variation was observed with values of N_{Pt+Co} ranging between 5 and 6.

Table 17 **Summary of N_{Pt+Co} and $N_{Pt/Co}$ values for PtCo (3:1) at both the Co K and Pt L_{III} edges under a range of conditions.**

Condition	Co K		Pt L_{III}	
	N_{Pt+Co}	$N_{Pt/Co}$	N_{Pt+Co}	$N_{Pt/Co}$
As prepared	4.0 ±0.6	3.2 ±1.4	5.5 ±0.3	4.0 ±0.6
Half-cell O.C.	6.9 ±0.9	5.6 ±3.1	4.7 ±0.4	4.0 ±0.8
Half-cell 0.0 V	7.4 ±0.5	6.1 ±1.8	6.2 ±0.5	5.0 ±1.5
Mini-cell O.C.	4.5 ±0.5	6.1 ±3.5	5.5 ±0.5	3.1 ±0.8
Mini-cell 0.7 V	4.9 ±0.5	4.4 ±1.7	5.9 ±0.5	5.0 ±1.7

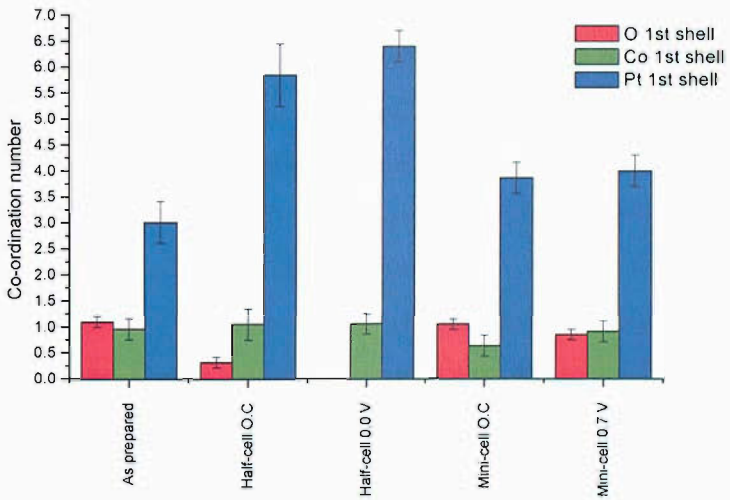

Figure 23 **First shell coordination numbers for the PtCo (3:1) catalyst taken from EXAFS at the Co K edge under varying conditions.**

A multiple scattering peak is present in the Fourier transform (figure 21) between 5.41 and 5.43 Å, a slightly shorter distance than the multiple scattering peak in the PtCr (3:1) case. The multiple scattering path that gave the smallest R_{exafs} value consisted of: Co – Pt – Q_a where Q_a corresponds to a mixed site containing Pt and Co. This was found to give a better fit than when Q_a was equivalent to pure Pt or Co. The fraction of metal atoms in the mixed site could be refined to minimise R_{exafs}. The ratio of Pt:Co in the mixed site ranged from 0.5:0.5 to 0.6:0.4 indicating a well mixed catalyst while the presence of multiple scattering suggests that the Co is inside the particle. Further evidence of a well mixed catalyst comes from the contraction of the Pt-Pt distance. The distance of 2.73 Å remained constant across all conditions and lies between the values of 2.72 and 2.74 Å for the PtCr (1:1) and (3:1) catalysts, respectively.

3.5.3.3 PtTi (1:1)

k^2 weighted EXAFS data with the corresponding Fourier transform obtained at the Ti K and Pt L_{III} edges for the PtTi (1:1) catalyst are shown in figures 24 and 25, respectively. Data were collected under the following conditions: as prepared catalyst in air, O.C. and 0.0 V vs. RHE in the half-cell, O.C. and 0.7 V vs. RHE in the mini-cell. The parameters obtained by fitting the data at the Ti K and Pt L_{III} edges are shown in tables 18 and 19, respectively. The noise in the EXAFS data at the Ti K edge (figure 24) demonstrates the difficulty of using lower energy X-rays compared to the Cr and Co K edges. The problem is particularly severe when using *in situ* cells such as the flooded half-cell or mini-cell. This is because the X-ray absorption of the Kapton window or electrolyte becomes greater than the Ti resulting in the absorption edge being masked. The noise can be reduced by collecting more scans. For example, the EXAFS data in figure 24(g) required averaging of 12 scans. Due to the time taken to collect the scans, EXAFS data has not been collected under polarised conditions in the mini-cell.

The most noticeable difference in the PtTi EXAFS data (figure 24) compared to the PtCr and PtCo catalysts are the large amplitude oscillations in the low k region (4 to 6 $Å^{-1}$) at the secondary metal K edge. This is a result of backscattering from low Z neighbours such as oxygen and is reflected in the fit (table 18) with very large

numbers of O neighbours across all conditions. For the as prepared catalyst there were 2.3 O neighbours falling to 1.6 under both half and mini-cell conditions. This change was accompanied by an increase in the number of metal neighbours in the first shell. Despite this, the total number of metal neighbours remains small with a maximum value of 4.5 in the half-cell at 0.0 V vs. RHE. This corresponds with the rapid dampening of the EXAFS data in the high k region (8 to 12 $Å^{-1}$).

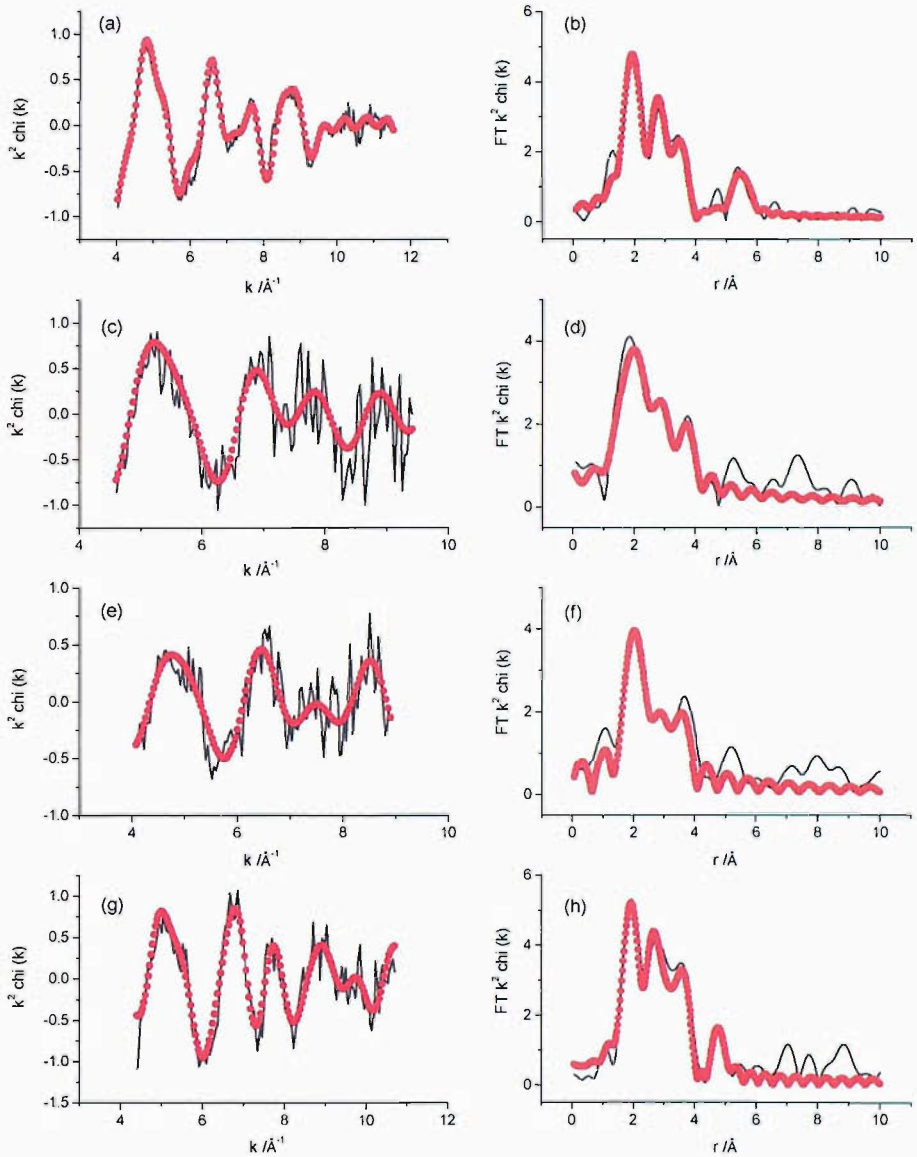

Figure 24 **k^2 weighted Ti K edge experimental data and fit (left) and corresponding Fourier transform (right) phase corrected for backscattering from O. PtTi 1:1 catalyst, (a & b): as prepared, (c & d): half-cell O.C., (e & f): half-cell 0.0 V vs. RHE, (g & h): mini-cell O.C., (i & j): mini-cell 0.7 V vs. RHE.**

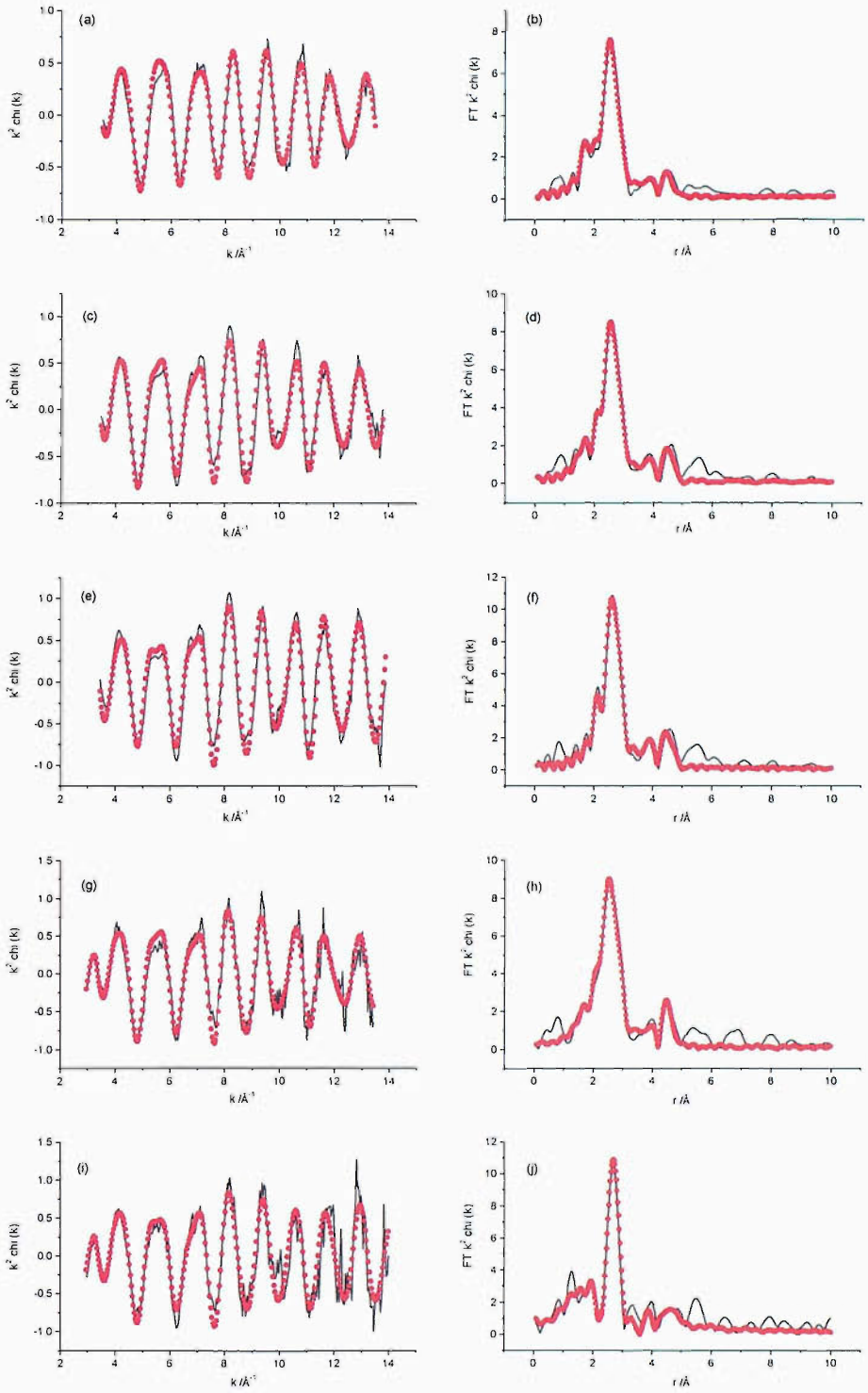

Figure 25 **k^2 weighted Pt L_{III} edge experimental data and fit (left) and corresponding Fourier transform (right) phase corrected for backscattering from Pt. PtTi 1:1 catalyst, (a & b): as prepared, (c & d): half-cell O.C., (e & f): half-cell 0.0 V vs. RHE, (g & h): mini-cell O.C., (i & j): mini-cell 0.7 V vs. RHE.**

Table 18 Structural parameters for the PtTi (1:1) catalyst under varying conditions obtained by fitting the Ti K edge EXAFS data.

Condition	Shell	Calculated parameters (Ti K edge)				
		N	*R* /Å	$2\sigma^2$ /Å^2	E_f /eV	R_{exafs}
As prepared	Ti-O	2.3 ±0.1	1.99 ±0.009	0.012 ±0.001	-9.1 ±1	23.99
	Ti-Pt	1.3 ±0.2	2.76 ±0.01	0.012 ±0.003		
	Ti-Ti	1.0 ±0.1	3.17 ±0.01	0.009 ±0.003		
	Ti-Pt	1.3 ±0.3	3.60 ±0.02	0.011 ±0.003		
	Ti-Ti	4.2 ±0.7	5.52 ±0.02	0.014 ±0.003		
Half-cell O.C. (0.954 V vs. RHE)	Ti-O	1.6 ±0.4	1.90 ±0.05	0.009 ±0.005	2.3 ±6	56.44
	Ti-Pt	2.4 ±1.2	2.73 ±0.05	0.014 ±0.01		
	Ti-Ti	0.7 ±0.6	2.50 ±0.07	0.014 ±0.02		
Half-cell (0.0 V vs. RHE)	Ti-O	1.6 ±0.3	2.04 ±0.04	0.012 ±0.006	-11.6 ±4	48.40
	Ti-Pt	3.4 ±0.8	2.83 ±0.03	0.011 ±0.005		
	Ti-Ti	1.1 ±0.3	2.56 ±0.03	0.011 ±0.008		
Mini-cell O.C. (0.984 V vs. RHE)	Ti-O	1.6 ±0.2	1.93 ±0.02	0.006 ±0.003	3.4 ±2	34.82
	Ti-Pt	2.7 ±0.5	2.77 ±0.02	0.009 ±0.002		
	Ti-Pt	4.9 ±0.9	3.14 ±0.02	0.013 ±0.003		
	Ti-Ti	2.1 ±0.8	4.69 ±0.05	0.013 ±0.009		

Table 19 Structural parameters for the PtTi (1:1) catalyst under varying conditions obtained by fitting the Pt L_{III} edge EXAFS data.

Condition	Shell	Calculated parameters (Pt L_{III} edge)				
		N	*R* /Å	$2\sigma^2$ /Å^2	E_f /eV	R_{exafs}
As prepared	Pt-O	0.5 ±0.1	2.02 ±0.01	0.003 ±0.002	-13.4 ±0.7	21.59
	Pt-Ti	0.9 ±0.1	2.73 ±0.008	0.005 ±0.001		
	Pt-Pt	4.8 ±0.3	2.72 ±0.004	0.013 ±0.0007		
	Pt-Pt	1.7 ±0.4	3.86 ±0.013	0.010 ±0.002		
	Pt-Ti	2.4 ±0.6	4.71 ±0.02	0.012 ±0.004		
Half-cell O.C. (0.954 V vs. RHE)	Pt-O	0.5 ±0.1	1.99 ±0.02	0.007 ±0.005	-14.1 ±0.8	24.80
	Pt-Ti	0.8 ±0.2	2.75 ±0.01	0.008 ±0.003		
	Pt-Pt	6.1 ±0.4	2.75 ±0.004	0.012 ±0.0005		
	Pt-Pt	2.8 ±0.6	3.89 ±0.01	0.013 ±0.002		
	Pt-Ti	3.6 ±0.7	4.78 ±0.01	0.009 ±0.002		
Half-cell (0.0 V vs. RHE)	Pt-Ti	0.9 ±0.3	2.77 ±0.02	0.012 ±0.005	-13.8 ±0.8	24.44
	Pt-Pt	6.9 ±0.3	2.76 ±0.003	0.010 ±0.0004		
	Pt-Pt	3.0 ±0.7	3.89 ±0.01	0.011 ±0.002		
	Pt-Ti	4.4 ±0.8	4.78 ±0.01	0.009 ±0.003		
Mini-cell O.C. (0.984 V vs. RHE)	Pt-O	0.7 ±0.2	2.00 ±0.03	0.018 ±0.01	-13.3 ±0.7	30.32
	Pt-Ti	1.1 ±0.2	2.74 ±0.02	0.008 ±0.003		
	Pt-Pt	6.0 ±0.5	2.76 ±0.005	0.011 ±0.0007		
	Pt-Pt	2.5 ±0.8	3.91 ±0.02	0.011 ±0.003		
	Pt-Ti	4.1 ±0.9	4.78 ±0.01	0.009 ±0.003		
Mini-cell (0.7 V vs. RHE)	Pt-O	0.5 ±0.2	2.00 ±0.05	0.013 ±0.01	-12.4 ±1.0	35.93
	Pt-Ti	0.9 ±0.4	2.76 ±0.03	0.012 ±0.007		
	Pt-Pt	6.7 ±0.6	2.75 ±0.005	0.011 ±0.0008		
	Pt-Pt	1.8 ±1.2	3.93 ±0.03	0.012 ±0.006		
	Pt-Ti	3.7 ±1.3	4.76 ±0.02	0.010 ±0.005		

At the Pt L_{III} edge, fits of the data (table 19) showed far fewer O neighbours with values from 0.5 to 0.7 for the as prepared catalyst, half-cell at O.C. and mini-cell at O.C. The platinum seems to be far more susceptible to the changing conditions than Ti. For example, the platinum can be fully reduced as shown by the complete loss of O neighbours at 0.0 V vs. RHE in the half-cell (figure 26). This contrasts with results at the Ti K edge where the O coordination number remains constant, between 1.6 and 1.7. This suggests that the increase in metal neighbours observed under *in situ* conditions at both edges can be accounted for by the reduction of Pt.

Similar numbers of Pt neighbours within error were observed at the Pt edge under *in situ* conditions with values between 6 and 7. The result suggests that even under the very oxidising conditions of the ORR in the mini-cell, the catalyst appears more reduced in nature relative to the catalyst in air. The main difference in this case was the presence of water vapour in the oxygen gas flow. This emphasises the importance of being able to collect EXAFS data under operating conditions. The values of $N_{Pt/Ti}$ have also been included in figure 26 and show far larger ratios than the prepared atomic ratio of 1 indicating deviation of the composition of the particle from the composition prepared. This arises due to the segregation of Ti to the surface of the particle and/or the presence of a separate titanium oxide phase.

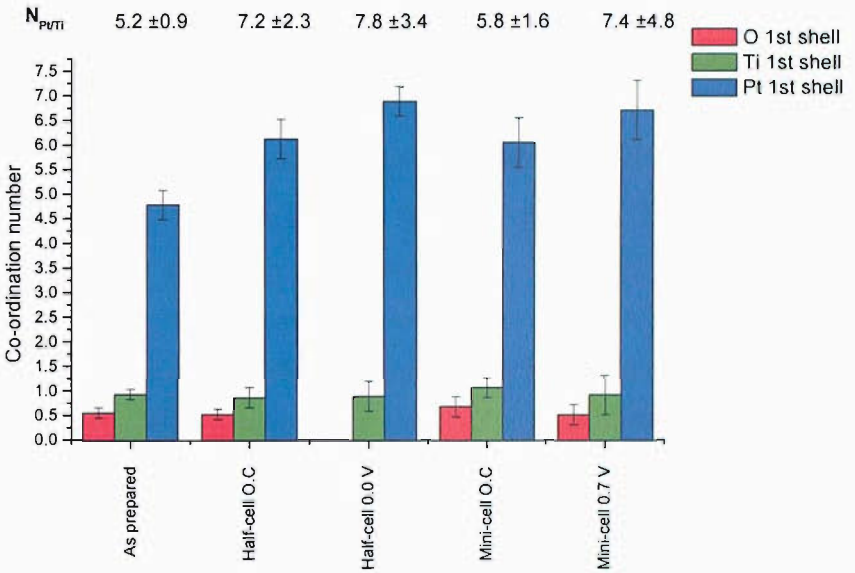

Figure 26 **First shell coordination numbers for the PtTi (1:1) catalyst taken from EXAFS at the Pt L_{III} edge under varying conditions. $N_{Pt/Ti}$ values calculated from ratio of N_{Pt} to N_{Ti}.**

Unlike the PtCr and PtCo catalysts, the Fourier transforms (figure 24) showed no clear multiple scattering peaks at the Ti K edge. This suggests that not much of the Ti is incorporated into or onto the Pt particles and that most of it is associated with a separate Ti oxide phase. At the Pt L_{III} edge, increases in metal neighbours were observed in the second and third coordination shells under *in situ* conditions suggesting small increases in the incorporation of Ti into the particles. However, this is primarily due to reduction of Pt neighbours as the numbers of Ti neighbours remain relatively similar. Further evidence of segregation comes from the Pt-Pt

distance. For the as prepared catalyst a distance of 2.72 Å was used for fitting the Pt first shell indicating a significant contraction relative to a pure Pt catalyst. Under half and mini-cell conditions, the distance increased to a value between 2.75 and 2.76 Å. Increased segregation of the Ti phase would result in this change in the Pt-Pt distance.

3.6 *Ex situ* XRD

The principle of EXAFS relies on giving an insight into the average environment of the element in question. This proves to be an advantage as there is no reliance on having a system with long range order. The ability of EXAFS to measure the average local environment also has a number of disadvantages. EXAFS gives no indication as to whether there are separate phases present within the catalyst. As a result of this it is important to be able to combine EXAFS with other techniques such as XRD. XRD provides information on the presence of separate phases such as non-alloyed pure metal phases or oxide phases. In addition, XRD can be used to determine the lattice parameter and crystallite size (table 20). The crystalline size was calculated using the Scherrer equation and the values in table 20 were determined from the mean of the 5 strongest reflections or 4 in the case of the PtCr (1:1) catalyst. The XRD patterns were collected at Johnson Matthey by their technical staff.

Table 20 Lattice parameters and particle size for PtCr, PtCo and PtTi cathode catalysts determined using *ex situ* XRD. Lattice parameters for PtCr (1:1) based on a cubic phase.

Catalyst	Lattice Parameter /Å	Particle Size /nm
PtCr (3:1)	3.87	6.0
PtCr (1:1)	3.86	8.5
PtCo (3:1)	3.85	4.7
PtTi (1:1)	3.90	5.0

The XRD pattern for the PtCr (3:1) catalyst (figure 27) indicated that the sample was composed of a single poorly crystalline platinum chromium alloy phase with crystallographic parameters very close to cubic platinum chromium, Pt_3Cr. The diffraction pattern also showed the presence of superlattice lines which are

indicative that ordering of the crystal system has taken place. There was no evidence to indicate the presence of separate crystalline platinum or chromium phases. However, the possible presence of trace amounts of poorly crystalline platinum could not be ruled out. There was no evidence to indicate the presence of additional platinum chromium phases or oxide phases.

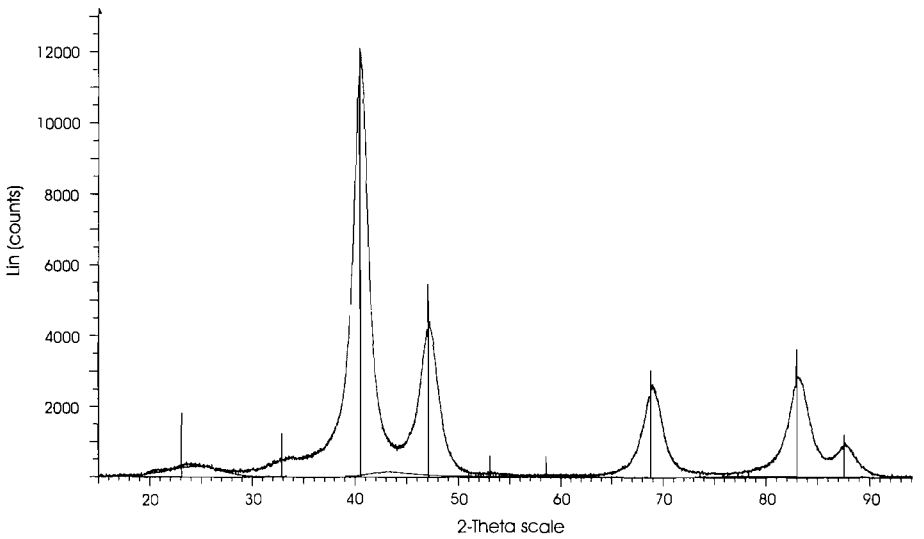

Figure 27 XRD pattern for the as prepared PtCr (3:1) catalyst.

The XRD pattern (figure 28) showed that the PtCr (1:1) catalyst was composed of at least two, possibly three poorly crystalline platinum chromium alloy phases. No reference diffraction data were available to characterise the phases exactly. However, the two predominant phases were very close in crystal parameters to cubic platinum chromium, Pt_3Cr and tetragonal platinum chromium, PtCr. There were a number of weaker unidentified reflections which probably indicated a third phase. However, as the sample cannot be characterised due to the lack of available diffraction data, the possibility that these weaker reflections were related to the predominant two phase cannot be ruled out. As in the case of the PtCr (3:1) catalyst there was no evidence of separate crystalline platinum or chromium particles.

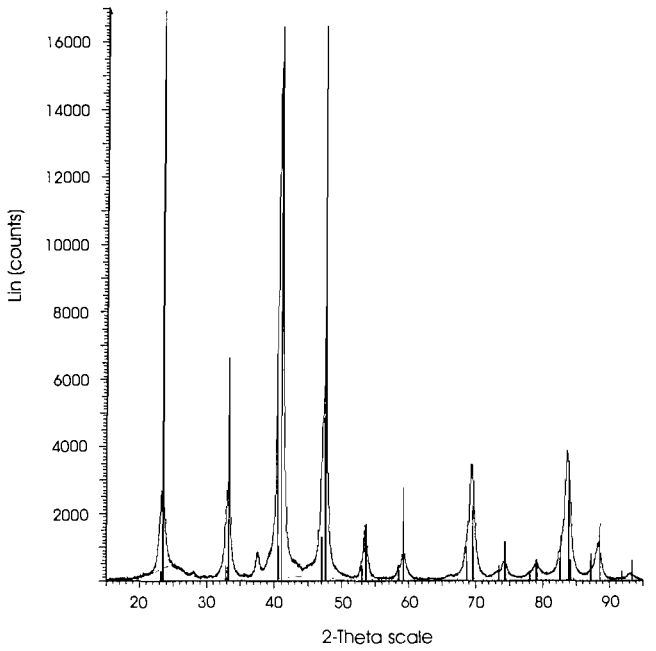

Figure 28 XRD pattern for the as prepared PtCr (1:1) catalyst.

The XRD pattern for the PtCo (3:1) catalyst is shown in figure 29. The predominant phase in the PtCo (3:1) catalyst was very close in crystallographic parameters to cubic platinum cobalt, Pt_3Co. Further analysis of the diffraction pattern revealed this was the only phase present with no indication of crystalline platinum or cobalt. The diffraction also showed slight evidence of superlattice lines indicating a degree of ordering within the sample.

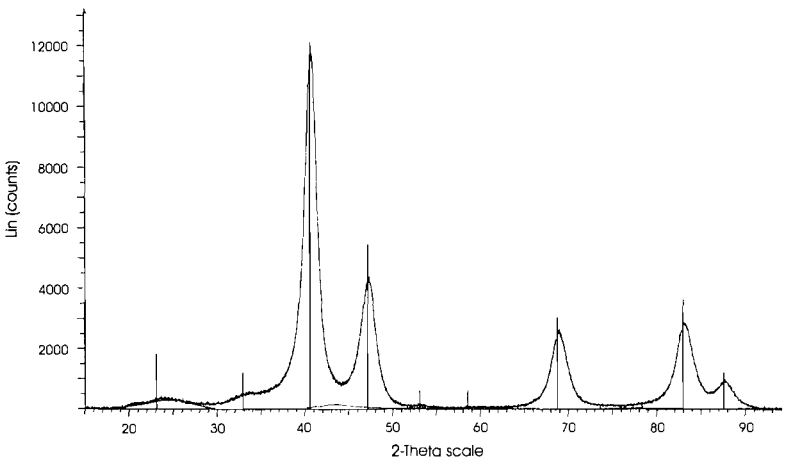

Figure 29 XRD pattern for the as prepared PtCo (3:1) catalyst.

The PtTi (1:1) catalyst was the only case where trace amounts of oxide was found. The diffraction pattern (figure 30) indicated that the catalyst comprised

predominantly of poorly crystalline platinum titanium, Pt_3Ti and trace amount of titanium oxide, TiO_2 (anatase). It was not possible to indicate whether any separate platinum crystallites were present in minor amounts.

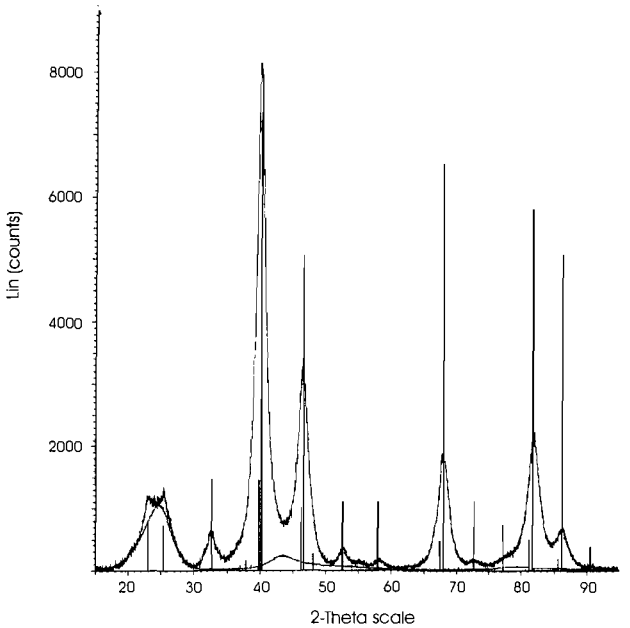

Figure 30 XRD pattern for the as prepared PtTi (1:1) catalyst.

4 DISCUSSION

The following section aims to bring together the electrochemical and structural data for the four cathode catalysts. The catalyst activities were compared by normalising the currents using the *in situ* platinum surface area determined from the CO stripping charge (specific activity) and also using the Pt loadings (mass activity). In terms of decreasing activities, the orders in the mini-cell environment were as follows:

Specific activity	PtCo > PtCr (3:1) > PtCr (1:1) > Pt > PtTi
Mass activity	PtCo > PtCr (3:1) > Pt > PtTi > PtCr (1:1)

These observed trends will be related to the electronic, surface and bulk structural properties as determined by cyclic voltammetry, XAS and XRD.

4.1 Electronic Properties

The electronic property of the Pt was found to vary depending on the secondary metal and the amounts in which it was present. The activity for oxygen reduction is thought to be sensitive to the adsorption strength of oxygen intermediates on the Pt surface [12,17,44]. A mechanism was put forward by Toda *et al.* [15] in which the increase in the 5d vacancies led to an increased 2π electron donation from oxygen to the surface Pt. This was thought to result in an increased strength of the metal-oxygen bond and a weakening of the O-O bond. In addition, the electronic properties have been found to have a strong correlation with the geometric parameters and this will be discussed in section 4.3.

The XANES were collected for the as prepared catalyst and under both half-cell and mini-cell environments. However, in terms of the order of specific activities mentioned previously, it is the mini-cell data which is important. At O.C. in the mini-cell, the relative Pt d-band vacancies decreased as follows: PtCo > PtCr (1:1) > PtCr (3:1) > PtTi. This follows the same trend as the secondary metals electronegativity and, with the exception of the PtCr catalysts, good agreement was found with the specific activities. A possible explanation for the variation of the PtCr catalysts is the accuracy of the specific activity for the PtCr (1:1) catalyst. As a result of the large particle size, the Pt surface area was found to be significantly lower than the values determined for the other catalysts (table 7). Therefore, errors in this measurement would have a more severe impact on the accuracy of the specific activity data.

The relative d-band vacancies in the half-cell were all smaller than those found in the mini-cell, indicating that the catalysts were more reduced. As mentioned in section 3.5.1, HSO_4^- species adsorb strongly to platinum and have been shown to alter the white line region. The effect of the electrolyte was also noted by Stamenkovic *et al.* [27] during studies of well-defined Pt_3Ni and Pt_3Co alloy surfaces. They carried out cyclic voltammetry in $HClO_4$ and H_2SO_4 and found that the coverage of surface oxides was reduced in the latter electrolyte. Changes to the ordering of the relative d-band vacancies were found in the flooded environment. For example the order at 0.0 V vs. RHE in the half-cell is as follows: PtCr (1:1) >

PtCr (3:1) > PtCo > PtTi > Pt. The low relative vacancies observed in the PtCo case may reflect the dissolution of Co in H_2SO_4, as observed in the EXAFS, reducing the electronic effect of the secondary metal.

In all cases the secondary metal caused an increase in the d-band vacancy of Pt relative to the 40 wt. % Pt catalyst. The fact that the specific activity of PtTi falls below the Pt catalyst suggests that the activities cannot be fully explained by an electronic effect. This discrepancy will be examined in the following sections where the surface and bulk structural properties will be considered.

4.2 Surface Properties

Cyclic voltammetry provides a good indication of the structure at the surface of the catalyst. Pronounced hydrogen adsorption/desorption peaks closely resembling the pure Pt catalysts were observed for all four catalysts. This indicates the presence of polycrystalline Pt at the surface of the particles. Unlike the other catalysts, the cyclic voltammetry for the PtCr (1:1) catalyst showed only one clearly defined peak. A possible explanation for this comes from the XRD where, unlike the PtCr (3:1) case, a tetragonal alloy phase was identified in addition to the cubic phase. If this phase was present at the surface of the particles this would lead to changes in the hydrogen adsorption/desorption region. Comparisons of specific activities for the PtCr (1:1) and PtCr (3:1) catalysts show that the tetragonal phase does not give a significant improvement over the cubic phase in terms of catalyst performance.

Estimations of surface composition were made based on theoretical dispersions and experimentally determined active surface areas. However, care must be taken when correlating the surface composition to the activity of the catalysts as the measurements were made in two very different environments. The (3:1) catalysts both showed very high platinum contents at the surface of the particles whereas the (1:1) catalysts showed reduced levels. The high specific activity of the PtCr (1:1) suggests that the high secondary metal content at the surface is not detrimental to the oxygen reduction reaction. However, the nature of the secondary metal may influence the kinetics. In the case of the PtTi (1:1) catalyst, large currents were

observed in the double layer region suggesting the presence of oxide species which was confirmed by both the Ti EXAFS and XRD data.

Assuming that the majority of oxide species are present at the surface of the particle XAS can provide information on the surface properties. The XANES at the secondary metal K edge provide information on the nature of the secondary element and in all cases the XANES suggested the presence of oxide. This was particularly apparent in the case PtTi case where very pronounced pre-edge features were observed. In agreement with the electrochemistry, further analysis of the pre-edge feature indicated TiO_2 which remained in both half-cell and mini-cell conditions providing evidence of poor alloying in the PtTi catalyst. The observations made from the XANES were confirmed by the EXAFS. Oxygen neighbours were shown to fit the chi data under all conditions with the exception of PtCo (3:1) at 0.0 V vs. RHE in the half-cell where the cobalt was fully reduced. However, this may be a result of the electrolyte causing dissolution of cobalt, as shown previously (section 3.5.3.2). For the PtCr and PtCo catalysts, the numbers of O neighbours under mini-cell conditions resemble the as prepared catalyst. In the case of the PtTi catalyst, the O neighbours remained constant for the half-cell and mini-cell environments. This can be related to the electrochemically non-reducible TiO_2 phase detected by XRD (section 4.3).

With the exception of PtTi, the presence of oxidised secondary metal at the surface does not reduce the activity of the catalyst. In fact, the oxide may have a beneficial influence on the electronic properties of the particle [23]. The poor activity of the PtTi catalyst demonstrates that the oxide must be in contact and incorporated into the surface of the particle for improvements to be seen. However, comparing the electronic properties of the PtCr (1:1) and PtCr (3:1) (section 4.1) catalysts with their respective O coordination number suggests that the electronic effect of the surface oxides is small. This demonstrates that incorporating the secondary metal into the bulk of the particle results in a more significant change in d-band vacancies.

The inhibition of chemisorbed oxygenated species onto the Pt surface is thought to play an important role in the catalysts activity towards oxygen reduction [14,45]. Mukerjee *et al.* [14] found that Co exhibited a significantly lower extent of oxide

formation relative to Pt. Although the onset potential is difficult to identify, the CVs in figure 2 show very similar potentials and when normalised to the Pt area provide no evidence that oxide formation is being inhibited. EXAFS at the Pt L_{III} edge provides a way of quantifying the O content at the platinum surface. With the exception of the PtCr (3:1) as prepared catalyst, no O neighbours were used in fitting the EXAFS data for both the PtCr catalysts. As mentioned in section 3.5.3.1, the particle size influences the average number of oxygen neighbours as it determines the fraction of atoms at the surface of the particle. The PtCo and PtTi catalysts have similar particle sizes of 4.7 and 5.0 nm, respectively, allowing direct comparisons to be made. In the mini-cell, for the PtTi catalyst, 0.5 to 0.7 O neighbours were used in the fits at the Pt L_{III} edge compared with 0.7 to 0.9 O neighbours in the PtCo case. The greater activity of PtCo over the PtCr and PtTi catalysts suggest that inhibition of oxide formation is not the dominating factor in improved performance.

4.3 Bulk Structural Properties

The factors affecting the bulk properties of the catalyst include the lattice parameter, particle size and the degree of segregation within the particle. These factors will be considered using a combination of EXAFS and XRD.

A comparison of lattice parameters obtained from EXAFS collected at O.C. in the mini-cell environment is shown in figure 31. The Pt-Pt distance determined by *ex situ* XRD has been included for comparison. All show a contraction in Pt-Pt distance relative to the bulk value and good agreement was found between the XRD and EXAFS parameters. The improved performance with shorter Pt-Pt distances can be related to more favourable bonding geometry. A closer match between Pt atom separation and the O-O distance increases the chances of side on adsorption favouring $4e^-$ reduction. However, the Pt-Pt lattice contractions determined by XRD correlate exactly with the d-band vacancies (section 4.1). In order to determine whether one dominates over the other or if both play a part, the two properties must be separated. However, as they appear to be intrinsically linked this proves very difficult.

The similarity between Pt-M and M-Pt distances for the PtCr (3:1) and (1:1) catalysts indicates a well mixed particle. Differences for the PtCo (3:1) catalyst suggest a degree of segregation while the errors in the PtTi (1:1) data at the Ti K edge make it difficult to draw conclusions.

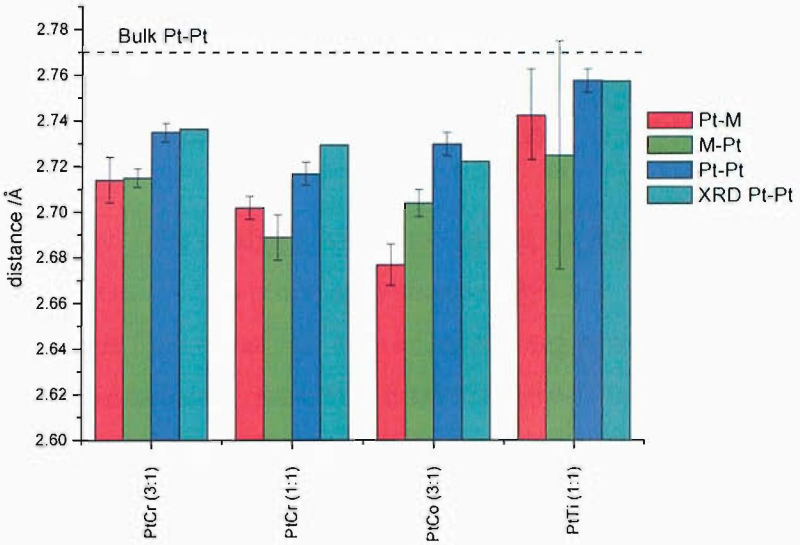

Figure 31 **Comparison of lattice parameters determined by EXAFS data collected at the Pt L_{III} and 2nd metal K edge in the mini-cell environment at O.C. The Pt-Pt distance determined by *ex situ* XRD has been included for comparison.**

More detailed analysis of segregation can be gained from the relative numbers of metal neighbours in the first coordination shell ($N_{Pt/Cr}$). From the platinum perspective both PtCr catalysts show values of $N_{Pt/Cr}$ very close to the atomic ratios indicating well mixed catalysts. From the chromium perspective, the PtCr (3:1) catalyst showed no Cr neighbours while deviation from the atomic ratio was observed for the PtCr (1:1) catalyst. This may be a result of a fraction of Cr remaining oxidised at the surface while the remaining Cr is well mixed in the bulk. A database put together by Norskov *et al.* [46,47] used density functional calculations to determine segregation energies for binary transition metal alloys. This can be used to give an idea of the positioning of non-oxidised Cr within the bulk based on the most thermodynamically stable arrangement. In the case of PtCr, a positive segregation energy between 0.3 and 0.7 eV was found indicating a situation where the impurity, Cr, prefers to remain in the interior of the host. The segregation energy is defined as the energy gain by interchanging an impurity in the bulk with a

host atom in the surface in the dilute limit. In the case of the PtCo catalyst deviation from the atomic ratio was observed at both edges indicating a more segregated structure when compared to the PtCr catalysts. This could be due to dissolution of Co under *in situ* conditions resulting in a change of the atomic ratio. As in the PtCr case, according to Norskov *et al.* the Co would prefer to remain in the interior of the particle. Any loss of Co does not seem detrimental to the catalyst's performance towards oxygen reduction and the remaining Co still exhibits a strong electronic affect (section 4.1) and contraction of the Pt-Pt distance.

Unlike the PtCr and PtCo catalysts, XRD showed that the PtTi catalyst contained a separate oxide phase. EXAFS provides evidence of this with large values of $N_{Pt/Ti}$ indicating deviation from the atomic ratio and a very segregated particle. This may explain the poor performance of the PtTi catalyst in terms of catalysts activity. Based on Pt-Pt distances, electronic and surface properties, PtTi would be expected to show an improvement over the pure Pt catalyst, albeit small. The presence of a separate TiO_2 phase, in addition to having no beneficial properties, has an adverse affect on its performance and suggests a problem with the preparation method. The beneficial properties of Ti may be seen by reducing the Ti content of the catalyst to a ratio that more closely resembles the cubic phase Pt_3Ti and by increasing the heat treatment temperature to ensure improved alloying.

The particle sizes, determined from XRD, ranged from 4.7 nm for the PtCo (3:1) catalyst up to 8.5 nm for the PtCr (1:1) catalyst (table 20). The distribution of surface sites changes with particle size and can in turn, alter the catalysts performance for oxygen reduction which is a structure-sensitive reaction. The effect is particularly pronounced for particles smaller than ~3.5 nm [6]. However, the particles used in this study are all larger than this and the narrow range of particle size minimises the effect. As a result, particle size effects cannot explain the variation in activities observed.

5 CONCLUSIONS

The Pt-Pt distance was found to be intrinsically linked to the Pt electronic properties and gave the best indication of oxygen reduction activity. Improved performance as a result of contraction of the Pt-Pt distance was attributed to the more favourable geometry benefiting the initial adsorption of molecular oxygen. The schematic in figure 32 demonstrates that a shorter Pt-Pt distance will more closely match the O-O bond allowing greater overlap between the oxygen molecular orbitals and the orbitals of surface platinum atoms. In terms of Pt electronic properties, increases in the 5d band vacancies, corresponding to shorter Pt-Pt distances, is thought to cause increased electron donation from oxygen to the surface Pt resulting in a weakening of the O-O bond.

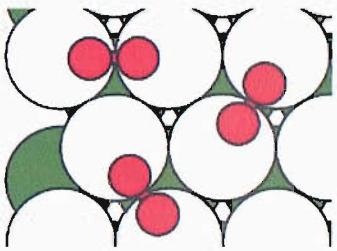

Figure 32 Schematic showing the adsorption of molecular oxygen on a platinum surface [48].

In contrast, Mukerjee *et al.* [13] have said that the important feature is the strength of the Pt-OH bond. If this bond is stronger, the number of free sites for molecular oxygen adsorption is limited resulting in reduced catalyst performance. To investigate this, the coverage of oxide on the Pt sites (N_{Pt-O}) was examined. No correlation between the Pt-O coordination number and catalyst activity was found. However, there are significant differences in the manner in which the XAS data were collected. Mukerjee *et al.* soaked the catalysts in 2M KOH prior to use, removing any residual oxides and unalloyed secondary metal. Their XAS data were collected in a flooded cell using $HClO_4$. The conclusions stated above are based on results for the untreated catalyst where the XAS data has been collected in a working fuel cell environment.

The results presented in this chapter highlight the importance of the data collection method. Half-cell studies carried out in addition to those in the mini-cell environment showed significant variation. More reducing conditions were observed with high numbers of metal neighbours and low numbers of oxygen neighbours. This was thought to be a result of the electrolyte and was particularly apparent for the PtCo catalyst where leaching of cobalt from the particle was observed.

6 REFERENCES

1. Ralph, T. R.; Hogarth, M. P. *Platinum Metals Rev.* **2002**, *46*, 3.
2. Yeager, E. *Electrochimica Acta* **1984**, *29*, 1527.
3. Yeager, E. *Journal of Molecular Catalysis* **1986**, *38*, 5.
4. Damjanovic, A.; Genshaw, M. A.; Bockris, J. O. M. *Journal of Chemical Physics* **1966**, *45*, 4057.
5. Gattrell, M.; MacDougall, B. *Handbook of Fuel Cells - Volume 2: Electrocatalysis*; John Wiley and Sons, 2003.
6. Kinoshita, K. *Journal of the Electrochemical Society* **1990**, *137*, 845.
7. Markovic, N.; Gasteiger, H.; Ross, P. N. *Journal of the Electrochemical Society* **1997**, *144*, 1591.
8. Luczak, F. J.; Landsman, D. A. *United States Patent*, 1984; Vol. 4 447 506.
9. Luczak, F. J.; Landsman, D. A. *United State Patent*, 1987; Vol. 4 677 092.
10. Beard, B. C.; Ross, P. N. *Journal of the Electrochemical Society* **1990**, *137*, 3368.
11. Glass, J. T.; Cahen, G. L.; Stoner, G. E. *Journal of the Electrochemical Society* **1987**, *134*, 58.
12. Min, M. K.; Cho, J. H.; Cho, K. W.; Kim, H. *Electrochimica Acta* **2000**, *45*, 4211.
13. Mukerjee, S.; Srinivasan, S.; Soriaga, M. P.; McBreen, J. *Journal of the Electrochemical Society* **1995**, *142*, 1409.
14. Mukerjee, S.; Srinivasan, S.; Soriaga, M. P.; McBreen, J. *Journal of Physical Chemistry* **1995**, *99*, 4577.
15. Toda, T.; Igarashi, H.; Uchida, H.; Watanabe, M. *Journal of the Electrochemical Society* **1999**, *146*, 3750.
16. Paulus, U. A.; Wokaun, A.; Scherer, G. G.; Schmidt, T. J.; Stamenkovic, V.; Radmilovic, V.; Markovic, N. M.; Ross, P. N. *Journal of Physical Chemistry B* **2002**, *106*, 4181.
17. Markovic, N. M.; Ross, P. N. *Surface Science Reports* **2002**, *45*, 121.
18. Hwang, B. J.; Tsai, Y. W.; Sarma, L. S.; Chen, C. H.; Lee, J. F.; Strehblow, H. H. *Journal of Physical Chemistry B* **2004**, *108*, 15096.

19. Nashner, M. S.; Frenkel, A. I.; Adler, D. L.; Shapley, J. R.; Nuzzo, R. G. *Journal of the American Chemical Society* **1997**, *119*, 7760.
20. Nashner, M. S.; Frenkel, A. I.; Somerville, D.; Hills, C. W.; Shapley, J. R.; Nuzzo, R. G. *Journal of the American Chemical Society* **1998**, *120*, 8093.
21. Murthi, V. S.; Urian, R. C.; Mukerjee, S. *Journal of Physical Chemistry B* **2004**, *108*, 11011.
22. Beard, B. C.; Ross, P. N. *Journal of the Electrochemical Society* **1986**, *133*, 1839.
23. Shim, J.; Lee, C. R.; Lee, H. K.; Lee, J. S.; Cairns, E. J. *Journal of Power Sources* **2001**, *102*, 172.
24. Mukerjee, S.; McBreen, J. *Journal of Electroanalytical Chemistry* **1998**, *448*, 163.
25. Benfield, R. E. *Journal of the Chemical Society-Faraday Transactions* **1992**, *88*, 1107.
26. Borodzinski, A.; Bonarowska, M. *Langmuir* **1997**, *13*, 5613.
27. Stamenkovic, V.; Schmidt, T. J.; Ross, P. N.; Markovic, N. M. *Journal of Physical Chemistry B* **2002**, *106*, 11970.
28. Yang, H.; Alonso-Vante, N.; Leger, J. M.; Lamy, C. *Journal of Physical Chemistry B* **2004**, *108*, 1938.
29. Guerin, S.; Hayden, B. E.; Lee, C. E.; Mormiche, C.; Owen, J. R.; Russell, A. E.; Theobald, B.; Thompsett, D. *Journal of Combinatorial Chemistry* **2004**, *6*, 149.
30. Thompsett, D. *Handbook of Fuel Cells - Volume 3: Fuel Cell Technology and Applications*; John Wiley and Sons, 2003.
31. Rho, Y. W.; Velev, O. A.; Srinivasan, S.; Kho, Y. T. *Journal of the Electrochemical Society* **1994**, *141*, 2084.
32. Rho, Y. W.; Srinivasan, S.; Kho, Y. T. *Journal of the Electrochemical Society* **1994**, *141*, 2089.
33. Paganin, V. A.; Freire, T. J. P.; Ticianelli, E. A.; Gonzalez, E. R. *Review of Scientific Instruments* **1997**, *68*, 3540.
34. Salgado, J. R. C.; Antolini, E.; Gonzalez, E. R. *Journal of Physical Chemistry B* **2004**, *108*, 17767.
35. Pantelouris, A.; Modrow, H.; Pantelouris, M.; Hormes, J.; Reinen, D. *Chemical Physics* **2004**, *300*, 13.

36. Moen, A.; Nicholson, D. G.; Clausen, B. S.; Hansen, F. L.; Molenbroek, A.; Steffensen, G. *Chemistry of Materials* **1997**, *9*, 1241.
37. Kelementiev, K. XANES dactyloscope Ruhr-Universitat Bochum, 2004.
38. Poumellec, B.; Marucco, J. F.; Touzelin, B. *Physical Review B* **1987**, *35*, 2284.
39. Carrrette, L. P. Characterisation of the Strong Metal-Support Interaction (SMSI) in Electrocatalysts. PhD, University of Southampton, 1998.
40. Farges, F.; Brown, G. E.; Rehr, J. J. *Physical Review B* **1997**, *56*, 1809.
41. Maniguet, S. EXAFS Studies of Carbon Supported Fuel Cell Electrocatalysts. PhD, University of Southampton, 2002.
42. Watanabe, M.; Tsurumi, K.; Mizukami, T.; Nakamura, T.; Stonehart, P. *Journal of the Electrochemical Society* **1994**, *141*, 2659.
43. Toda, T.; Igarashi, H.; Watanabe, M. *Journal of Electroanalytical Chemistry* **1999**, *460*, 258.
44. Mukerjee, S.; McBreen, J.; Reilly, J. J.; Johnson, J. R.; Adzic, G.; Petrov, K.; Kumar, M. P. S.; Zhang, W.; Srinivasan, S. *Journal of the Electrochemical Society* **1995**, *142*, 2278.
45. Shukla, A. K.; Neergat, M.; Bera, P.; Jayaram, V.; Hegde, M. S. *Journal of Electroanalytical Chemistry* **2001**, *504*, 111.
46. Christoffersen, E.; Liu, P.; Ruban, A.; Skriver, H. L.; Norskov, J. K. *Journal of Catalysis* **2001**, *199*, 123.
47. Christoffersen, E.; Stoltze, P.; Norskov, J. K. *Surface Science* **2002**, *505*, 200.
48. Lei, C. Using Ultrafast Extreme-ultraviolet Pulses for Time-resolved Dynamics of Molecules Chemisorbed on Metal Surfaces. PhD, University of Michigan, 2003.

Chapter Six: Conclusions and Further Work

The primary aim of this thesis has been to relate catalyst structure to performance. This has involved the development of a miniaturised PEM fuel cell (Chapter 3) allowing *in situ* XAS experiments to be carried out under realistic environments. The importance of these experiments has been highlighted by the results obtained for both anode and cathode catalysts.

A study of a series of PtRu anode catalysts with varying compositions was carried out in chapter 4. The PtRu catalyst with a 1:1 ratio was found to have the highest CO tolerance and optimum activity for methanol oxidation. EXAFS analysis under flooded conditions revealed that for platinum rich catalysts the bulk compositions did not match that of the surface. These particles were described as having a ruthenium rich core and Pt rich surface composition.

The 1:1 PtRu catalyst was investigated further using the *in situ* XAS mini-cell. The results highlighted the need for good mass transport and electrochemical contact to ensure full utilisation of the catalyst layer. Studies using reformate demonstrated the poor sensitivity of EXAFS towards surface species present on the catalyst particles. Further work could involve investigating ways of overcoming the limitations of the data analysis to allow detection of adsorbed surface species. Also, the mini-cell could be modified with relative ease to allow *in situ* studies of catalysts for methanol oxidation.

A study of platinum based cathode catalysts with varying secondary metals including: Cr, Co and Ti were carried out in chapter 5. The Pt-Pt distance, intrinsically linked to the Pt electronic properties, was identified as the dominating factor in terms of activity for oxygen reduction. The *in situ* studies under realistic conditions indicated that site blocking from Pt-OH was not correlated to the catalyst activity. Further work in this area could concentrate on improving the *in situ* XAS data quality at the secondary metal K absorption edge allowing shorter data collection times and more accurate data fits. This is very relevant for catalysts

containing titanium due to the low energy of the K absorption edge. To achieve this, changes in the cell design would be required. In particular, scatter from the humidifiers positioned above the cell window is significant at low energies.

The mini-cell opens up the possibility for a wide range of experiments. For both anode and cathode catalysts, stability is of key importance for the successful commercialisation of fuel cells [1,2]. Catalyst sintering and leaching of the secondary metal leads to reduced performance and limits the lifetime of a fuel cell. A number of factors can accelerate these processes for example: air bleeds and cell reversal. Air bleeds are used for fuel cells operating with reformate. The air reduces coverage of CO on the surface by catalytic oxidation allowing improved hydrogen electro-oxidation activity. Recombination reactions and CO oxidation are both highly exothermic and cause an increase in the local temperature within the MEA [3]. This can cause sintering of the anode catalyst. Cell reversal refers to a switch in polarity of the cell and can arise due to fuel or oxidant starvation. If the cell is starved of oxidant, the current flowing through the cathode is sustained by hydrogen evolution. This condition produces a significant amount of heat so catalyst stability is again an issue. The problem is more severe if the anode is starved of fuel. This causes an increase in the anode potential until water electrolysis occurs. The high potentials at the anode result in significant damage to the catalyst and carbon support [3].

By carrying out experiments over longer timescales, *in situ* XAS provides an ideal way of following these processes under realistic conditions. This should facilitate a greater understanding of the catalyst characteristics required for high stability which is essential for further development of fuel cell catalysts.

REFERENCES

1. Knights, D. S.; Colbow, K. M.; St Pierre, J.; Wilkinson, D. P. *Journal of Power Sources* **2004**, *127*, 127.
2. Ball, S. C. *Platinum Metals Rev.* **2005**, *49*, 27.
3. Ralph, T. R.; Hogarth, M. P. *Platinum Metals Rev.* **2002**, *46*, 117.